Adam Mickiewicz University, Poznań
Faculty of Physics
Astronomical Observatory Institute

Asteroid phase curves using dense ground-based lightcurves and sparse survey data

Emil Wilawer
PhD Thesis

supervisor: prof. UAM dr hab. Agnieszka Kryszczyńska
auxiliary supervisor: dr Dagmara Oszkiewicz

2024

Summary

The study of asteroids is essential for understanding the formation and evolution of the Solar System and other planetary systems. Analysing magnitude phase curves helps determine properties like size, albedo, surface characteristics, and composition of the objects. Traditional phase curves from dense ground-based observations are high-quality but costly and time-consuming, limiting the number of asteroids studied (Oszkiewicz et al., 2021). Sparse data from sky surveys like Gaia and ATLAS offer extensive photometric measurements but lack the temporal resolution for good phase curves on their own. This dissertation develops approaches to combine dense ground-based data with sparse sky survey data to obtain high-quality magnitude phase curves (Wilawer et al., 2022; Wilawer et al., 2024).

Gaia, though not dedicated to asteroid observation, provides numerous good-quality photometric measurements for thousands of objects. Using Gaia Data Release 2 and the combined dense ground-based data, I determined asteroid rotation periods and created composite lightcurves. Dense ground-based data refined the lightcurve shapes, and calibrated sparse GDR2 data were adjusted for amplitude to define phase curve points. This method allowed for the determination of the slope parameter β of the phase curve for several dozen objects, showing improvements over using sparse data alone and yielding results consistent with the literature.

In another study, I combined ground-based data with data from the two-filter ATLAS sky survey. The ATLAS data, taken in two broad filters, enabled the comparison of the wavelength dependency on the phase curve. Using a modified inversion method (Muinonen et al., 2022), I obtained the parameters G_1 and G_2 of the photometric function H, G_1, G_2 for several dozen asteroids, comparing them with albedo and taxonomic types from the literature. In many cases, particularly for S-type asteroids, distinct domains of G_1 and G_2 were found for both filters. This was then explained in the context of phase curve shape dependence on albedo for different taxonomic types. Most of the results were consistent with known taxonomic types, and more probable pole solutions were identified in a few cases. Likely classifications were proposed for asteroids with unknown taxonomic types. The wavelength dependence, which refers to how the observed brightness of an asteroid varies with the wavelength of light, was most clearly observed for S-type asteroids.

In the context of exponentially increasing data and new, larger sky surveys, the combined use of dense and sparse photometric data improves the accuracy of derived phase curve parameters. This approach enables the accurate determination of phase curve parameters for more objects and the prediction of taxonomic complexes without spectroscopic observations. Additionally, it serves as a valuable tool for verifying asteroid modelling results.

Keywords

asteroids – minor planets – photometry – phase curves – survey data

Streszczenie

Badanie planetoid jest kluczowe dla zrozumienia procesów formowania i ewolucji Układu Słonecznego oraz innych systemów planetarnych. Analiza krzywych fazowych pomaga określić właściwości takie jak rozmiar, albedo, cechy powierzchniowe oraz skład dla tych obiektów. Tradycyjne krzywe fazowe z gęstych obserwacji naziemnych są wysokiej jakości, ale kosztowne i czasochłonne, co ogranicza liczbę badanych planetoid (Oszkiewicz et al., 2021). Rzadkie dane z przeglądów nieba, takich jak Gaia i ATLAS, oferują obszerne pomiary fotometryczne, ale brakuje im rozdzielczości czasowej, aby tego typu dane były wystarczajace do skonstruowania dobrej jakosci krzywych fazowych. W tej rozprawie opracowałem metodę łączącą gęste dane naziemne z rzadkimi danymi z przeglądów nieba w celu uzyskania wysokiej jakości krzywych fazowych (Wilawer et al., 2022; Wilawer et al., 2024).

Gaia, mimo że nie jest dedykowana do obserwacji planetoid, dostarcza liczne pomiary fotometryczne dobrej jakości dla tysięcy obiektów. Korzystając z katalogu Gaia DR2 połączonego z gęstymi obserwacjami naziemnymi, określiłem okresy rotacji planetoid i stworzyłem złożone krzywe zmian blasku. Gęste dane naziemne pomogły okreslić kształt krzywych zmian blasku, a skalibrowane rzadkie dane z Gaia DR2 zostały poddane korekcie na amplitudę, co umożliwiło umieszczenie ich na odpowiednim miejscu na krzywej fazowej. Metoda ta umożliwiła określenie parametru nachylenia β krzywej fazowej dla kilkudziesięciu obiektów, pokazując poprawę w stosunku do wykorzystania tylko danych rzadkich oraz dając wyniki zgodne z literaturą.

W kolejnym badaniu połączyłem dane naziemne z danymi z przeglądu nieba ATLAS, prowadzonego w dwóch szerokopasmowych filtrach. Dane z przegladu ATLAS umożliwiły porównanie krzywych fazowych uzyskanych dla różnych długości fali. Za pomocą zmodyfikowanej metody inwersji Muinonen et al. (2022) uzyskałem parametry G_1 i G_2 funkcji fotometrycznej H, G_1, G_2 dla kilkudziesięciu planetoid, a następnie porównałem je z albedo i typami taksonomicznymi z literatury. W wielu przypadkach, szczególnie planetoid typu S, znaleziono odrębne obszary dla G_1 i G_2 w obu filtrach. Zjawisko to zostało wytłumaczone w kontekście zależności kształtu krzywej fazowej od albedo i typu taksonomicznego. Większość wyników była zgodna ze znanymi typami taksonomicznymi, a w kilku przypadkach zidentyfikowałem bardziej prawdopodobne rozwiązania dla biegunów. Zaproponowałem też potencjalne klasyfikacje dla planetoid o nieznanym typie taksonomicznym. Występowanie zjawiska zależności kształtu krzywych fazowych od długości fali było najbardziej wyraźne dla planetoid typu S.

W kontekście wykładniczo rosnącej ilości danych i nowych, większych przeglądów nieba, połączone wykorzystanie gęstych i rzadkich danych fotometrycznych poprawia dokładność parametrów krzywych fazowych. To podejście umożliwia dokładne określenie parametrów krzywych fazowych dla większej liczby obiektów oraz przewidywanie kompleksów taksonomicznych bez potrzeby wykonywania obserwacji spektroskopowych. Dodatkowo, stanowi cenne narzędzie do weryfikacji wyników modelowania planetoid.

Słowa kluczowe

planetoidy – małe ciała Układu Słonecznego – fotometria – krzywe fazowe – dane z przeglądów nieba

List of publications

1. Oszkiewicz, D., Wilawer, E., Podlewska-Gaca, E., Kryszczyńska, A., Kwiatkowski, T., Troianskyi, V., Koleńczuk, P., Föhring, D., Galád, A., Skiff, B. A., Geier, S., Borczyk, W., Moskovitz, N. A., Gajdoš, Š., Világi, J., Polcic, L., Kashuba, V., Benishek, V., & Shevchenko, V. (2021). First survey of phase curves of V-type asteroids. *Icarus*, *357*, 114158. https://doi.org/https://doi.org/10.1016/j.icarus.2020.114158

2. Wilawer, E., Oszkiewicz, D., Kryszczyńska, A., Marciniak, A., Shevchenko, V., Belskaya, I., Kwiatkowski, T., Kankiewicz, P., Horbowicz, J., Kudak, V., Kulczak, P., Perig, V., & Sobkowiak, K. (2022). Asteroid phase curves using sparse Gaia DR2 data and differential dense light curves. *Monthly Notices of the Royal Astronomical Society*, *513*(3), 3242–3251. https://doi.org/10.1093/mnras/stac1008

3. Wilawer, E., Muinonen, K., Oszkiewicz, D., Kryszczyńska, A., & Colazo, M. (2024). Phase curve wavelength dependency as revealed by shape- and geometry- corrected asteroid phase curves. *Monthly Notices of the Royal Astronomical Society*, *531*(2), 2802–2816. https://doi.org/10.1093/mnras/stae1282

Contents

Introduction

1.1 Asteroid photometric studies

Asteroids are small, rocky, irregular-shaped bodies that are remnants left over from the early formation of the Solar System about 4.6 billion years ago. They are a great source of information about the origins and evolution of planetary systems. In general, asteroids rotate about their main axis of inertia, and their surface is covered by a regolith, which is composed of dust and rocks of varying sizes. Figure 1 shows an image of the asteroid (4) Vesta, taken by NASA's Dawn spacecraft, illustrating the typical appearance and features observed in photometric studies.

Currently, photometry is the most successful method for studying the physical parameters of such objects. By analysing lightcurves (changes in brightness as a function of time), one is able to determine the rotational period, estimate shape, and spin axes coordinates. In addition, their phase curves give information about the variation of the disk-integrated brightness over the phase angle (the angle between the Sun, the asteroid, and the observer). The magnitude phase curves show that the brightness of an asteroid increases linearly with decreasing phase angle for large angles to about 7° and exponentially for smaller phase angles. At phase angles $< 7°$, the so-called opposition effect is observed, which appears as a non-linear increase in brightness (Muinonen et al., 2010a). This effect is primarily attributed to coherent backscattering and shadow hiding, where the former involves constructive interference of light waves, and the latter involves the reduction of shadows on the asteroid's surface (Muinonen et al., 2010b).

To describe this behaviour, several photometric models have been developed over the years: Hapke's (Hapke, 1963, 1966, 1981, 1984, 1986, 2002, 2008, 2012; Hapke & Wells,

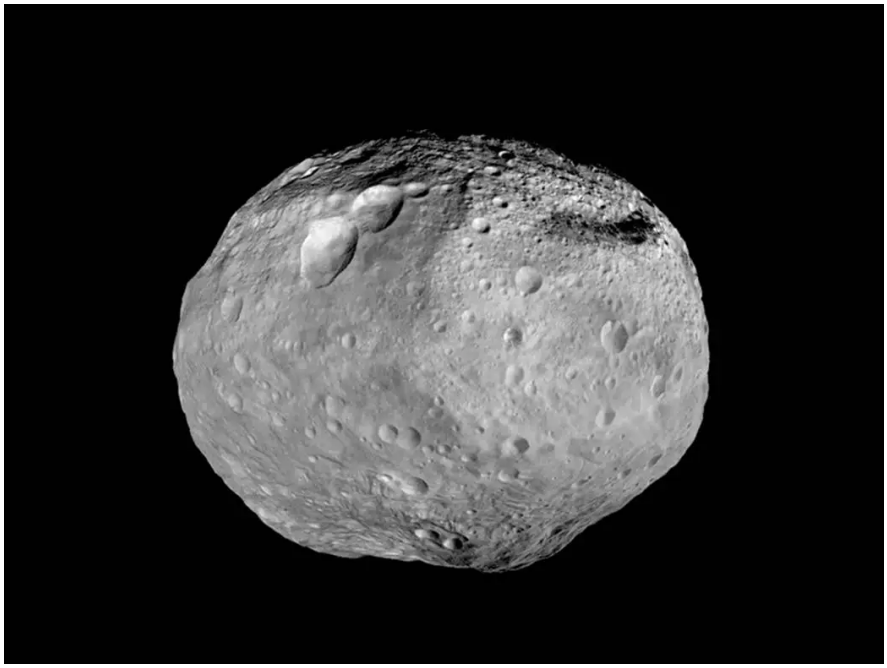

Figure 1: Image of an asteroid (4) Vesta taken by NASA's Dawn spacecraft. Image credit: NASA/JPL-Caltech/UCAL/MPS/DLR/IDA

1981), Akimov's (Akimov, 1975, 1979, 1988) and Shkuratov's (Shkuratov et al., 2011). In 1985, the International Astronomical Union adopted the H, G photometric model developed by Bowell et al. (1989), where H is the absolute magnitude defined as the apparent brightness in the Johnson V-band observed at a zero-degree phase angle reduced to a distance of 1 AU from both the Sun and the observer, and G is the slope parameter describing the shape of the phase curve. Although the H, G magnitude system successfully describes the shape of the phase curve over the wide range of phase angles, it does not accurately fit the opposition effect, especially for very dark or bright objects (Belskaya & Shevchenko, 2000). Muinonen et al. (2010a) proposed new H, G_1 G_2 and H, G_{12} phase functions. The was further improved by introducing H, G_{12}^* (Penttilä et al., 2016) to use with low-quality data.

The photometric phase curve reveals key details about the characteristics of the asteroids' surface, such as geometric albedo, composition, porosity, roughness, and grain size distribution. In particular, when asteroids are observed at phase angles greater than 7°, the high steepness of the phase curve indicates objects with low albedo and exposed regolith. In contrast, a flat phase curve suggests high-albedo asteroids with a clear presence of light scattering in their regolith. Phase curves can be an alternative to spectra in determining taxonomic

types. Figure 2 shows the phase curves for five main taxonomic types.

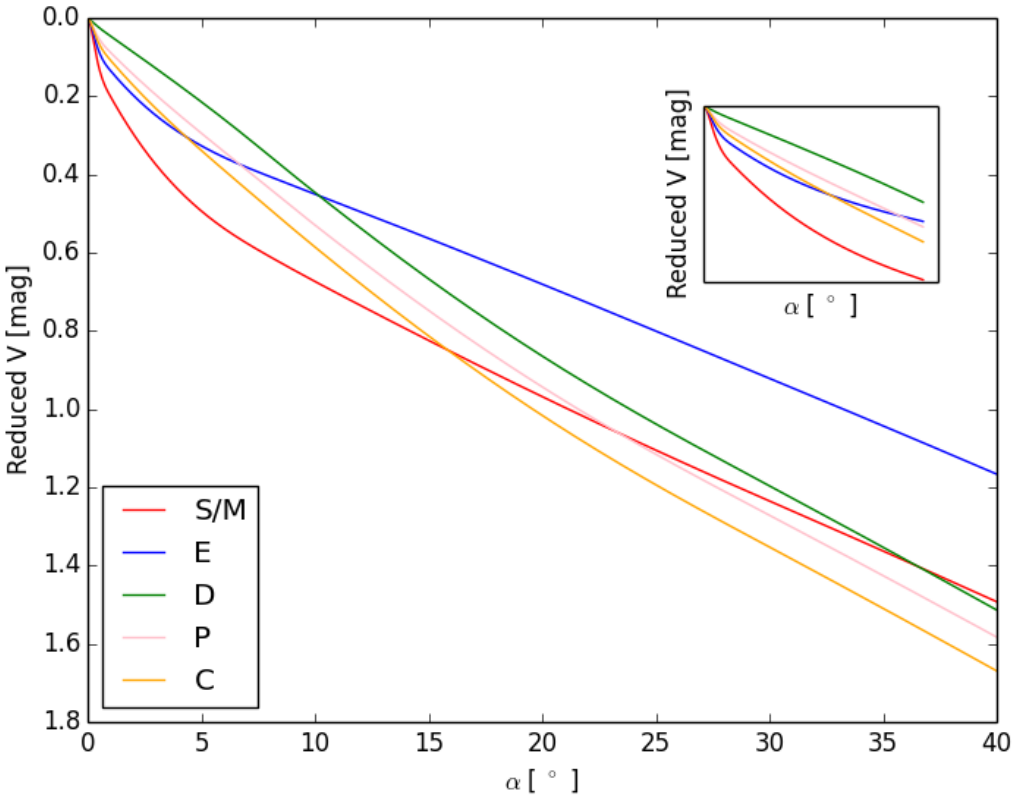

Figure 2: Phase curves for different taxonomic types. They can be used to constrain the asteroid's taxonomic classification. Adapted from Penttilä et al. (2016).

Traditionally, phase curves are derived from calibrated photometry dense lightcurves obtained from targeted ground-based observations. Observations are influenced by the modulation of the apparent magnitude resulting from the irregular shape and rotation of the asteroid, as well as potential offsets arising from varying viewing geometry when combining data from different apparitions to cover a wide range of phase angles. Examples of such targeted observational campaigns can be found in Oszkiewicz et al. (2021), Pravec et al. (2012), Shevchenko (1997), and Shevchenko et al. (2010), Shevchenko et al. (2016), Shevchenko et al. (2021). Due to the time-consuming nature of this approach, high-quality phase curves are available for merely a few hundred objects.

On the other hand, phase curves for many asteroids can be obtained using sparse photometric measurements from various surveys, but they often come with large uncertainties

(Alvarez-Candal et al., 2022; Vereš et al., 2015).

A vast amount of photometric data is available from various space missions and sky surveys. Gaia, a space-based observatory launched by the European Space Agency (ESA), is designed to precisely map the positions and proper motions of stars in our Galaxy. Although not primarily focused on asteroids, Gaia DR2 (Spoto et al., 2018) contains data for more than 14 000 asteroids, and Gaia DR3 (Tanga et al., 2023) provides data for more than 150 000 asteroids. Most of them were obtained at phase angles greater than 10°. The upcoming full data release of version DR4 is expected to provide data for 350 000 objects. The Sloan Digital Sky Survey (York et al., 2000), is a ground-based project that has extensively mapped the sky at multiple wavelengths, focussing on extragalactic objects. SDSS has contributed to the asteroid research by observing almost 50 000 objects in our Solar System. TESS (Transiting Exoplanet Survey Satellite), operated by NASA, searches for exoplanets by monitoring the brightness of stars. Although it is primarily focused on exoplanets, TESS also captured over 10 000 000 data points for 42 000 asteroids (Woods et al., 2021). The number of asteroids observed by the planned Large Synoptic Survey Telescope (LSST) sky survey will exceed 5 millions objects.

In addition, there are surveys that were designed with asteroid observations in mind. Pan-STARRS (Panoramic Survey Telescope and Rapid Response System) (Chambers & Pan-STARRS Team, 2018) was designed specifically to survey the sky, detect and track moving objects, especially Near-Earth Asteroids (NEA) and Potentially Hazardous Asteroids (PHA), Lincoln Near-Earth Asteroid Research (Stokes et al., 2000) which observed more than 150 000 asteroids, and Asteroid Terrestrial-impact Last Alert System (Heinze et al., 2018) providing data for 580 000 asteroids in two distinct filters: cyan and orange.

1.2 The aim of the thesis

Traditional phase curve retrieval requires costly, time-consuming observations carried out over months (typically, obtaining dense lightcurves from several months of observations for a single object). These observations enable the determination of accurate phase curves. However, due to the amount of time dedicated to each object, obtaining such phase curves for many objects is very limited, if not impossible. This hinders population-level studies.

On the other hand, large sky surveys such as Gaia, ATLAS, or LSST, produce vast amounts of data, allowing for the determination of phase curves for a large number of objects. However, these surveys sample photometric lightcurves at random points, resulting in random geometries. Therefore, phase curves determined based on survey data have been of low quality. It is necessary to adapt the methods of determining phase curves to specific sky surveys and to consider corrections for the amplitude of the lightcurves, asteroid's shape, and the observing geometry. Furthermore, these data are subject to various systematic and random errors and are conducted in different filters. Additionally, some sky surveys do not produce data at small phase angles and are not suitable for traditional modelling. Therefore, it was necessary to develop and implement methods for determining phase curves tailored to these data.

The primary goal of this work was to develop new approaches for determining phase curves that are adapted to data from both sky surveys and traditional ground-based observations, and to apply these methods to the available photometric data. Novel methods and approaches are necessary to obtain phase curves from such vast datasets with the best possible precision and accuracy.

In Chapter 2 I describe the methodology standards and software tools utilised in this work. In Chapter 3 I present the results obtained from my studies and their corresponding publications. In Chapter 4 I discuss the conclusions drawn from this research and propose directions for future work.

Methodology and software

2.1 Data reduction and photometry

Aperture photometry is a crucial first step in obtaining an asteroid phase curve. The process begins with the reduction of raw FITS frames, including bias correction, dark subtraction, and flat-fielding, to ensure accurate measurements. Figure 3 illustrates the impact of reduction on raw FITS frames, showing the before and after effects of the reduction processes. Next, an appropriate aperture size is selected to encompass the target asteroid's flux, while an annulus around the aperture is used to measure the background sky brightness. It is essential to include comparison stars (the ones of known brightness) within the frame to calibrate the asteroid's brightness and account for atmospheric variations. By summing the pixel values within the aperture and subtracting the background, we obtain the asteroid's brightness. This measured brightness is then converted to a standardised magnitude, providing the data needed for phase curve analysis.

2.1.1 Photometry Pipeline

The Photometry Pipeline (PP) (Mommert, 2017) is an automated software suite designed for the streamlined analysis of reduced data obtained from small to medium-sized observatories. It facilitates the entire photometric process, from image registration to target identification, with minimal human intervention. PP utilises well-established tools such as Source Extractor[1] and SCAMP[2] for source identification, aperture photometry, and image registration.

Key features of PP include:

[1] https://www.astromatic.net/software/sextractor/
[2] https://www.astromatic.net/software/scamp/

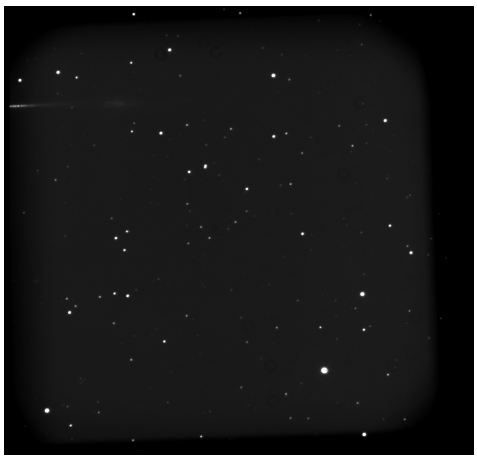

(a) Raw frame.

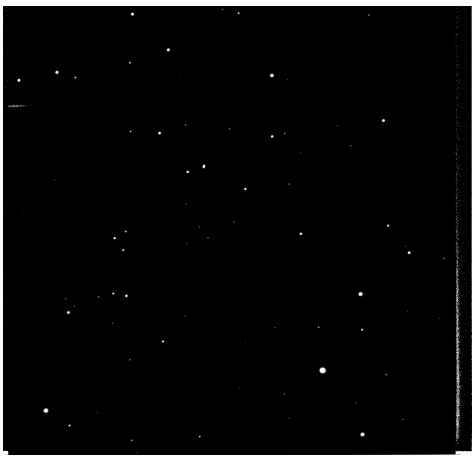

(b) Reduced frame.

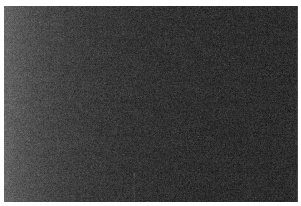

(c) Bias frame.

(d) Dark frame.

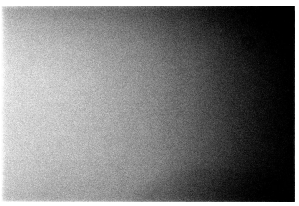

(e) Flat frame.

Figure 3: Illustration of various types of FITS frames used in astronomical imaging. (a) Raw FITS frame containing unprocessed astronomical data and instrumental artefacts. (b) Reduced FITS frame corrected for bias, dark current, and flat-fielding, resulting in accurate astronomical measurements. (c) Bias frame capturing the electronic offset or bias present in the camera's sensor. (d) Dark frame recording the thermal signal produced by the camera's sensor in the absence of light. (e) Flat frame capturing spatial variations in sensitivity across the camera's sensor.

- automated aperture photometry utilizing curve-of-growth analysis;
- photometric calibration in various filters (e.g., ugriz, BVRI, JHK) based on catalogue coverage;
- full support for photometry of moving targets;
- target identification based on tabulated positions, adjusted to both fixed and moving targets;
- utilization of Gaia (DR1) astrometry for image registration.

Although PP has been primarily developed for asteroid observations, it is adaptable to various types of imaging data. It is particularly well-suited for datasets with a field-of-view of

several arcminutes, ensuring an adequate number of background stars for reliable registration and photometric calibration. The calibrated magnitudes produced by PP typically exhibit accuracies within ≤ 0.03 mag, with astrometric accuracies around 0.3 arcsec relative to the catalogues used in registration. Figure 4 illustrates the functionality of the PP by showcasing detected light sources on a frame and the resulting lightcurve of an asteroid.

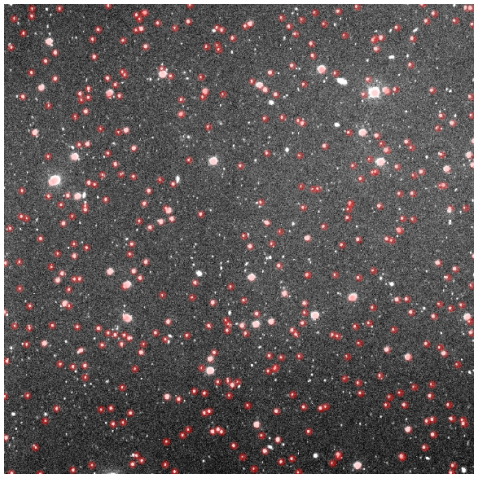

(a) All light sources detected by PP in a single frame.

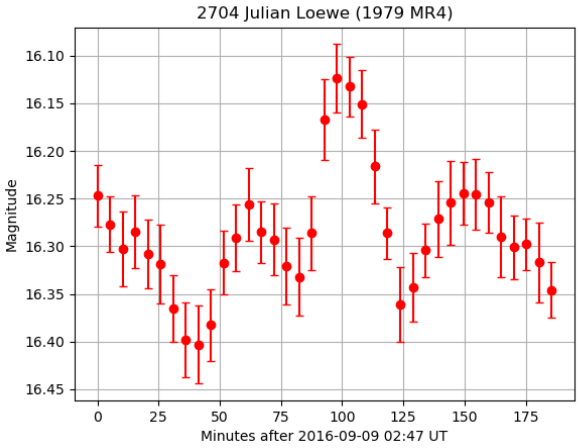

(b) Final lightcurve of an asteroid produced by PP.

Figure 4: Illustration of the Photometry Pipeline functionality. (a) A frame showing all detected light sources (marked with red circles). (b) The resulting lightcurve of an asteroid, with relative magnitudes obtained using the Lowell Observatory Hall 42-inch telescope. Errors arise from the calibration process using the Pan-STARRS catalogue.

During my doctoral studies, I had the opportunity to visit the Lowell Observatory in 2018 and work under the guidance of Dr. Michael Mommert. During my time there, I learnt about the Photometry Pipeline software firsthand. M. Mommert showed me how to use the software for analysing the brightness of asteroids, how to customise its settings, how to read and analyse the output, how to debug occurring errors, and how to integrate it with different telescopes. This experience was invaluable, as it allowed me to set up a local version of the PP on the Astronomical Observatory Institute of Adam Mickiewicz University servers.

At the time being, the software widely used in the photometry process at the observatory was the STARLINK[3] package. The photometry process using this software has been refined over the years in terms of parameter selection and the quality of the obtained results. However,

[3] https://starlink.eao.hawaii.edu/starlink/WelcomePage

it was a semi-automated process — a set of auxiliary scripts required manual intervention, which became a bottleneck as the influx of data increased.

In response to the growing volume of data for analysis, my efforts facilitated the automation of the photometry process within our institute, which is especially crucial considering the increasing volume of data being processed and the development of new telescopes. My main goal was to align the PP with our internal photometry standards while processing observational data gathered by the telescopes frequently used within our institute. Following a series of comparison tests, doubling the automatic aperture size selected by PP emerged as the solution to ensure consistent results. Furthermore, I had to create configuration entries for the telescopes to enable PP to effectively process the data from them. The data that needed to be provided in the telescope configuration included frame orientation, binning, mapping keywords from FITS headers, and filter names. I established and tested configurations for RBT/PST2 (Roman Baranowski Telescope/Poznań Spectroscopic Telescope 2 in Arizona, USA), UBC (University of British Columbia telescope in Cerro Tololo, Chile), and PIT (Poznań Imaging Telescope in Borowiec, Poland) telescopes. I conducted training sessions to share my knowledge with interested colleagues, equipping them with the skills to utilise PP in the research conducted at our institute effectively. The modified version of the software is publicly available on my GitHub page[4].

2.1.2 ATLAS6

I participated in the European Space Agency (ESA) grant: Service for Archival NEO Orbital and Rotational Data Analysis (SANORDA), (Kluwak et al., 2021). The main objective of SANORDA was to develop a service that provides access to archival orbital and photometric data on near-Earth asteroids, offering users a convenient platform for data search and visualisation. I was particularly involved in the development of the ATLAS6 format (Wilawer and Kwiatkowski (2017); described here) and PCFit software (Wilawer (2018); described in Section 2.2.3).

ATLAS6 is a file format designed for storing photometric data of asteroids. It was designed on the foundations laid by the preexisting ATLAS4 and ATLAS5 formats used by the Asteroid Photometric Catalog and Standard Asteroid Photometric Catalog, respectively

[4] https://github.com/wilawerek/photometrypipeline

(Lagerkvist et al., 1987). In line with grant objectives, specific improvements were implemented in the ATLAS6 format. Notably, the SANORDA service, primarily designed for Near Earth Objects (NEOs), emphasised the need to accommodate dynamically changing observational geometries. To address this, the original `DATA` block of the ATLAS4 and ATLAS5 files was augmented. The heliocentric Cartesian coordinates (x, y, z) of both the asteroid and the telescope were integrated, facilitating correction of observations. Moreover, this enhancement allows for the adjustment of observed asteroid brightness concerning the varying distance from the Earth and the Sun. The centre of the reference frame was shifted from the Earth's centre to the topocentric position of the telescope for more accurate computations.

Additionally, this format has been adopted as the input format for PerFit software (Kwiatkowski et al., 2009) used to accurately determine the rotation period of asteroids based on photometric observations using Fourier series fitting.

2.1.3 PerFit

PerFit is a Python software utilised to determine the asteroid lightcurve shape and the synodic rotation period. The software approximates the variations of the asteroid light $V(t)$ using a Fourier series, which depends on time t and period P. The equation used for modelling is:

$$V(t) = \overline{V} + \sum_{k=1}^{n} \left(A_k \sin \frac{2\pi k(t - t_0)}{P} + B_k \cos \frac{2\pi k(t - t_0)}{P} \right), \tag{1}$$

where $\overline{V}$ is the average brightness for a single lightcurve, A_k and B_k are Fourier coefficients, P is the synodic period, t is the time of a given observation, and t_0 is the time of the first observation in the provided dataset. Assuming the synodic period is a fixed value, the relation is linear, so the fit can be performed using the least-squares method. This involves finding the best-fitting parameters $\overline{V}$, A_k, and B_k by minimising the value χ^2, which measures the goodness of fit. See Kwiatkowski et al. (2009) for a more detailed description.

In Wilawer et al. (2022) (detailed in Section 3.2), I customised the existing PerFit software to suit the specific needs of my study. This involved adapting the software to effectively manage a combination of sparse data from Gaia DR2 and dense ground-based data. In addition, I refined the composite lightcurve plots to enhance their clarity and readability.

2.2 Phase function fitting

Selecting the appropriate magnitude phase function is essential for accurate phase function fitting, as it depends on the nature and quality of the observational data. This section covers the magnitude phase functions and traditional phase curves as well as the methods I used in my research to derive phase curves from sparse data.

2.2.1 Magnitude phase functions

The H, G phase function

To describe the magnitude-phase angle relationship, Bowell et al. (1989) proposed the H, G photometric model, which was adopted by the International Astronomical Union (IAU) in 1985. In this model, H represents the absolute magnitude in the Johnson V filter observed at a phase angle of 0°, while G is the slope parameter that describes the shape of the phase curve.

The model expresses the reduced observed magnitudes $V(\alpha)$ as follows:

$$\begin{aligned} 10^{-0.4V(\alpha)} &= a_1\phi_1(\alpha) + a_2\phi_2(\alpha) \\ &= 10^{-0.4H}[(1-G)\phi_1(\alpha) + G\phi_2(\alpha)], \end{aligned} \tag{2}$$

where α is the phase angle, $V(\alpha)$ is the V magnitude reduced to unit distances from Earth and Sun, and $\phi_1(\alpha)$ and $\phi_2(\alpha)$ are the basis functions normalized to unity for $\alpha = 0°$. These functions are given by:

$$\begin{aligned} \phi_1(\alpha) =& w\left(1 - \frac{0.986\sin\alpha}{0.119 + 1.341\sin\alpha - 0.754\sin^2\alpha}\right) \\ &+ (1-w)\exp\left(-3.332\tan^{0.631}\frac{1}{2}\alpha\right), \\ \phi_2(\alpha) =& w\left(1 - \frac{0.238\sin\alpha}{0.119 + 1.341\sin\alpha - 0.754\sin^2\alpha}\right) \\ &+ (1-w)\exp\left(-1.862\tan^{1.218}\frac{1}{2}\alpha\right), \\ w =& \exp\left(-90.56\tan^2\frac{1}{2}\alpha\right). \end{aligned} \tag{3}$$

The coefficients a_1 and a_2 can be derived from observations using linear least-squares methods. The absolute magnitude H and the coefficient G are then calculated as follows:

$$H = -2.5 \log_{10}(a_1 + a_2), \quad G = \frac{a_2}{a_1 + a_2}. \tag{4}$$

Despite this function accurately describing the phase function shape up to 120° phase angle, it does not fit the opposition effect well for very dark and very bright objects.

The $H,\ G_1,\ G_2$ phase function

The $H,\ G_1,\ G_2$ phase function, a significant improvement over the H, G phase function, was introduced by Muinonen et al. (2010a) and later adopted by the IAU in 2012. In this model, the reduced observed magnitudes $V(\alpha)$ can be obtained from:

$$\begin{aligned} 10^{-0.4V(\alpha)} &= a_1\phi_1(\alpha) + a_2\phi_2(\alpha) + a_3\phi_3(\alpha) \\ &= 10^{-0.4H}[G_1\phi_1(\alpha) + G_2\phi_2(\alpha) + (1 - G_1 - G_2)\phi_3(\alpha)] \end{aligned} \tag{5}$$

The basis functions ϕ_1, ϕ_2, ϕ_3 are defined as follows:

- for $0° < \alpha \leq 7.5°$:
  - $\phi_1(\alpha) = 1 - \frac{6\alpha}{\pi}$;
  - $\phi_2(\alpha) = 1 - \frac{9\alpha}{5\pi}$;
  - $\phi_3(\alpha)$ is defined using cubic splines defined in Table 2.
- for $7.5° < \alpha \leq 30°$:
  - $\phi_1(\alpha)$ is defined using cubic splines defined in Table 1;
  - $\phi_2(\alpha)$ is defined using cubic splines defined in Table 1;
  - $\phi_3(\alpha)$ is defined using cubic splines defined in Table 2.
- for $30° < \alpha \leq 150°$:
  - $\phi_1(\alpha)$ is defined using cubic splines defined in Table 1;
  - $\phi_2(\alpha)$ is defined using cubic splines defined in Table 1;

– $\phi_3(\alpha) = 0$.

Values at intermediate phase angles are determined using cubic splines that pass through the listed points, ensuring that the first derivatives are continuous at each point. The boundary values used for the cubic splines are as follows: $\phi_1'(\frac{\pi}{24}) = -\frac{6}{\pi}$, $\phi_1'(\frac{5\pi}{6}) = -9.1328612 \times 10^{-2}$, $\phi_2'(\frac{\pi}{24}) = -\frac{9}{5\pi}$, $\phi_2'(\frac{5\pi}{6}) = -8.6573138 \times 10^{-8}$, $\phi_3'(0) = -1.0630097$, $\phi_3'(\frac{\pi}{6}) = 0$.

Table 1: The basis functions ϕ_1 and ϕ_2 of the $H,\ G_1,\ G_2$ phase function.

α [°]	$\phi_1(\alpha)$	$\phi_2(\alpha)$
7.5	7.5×10^{-1}	9.25×10^{-1}
30.0	3.3486016×10^{-1}	6.2884169×10^{-1}
60.0	1.3410560×10^{-1}	3.1755495×10^{-1}
90.0	5.1104756×10^{-2}	1.2716367×10^{-1}
120.0	2.1465687×10^{-2}	2.2373903×10^{-2}
150.0	3.6396989×10^{-3}	1.6505689×10^{-4}

Table 2: The basis function ϕ_3 of the $H,\ G_1,\ G_2$ phase function.

α [°]	$\phi_3(\alpha)$
0.0	1
0.3	8.3381185×10^{-1}
1.0	5.7735424×10^{-1}
2.0	4.2144772×10^{-1}
4.0	2.3174230×10^{-1}
8.0	1.0348178×10^{-1}
12.0	6.1733473×10^{-2}
20.0	1.6107006×10^{-2}
30.0	0

Similar to the $H,\ G$ photometric function, the coefficients a_1, a_2, a_3 can be derived from observations using linear least-squares. The absolute magnitude H and the coefficients G_1 and G_2 are calculated as follows:

$$\begin{aligned} H &= -2.5 \log_{10}(a_1 + a_2 + a_3), \\ G_1 &= \frac{a_1}{(a_1 + a_2 + a_3)}, \\ G_2 &= \frac{a_2}{(a_1 + a_2 + a_3)}. \end{aligned} \tag{6}$$

This three-parameter photometric function is best used with high-quality observational data, providing more accurate phase curve fits compared to the two-parameter $H,\ G$ model.

The H, G_{12} phase function

In this model, the G_1 and G_2 parameters of the previous photometric function are replaced by a single parameter, G_{12}. The reduced observed magnitudes $V(\alpha)$ can be obtained from:

$$10^{-0.4V(\alpha)} = L_0[G_1\phi_1(\alpha) + G_2\phi_2(\alpha) + (1 - G_1 - G_2)\phi_3(\alpha)], \tag{7}$$

where

$$\begin{aligned} G_1 &= \begin{cases} 0.7527G_{12} + 0.06164, & G_{12} < 0.2 \\ 0.9529G_{12} + 0.0216, & G_{12} \geq 0.2, \end{cases} \\ G_2 &= \begin{cases} -0.9612G_{12} + 0.6270, & G_{12} < 0.2 \\ -0.6125G_{12} + 0.5572, & G_{12} \geq 0.2, \end{cases} \end{aligned} \tag{8}$$

and L_0 is the disk-integrated brightness at a phase angle of $\alpha = 0°$. The basis functions ϕ_1, ϕ_2, and ϕ_3 are those of the H, G_1, G_2 photometric function. In this case, the coefficients L_0 and G_{12} can be derived from observations using non-linear least-squares fitting.

The linear-exponential phase function

In addition to the phase functions described above, a linear-exponential model can also be used to represent the magnitude-phase angle relationship. This model is particularly useful for fitting data subsets with specific characteristics or limited observational data. The linear-exponential function on magnitude scale is defined as:

$$-2.5 \log \phi(\alpha) = -m_0 \exp -\frac{\alpha}{\alpha_0} + m_0 + \beta_0 \alpha, \tag{9}$$

where α is the phase angle, m_0 is the amplitude and α_0 is the width of the opposition effect, and β_0 is the slope parameter.

This model captures both the linear increase in brightness with phase angle and the non-linear opposition effect observed at small phase angles, making it a versatile tool for analysing photometric data.

2.2.2 Traditional approach using lightcurve maxima

Traditionally, asteroid phase curves are derived from dense relative photometry. Preferably obtained at varying phase angles and approximately the similar viewing geometry to account

for changes in brightness owing to aspect, irregular shape, and rotation, and possibly covering data at $\alpha < 1^\circ$ for best-quality phase curves. However, this is not always possible due to geometric constraints. The first crucial step is to incorporate the light-time correction to account for the time it takes for light to travel from the asteroid to the observer. This correction can be calculated using the equation $t_0 = t - \frac{\Delta}{c}$, where t represents the time of observing the object from the observer's position, Δ denotes the distance between the object and the observer, and c denotes the speed of light.

The next step involves correcting the brightness of an object to a unit distance of 1 au from the observer and the Sun resulting in reduced magnitudes: $m_0 = m - 5 \cdot \log_{10}(\Delta \cdot r)$, where m represents the relative brightness in magnitude, Δ denotes the object's distance from the observer, and r indicates the object's distance from the Sun.

The last correction to apply is the lightcurve amplitude correction, which accounts for changes in brightness as a result of the rotation of an asteroid. This correction is necessary to reduce the scatter on the phase curve. This correction ensures that the resulting phase curves accurately represent the overall brightness variation of the asteroid as a function of phase angle.

To perform the amplitude correction, the initial step involves applying Equation 1 to the dataset. By modifying $\overline{V}$, the dataset is shifted vertically, thereby reducing the dispersion of brightness values. The least-squares method is used to achieve this optimal alignment, ensuring an accurate fit on the y-axis. This adjustment aligns the brightness levels across different observations, enhancing data consistency and comparability. With $\overline{V}$ determined, V_{max} can be calculated by adding half of the amplitude from the Fourier fit.

In constructing the phase curve, I opted to utilise the peak brightness instead of the average or minimum brightness of the lightcurve. This decision was based on the fact that peak brightness values typically have smaller uncertainties than minima or mid-values. Additionally, maxima are the least influenced by the amplitude variations of the lightcurve, which vary with the phase angle (Dunlap et al., 1973; Sather, 1976). When merging data from various oppositions, where the asteroid is observed from different aspects, the peak brightness is less affected by changes in aspect compared to the mean brightness (Dunlap & Gehrels, 1969). Using the brightness minima in creating phase curves may introduce significant errors due to the typically lower signal-to-noise ratio at these points.

In conclusion, after obtaining the maximum brightness for individual lightcurves, we proceed to construct a plot of $V_{max}(\alpha)$, where α denotes the phase angle. Each lightcurve contributes one point to the phase curve, allowing us to visualise the magnitude phase curve, showcasing the asteroid's brightness variation as a function of the phase angle. An example of a phase curve is shown in Figure 5. These data are then fitted with various magnitude phase functions.

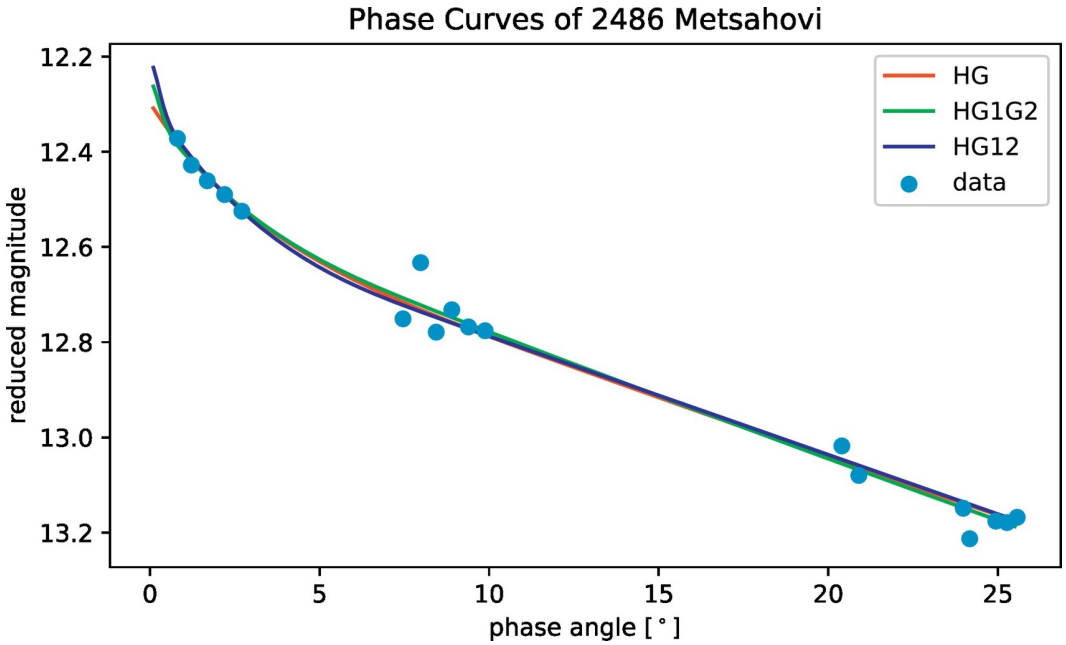

Figure 5: An example of a magnitude phase curve for asteroid (2486) Metsahovi. Blue dots represent V_{max} derived from each lightcurve. Red, green, and blue lines represent the fitted H, G; H, G_1, G_2; H, G_{12} magnitude phase functions respectively. Source: (Oszkiewicz et al., 2021)

2.2.3 PCFit

During my doctoral studies, I was one of the main developers of PCFit (Wilawer, 2018). It is a software written in Python whose task is to fit the traditional phase functions H, G; H, G_1, G_2; and H, G_{12} to the observational data (Bowell et al., 1989; Muinonen et al., 2010a). The input data should be saved in a modified `.tab` format used in the Kharkiv Asteroid Magnitude-Phase Relations database (Shevchenko et al., 2010). The input file should contain information about the asteroid's number and name, observing time, ecliptic coordinates of the asteroid, observation geometry, and object brightness in magnitudes. My modified `.tab`

version requires an additional column with the name of the filter used during the observation. Each row in the input file shall correspond to an observational night. The software individually fits each of the phase functions to the data and calculates the absolute brightness H, and the phase curve parameters corresponding to the given phase function. The final files consist of a text file with parameter values and a plot depicting the input data and fitted functions. Figure 5 shows a plot generated by PCFit.

This software was developed as part of the NEO Phase-curve Analysis Tool under the European Space Agency grant: SANORDA. (Wilawer, 2018). The application of this software is shown in Oszkiewicz et al. (2021).

2.2.4 Phase curves from mixed dense and sparse data

Traditional ground-based observations are conducted over several months, sometimes extending to half a year. These observations usually cover a significant portion or even the entire rotation period of the target during a single night. However, this approach is feasible for only a small set of targets. In contrast, sky surveys provide sparse data, offering only a few observational points per day but for many objects. This introduces challenges in deriving phase curves from such data alone. Since the observations are not specifically targeted, the collected points are distributed randomly over time and in various geometric contexts. This randomness makes it difficult to determine the rotational period and to create composite lightcurves. To address these challenges and fully utilise the sparse data, a new method for incorporating them into the phase curve was needed.

In Wilawer et al. (2022) I presented a method that I developed to successfully derive phase curves using dense ground-based data combined with sparse data from Gaia DR2 (Gaia Collaboration et al., 2016). In Wilawer et al. (2024) I combined dense lightcurves with sparse ATLAS dual-band photometry.

Linear phase curves with Gaia DR2 data

Photometric data from Gaia DR2 consist of sparse measurements, with single brightness observations distributed over long intervals. A phase curve derived solely from such points may be prone to errors, as the observing geometry can change significantly over time, affecting the

fitted phase function parameters. Correcting for these geometric changes requires knowledge of the asteroid's rotation period and lightcurve shape. At the time of the study, the Gaia data had too few observational points to directly determine the lightcurve shape, making it impossible to obtain a high-quality phase curve.

To address this, I used traditional dense differential observational data from ground-based observatories during the Gaia epoch (2014-2016). This data was used to determine the lightcurve shape and rotation period. Subsequently, Gaia data were overlaid on the derived brightness curve to apply the necessary corrections.

I utilised PerFit software (described in Section 2.1.3) to determine the rotation period and create a composite lightcurve using both dense and sparse data. Dense ground-based observations helped estimate the shape of the lightcurve, allowing for amplitude corrections to be applied to the sparse points and correctly placing them on the curve. This enabled interpolation of the maximum brightness for each Gaia observation based on the fitted Fourier series. The obtained maximum brightness values were then used to construct the phase curve.

Since Gaia observes asteroids at phase angles greater than 10°, I fitted a linear function. The parameters of this function allowed me to determine the slope parameter β. The results obtained using this method are described in Section 3.2.

Bayesian lightcurve inversion using ATLAS data

The Bayesian lightcurve inversion method is a sophisticated statistical approach for deducing the physical properties of asteroids from their observed lightcurves. It combines observational data with prior knowledge to estimate model parameters, providing a probabilistic framework that includes uncertainty quantification.

The forward model of asteroid light scattering utilises the Lommel-Seeliger surface reflection coefficient to describe the light scattering properties of the asteroid surfaces (Muinonen et al., 2022). The Lommel-Seeliger reflection coefficient is given by:

$$\begin{aligned} R_{LS}(\mu, \mu_0, \phi) &= 2p\phi_{11}(\alpha)\frac{1}{\mu + \mu_0}, \\ \mu_0 &= cos\iota, \\ \mu &= cos\epsilon, \end{aligned} \tag{10}$$

where p is the geometric albedo, α is the phase angle, ι is the angle of incidence, ϵ is the angle of emergence, and ϕ is the azimuth angle with the Sun at $\phi = 0°$. The phase function $\phi_{11}(\alpha)$ is expressed as:

$$\begin{aligned} \phi_{11}(\alpha) &= \frac{\phi(\alpha)}{\phi_{LS}(\alpha)}, \\ \phi_{LS}(\alpha) &= 1 - \sin\frac{1}{2}\alpha \, \tan\frac{1}{2}\alpha \, \ln(\cot\frac{1}{4}\alpha), \\ \phi_{11}(0) &= \phi(0) = \phi_{LS}(0) = 1 \end{aligned} \tag{11}$$

where ϕ is the phase function and $\phi_{LS}(\alpha)$ is the phase function for a spherical asteroid with isotropic single scattering $\phi_{11} = 1$.

When using the convex shape model, the parameters of the asteroid forward model are described by the vector:

$$\mathbf{P} = (P, \lambda, \beta, \varphi_0, s_{00}, \ldots, s_{l_{\max} l_{\max}}, G_1, G_2)^T, \tag{12}$$

where the parameters (unknowns) are: the rotation period, ecliptic pole longitude and latitude, rotational phase, spherical harmonics coefficients and the two H, G_1, G_2 phase function parameters.

The Bayesian inverse method is formulated in magnitude space, incorporating an observational error model. It employs a random walk Markov Chain Monte Carlo (MCMC) method to characterise the multidimensional probability density of the free parameters. This involves creating virtual observations by adding Gaussian random errors to the original observations and using these to construct an MCMC proposal probability density based on least squares solutions. (Muinonen et al., 2020; Muinonen et al., 2022)

Given the complexity introduced by photometry in multiple colours provided by ATLAS, the method solves the inverse problem in two stages. First, it addresses the spin and shape parameters using dense, differential ground-based photometry without modelling the photometric phase function. A simplified two-parameter linear-exponential phase function is used for these computations. Second, the method uses the derived spin and shape solutions in an additional MCMC process that samples both the photometric parameters (G_1, G_2) and the existing spin and shape parameters. This stage involves separate treatments for the cyan and orange photometry, which ultimately yields MCMC samples of ($G_{1\text{cyan}}$, $G_{2\text{cyan}}$) and

$(G_{1\mathrm{orange}},\ G_{2\mathrm{orange}})$.

The process begins with the initial treatment of photometric lightcurves, classifying them into differential or absolute, and further into dense or sparse categories. Dense lightcurves are fitted with cubic splines, with the number of nodes determined statistically using the Bayesian information criterion. Initial error models are assigned on the basis of the root-mean-square (RMS) values of these spline fits for dense lightcurves, and initial values are set for sparse lightcurves.

Following this, the spherical harmonics coefficients for the Gaussian surface density are computed using the input axial ratios of a realistic ellipsoid. This is followed by computing least squares solutions using a simplified, fixed observational error model, which is then iteratively refined to improve accuracy.

Virtual lightcurves are generated by adding Gaussian errors to the original lightcurves. The least-squares solutions for these virtual lightcurves are computed, and these solutions guide the random-walk MCMC computations, incorporating additional randomisation within the parameter space.

In the final step, the sparse lightcurves in two colours are analysed using the spin and shape solutions obtained from dense ground-based lightcurves through MCMC. MCMC samples provide a statistical description of the parameters, allowing a robust estimation of the physical characteristics of the asteroid.

During my research visit to the University of Helsinki, Professor Karri Muinonen introduced me to this method and explained the functionality of the various modules of the lightcurve inversion (LCI) software, previously applied only to the sparse data alone. We discussed method modifications and established the best procedure to be used with the combined dataset at hand. The first attempts to use the software for the Wilawer et al. (2024) publication, which focused on comparing the results in two filters, led to refinements of the computational methods and expansion of the software with new functionalities. Specifically, we developed a procedure to integrate dense ground-based data, which define the asteroid model, with sparse survey data used to determine the phase curve parameters. This included treating ground-based and sparse data separately before combining them in the analysis. These updates were vital for effectively handling three sets of observational data across different LCI modules: differential dense ground-based data and calibrated sparse data in cyan

and orange filters from the ATLAS survey. The positive findings, discussed in Section 3.3, represent a successful validation of the new software version.

This new approach, alongside with latest LCI version, can be applied to other sky surveys that provide multi-filter data, allowing for even more in-depth analyses of the phase curve parameters.

2.2.5 Supercomputer adaptation

Since the method described in Section 2.2.4 is computationally intensive, I performed all calculations using the LCI software on the computer cluster at the Poznań Supercomputing and Networking Center[5] (PSNC, *pol.* Poznańskie Centrum Superkomputerowo-Sieciowe). I personally adjusted and adapted the code to the supercomputer, which made it possible to efficiently handle large-scale data processing and complex computations.

The LCI software consists of multiple modules responsible for successive stages of calculations, each accepting input files: configuration files, observational data, and (latter modules) output files from previous steps. To ensure optimal performance, I conducted tests to fine-tune the parameters for each step and prepared the necessary configuration files.

To automate the entire experiment, which involves a sequence of calculations for each object, I wrote wrapper scripts in BASH. These scripts used the SLURM queueing system implemented in the cluster, which allowed efficient job scheduling and resource management. The wrapper scripts were responsible for triggering the subsequent LCI modules and managing the input/output data. This automation allowed for the asynchronous processing of multiple objects, significantly enhancing computational efficiency. By distributing the workload, I was able to reduce the overall computation time and handle larger datasets.

Overall, the entire computation consumed over 170 000 hours of processor time. A detailed flowchart of the experiment, distinguishing observational data (purple, cyan, and orange diamonds), input/output files (grey diamonds), the LCI modules used (green rectangles) and file operations (grey rectangles) is presented in Figure 6. More detailed information regarding the computational workflow can be found in Wilawer et al. (2024). This approach demonstrates the effective utilisation of high-performance computing resources to tackle computationally demanding tasks in astronomical research.

[5] https://www.psnc.pl/

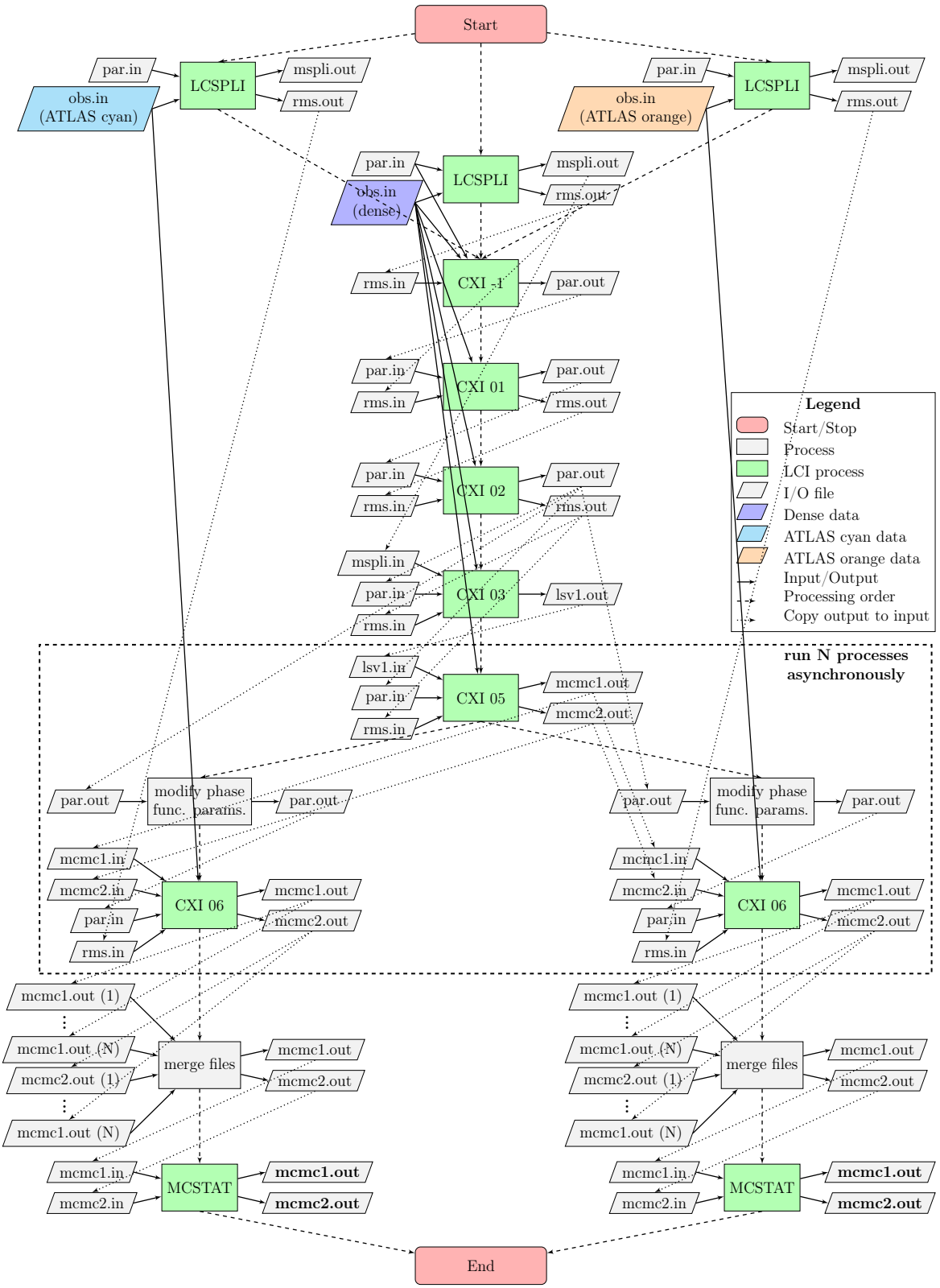

Figure 6: LCI computations flowchart. Detailed description in Section 2.2.5. Adapted from Wilawer et al. (2024).

Results

During my doctoral studies, I contributed to three significant publications, which illustrate my advancement in the field and my scientific achievements during this period. The following is a summary of these publications and findings.

3.1 Publication I: Oszkiewicz et al. (2021)

Oszkiewicz, D., Wilawer, E., Podlewska-Gaca, E., Kryszczyńska, A., Kwiatkowski, T., Troianskyi, V., Koleńczuk, P., Föhring, D., Galád, A., Skiff, B. A., Geier, S., Borczyk, W., Moskovitz, N. A., Gajdoš, Š., Világi, J., Polcic, L., Kashuba, V., Benishek, V., & Shevchenko, V. (2021). First survey of phase curves of V-type asteroids. *Icarus*, *357*, 114158. https://doi.org/https://doi.org/10.1016/j.icarus.2020.114158

This paper focuses on the analysis of magnitude phase curves for basaltic V-type asteroids, which are regarded as integral components of planetary crusts and mantles, often dislodged by collisional impacts, thereby containing valuable insights into the early stages of solar system formation. The majority of these objects are situated within the inner Main Belt, specifically within the Vesta family, named after the first discovered and largest asteroid of that type, (4) Vesta. Asteroids exhibiting comparable spectral and dynamical characteristics to (4) Vesta are termed Vestoids. Additionally, a small number of V-type asteroids have been identified in the outer regions of the Main Belt as well as among Near-Earth Asteroids, characterized by spectral properties.

We chose 20 V-type asteroids located outside the dynamical Vesta family, considering observing conditions suitable for our team's small- and medium-sized telescopes. Period length was also a filtering criterion, prioritising objects with short rotational periods to enable

the acquisition of complete lightcurves within a single observing night. As observations at minimal phase angles are crucial, for several objects, we have obtained data across multiple oppositions to ensure satisfactory phase angle coverage.

In this paper, we applied the traditional phase curve fitting (Section 2.2.2) with the Photometry Pipeline (Section 2.1.1) PCFit software (Section 2.2.3). We found no evidence for multiple clusters in the G_1 and G_2 phase curve parameter space for V-type asteroids. We derived global G_1 and G_2 parameters that can be utilised to fit the phase curve of poorly observed V-types. During the course of this study, I realised how time-consuming and object-limited the traditional phase curve fitting approach is. This inspired me to investigate the possibility of using survey data to maximise their precision.

3.2 Publication II: Wilawer et al. (2022)

Wilawer, E., Oszkiewicz, D., Kryszczyńska, A., Marciniak, A., Shevchenko, V., Belskaya, I., Kwiatkowski, T., Kankiewicz, P., Horbowicz, J., Kudak, V., Kulczak, P., Perig, V., & Sobkowiak, K. (2022). Asteroid phase curves using sparse Gaia DR2 data and differential dense light curves. *Monthly Notices of the Royal Astronomical Society*, *513*(3), 3242–3251. https://doi.org/10.1093/mnras/stac1008

In this paper, I investigated asteroid phase curves derived from a combination of dense ground-based differential data from the Astronomical Observatory Institute of Adam Mickiewicz University database and sparse Gaia DR2 data. Previous approaches faced limitations due to nature of the sparse data and inaccuracies in observations (Alvarez-Candal et al., 2022; Oszkiewicz et al., 2021). To address this issues, I proposed a novel approach that integrates sparse Gaia data with ground-based observations to enchance accuracy of phase curves. This approach underscores existing challenges in accurately modelling phase curves due to sparse data and observational limitations.

I selected data from both Gaia and ground-based observations to construct composite lightcurves. The available ground-based observations spanned several decades, but for consistency, only data from the Gaia DR2 era (2014–2016) were used. The asteroids chosen for this study had both differential ground-based photometry and Gaia measurements obtained

at at least three different phase angles.

In this work, I outline my phase curve fitting algorithm (detailed in Section 2.2.4), which integrates differential ground-based photometry with absolute Gaia measurements. Fourier series were used to fit composite lightcurves, and linear regression was applied to derive phase slopes. This approach accounted for rotational brightness changes and complex lightcurve morphologies.

As a result, I obtained composite lightcurves and linear functions fitted to the data for 26 asteroids. By comparing linear fits derived from ground-based photometry alone, ground-based photometry combined with Gaia data, and raw Gaia data, and by analysing the reduction in scatter around the linear functions, I demonstrated the importance of incorporating ground-based data into the sparse data for creating accurate magnitude phase curves.

Figure 7 displays a composite lightcurve that integrates Gaia observations (in black) and ground-based measurements (in colour), along with the derived lightcurve shape (solid red line). Figure 8 presents the linear part of the phase curve, featuring Gaia data and the corresponding linear fits. The figure illustrates: Gaia data alone (in blue), Gaia data with amplitude correction based on the literature (in green), derived by PerFit (in orange), and adjusted derived period (in black). The residuals for each data set, indicating the goodness of fit, are shown at the bottom, showcasing the improvements of combining dense and sparse observations.

Additionally, for one object, we applied this method to combined calibrated ground-based data in the Johnson V band and sparse Gaia data. The Gaia data were transformed to the Johnson V band. This approach leverages the availability of sparse data along with dense observations at small phase angles, allowing for an even better estimation of phase curve parameters. The resulting phase curve is shown in Figure 9.

This method can now be applied to other objects in the Gaia catalogue, including those in the upcoming Gaia DR4, provided that ground-based observations during the Gaia epoch are available.

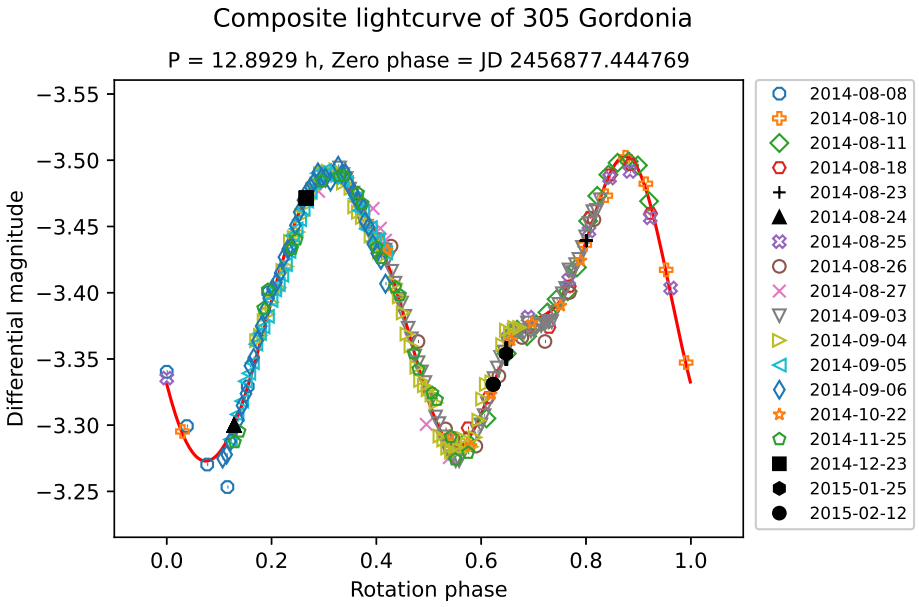

Figure 7: Composite lightcurve for asteroid (305) Gordonia combining ground-based data (colour) with Gaia data (black) with derived lightcurve shape (red line). (Wilawer et al., 2022)

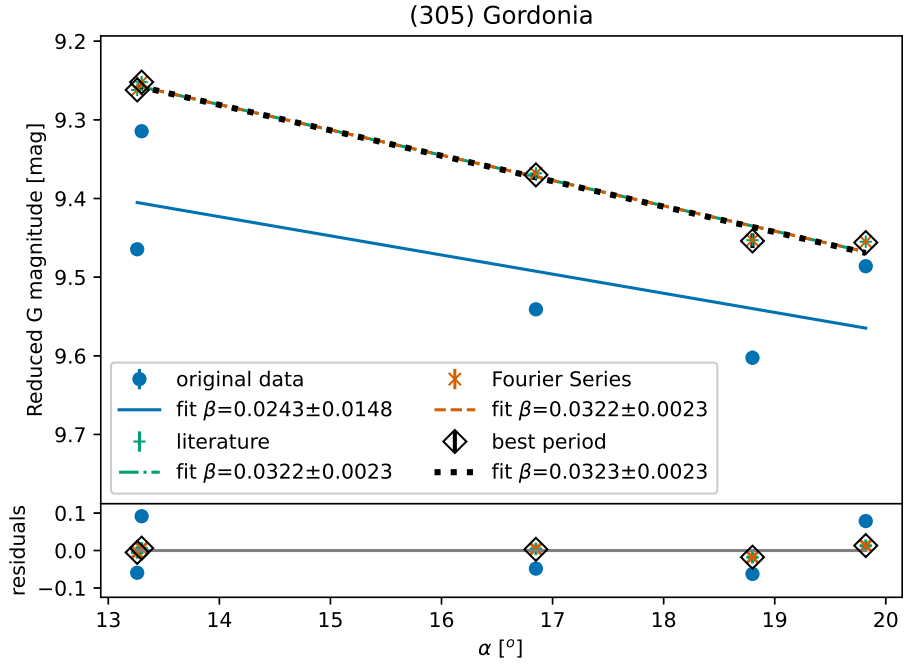

Figure 8: Linear part of the phase curve for asteroid (305) Gordonia. (Wilawer et al., 2022)

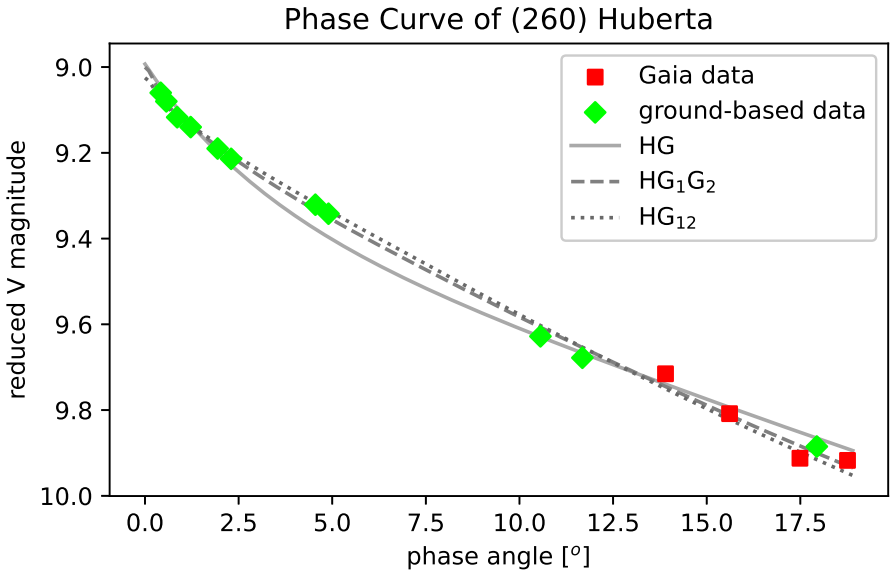

Figure 9: Phase curve for asteroid (240) Huberta from combined calibrated dense ground-based and sparse data. Gaia data was transformed to Johnson V-band. (Wilawer et al., 2022)

3.3 Publication III: Wilawer et al. (2024)

Wilawer, E., Muinonen, K., Oszkiewicz, D., Kryszczyńska, A., & Colazo, M. (2024). Phase curve wavelength dependency as revealed by shape- and geometry- corrected asteroid phase curves. *Monthly Notices of the Royal Astronomical Society*, *531*(2), 2802–2816. https://doi.org/10.1093/mnras/stae1282

In this study, I conducted a comprehensive analysis of phase curve G_1 and G_2 parameters for 35 well-observed asteroids, focusing on their relationship with albedo and taxonomic classification. I employed a robust methodology (described in Section 2.2.4) using combined ground-based and ATLAS sparse observational data to derive phase curve parameters corrected for shape and geometry, allowing us to elucidate key insights into the photometric behaviour of these celestial bodies, especially when taking two difference filters into account.

The analysis involved meticulous processing of observational data from cyan and orange ATLAS filters, allowing us to discern wavelength dependence in the phase curve parameters. By carefully examining the distribution of parameters G_1 and G_2 across different filters, I

discovered systematic trends, particularly in S-complex asteroids, where we observed smaller G_2 values in the cyan filter due to lower albedo, resulting in steeper phase curves.

Furthermore, the investigation into double-pole cases involved detailed scrutiny of opposition effect amplitudes and slope values, enabling us to identify preferred pole solutions that align with taxonomic classifications. This involved a rigorous comparison with theoretical expectations and consideration of observational uncertainties to ensure the accuracy of the conclusions. Figure 10 illustrates the phase curves and slope differences for asteroid (487) Venetia, organised in a 2x2 grid. Each column represents one of the two pole solutions. The top plots in each column show the phase curves in the cyan and orange filters, while the bottom plots depict the differences in the slopes of these phase curves. The figure clearly demonstrates that the two pole solutions result in distinct phase curves and colour slopes. When combined with taxonomic and albedo comparisons, this evidence supports the second pole as the preferred solution.

Additionally, our analysis of colour slope variation with phase angle underscored the importance of considering observational uncertainties, particularly at small phase angles. Although the results generally aligned with taxonomic classifications, we noted discrepancies for some objects, suggesting potential misidentifications or influences of surface properties.

The difference in phase curve slopes for cyan and orange filters, particularly noticeable at phase angles $\alpha < 7^\circ$ within the opposition effect zone, approaches 0 at larger phase angles. These variations indicate filter-dependent changes in the morphology of the phase curve. It should be noted that the ATLAS catalogue contains limited data points at very small phase angles where the opposition effect manifests. Consequently, the phase curve in this range is extrapolated, introducing significant uncertainties. A more comprehensive study focussing on this aspect of the phase curve is necessary to further explore the wavelength dependency of magnitude-phase relationships and the effects of phase reddening and bluing.

In conclusion, this study contributes to the understanding of asteroid photometry by providing detailed insights into the phase curve parameters and their relationships with taxonomic classifications and observational data. By elucidating wavelength dependence and refining pole solutions, we enhance our knowledge of asteroid physical properties and their implications for broader astronomical studies.

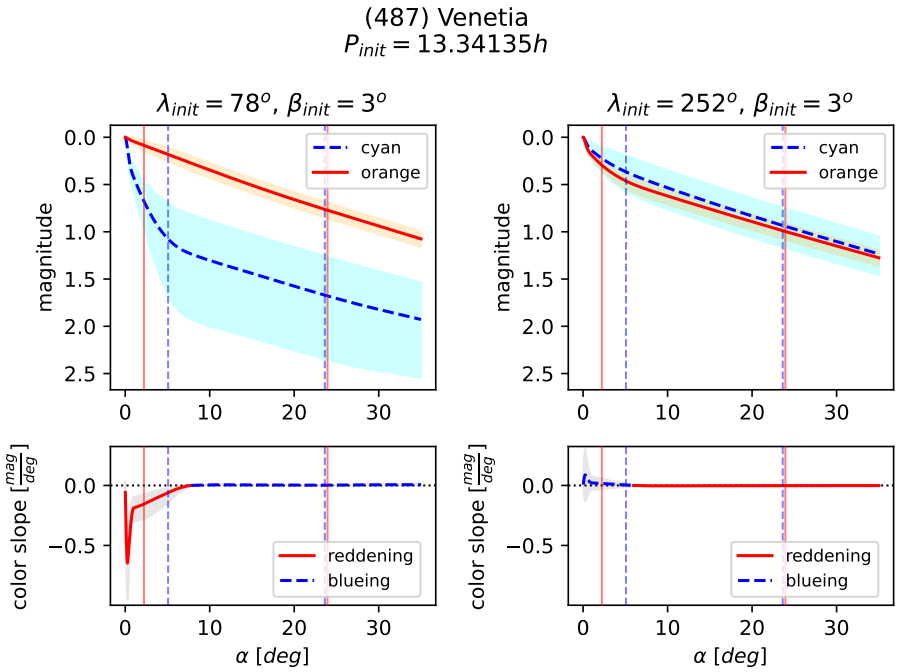

Figure 10: Top: phase curves for asteroid (487) Venetia using the H, G_1, G_2 magnitude phase function. The shaded envelope represents the range that encompasses the uncertainties.
Bottom: colour slope, representing the difference between the first derivatives of the phase function with respect to the phase angle in the two filters.
The vertical lines encompass the range of observed phase angles separately in both filters.
(Wilawer et al., 2024)

Conclusions and future prospects

During my Ph.D. studies, I participated in the derivation of accurate phase curves with the traditional approach. This led me to the recognition of the limitations of this approach.

Next, I have developed and applied novel approaches for deriving magnitude phase curves of asteroids by combining dense ground-based differential photometry with sparse data from sky survey catalogues Gaia DR2 and ATLAS. This approach addresses the limitations of the traditional approach to constructing phase curves, which heavily relies on dense, costly, and time-consuming ground-based data collection. By leveraging the extensive, albeit sparse, datasets provided by sky surveys, this method allows efficient and accurate determination of phase curve parameters for an extensive number of asteroids.

The integration of Gaia DR2 data with ground-based observations has shown significant improvements in the accuracy of derived phase curve parameters compared to the use of sparse data alone. Correction for observation geometry and amplitude adjustments, facilitated by dense lightcurve data, has proven essential in refining these parameters. The successful determination of the slope parameter β for multiple objects, in accordance with the values of the existing literature, validates the effectiveness of this combined data approach.

Further exploration with ATLAS data demonstrated the potential to investigate wavelength dependency in phase curves, providing deeper insight into the asteroid composition and surface properties. The application of the latest version of LCI software to this combined dataset resulted in accurate H, G_1, G_2 photometric function parameters G_1 and G_2, with distinct domains emerging for different taxonomic types, especially for C- and S-complex objects. Such a detailed analysis has been carried out for the first time in the field of asteroid magnitude phase curve research. This method could be used as a valuable tool for validating pole solutions as well as for taxonomic classification.

As the volume of astronomical asteroid data continues to grow exponentially, the methods

presented in this work will facilitate extensive use of these datasets such as Gaia DR4 or LSST. The next steps in the field involve refining these techniques to handle even larger datasets and enhancing automation to further streamline the data processing pipeline. Applying these methods to data captured using various filters, particularly narrowband filters, will enable a more comprehensive exploration of wavelength dependency for different taxonomic classes. The results obtained through this approach can then be compared with spectroscopic data for validation and further insight. Moreover, determining phase curves derived from both visible and infrared data could help investigate the reddening effect more effectively.

In conclusion, immersive volumes of data pose challenges that require optimised processing to tackle their scale and complexity. The methodologies developed in this dissertation represent a significant advancement in asteroid phase curve determination. They not only refine the precision and efficiency of deriving phase curves but also open up new avenues for research and discovery, utilising extensive datasets from upcoming sky surveys, and bring phase curves research to the big data level.

Bibliography

Akimov, L. A. (1975). Influence of mesorelief on the brightness distribution over a planetary disk. Soviet Ast., *19*, 385.

Akimov, L. A. (1979). On the brightness distributions over the lunar and planetary disks. Soviet Ast., *23*, 231–235.

Akimov, L. A. (1988). Light reflection by the moon. ii. *Kinematika i Fizika Nebesnykh Tel*, *4*, 10–16.

Alvarez-Candal, A., Benavidez, P. G., Bagatin, A. C., & Santana-Ros, T. (2022). Phase curves of small bodies from the sloan moving objects catalog. A&A, *657*, A80. https://doi.org/10.1051/0004-6361/202141033

Belskaya, I. N., & Shevchenko, V. G. (2000). Opposition effect of asteroids. *Icarus*, *147*(1), 94–105. https://doi.org/10.1006/icar.2000.6410

Bowell, E., Hapke, B., Domingue, D., Lumme, K., Peltoniemi, J., & Harris, A. W. (1989). Application of photometric models to asteroids. In *Asteroids II* (pp. 524–556). University of Arizona Press.

Chambers, K., & Pan-STARRS Team. (2018). The pan-starrs1 surveys. *American Astronomical Society Meeting Abstracts #231*, *231*, Article 102.01, 102.01.

Dunlap, J. L., & Gehrels, T. (1969). Minor Planets. III. Lightcurves of a Trojan Asteroid. AJ, *74*, 796. https://doi.org/10.1086/110860

Dunlap, J. L., Gehrels, T., & Howes, M. L. (1973). Minor planets and related objects. IX. Photometry and polarimetry of (1685) Toro. AJ, *78*, 491. https://doi.org/10.1086/111447

Gaia Collaboration, Prusti, T., de Bruijne, J. H. J., Brown, A. G. A., Vallenari, A., Babusiaux, C., Bailer-Jones, C. A. L., Bastian, U., Biermann, M., Evans, D. W., Eyer, L., Jansen, F., Jordi, C., Klioner, S. A., Lammers, U., Lindegren, L., Luri, X., Mignard, F., Milligan, D. J., Panem, C., Poinsignon, V., Pourbaix, D., Randich, S., Sarri, G., Sartoretti, P., Siddiqui, H. I., Soubiran, C., Valette, V., van Leeuwen, F., Walton, N. A., Aerts, C., Arenou, F., Cropper, M., Drimmel, R., Høg, E., Katz, D., Lattanzi, M. G., O'Mullane, W., Grebel, E. K., Holland, A. D., Huc, C., Passot, X., Bramante, L., Cacciari, C., Castañeda, J., Chaoul, L., Cheek, N., De Angeli, F., Fabricius, C., Guerra, R., Hernández, J., Jean-Antoine-Piccolo, A., Masana, E., Messineo, R., Mowlavi, N., Nienartowicz, K., Ordóñez-Blanco, D., Panuzzo, P., Portell, J., Richards, P. J., Riello, M., Seabroke, G. M., Tanga, P., Thévenin, F., Torra, J., Els, S. G., Gracia-Abril, G., Comoretto, G., Garcia-Reinaldos, M., Lock, T., Mercier, E., Altmann, M., Andrae, R., Astraatmadja, T. L., Bellas-Velidis, I., Benson, K., Berthier, J., Blomme, R., Busso, G., Carry, B., Cellino, A., Clementini, G., Cowell, S., Creevey, O., Cuypers, J., Davidson, M., De Ridder, J., de Torres, A., Delchambre, L., Dell'Oro, A., Ducourant, C., Frémat, Y., García-Torres, M., Gosset, E., Halbwachs, J.-L., Hambly, N. C., Harrison, D. L., Hauser, M., ... Zschocke, S. (2016). The gaia mission. *aap*, *595*, A1. https://doi.org/10.1051/0004-6361/201629272

Hapke, B. (1963). A theoretical photometric function for the lunar surface. *Journal of Geophysical Research (1896-1977)*, *68*(15), 4571–4586. https://doi.org/https://doi.org/10.1029/JZ068i015p04571

Hapke, B. (1966). Ali improved theoretical lunar photometric function. AJ, *71*, 333. https://doi.org/10.1086/109924

Hapke, B. (1981). Bidirectional reflectance spectroscopy: 1. theory. *Journal of Geophysical Research: Solid Earth*, *86*(B4), 3039–3054. https://doi.org/https://doi.org/10.1029/JB086iB04p03039

Hapke, B. (1984). Bidirectional reflectance spectroscopy: 3. correction for macroscopic roughness. Icarus, *59*(1), 41–59. https://doi.org/https://doi.org/10.1016/0019-1035(84)90054-X

Hapke, B. (1986). Bidirectional reflectance spectroscopy 4. the extinction coefficient and the opposition effect. Icarus, *67*(2), 264–280. https://doi.org/10.1016/0019-1035(86)90108-9

Hapke, B. (2002). Bidirectional reflectance spectroscopy. 5. the coherent backscatter opposition effect and anisotropic scattering. Icarus, *157*(2), 523–534. https://doi.org/10.1006/icar.2002.6853

Hapke, B. (2008). Bidirectional reflectance spectroscopy. 6. effects of porosity. Icarus, *195*(2), 918–926. https://doi.org/10.1016/j.icarus.2008.01.003

Hapke, B. (2012). Bidirectional reflectance spectroscopy 7. the single particle phase function hockey stick relation. Icarus, *221*(2), 1079–1083. https://doi.org/10.1016/j.icarus.2012.10.022

Hapke, B., & Wells, E. (1981). Bidirectional reflectance spectroscopy: 2. experiments and observations. *Journal of Geophysical Research: Solid Earth*, *86*(B4), 3055–3060. https://doi.org/https://doi.org/10.1029/JB086iB04p03055

Heinze, A. N., Tonry, J. L., Denneau, L., Flewelling, H., Stalder, B., Rest, A., Smith, K. W., Smartt, S. J., & Weiland, H. (2018). A first catalog of variable stars measured by the asteroid terrestrial-impact last alert system (atlas). AJ, *156*(5), Article 241, 241. https://doi.org/10.3847/1538-3881/aae47f

Kluwak, T., Murawiecka, M., Baksalary, J., Taberski, G., Adamczyk, A., Bosy, A., & Śniecińska, E. (2021). Support tools for NEO observers. *8th European Conference on Space Debris*, Article 143, 143.

Kwiatkowski, T., Kryszczyńska, A., Polińska, M., Buckley, D. A. H., O'Donoghue, D., Charles, P. A., Crause, L., Crawford, S., Hashimoto, Y., Kniazev, A., Loaring, N., Romero Colmenero, E., Sefako, R., Still, M., & Vaisanen, P. (2009). Photometry of 2006 rh 120: An asteroid temporary captured into a geocentric orbit. *Astronomy & Astrophysics*, *495*(3), 967–974. https://doi.org/10.1051/0004-6361:200810965

Lagerkvist, C. .-., Barucci, M. A., Capria, M. T., Fulchignoni, M., Guerriero, L., Perozzi, E., & Zappala, V. (1987). *Asteroid photometric catalogue.*

Mommert, M. (2017). PHOTOMETRYPIPELINE: An automated pipeline for calibrated photometry. *Astronomy and Computing*, *18*, 47–53. https://doi.org/https://doi.org/10.1016/j.ascom.2016.11.002

Muinonen, K., Torppa, J., Wang, X. .-., Cellino, A., & Penttilä, A. (2020). Asteroid lightcurve inversion with bayesian inference. A&A, *642*, Article A138, A138. https://doi.org/10.1051/0004-6361/202038036

Muinonen, K., Belskaya, I. N., Cellino, A., Delbò, M., Levasseur-Regourd, A.-C., Penttilä, A., & Tedesco, E. F. (2010a). A three-parameter magnitude phase function for asteroids. Icarus, *209*(2), 542–555. https://doi.org/10.1016/j.icarus.2010.04.003

Muinonen, K., Tyynelä, J., Zubko, E., & Videen, G. (2010b). Coherent backscattering in planetary regoliths. In A. A. Kokhanovsky (Ed.), *Light scattering reviews 5: Single light scattering and radiative transfer* (pp. 477–518). Springer Berlin Heidelberg. https://doi.org/10.1007/978-3-642-10336-0_11

Muinonen, K., Uvarova, E., Martikainen, J., Penttilä, A., Cellino, A., & Wang, X. (2022). Asteroid photometric phase functions from bayesian lightcurve inversion. *Frontiers in Astronomy and Space Sciences*, *9*, Article 821125, 821125. https://doi.org/10.3389/fspas.2022.821125

Oszkiewicz, D., Wilawer, E., Podlewska-Gaca, E., Kryszczyńska, A., Kwiatkowski, T., Troianskyi, V., Koleńczuk, P., Föhring, D., Galád, A., Skiff, B. A., Geier, S., Borczyk, W., Moskovitz, N. A., Gajdoš, Š., Világi, J., Polcic, L., Kashuba, V., Benishek, V., & Shevchenko, V. (2021). First survey of phase curves of V-type asteroids. *Icarus*, *357*, 114158. https://doi.org/https://doi.org/10.1016/j.icarus.2020.114158

Penttilä, A., Shevchenko, V., Wilkman, O., & Muinonen, K. (2016). H, g1, g2 photometric phase function extended to low-accuracy data. Planet. Space Sci., *123*, 117–125. https://doi.org/10.1016/j.pss.2015.08.010

Pravec, P., Harris, A. W., Kušnirák, P., Galád, A., & Hornoch, K. (2012). Absolute magnitudes of asteroids and a revision of asteroid albedo estimates from wise thermal observations. Icarus, *221*(1), 365–387. https://doi.org/10.1016/j.icarus.2012.07.026

Sather, R. E. (1976). Minor planets and related objects. XIX. Shape and pole orientation of (39) Laetitia. AJ, *81*, 67–73. https://doi.org/10.1086/111854

Shevchenko, V. G. (1997). Analysis of asteroid brightness-phase relations. *SoSyR*, *31*(3), 219.

Shevchenko, V. G., Belskaya, I. N., Lupishko, D. F., Krugly, Y. N., Chiorny, V. G., & Velichko, F. P. (2010). Kharkiv asteroid magnitude-phase relations v1.0. *NASA Planetary Data System*, Article EAR-A-COMPIL-3-MAGPHASE-V1.0, EAR-A-COMPIL-3-MAGPHASE–V1.0.

Shevchenko, V. G., Belskaya, I. N., Muinonen, K., Penttilä, A., Krugly, Y. N., Velichko, F. P., Chiorny, V. G., Slyusarev, I. G., Gaftonyuk, N. M., & Tereschenko, I. A. (2016). Asteroid observations at low phase angles. iv. average parameters for the new H, G1, G2 magnitude system. Planet. Space Sci., *123*, 101–116. https://doi.org/10.1016/j.pss.2015.11.007

Shevchenko, V. G., Mikhalchenko, O. I., Belskaya, I. N., Slyusarev, I. G., Chiorny, V. G., Krugly, Y. N., Hromakina, T. A., Dovgopol, A. N., Kiselev, N. N., Rublevsky, A. N., Antonyuk, K. A., Novichonok, A. O., Kusakin, A. V., Reva, I. V., Inasaridze, R. Y., Ayvazian, V. V., Kapanadze, G. V., Molotov, I. E., Oszkiewicz, D., & Kwiatkowski, T. (2021). Photometry of selected outer main belt asteroids. Planet. Space Sci., *202*, Article 105248, 105248. https://doi.org/10.1016/j.pss.2021.105248

Shkuratov, Y., Kaydash, V., Korokhin, V., Velikodsky, Y., Opanasenko, N., & Videen, G. (2011). Optical measurements of the moon as a tool to study its surface [Exploring Phobos]. *Planetary and Space Science*, *59*(13), 1326–1371. https://doi.org/https://doi.org/10.1016/j.pss.2011.06.011

Spoto, F., Tanga, P., Mignard, F., Berthier, J., Carry, B., Cellino, A., Dell'Oro, A., Hestroffer, D., Muinonen, K., Pauwels, T., et al. (2018). Gaia data release 2-observations of solar system objects. A&A, *616*, A13. https://doi.org/10.1051/0004-6361/201832900

Stokes, G. H., Evans, J. B., Viggh, H. E. M., Shelly, F. C., & Pearce, E. C. (2000). Lincoln near-earth asteroid program (linear). Icarus, *148*(1), 21–28. https://doi.org/10.1006/icar.2000.6493

Tanga, P., Pauwels, T., Mignard, F., Muinonen, K., Cellino, A., David, P., Hestroffer, D., Spoto, F., Berthier, J., Guiraud, J., et al. (2023). Gaia data release 3 - the

solar system survey. *Astronomy & Astrophysics*, *674*, A12. https://doi.org/10.1051/0004-6361/202244765

Vereš, P., Jedicke, R., Fitzsimmons, A., Denneau, L., Granvik, M., Bolin, B., Chastel, S., Wainscoat, R. J., Burgett, W. S., Chambers, K. C., Flewelling, H., Kaiser, N., Magnier, E. A., Morgan, J. S., Price, P. A., Tonry, J. L., & Waters, C. (2015). Absolute magnitudes and slope parameters for 250,000 asteroids observed by pan-starrs ps1 – preliminary results. *Icarus*, *261*, 34–47. https://doi.org/https://doi.org/10.1016/j.icarus.2015.08.007

Wilawer, E., Muinonen, K., Oszkiewicz, D., Kryszczyńska, A., & Colazo, M. (2024). Phase curve wavelength dependency as revealed by shape- and geometry- corrected asteroid phase curves. *Monthly Notices of the Royal Astronomical Society*, *531*(2), 2802–2816. https://doi.org/10.1093/mnras/stae1282

Wilawer, E., Oszkiewicz, D., Kryszczyńska, A., Marciniak, A., Shevchenko, V., Belskaya, I., Kwiatkowski, T., Kankiewicz, P., Horbowicz, J., Kudak, V., Kulczak, P., Perig, V., & Sobkowiak, K. (2022). Asteroid phase curves using sparse Gaia DR2 data and differential dense light curves. *Monthly Notices of the Royal Astronomical Society*, *513*(3), 3242–3251. https://doi.org/10.1093/mnras/stac1008

Wilawer, E. (2018). *NEO phase curve calculation library* (PLP-066 SANORDA Technical Report No. 16). Astronomical Observatory Institute UAM. Poznań.

Wilawer, E., & Kwiatkowski, T. (2017). *Specification of the ATLAS6 format* (PLP-066 SANORDA Technical Report No. 4). Astronomical Observatory Institute UAM. Poznań.

Woods, D. F., Ruprecht, J. D., Kotson, M. C., Main, E. L., Evans, E. W., Varey, J. D., Vaillancourt, J. E., Viggh, H. E. M., Brown, J. J., & Pál, A. (2021). Asteroid observations from the transiting exoplanet survey satellite: Detection

processing pipeline and results from primary mission data. PASP, *133*(1019), Article 014503, 014503. https://doi.org/10.1088/1538-3873/abc761

York, D. G., Adelman, J., Anderson, J., John E., Anderson, S. F., Annis, J., Bahcall, N. A., Bakken, J. A., Barkhouser, R., Bastian, S., Berman, E., Boroski, W. N., Bracker, S., Briegel, C., Briggs, J. W., Brinkmann, J., Brunner, R., Burles, S., Carey, L., Carr, M. A., Castander, F. J., Chen, B., Colestock, P. L., Connolly, A. J., Crocker, J. H., Csabai, I., Czarapata, P. C., Davis, J. E., Doi, M., Dombeck, T., Eisenstein, D., Ellman, N., Elms, B. R., Evans, M. L., Fan, X., Federwitz, G. R., Fiscelli, L., Friedman, S., Frieman, J. A., Fukugita, M., Gillespie, B., Gunn, J. E., Gurbani, V. K., de Haas, E., Haldeman, M., Harris, F. H., Hayes, J., Heckman, T. M., Hennessy, G. S., Hindsley, R. B., Holm, S., Holmgren, D. J., Huang, C.-h., Hull, C., Husby, D., Ichikawa, S.-I., Ichikawa, T., Ivezić, Ž., Kent, S., Kim, R. S. J., Kinney, E., Klaene, M., Kleinman, A. N., Kleinman, S., Knapp, G. R., Korienek, J., Kron, R. G., Kunszt, P. Z., Lamb, D. Q., Lee, B., Leger, R. F., Limmongkol, S., Lindenmeyer, C., Long, D. C., Loomis, C., Loveday, J., Lucinio, R., Lupton, R. H., MacKinnon, B., Mannery, E. J., Mantsch, P. M., Margon, B., McGehee, P., McKay, T. A., Meiksin, A., Merelli, A., Monet, D. G., Munn, J. A., Narayanan, V. K., Nash, T., Neilsen, E., Neswold, R., Newberg, H. J., Nichol, R. C., Nicinski, T., Nonino, M., Okada, N., Okamura, S., Ostriker, J. P., ... SDSS Collaboration. (2000). The sloan digital sky survey: Technical summary. AJ, *120*(3), 1579–1587. https://doi.org/10.1086/301513

Appendices

Appendix A

Publication I: Oszkiewicz at al. (2021)

Icarus 357 (2021) 114158

Contents lists available at ScienceDirect

Icarus

journal homepage: www.elsevier.com/locate/icarus

Research Paper

First survey of phase curves of V-type asteroids

Dagmara Oszkiewicz [a,*], Emil Wilawer [a], Edyta Podlewska-Gaca [a], Agnieszka Kryszczyńska [a], Tomasz Kwiatkowski [a], Volodymyr Troianskyi [a,b], Paweł Koleńczuk [a], Dóra Föhring [c], Adrián Galád [d], Brian A. Skiff [e], Stefan Geier [f,g], Wojciech Borczyk [a,1], Nicholas A. Moskovitz [e], Štefan Gajdoš [d], Jozef Világi [d], Ludovít Polcic [d], Volodymyr Kashuba [b], Vladimir Benishek [h], Vasilij Shevchenko [i]

[a] Astronomical Observatory Institute, Faculty of Physics, A. Mickiewicz University, Słoneczna 36, 60-286 Poznań, Poland
[b] Astronomical Observatory of Odessa I.I.Mechnikov, National University, Marazlievskaya 1v, 65014, Odessa, Ukraine
[c] Institute for Astronomy, University of Hawaii, 2680 Woodlawn Drive, Honolulu, HI 96822, USA
[d] Modra Observatory, Department of Astronomy, Physics of the Earth, and Meteorology, FMPI UK, Bratislava SK-84248, Slovakia
[e] Lowell Observatory, 14000 W Mars Hill Rd, 86001 Flagstaff, AZ, USA
[f] Gran Telescopio Canarias (GRANTECAN), Cuesta de San José s/n, E-38712, Breña Baja, La Palma, Spain
[g] Instituto de Astrofísica de Canarias, Vía Láctea s/n, E38200, La Laguna, Tenerife, Spain
[h] Belgrade Astronomical Observatory, Volgina 7, 11060, Belgrade 38, Serbia
[i] Department of Astronomy and Space Informatics, V.N. Karazin Kharkiv National University, 4 Svobody Sq., Kharkiv 61022, Ukraine

ARTICLE INFO

Keywords:
Asteroids
Rotation
Photometry

ABSTRACT

The V-type asteroids are of major scientific interest as they may sample multiple differentiated planetesimals. Determination of their physical properties is crucial for understanding the diversity and multiplicity of planetesimals. Previous studies have suggested distinct polarimetric behaviours for the V-type asteroids. Similarly to phase-polarization curves, asteroid phase-magnitude curves (hereinafter called "phase curves") are also diagnostic of surface and regolith properties, and can be used to unveil a variety of distinct behaviours.

We present well determined phase curves for ~20 V-type asteroids for the first time. Their phase curve parameters are consistent with those for moderate and high albedo asteroids. The computed median G_{12} parameter for the V-type asteroids is $G_{12}^* = 0.14$. We do not find substantial evidence for any clustering into distinct phase curve parameters groups. Only one asteroid (2763) Jeans shows exceptionally high G_2 value. The derived median G_{12} may be used in single parameters fitting of V-type asteroids.

1. Introduction

Basaltic V-type asteroids are considered collisionally freed fragments of crusts and mantles of differentiated planetesimals, the building blocks of planets. Therefore they provide important constrains on dynamical and thermal processes in the early Solar System.

Most of those objects are located in inner Main Belt primarily in the Vesta family and are considered the parent bodies of the howardite–eucrite–diogenite (HED) meteorites. This has been evidenced through spectral (McCord et al. 1970; Consolmagno and Drake 1977; Binzel and Xu 1993; Burbine et al. 2001; Florczak et al. 2002; Cochran et al. 2004; Duffard et al. 2006; De Sanctis et al. 2011; Moskovitz et al. 2010; Hardersen et al. 2014) and dynamical studies (Carruba et al. 2005; Nesvorný et al. 2008).

Around twenty V-type asteroids have been confirmed beyond 2.5 AU, in the mid and outer main-belt (MOVs) (Lazzaro et al. 2000; Hardersen et al. 2004; Roig et al. 2008; Moskovitz et al. 2008; Duffard and Roig 2009; Leith et al. 2017; Ieva et al. 2018; Medeiros et al. 2019; Migliorini et al. 2018). Majority of MOVs show spectral properties distinct from Vestoids (Hardersen et al. 2004; Leith et al. 2017; Ieva et al. 2018; Medeiros et al. 2019; Migliorini et al. 2018) and are dynamically unlikely to be parts of Vesta (e.g. Michtchenko et al. (2002); Roig et al. (2008)), and thus are known as non-Vestoids. For up to date review of the V-types and their relation to the differentiated

* Corresponding author.
E-mail address: dagmara.oszkiewicz@amu.edu.pl (D. Oszkiewicz).
[1] This document is the results of the research project funded by the National Center of Science, Poland. ORCID(s): 0000–0002–5356-6433 (D. Oszkiewicz)

https://doi.org/10.1016/j.icarus.2020.114158
Received 30 June 2020; Received in revised form 2 October 2020; Accepted 6 October 2020
Available online 11 October 2020
0019-1035/

Table 1
The observed asteroids with rotation periods from Oszkiewicz et al. (2020), geometric albedos, opposition dates, minimum phase angle observed and number of lightcurves.

Asteroid	Rotation period (h)	p_v	Opp. dates	α_{min} (deg)	N
(2442) Corbett	11.456 ± 0.001	0.26 ± 0.04	2013.09.19, 2015.01.14	6.02	25
(2486) Metsahovi	4.4499 ± 0.0001	0.27 ± 0.03	2019.09.17	0.72	19
(2566) Kirghizia	4.4489 ± 0.0001	0.26 ± 0.03	2013.02.03, 2015.10.10, 2017.02.28	1.95	28
(2653) Principia	5.5225 ± 0.0001	0.26 ± 0.09	2017.09.12, 2019.01.13	3.04	29
(2763) Jeans	7.8020 ± 0.0001	0.41 ± 0.08	2016.11.30	2.42	15
(2823) van der Laan	2.6262 ± 0.0001	0.32 ± 0.05	2016.09.11	3.14	13
(2912) Lapalma	5.7106 ± 0.0001	0.46 ± 0.05	2018.01.12	2.75	8
(3849) Incidentia	2.7768 ± 0.0002	0.40 ± 0.04	2013.10.31, 2019.03.29	1.38	11
(3869) Norton	7.6034 ± 0.0001	0.16 ± 0.03	2013.11.23, 2017.12.10	0.80	22
(4383) Suruga	3.4074 ± 0.0001	0.32 ± 0.04	2017.02.22, 2019.11.07	4.28	26
(4434) Nikulin	2.8272 ± 0.0003	0.35 ± 0.04	2017.01.14, 2018.04.24	2.97	15
(4692) SIMBAD	2.7351 ± 0.0001	0.36 ± 0.05	2015.01.31, 2017.11.23	2.60	16
(5037) Habing	2.8290 ± 0.0001	0.32 ± 0.07	2018.08.16, 2020.02.09	2.02	26
(5525) 1991 TS4	14.078 ± 0.001	0.40 ± 0.05	2014.09.03, 2016.02.04, 2019.01.02	0.87	28
(5754) 1992 FR2	8.9022 ± 0.0001	0.28 ± 0.03	2016.04.13, 2017.10.26	3.81	40
(7558) Yurlov	4.1157 ± 0.0001	0.36 ± 0.11	2013.09.28, 2018.01.06, 2019.05.25	1.22	24
(8761) Crane	2.6379 ± 0.0001	0.36 ± 0.11	2016.11.15, 2018.03.26	2.60	19
(9481) Menchu	3.0519 ± 0.0001	0.20 ± 0.05	2014.03.24	2.60	6
(9531) Jean-Luc	2.4999 ± 0.0001	0.28 ± 0.05	2018.11.24	5.30	22
(27192) Selenali	5.5741 ± 0.0001	0.36 ± 0.11	2015.10.28	3.09	10

planetesimals we refer the reader to Burbine et al. (2017); Oszkiewicz et al. (2015).

Whether some V-types in the inner main belt are unrelated to Vesta is yet to be evidenced and currently debated (Bottke et al. 2006; Nesvorný et al. 2008; Scott et al. 2009; Moskovitz et al. 2010; Wasson 2013; Oszkiewicz et al. 2017, 2019). Spectral separation of those objects may be ambiguous - as shown by ion irradiation experiments (Fulvio et al. 2016) spectral slopes are strongly influenced by space weathering. Therefore additional physical parameters may have to be considered to distinguish non-Vestoids.

Recently Gil-Hutton et al. (2017) studied the polarimetric curves of V-types and found a diversity of behaviours. Some of the V-type asteroids in contrast to (4) Vesta showed a shallow polarimetric minimum and a small inversion angle. That group included asteroid (1459) Magnya - a known outer Main Belt non-Vestoid. Furthermore observations of (2579) Spartacus and possibly (3944) Halliday showed a large (24–26) inversion angle. It is worth noticing that (2579) Spartacus has unusual spectral properties as compared to other V-types (low bar area ratio - BAR Oszkiewicz et al. (2019)), (3944) Halliday was also spectrally observed but the BAR is not specified (Migliorini et al. 2017). Gil-Hutton et al. (2017) attributed those distinct polarimetric behaviours to different regolith particle sizes, however in general mineralogical differences cannot be excluded.

The shape of asteroid phase-curves is also known to relate to surface properties, thus can provide an independent perspective. These curves describe the relation between asteroids brightness (reduced to 1 AU from the Sun and observer and corrected for lightcurve amplitude) and phase-angle (Sun-asteroid-observer angle). At low phase-angles lack of self-shadowing (among regolith particles) and the coherent backscattering mechanisms cause additional brightening, giving rise to the so called opposition effect (OE), see Muinonen et al. (2010b) for a review.

Up to date several phase functions have been proposed to model that dependence. Still commonly used is the H,G phase function proposed by Bowell et al. (1989) and approved by the International Astronomical Union (IAU) in 1985. That theoretical function is based on the Lumme-Bowell photometric model (Lumme and Bowell 1981). Another popular photometric model is that by Hapke (1986) relating directly to topographic roughness, regolith compaction and other surface parameters. The conversion between those two systems can be found in Verbiscer and Veverka (1995). Currently the IAU approved and recommended phase functions are the H, G_1, G_2 and H, G_{12} functions, empirically developed by Muinonen et al. (2010a) and extended by Penttila et al. (2016) to work with low-quality photometric data. The three parameter phase function (H, G_1, G_2) was designed to improve fits to the existing high quality data and the two parameter phase function deriving from it (H, G_{12}) to better predict absolute magnitudes for objects having a small number of observations. Several other less common functions have been applied to both observational data and laboratory measurements (Akimov 1988; Shkuratov et al. 1994; Belskaya and Shevchenko 2000; Muinonen et al. 2002; Kaasalainen et al. 2003; Shkuratov et al. 2018) in the literature.

Morphology of asteroid phase curves have been found observationally to link to surface properties. Amplitude and width of the opposition effect relates to asteroid geometric albedo[2] (Belskaya and Shevchenko 2000; Carbognani et al. 2019). Asteroids with moderate albedos (i.e. S and M types) display high OE amplitudes, whereas low- (i.e. P-, C- types) and high-albedo (E-types) objects show smaller amplitudes (Belskaya and Shevchenko 2000).

In general, low-albedo objects exhibit steep phase curves, characterized by a small G slope parameter (H,G system), small G_2 and large G_1 parameters in the (H,G_1,G_2) system, and large G_{12} parameter (H, G_{12} system). High-albedo objects show large G slope and G_2 parameter, small G_1, G_{12} parameter and shallow phase curves (Oszkiewicz et al. 2011, 2012; Shevchenko et al. 2016).

Phase-curve parameters also vary for different taxonomic types (Harris and Young 1989; Oszkiewicz et al. 2011, 2012; Vereš et al. 2015; Shevchenko et al. 2016). That correlation was observed for a large number of asteroids having low-quality photometry (Oszkiewicz et al. 2011, 2012; Vereš et al. 2015) as well as for smaller subset of objects having accurate measurements (Harris and Young 1989; Shevchenko et al. 2016). To better understand those correlations and the variability of the phase-curves within spectral classes, an increase in the number of high quality phase curves is needed. Especially new phase curves are required for asteroids from spectral classes with few or no phase-curves observed, such as the V class.

More practically, phase-curves are used to derive absolute magnitudes (which relate to asteroid diameters) and then predict apparent magnitudes. As shown by Pravec et al. (2012) absolute magnitudes available in large databases (such as MPCORB, Pisa AstDyS and JPL Horizons) computed based on sparse data can have a systematic error of 0.1 mag for bright (H<10 mag) and 0.4–0.5 mag for faint asteroids. Part of that bias may be due to assumed constant G slope values (typically G=0.15 in the H,G system) for all objects. Furthermore absolute magnitudes vary between different apparitions (except for an ideal

[2] Geometric albedo - the ratio of asteroid brightness at zero phase angle to that of an idealized Lambertian disk having the same cross-section

Table 2
Phase curve parameters obtained by in this work and those by (1) Waszczak et al. (2015) (we indicate also opposition years for which the parameters were computed), (2) Vereš et al. (2015) (± denotes the uncertainty and the values in the brackets estimated errors, see Vereš et al. (2015) for details) and (3) Oszkiewicz et al. (2011). For the asteroids observed within this project we include lightcurve amplitudes. Note that the H,G_{12} function has a tendency to underestimate the uncertainties. Therefore we do not list them for objects for which we believe H,G_{12} underestimated the uncertainties. Geometric albedos are from Mainzer et al. (2016) or estimated from the linear linear slope based on the relation presented in Belskaya and Shevchenko (2018) (marked with a star).

Object	p_v	Author	H	G	H	G_1	G_2	H	G_{12}	amplitude
(2442) Corbett	0.255±0.043	(1) 2013	12.758±0.001	0.405±0.002	12.552±0.003	0.484±0.022	0.023±0.0	12.656±0.001	0.110±0.002	
		(2)	12.85±0.47	0.075±0.14				13.03±0.25	0.71±0.36	
			(±0.52)	(±0.20)				(±0.02)	(±-0.46)	
		(3)	12.59±0.07	0.25±0.07	12.59±0.22	0.40±0.33	0.33±0.1	12.55±0.02	0.36±0.11	
		this work	12.84±0.02	0.42±0.02	12.54±0.37	0.022±0.19	0.49±0.05	12.73	0.11±0.0	0.206
		this work	12.87±0.01		12.58±0.37			12.76		0.237
(2486) Metsahovi	0.268±0.031	(1)	–	–	–	–	–	–	–	
		(2)	12.90±0.20	0.23±0.0				12.93±0.23	0.54±0.02	
			(±0.22)	(±0.05)				(±0.08)	(±-0.01)	
		(3)	12.53±0.06	0.30±0.06	12.59±0.18	0.47±0.31	0.36±0.1	12.45±0.02	0.28±0.10	
		this work	12.30±0.03	0.37±0.05	12.25±0.08	0.25±0.18	0.47±0.08	12.21	0.091±0.13	0.098
(2566) Kirghizia	0.264±0.029	(1)	–	–	–	–	–	–	–	
		(2)	–		–			–		
		(3)	12.31±0.07	0.24±0.07	12.17±0.2	0.23±0.3	0.36±0.1	12.29±0.02	0.36±0.13	
		this work	11.96±0.01	0.38±0.01	11.96±0.05	0.22±0.06	0.53±0.02	11.86	0.14±0.02	0.529
		this work	12.00±0.01		12.02±0.04			11.9		0.911
		this work	11.92±0.01		11.95± 0.05			11.82		0.947
(2653) Principia	0.256±0.091	(1)	–	–	–	–	–	–	–	
		(2)	12.43±0.24	0.31±0.1				12.27±0.14	0.65±0.21	
			(±0.31)	(±0.11)				(±-0.01)	(±0.16)	
		(3)	12.18±0.07	0.29±0.08	12.17±0.22	0.34±0.3	0.39±0.09	12.11±0.02	0.27±0.10	
		this work	12.05±0.01	0.46±0.01	12.01±0.04	0.13±0.04	0.61±0.01	11.95	0.05±0.01	0.465
		this work	12.01±0.01		11.97±0.04			11.91		0.22
(2763) Jeans	0.412±0.079	(1) 2014	12.336±0.001	0.395±0.015	12.434±0.011	0.0±0.13	0.04±0.003	12.250±0.001	0.0±0.013	
		(2)	–		–			–		
		(3)	12.26±0.06	0.22±0.05	12.16±0.18	0.3±0.25	0.33±0.08	12.24±0.02	0.4±0.1	
		this work	12.32±0.02	0.66±0.04	12.32±0.14	0.04±0.21	0.81±0.05	12.23	−0.21±0.08	0.102
(2823) van der-Laan	0.322±0.051	(1)	–	–	–	–	–	–	–	
		(2)	13.75±0.31	0.23±0.0				13.74±0.27	0.48±0.03	
			(±0.18)	(±0.05)				(±0.12)	(±-0.06)	
		(3)	13.14±0.07	0.31±0.07	13.31±0.28	0.57±0.47	0.37±0.1	13.05±0.03	0.25±0.09	
		this work	13.13±0.01	0.35±0.01	13.05±0.02	0.23±0.03	0.45±0.01	13.03	0.17±0.01	0.061
		this work	13.13±0.004		13.05±0.02			13.03		0.069
(2912) Lapalma	0.456±0.052	(1)	–	–	–	–	–	–	–	
		(2)	–		–			–		
		(3)	12.51±0.09	0.21±0.09	12.45±0.46	0.35±0.64	0.30±0.1	12.51±0.02	0.43±0.15	
		this work	12.06±0.02	0.35±0.03	12.01±0.11	0.25±0.14	0.46±0.03	11.96	0.16±0.07	0.934
(3849) Incidentia	0.398±0.041	(1) 2013	13.002±0.001	0.355±0.002	12.884±0.002	0.408±0.006	0.026±0.0	12.928±0.001	0.145±0.002	
		(2)	–		–			–		
		(3)	12.86±0.05	0.26±0.05	12.92±0.18	0.51±0.33	0.31±0.1	12.81±0.02	0.36±0.10	
		this work	12.9±0.004	0.46±0.01	12.78±0.02	0.03±0.04	0.61±0.02	12.81	0.03±0.01	0.154
		this work	12.75±0.004		12.64±0.01			12.67		0.1
(3869) Norton	0.162±0.029	(1)	–	–	–	–	–	–	–	
		(2)	12.39±0.26	0.23±0.0				12.42±0.24	0.41±0.004	
			(±0.19)	(±0.09)				(±0.02)	(±-0.12)	
		(3)	12.62±0.09	0.33±0.11	12.11±0.20	−0.21±0.18	0.51±0.06	12.52±0.06	0.19±0.08	
		this work	12.18±0.02	0.41±0.03	12.24±0.05	0.42±0.09	0.46±0.04	12.09	0.1±0.04	0.085
		this work	12.27±0.02		12.34 ±0.05			12.18		0.087
(4383) Suruga	0.320 ±0.038	(1)	–	–	–	–	–	–	–	
		(2)	12.86±0.29	0.25±0.0				12.83±0.25	0.43±0.007	
			(±0.17)	(±0.11)				(±0.05)	(±-0.10)	

(*continued on next page*)

Table 2 (*continued*)

Object	p_v	Author	H	G	H	G_1	G_2	H	G_{12}	amplitude
		(3)	13.09±0.1	0.33±0.12	12.79±0.27	0.02±0.28	0.46±0.07	12.98±0.06	0.19±0.09	
		this work	12.91±0.02	0.40±0.03	12.65±0.14	0.02±0.12	0.51±0.02	12.8	0.14±0.03	0.124
		this work	12.83±0.02		12.58±0.14			12.72		0.125
(4434) Nikulin	0.354±0.038	(1)	–	–	–	–	–	–	–	
		(2)	13.72±0.29	0.25±0.0				13.68±0.31	0.43±0.003	
			(±0.34)	(±0.1)				(±0.1)	(±-0.11)	
		(3)	13.14±0.07	0.33±0.08	13.14±0.19	0.33±0.28	0.43±0.09	13.05±0.05	0.18±0.10	
		this work	13.02±0.02	0.34±0.02	12.91±0.09	0.21±0.11	0.45±0.03	12.91	0.19±0.02	0.046
		this work	12.97±0.02		12.87±0.09			12.86		0.079
(4692) SIMBAD	0.358±0.051	(1)	–	–	–	–	–	–	–	
		(2)	13.99±0.39	0.77±0.20				13.90±0.31	−0.38±0.38	
			(±0.32)	(±0.20)				(±0.19)	(±-0.21)	
		(3)	13.46±0.08	0.34±0.08	13.41±0.23	0.25±0.29	0.45±0.07	13.37±0.05	0.18±0.08	
		this work	13.35±0.01	0.37±0.01	13.24±0.04	0.19±0.07	0.47±0.02	13.25	0.14±0.01	0.102
		this work	13.4±0.01		13.28±0.04			13.3		0.18
(5037) Habing	0.315±0.067	(1)	–	–	–	–	–	–	–	
		(2)	–		–			–		
		(3)	13.13±0.07	0.21±0.06	13.18±0.28	0.52±0.43	0.27±0.12	13.14±0.02	0.46±0.12	
		this work	13.03±0.04	0.27±0.04	12.73±0.11	0.09±0.11	0.39±0.04	12.97	0.26±0.09	0.22
		this work	12.93±0.03		12.64±0.12			12.86		0.221
(5525) 1991 TS4	0.403±0.046	(1)	–	–	–	–	–	–	–	
		(2)	13.69±0.5	0.53±0.23				13.45±0.47	0.12±0.39	
			(±0.23)	(±0.10)				(±0.41)	(±0.04)	
		(3)	13.04±0.09	0.16±0.08	12.68±0.41	0.11±0.43	0.3±0.1	13.09±0.02	0.54±0.13	
		this work	13.0±0.01	0.36±0.02	12.98±0.03	0.34±0.06	0.42±0.03	12.91	0.15±0.02	0.263
		this work	12.99±0.01		13.0±0.03			12.9		0.293
		this work	12.95±0.02		12.91±0.04			12.86		0.32
(5754) 1992 FR2	0.277±0.031	(1)	–	–	–	–	–	–	–	
		(2)	13.39±0.36	0.51±0.23				13.30±0.27	−0.006±0.35	
			(±0.16)	(±-0.07)				(±0.03)	(±0.19)	
		(3)	12.80±0.09	0.20±0.08	12.97±0.73	0.65±1.38	0.22±0.12	12.82±0.02	0.47±0.13	
		this work	12.38±0.02	0.34±0.02	12.04±0.1	0.0062±0.08	0.45±0.02	12.27	0.19±0.02	0.772
		this work	12.4±0.02		12.07±0.1			12.29		0.867
(7558) Yurlov	0.25*	(1) 2013	13.354±0.003	0.29±0.015	13.620±0.011	0.0±0.186	0.028±0.001	13.278±0.003	0.265±0.025	
		(2)	13.90±0.35	0.35±0.13				13.67±0.24	0.46±0.26	
			(±0.37)	(±0.17)				(±-0.05)	(±-0.005)	
		(3)	13.36±0.07	0.19±0.07	13.56±0.49	0.75±0.9	0.21±0.2	13.38±0.02	0.50±0.12	
		this work	13.24±0.01	0.30±0.01	13.22±0.01	0.39±0.03	0.36±0.01	13.16	0.28±0.03	0.146
		this work	13.17±0.01		13.14±0.01			13.09		0.240
		this work	13.19±0.01		13.17±0.01			13.11		0.164
(8761) Crane	0.39*	(1)	–	–	–	–	–	–	–	
		(2)	14.23±0.67	0.2±0.11				13.27±0.52	0.19±0.36	
			(±0.25)	(±0.004)				(±-0.1)	(±0.07)	
		(3)	13.82±0.08	0.30±0.08	13.57±0.19	0.06±0.22	0.44±0.07	13.74±0.03	0.21±0.10	
		this work	13.7±0.01	0.39±0.01	13.61±0.03	0.17±0.04	0.50±0.01	13.6	0.12±0.01	0.22
		this work	13.67±0.01		13.58±0.03			13.57		0.205
(9481) Menchu	0.203±0.048	(1)	–	–	–	–	–	–	–	
		(2)	13.77±0.33	0.19±0.0				13.78±0.35	0.51±0.02	
			(±0.22)	(±0.03)				(±0.1)	(±-0.003)	
		(3)	14.20±0.06	0.29±0.06	14.11±0.12	0.20±0.19	0.43±0.09	14.12±0.04	0.21±0.12	
		this work	14.26±0.02	0.31±0.05	14.13±0.14	0.06±0.58	0.55±0.37	14.17	0.13±0.19	0.172
(9531) Jean-Luc	0.279±0.050	(1)	–	–	–	–	–	–	–	
		(2)	14.05±0.38	0.0009±0.13				14.30±0.17	0.86±0.26	
			(±0.14)	(±0.01)				(±0.07)	(±-0.03)	
		(3)	13.83±0.09	0.27±0.09	13.90±0.39	0.44±0.56	0.37±0.11	13.77±0.02	0.30±0.12	

(*continued on next page*)

Table 2 (*continued*)

Object	p_v	Author	H	G	H	G_1	G_2	H	G_{12}	amplitude
		this work	14.01±0.02	0.44±0.03	13.8±0.2	0.05±0.15	0.53±0.06	13.9	0.07±0.08	0.083
		(1)	–	–	–	–	–	–	–	
(27192) Selenali	0.21*	(2)	14.76±1.3 (±1.73)	0.71±0.34 (±0.65)				14.2±0.36 (±0.22)	1.48±0.49 (±0.56)	
		(3)	13.89±0.05	0.18± 0.05	13.77±0.21	0.31±0.29	0.29±0.09	13.92±0.02	0.49±0.11	
		this work	14.14±0.03	0.28±0.04	14.13±0.14	0.39±0.21	0.35±0.06	14.08	0.35±0.22	0.086

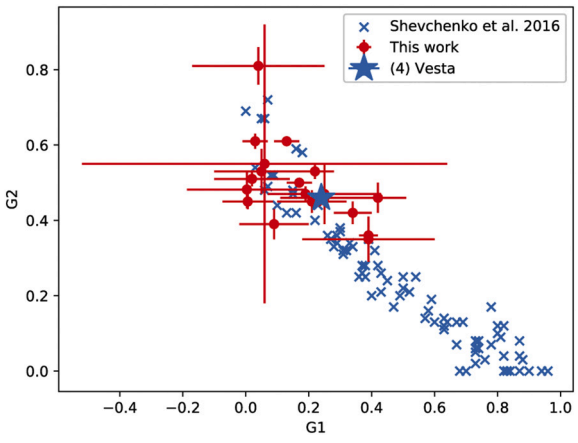

Fig. 1. Distribution of the observed asteroids in G_1, G_2 parameters phase space among other asteroid types. Parameters for (4) Vesta are taken from Shevchenko et al. (2016).

homogeneous sphere) and depend on aspect angle, asteroid shape, pole orientation, and orbital inclination. Current recommendations, especially for low quality data (0.3 mag scatter or more) or when insufficient measurements are available are to use separate G_{12}*-parameters for different taxonomic classes (Penttila et al., 2016). Those parameters have been firmly established for *E*-, S/M-, C-, P-, and D-type asteroids. An extension into other asteroid classes is needed. In this article we provide the G_{12}* value for the V-class, providing an incremental improvement to better prediction of their apparent magnitudes.

High quality phase curves are available only for a small number of objects, mostly owing to time-demanding observations and up to recently lack of calibration stars in the field-of-view of telescopes making the process of obtaining relative magnitudes difficult. However thanks to large survey catalogues such as PanSTARSS, SDSS, APASS and Gaia lack of calibration stars is no longer a problem. Therefore most of the historical differential photometry can now be converted into relative magnitudes if the raw/reduced CCD frames are available or the comparison stars are known. In this manuscript we re-reduce and re-calibrate historical data to derive an extended number of high quality asteroid phase-curves.

In this study we investigate phase curve parameters for V-types outside the Vesta family and compare them with that of (4) Vesta to verify the existence of distinct groups of V-type asteroids in the phase-curve parameters space. Similar study was already proposed by Medeiros et al. (2018), but so-far no results have been published. Therefore this study constitutes the first statistical study of phase curves among the V-type asteroids.

2. Target selection

We have selected 20 V-type asteroid that lie outside the dynamical Vesta family. Further more the targets had to **exhibit** apparent magnitudes and observing conditions (oppositions away from the Moon, away from the ecliptic plane, etc.) suitable for the small and moderate aperture telescopes accessible to our group. We focused mostly on objects with short rotational periods, such that the full lightcurve could be covered within one night. Due to weather constrains the minimal phase angle could not always be reached, thus for several targets we have obtained data in several oppositions.

3. Data reduction and calibration

The photometric data used for this paper have been collected with various telescopes during the years 2013–2020. The observing logs, bias,

Table 3
Median phase curve parameters (and their standard deviations) and parameters derived from the simultaneous fit (together with their uncertainties) to all the V-type data.

	G	G_1	G_2	G_{12}
Median	0.35 ± 0.09	0.2 ± 0.13	0.47 ± 0.07	0.14 ± 0.13
Simult.	0.38 ± 0.01	0.27 ± 0.02	0.48 ± 0.01	0.13 ± 0.01

dark, and flat-field standard reduction were described in (Oszkiewicz et al. 2020) and will not be repeated here. A brief summary of the observing circumstances is given in Table 1. Most of the data had photometric accuracy of 0.05 mag or better and the determined periods resulted in uncertainties ranging from 0.0001 h to 0.00001 h, which are well sufficient for **determination** of phase curves. For most objects we have obtained good phase angle coverage, however for some (like 2442 Corbett or 4843 Suruga) we were not able to accurately map the opposition spike. In Table 1 we listed the smallest phase angle reached for each object. Three objects were observed at a minimal phase angle less than 1, thirteen objects at less than 3, eighteen at less than 5 and two at a minimal phase angle larger than 5.

Due to **the** large amount of the CCD frames, the aperture photometry measurements have been carried out with the Photometric Pipeline (Mommert 2017). Unfortunately, in some cases a semi-automatic approach was necessary. It was done with the AUTOPHOTOM aperture photometry program included in the Starlink package (Currie et al. 2014).[3]

For the phase curve creation we decided to calibrate all observations to the Johnson's-Cousin's R_C band. Traditionally such phase curves are expressed in the V band but in many cases our observations were done in R and to make transformations more accurate we decided not to convert it further to V.

The calibration of the instrumental magnitudes to R_C band was done with the PanSTARRS DR1 (hereafter PS1) standard stars (Tonry et al. 2012). The catalogue r-g colours were used to transform the original r magnitudes to R_C band. This was done according to the transformation equations of (Chonis and Gaskell 2008).

As we did not know the transformation equations between the instrumental magnitudes and the standard R_C band we assumed they were identical if both the asteroid and the calibration star had solar colours of $g' - r' = 0.45 \pm 0.2$, $r' - i' = 0.14 \pm 0.2$. While most observations were done in instrumental R_C band, some were obtained in the SDSS r filter or even in a clear filter. The latter means the instrumental band was defined by the sensitivity of the CCD camera and for the front-illuminated chip was close to the broadened R_C band. Such instrumental and standard star magnitudes discrepancy can usually introduce substantial errors, but by limiting the choice of standard stars to those of solar colours it was greatly minimised.

To check the accuracy of our transformations we selected the worst cases: for observations done in a clear filter we selected PS1 stars with colours close to limits of the assumed solar star intervals. In all cases the spread of the obtained calibrated R_C magnitudes was within 0.01 mag which was at the level of the accuracy of instrumental magnitudes. As in practise we used a group of 3–9 PS1 solar type stars of slightly different colours we believe the accuracy of our calibration was limited by the accuracy of the aperture photometry.

After transforming all calibrated magnitudes to unit distances of the asteroid from the observer and the Sun, we combined data obtained on a single night to form a lightcurve. Naturally, for the phase curve creation we had to use lightcurves observed at different solar phase angles. They were obtained at different dates before and after opposition, covering a time span of several months. To combine them we first had to derive a synodical period of rotation. This was done by fitting a Fourier series of the 4–6 order to the lightcurve data (which also included finding the relative magnitude shifts for data from different epochs) reduced to the unit distances from the Sun and the observer, and corrected for the light time. In cases when the lightcurve shape was more complicated we considered higher Fourier orders. This, however, had its shortcomings as the lightcurve shape used to slightly change with the phase angle and the overfitting appeared.

In the analysis we first we used several lightcurves from a short time span to obtain the first approximation of the rotation period. It allowed us to add new lightcurves more distant in time. In the process the accuracy of the average synodical period increased so that we were able to combine lightcurves from several months in one fit. Such procedure allowed us to avoid period ambiguity and determine the relative shifts in magnitudes among the lightcurves caused by the phase angle changes. By making a simultaneous Fourier fit of all data we were able to also use incomplete lightcurves which did not cover the whole rotation cycle.

Next, the maximum brightness, as defined by the Fourier fit, was determined and assumed as the asteroid brightness at the specified solar phase angle. Note that the simultaneous fit of all data allowed us to derive maximum brightness also for the partial lightcurves (for example, if for some epoch the data covered only the lightcurve minimum, the relative shift to the full composite could be used to get its maximum).

For the phase curve creation we used the maximum rather than the average lightcurve brightness because the latter depends more on the lightcurve amplitude which in itself is a function of the phase angle (Dunlap et al. 1973; Sather 1976). Also, when combining data from different oppositions (at which the asteroid was observed at different aspects), lightcurve maxima are less effected by aspect changes than the means (Dunlap and Gehrels 1969). To illustrate that fact we simulated a set of lightcurves for a triaxial **ellipsoid** (a/b = 1.7, b/c = 1.2), scattering the light according to the Hapke function, with parameters typical for an average S-type asteroid (Kwiatkowski 1995). The change of aspect from 90° to 30°, at the phase angle of 20°, changed the maximum of the lightcurve (Max) by 0.2 mag, and the average of the lightcurve maximum and minimum **(Max + Min)/2** by as much as 0.6 mag.

Since all our data have been calibrated to the R_C band, the absolute magnitude H derived from them would also be expressed in R_C. However, to compare our absolute magnitudes to those of others it is possible

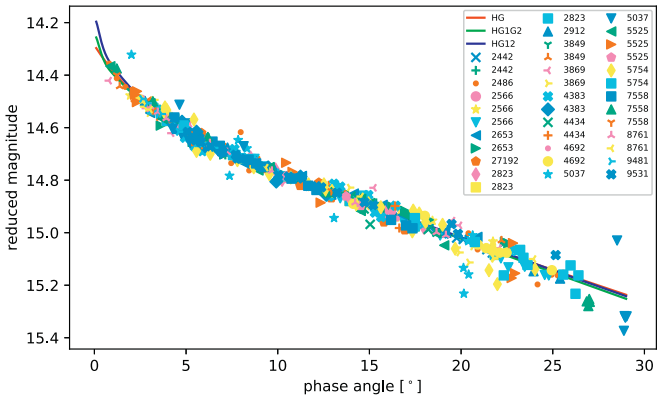

Fig. 2. Simultaneous fit to all (except for Jeans) V-type data. Data from different asteroids and subsequent apparitions are denoted by markers and colours. The fitted parameters are: $G_1 = 0.27 \pm 0.02$, $G_2 = 0.48 \pm 0.01$, $G_{12} = 0.13 \pm 0.01$, $G = 0.38 \pm 0.01$.

[3] The Starlink software is currently supported by the East Asian Observatory.

to correct our results to the traditional V band using the average $V - R$ colour of the V-type asteroids we observed. For most of them we found $r - i$ colours in the SDSSMOC catalogue and converted them to $V - R$ using the equation from Jester et al. (2005). From that we derived the average correction between R and V bands which resulted in the formula: $H_V = H_R + 0.34$, which can be used to transform H_R to H_V.

Since our absolute magnitudes are derived from lightcurve maxima, and some users might prefer them to be referred to the lightcurve average values, in Table 2 we also provide lightcurve amplitudes, which can be used for the conversion.

4. Results

We fitted three phase functions to our data (the H,G phase function (Bowell et al. 1989); the H, G_1, G_2 and H, G_{12} functions (Muinonen et al. 2010a)). All the fits were done in flux space as the functions are defined in the flux space and the data are of high quality. Fitting in the magnitude space is recommended for data with large photometric scatter (>0.3 mag) due to biases arising in magnitude space (Penttilä et al. 2016). We assumed the same single-point uncertainties for all the data, thus no weighing was applied. For the three parameter function (H, G_1, G_2) we used the constrained fitting presented in Penttilä et al. (2016), that is we imposed that $0 \leq G_1$, G_2, and $1 - G_1 - G_2 \leq 1$. For asteroids having data from multiple oppositions we used a simultaneous fit assuming the same slope parameters in all apparitions and different absolute magnitude values. This means that we fitted $N + 1$ parameters for the two parameter phase functions (H,G and H,G_{12}) and $N + 2$ parameters for the three parameter phase function (H,G_1,G_2), where N is the number of apparitions observed. Finally the data were plotted by shifting all phase curves to the brightest apparition. The shift is equivalent to the difference in absolute magnitudes between the apparitions. Combining data from multiple oppositions is a reasonable approach for small asteroids with homogeneous surface properties (all objects in this work have diameters < 10 km). It is however inadvisable for large objects that may display on average different surface properties at various geometries and aspect angles.

Generally we find that for our targets the H,G system tends to over estimate the H value with respect to the H,G_1,G_2 system and the H,G_{12} underestimates. This is consistent with Carbognani et al. (2019) who found systematic biases in the derived absolute magnitudes from various phase functions (the H,G function, the H,G_1,G_2 and that of Shevchenko (1997)). In particular the Shevchenko (1997) function produced brighter results than both the H,G_1,G_2 and H,G systems. The obtained differences were found to be around 0.2 mag and non-negligible. Median difference between the absolute magnitude values derived from the H, G_1,G_2 and H, G_{12} systems in our data is 0.06 mag and between the H,G_1, G_2 and H,G absolute magnitudes is 0.08 mag. The differences grow with the minimal phase angle observed and are larger for phase curves with larger magnitude scatter (typically objects with small lightcurve amplitude). The largest differences are for 2442 Corbett for which we have not covered the opposition spike well ($\alpha_{min} > 6°$). Interestingly the difference between the absolute magnitudes derived from the two parameter systems (H,G and H,G_{12}) seems to be systematic, stable around 0.1 mag and independent of the smallest phase angle covered and the data quality.

The resulting fits are shown in Figs. 3 to 22 and the numerical values are presented in Table 2. For reference we also list phase-curve parameters derived by other authors (Waszczak et al. (2015); Oszkiewicz et al. (2011); Vereš et al. (2015)). It should be however noted that phase-curve parameters derived from sparse data can be used in a statistical sense, but can be misleading when it comes to single objects. The unmatched slope parameters in Table 2 between the different authors and in some cases between the parameters derived from different oppositions by the same author strongly highlight the need for high quality phase-curves for single objects and for detailed studies.

Several factors make the detailed comparison of the phase curve parameters especially challenging. Correction for lightcurve amplitude varies between authors from no correction at all to fitting simple sinusoidal function to sparse data, selecting the maximum observed points from fragmental data to the removal of the actual lightcurve amplitude determined from dense lightcurves. Furthermore the phase curves may refer to the mean or maximum brightness on the lightcurves. Often different authors provide absolute magnitudes from different filters, the Johnson V or R are the most common. The data are fitted in magnitude or in flux space using linear or non-linear fitting algorithms (sometimes with constrains put on the best fit parameters), which may introduce large difference Penttilä et al. (2016) for sparse scattered data. Different reduction procedures including different stellar comparison stars or details such as selection of solar analogues may also play a role in the resulting parameters. Lastly the derived parameters may correspond to different apparitions and thus may not be directly comparable.

In Fig. 1 we show the distributions of the G_1, G_2 parameters for our objects. All the derived slope parameters are consistent with slopes of moderate and high geometric albedo objects typical for V-type asteroids including (4) Vesta, for which albedo can vary from ~ 0.28 to ~ 0.35 (Cellino et al. 2016) depending upon the epoch of observation, due to the known albedo heterogeneity of Vesta's surface, confirmed by in situ imaging by the Dawn space mission. The G_1, G_2 parameters of all the asteroids, (except for one object) are clustered around the G_1, G_2 values for the largest V-type asteroid (4) Vesta. There is no obvious separation into distinct groups of different phase curve parameters for the V-types. Gil-Hutton et al. (2017) showed a variety of polarimetric behavious among the V-types. The difference in polarimetric parameters was attributed to difference in regolith particle size. Shape of asteroid phase curves is also dependant on regolith particle size, thus similar diversity should also be visible in phase-curve parameters. However we do not find significant evidence for such a variety in the V-type phase curve parameters space. Only one asteroid ((2763) Jeans, a spectrally confirmed V-type by Moskovitz et al. (2010) has G_1, G_2 parameters that are more consistent with the taxonomic E-type objects. This finding should be confirmed in an independent opposition. It should be pointed out that (2763) Jeans also has a very high geometric albedo of $p_v = 0.412 \pm 0.079$ (Masiero et al. 2011; Mainzer et al. 2016).

Penttilä et al. (2016) recommended that low-quality phase curves should be fitted with phase functions with G_{12}* parameter fixed according to taxonomic type. That parameter was however not given for the V-type class. We estimated it here. Median phase curve parameters and those deriving from the simultaneous fit (except for Jeans) are summarised in Table 3. The simultanious fit to all the data is shown in Fig. 2. The derived values can be used in single parameter phase function to fit low quality V-type phase curves.

The derived median G_1, G_2 values are close to that of (4) Vesta shown in Shevchenko et al. (2016). The median G value differs from that obtained for (4) Vesta by other authors. For example Hasegawa et al. (2014) observed (4) Vesta during the 2006 opposition and derived phase curves in the B, R and z' bands. The resulting H, G parameters were $H_B = 3.96 \pm 0.01$ mag and $G_B = 0.30 \pm 0.02$, $H_R = 2.82 \pm 0.01$ mag and $G_R = 0.29 \pm 0.01$, and $H_{z'} = 3.08 \pm 0.02$ mag and $G_{z'} = 0.25 \pm 0.01$. Those data were later utilised by Fornasier et al. 2011 in connection with Rosetta spacecraft photfometry obtained in 2010 at a high phase angle ($\alpha = 52°$). They obtained photometric phase-curve of (4) Vesta and estimated the $H(R) = 2.80 \pm 0.01$ and $G = 0.27 \pm 0.01$. The discrepancy between the median G value (H,G phase function) derived by us and that of Vesta (Fornasier et al. (2011)) could be due to different surfaces

sampled.

5. Summary

We have derived well-determined phase-curve parameters for 20 V-type asteroids for the first time. The fits are derived based on high-quality data obtained by us. We estimated medium G, G_1,G_2,G_{12} slope parameters. The estimated medium G_{12} can be used in fitting low-quality V-type phase curves with a single parameter phase functions described in Penttilä et al. (2016).

We do not find substantial evidence for separation into two or more distinct slope-parameters V-type groups. Phase curve parameters for all (except for one) objects are clustered around that of (4) Vesta. One asteroid ((2763) Jeans) shows exceptionally high G_2 value which should be verified in another opposition.

Further work should be conducted to determine slope parameters of more V-types, including larger sample overlap with objects observed by Gil-Hutton et al. (2017) to confirm the diversity of the V-type population. Obtaining phase curves of non-Vestoids (such as those in the mid and outer Main Belt) may also help clarify if the variety of polarimetric behaviours found by Gil-Hutton et al. (2017) is due to particle size or mineralogical differences. Particular focus should be put to obtain high quality data at small phase angles and best at multiple oppositions to derive high accuracy phase-curve parameters.

Declaration of Competing Interest

None.

Acknowledgments

This work has been supported by grants No. 2017/25/B/ST9/00740 and 2017/26/D/ST9/00240 from the National Science Centre, Poland. The work at Modra was supported by the Slovak Grant Agency for Science VEGA, Grant 1/0911/17. The work at Sopot Observatory has been supported by the 2018 Shoemaker NEO Grant founded by the Planetary Society.

Based on observations made with 1.83 m Perkins, 1.07 m Hall and 0.79 m telescopes at Lowell Observatory, 2.24 m University of Hawaii telescope at Mauna Kea Observatory, 1.0 m Jacobus Kapteyn Telescope and 2.5 Nordic Optical Telescope at the Roque de los Muchachos Observatory on La Palma, 0.7 m Roman Baranowski telescope at Winer Observatory, 0.6 m Zeiss telescope at Modra Observatory, 0.8 m Odessa Multifunctional Telescope at Odessa-Mayaki Observatory and 0.35-m telescope at the Sopot Astronomical Observatory in Serbia.

Appendix A. Phase curves for individual objects

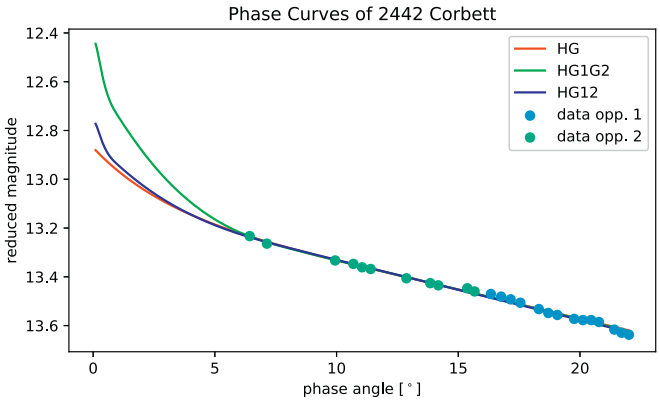

Fig. 3. Phase curves of asteroid (2442) Corbett derived based on data obtained in the 2013 and 2015 oppositions.

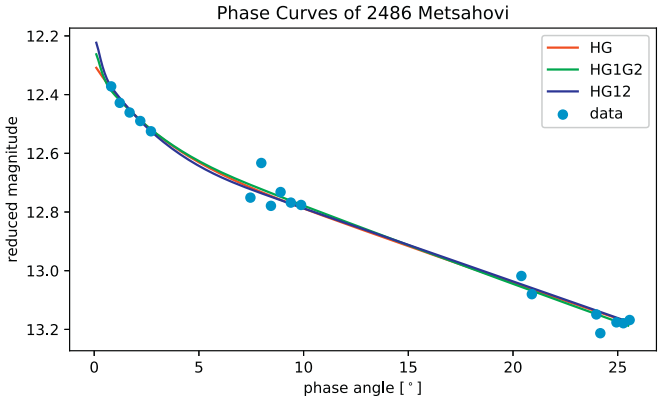

Fig. 4. Phase curves of asteroid (2486) Metsahovi derived based on data obtained in the 2019 opposition.

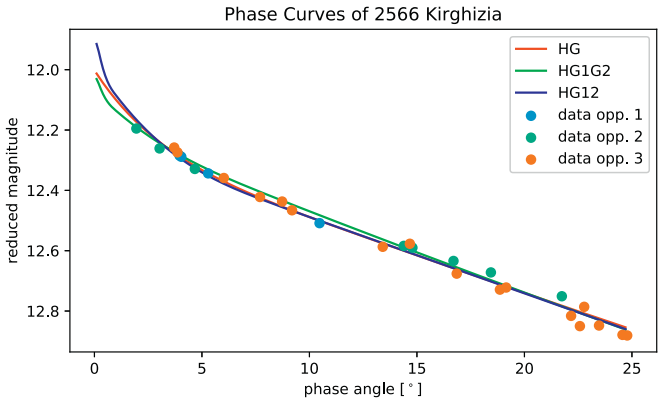

Fig. 5. Phase curves of asteroid (2566) Kirghizia derived based on data obtained in the 2013, 2015 and 2017 opposition.

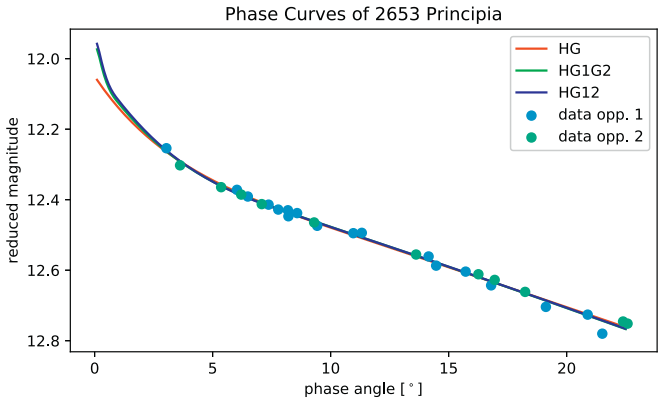

Fig. 6. Phase curves of asteroid (2653) Principia derived based on data obtained in the 2017 and 2018/19 opposition.

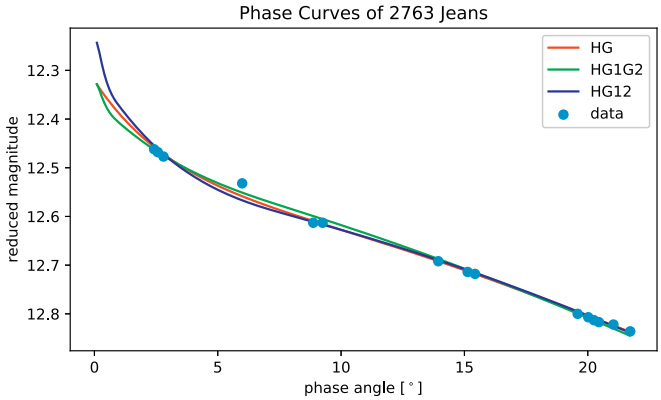

Fig. 7. Phase curves of asteroid (2763) Jeans derived based on data obtained in the 2016/17 opposition.

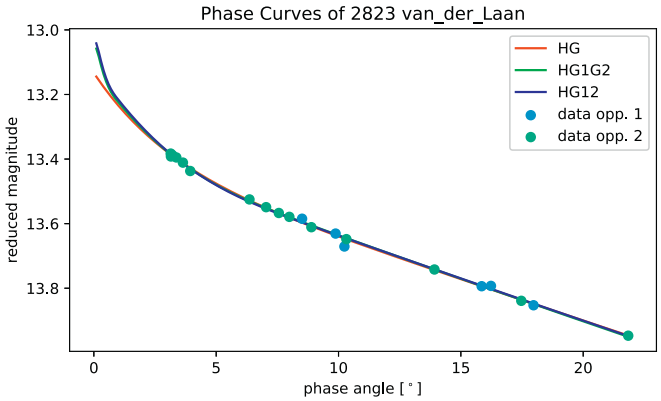

Fig. 8. Phase curves of asteroid (2823) van der Laan derived based on data obtained in year 2016.

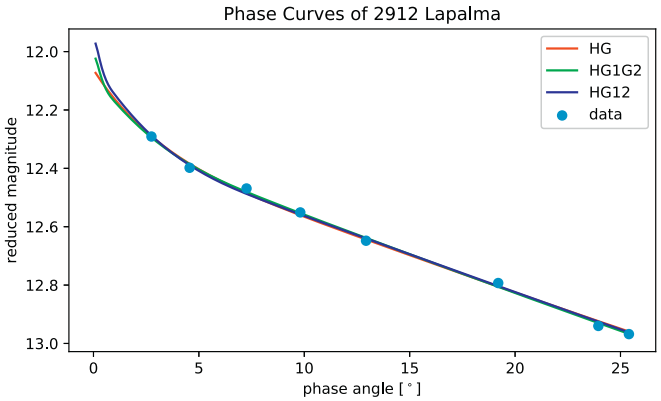

Fig. 9. Phase curves of asteroid (2912) Lapalma derived based on data obtained in year 2017/18.

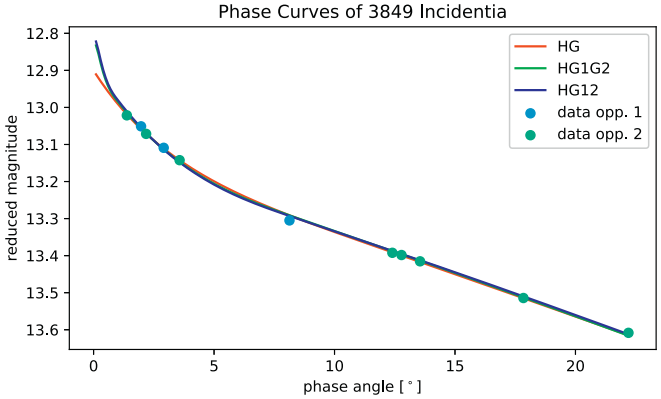

Fig. 10. Phase curves of asteroid (3849) Incidentia derived based on data obtained in the 2013 and 2019 oppositions.

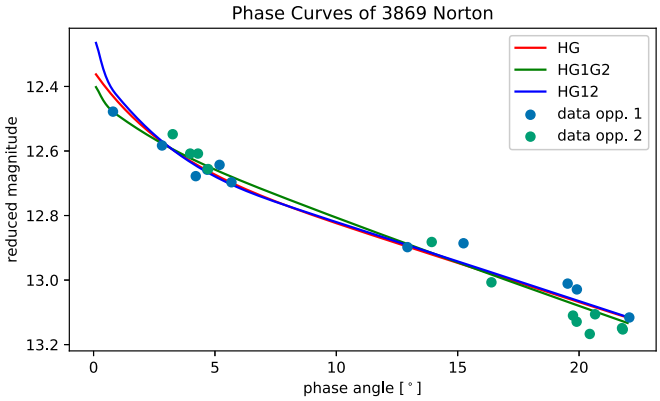

Fig. 11. Phase curves of asteroid (3869) Norton derived based on data obtained in 2013/2014 and 2017/18 opposition.

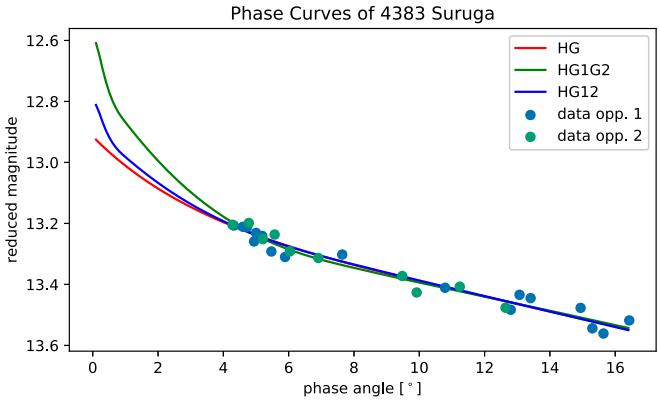

Fig. 12. Phase curves of asteroid (4383) Suruga derived based on data obtained in 2017 and 2019 opposition.

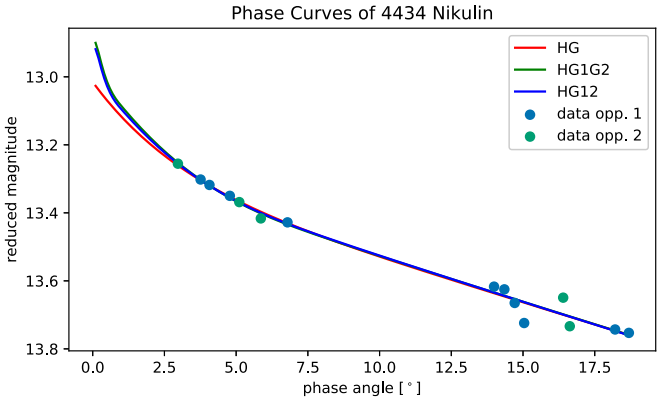

Fig. 13. Phase curves of asteroid (4434) Nikulin derived based on data obtained in years 2017 and 2018.

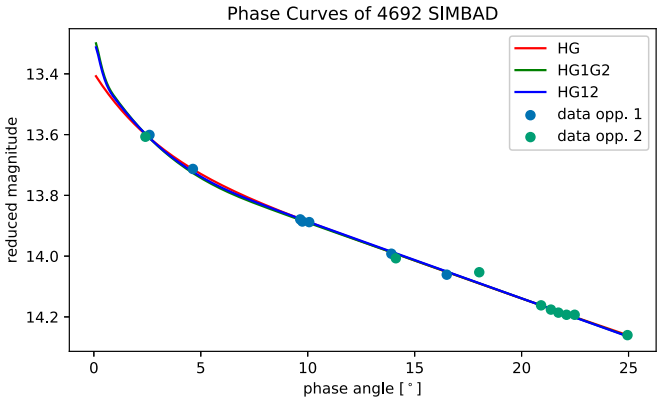

Fig. 14. Phase curves of asteroid (4692) SIMBAD derived based on data obtained in year 2014/15 and 2017.

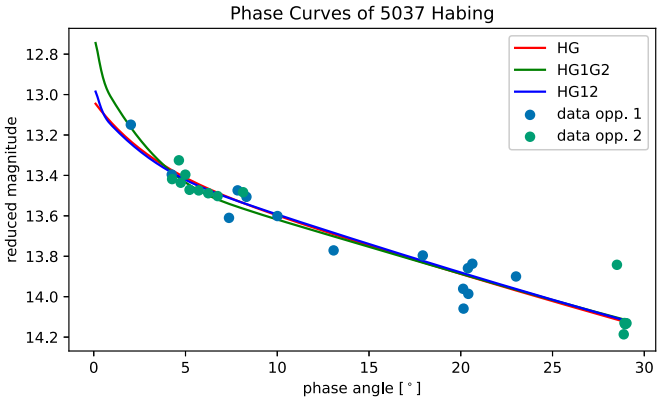

Fig. 15. Phase curves of asteroid (5037) Habing derived based on data obtained in year 2018 and 2019/20.

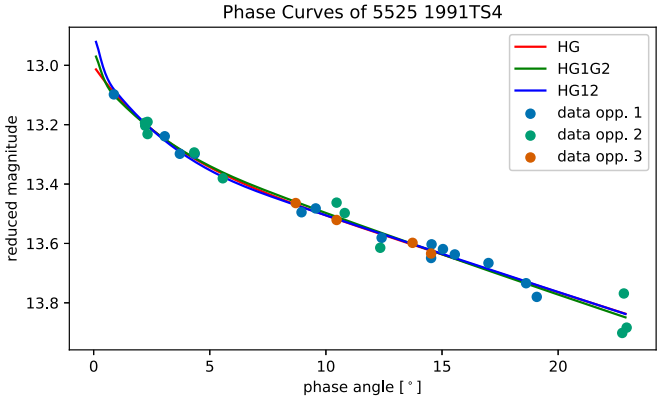

Fig. 16. Phase curves of asteroid (5525) 1991 TS4 derived based on data obtained in year 2014, 2016 and 2018/19.

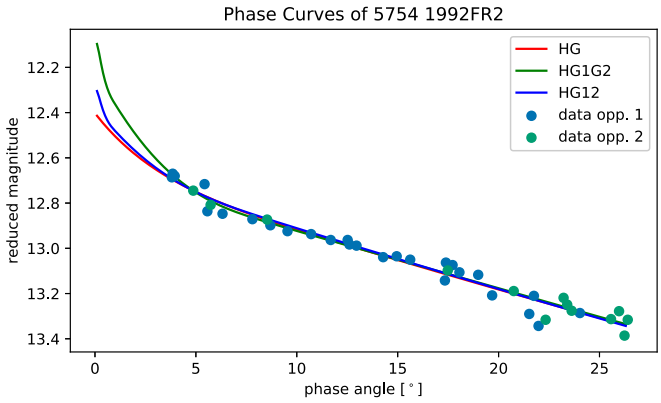

Fig. 17. Phase curves of asteroid (5754) 1992 FR2 derived based on data obtained in year 2016 and 2017/18.

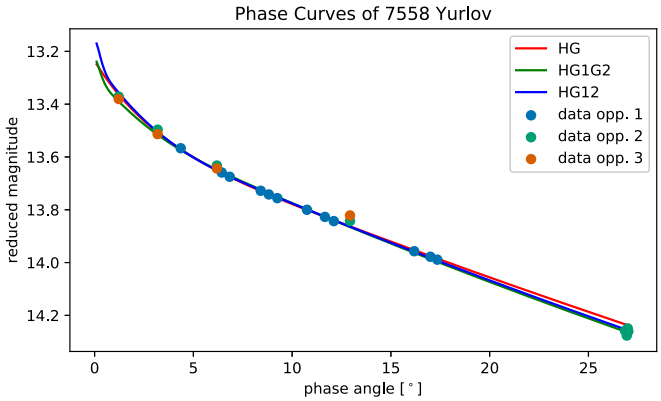

Fig. 18. Phase curves of asteroid (7558) Yurlov derived based on data obtained in year 2013, 2018 and 2019.

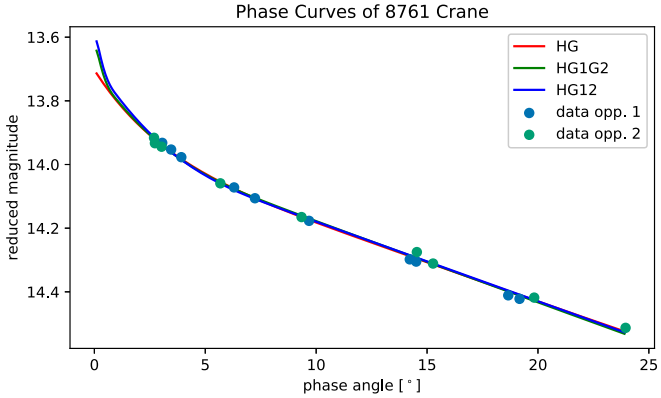

Fig. 19. Phase curves of asteroid (8761) Crane derived based on data obtained in years 2016, 2018.

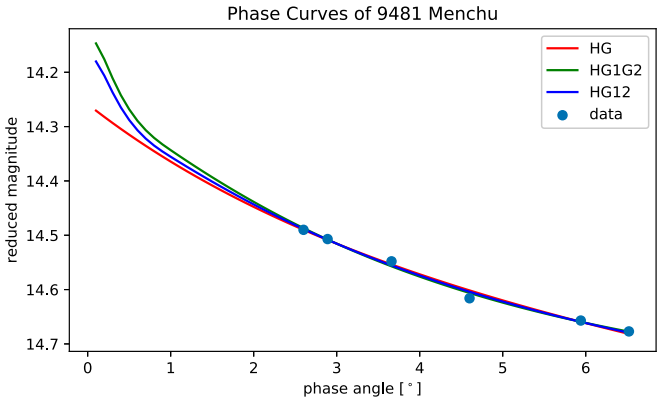

Fig. 20. Phase curves of asteroid (9481) Menchu derived based on data obtained in year 2014.

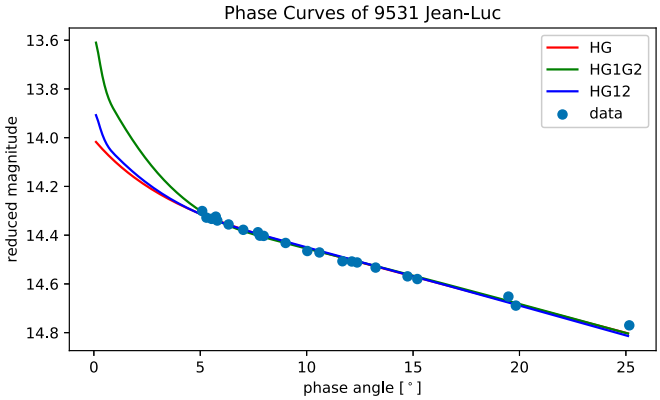

Fig. 21. Phase curves of asteroid (9531) Jean-Luc derived based on data obtained in year 2018/2019.

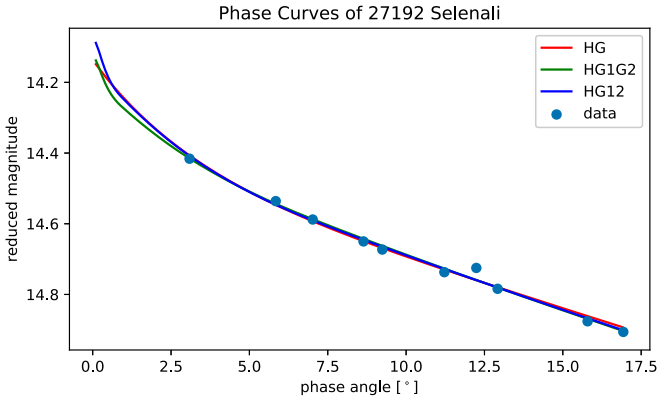

Fig. 22. Phase curves of asteroid (27192) Selenali derived based on data obtained in year 2015.

References

Akimov, L., 1988. Light reflection by the moon. Ii. Kinematika i Fizika Nebesnykh Tel 4, 10–16.

Belskaya, I., Shevchenko, V., 2000. Opposition effect of asteroids. Icarus 147, 94–105.

Belskaya, I., Shevchenko, V., 2018. Phase angle effects in brightness and polarization for different classes of small solar system bodies. In: European Planetary Science Congress, vol. 12. https://meetingorganizer.copernicus.org/EPSC2018/EPSC2018-730.pdf. EPSC2018–730.

Binzel, R.P., Xu, S., 1993. Chips off of asteroid 4 vesta: evidence for the parent body of basaltic achondrite meteorites. Sci 260, 186–191.

Bottke, W.F., Nesvorný, D., Grimm, R.E., Morbidelli, A., O'Brien, D.P., 2006. Iron meteorites as remnants of planetesimals formed in the terrestrial planet region. Nature 439, 821.

Bowell, E., Hapke, B., Domingue, D., Lumme, K., Peltoniemi, J., Harris, A.W., 1989. Application of photometric models to asteroids. Asteroids II 524–556.

Burbine, T.H., Buchanan, P.C., Binzel, R.P., Bus, S.J., Hiroi, T., Hinrichs, J., Meibom, A., McCoy, T.J., 2001. Vesta, vestoids, and the howardite, eucrite, diogenite group: relationships and the origin of spectral differences. Meteorit. Planet. Sci. 36, 761–781.

Burbine, T., Demeo, F., Rivkin, A., Reddy, V., 2017. Evidence for differentiation among asteroid families. In: Planetesimals: Early Differentiation and Consequences for Planets. *Cambridge University Press, Cambridge*, pp. 298–320.

Carbognani, A., Cellino, A., Caminiti, S., 2019. New phase-magnitude curves for some main belt asteroids, fit of different photometric systems and calibration of the albedo-photometry relation. Planetary and Space Science 169, 15–34.

Carruba, V., Michtchenko, T.A., Roig, F., Ferraz-Mello, S., Nesvorný, D., 2005. On the v-type asteroids outside the vesta family-i. interplay of nonlinear secular resonances and the yarkovsky effect: the cases of 956 elisa and 809 lundia, 441, pp. 819–829.

Cellino, A., Ammannito, E., Magni, G., Gil-Hutton, R., Tedesco, E., Belskaya, I., De Sanctis, M., Schröder, S., Preusker, F., Manara, A., 2016. The dawn exploration of (4) vesta as the 'ground truth'to interpret asteroid polarimetry. Mon. Not. R. Astron. Soc. 456, 248–262.

Chonis, T.S., Gaskell, C.M., 2008. Setting UBVRI photometric zero-points using Sloan digital sky survey ugriz magnitudes, 135, pp. 264–267.
Cochran, A.L., Vilas, F., Jarvis, K.S., Kelley, M.S., 2004. Investigating the vesta–vestoid–hed connection. Icarus 167, 360–368.
Consolmagno, G.J., Drake, M.J., 1977. Composition and evolution of the eucrite parent body: evidence from rare earth elements. Geochim. Cosmochim. Acta 41, 1271–1282.
Currie, M.J., Berry, D.S., Jenness, T., Gibb, A.G., Bell, G.S., Draper, P.W., 2014. Starlink software in 2013. In: Manset, N., Forshay, P. (Eds.), *Astronomical Data Analysis Software and Systems XXIII* (p. 391). Volume 485 of *Astronomical Society of the Pacific Conference Series*.
De Sanctis, M., Migliorini, A., Jasmin, F.L., Lazzaro, D., Filacchione, G., Marchi, S., Ammannito, E., Capria, M., 2011. Spectral and mineralogical characterization of inner main-belt v-type asteroids., 533, p. A77.
Duffard, R., Roig, F., 2009. Two new v-type asteroids in the outer main belt? Planetary Space Science 57, 229–234.
Duffard, R., Lazzaro, D., Licandro, J., De Sanctis, M.C., Capria, M.T., 2006. V-type asteroids: a mineralogical study, 38, pp. 1987–1990.
Dunlap, J.L., Gehrels, T., 1969. Minor planets. III. Lightcurves of a Trojan Asteroid, 74, p. 796.
Dunlap, J., Gehrels, T., Howes, M., 1973. Minor planets and related objects. Ix. Photometry and polarimetry of (1685) Toro. The Astronomical Journal 78, 491.
Florczak, M., Lazzaro, D., Duffard, R., 2002. Discovering new v-type asteroids in the vicinity of 4 vesta, *159*, pp. 178–182.
Fornasier, S., Mottola, S., Barucci, M., Sierks, H., Hviid, S., 2011. Photometric observations of asteroid 4 vesta by the osiris cameras onboard the rosetta spacecraft. Astronomy & Astrophysics 533, L9.
Fulvio, D., Perna, D., Ieva, S., Brunetto, R., Kanuchova, Z., Blanco, C., Strazzulla, G., Dotto, E., 2016. Spectral characterization of v-type asteroids–i. space weathering effects and implications for v-type neas. Mon. Not. R. Astron. Soc. 455, 584–595.
Gil-Hutton, R., López-Sisterna, C., Calandra, M., 2017. Polarimetric survey of main-belt asteroids-v. the unusual polarimetric behavior of v-type asteroids. Astronomy & Astrophysics 599, A114.
Hapke, B., 1986. Bidirectional reflectance spectroscopy: 4. The extinction coefficient and the opposition effect. Icarus 67, 264–280.
Hardersen, P.S., Gaffey, M.J., Abell, P.A., 2004. Mineralogy of asteroid 1459 magnya and implications for its origin, 167, pp. 170–177.
Hardersen, P.S., Reddy, V., Roberts, R., Mainzer, A., 2014. More chips off of asteroid (4) vesta: characterization of eight vestoids and their hed meteorite analogs, 242, pp. 269–282.
Harris, A., Young, J., 1989. Asteroid lightcurve observations from 1979–1981. Icarus 81, 314–364.
Hasegawa, Sunao, Miyasaka, Seidai, Tokimasa, Noritaka, Sogame, Akito, Ibrahimov, Mansur A., Yoshida, Fumi, Ozaki, Shinobu, Abe, Masanao, Ishiguro, Masateru, Kuroda, Daisuke, 2014. The opposition effect of the asteroid 4 Vesta. Publ. Astron. Soc. Jpn. 66 (5) (Oxford University Press).
Ieva, S., Dotto, E., Lazzaro, D., Fulvio, D., Perna, D., Mazzotta Epifani, E., Medeiros, H., Fulchignoni, M., 2018. Basaltic Material in the Main Belt: A Tale of Two (or More) Parent Bodies?, 479, pp. 2607–2614.
Jester, S., Schneider, D.P., Richards, G.T., Green, R.F., Schmidt, M., Hall, P.B., Strauss, M. A., Vanden Berk, D.E., Stoughton, C., Gunn, J.E., Brinkmann, J., Kent, S.M., Smith, J. A., Tucker, D.L., Yanny, B., 2005. The Sloan digital sky survey view of the Palomar-Green bright quasar survey. Astron. J. 130, 873–895.
Kaasalainen, S., Piironen, J., Kaasalainen, M., Harris, A., Muinonen, K., Cellino, A., 2003. Asteroid photometric and polarimetric phase curves: empirical interpretation. Icarus 161, 34–46.
Kwiatkowski, T., 1995. Sidereal period, pole and shape of asteroid 1620 Geographos, *294*, pp. 274–277.
Lazzaro, D., Michtchenko, T., Carvano, J., Binzel, R., Bus, S., Burbine, T., Mothé-Diniz, T., Florczak, M., Angeli, C., Harris, A.W., 2000. Discovery of a basaltic asteroid in the outer main belt. Science 288, 2033–2035.
Leith, T.B., Moskovitz, N.A., Mayne, R.G., DeMeo, F.E., Takir, D., Burt, B.J., Binzel, R.P., Pefkou, D., 2017. The compositional diversity of non-vesta basaltic asteroids, 295, pp. 61–73.
Lumme, K., Bowell, E., 1981. Radiative transfer in the surfaces of atmosphereless bodies. I-theory. Ii-interpretation of phase curves. Astron. J. 86, 1694–1721.
Mainzer, A., Bauer, J., Cutri, R., Grav, T., Kramer, E., Masiero, J., Nugent, C., Sonnett, S., Stevenson, R., Wright, E., 2016. Ear-a-compil-5-neowisediam-v1. 0. NASA Planetary Data System. https://pds.nasa.gov/ds-view/pds/viewDataset.jsp?dsid=EAR-A-COMPIL-5-NEOWISEDIAM-V1.0.
Masiero, J.R., Mainzer, A., Grav, T., Bauer, J., Cutri, R., Dailey, J., Eisenhardt, P., McMillan, R., Spahr, T., Skrutskie, M., et al., 2011. Main belt asteroids with wise/neowise. i. preliminary albedos and diameters. The Astrophysical Journal 741, 68.
McCord, T.B., Adams, J.B., Johnson, T.V., 1970. Asteroid vesta: spectral reflectivity and compositional implications. Sci 168, 1445–1447.
Medeiros, H., de Leon, J., Lazzaro, D., Rondon, E., Monteiro, F., Popescu, M., Pinilla-Alonso, N., Arcoverde, P., Morate, D., Rodrigues, T., et al., 2018. Mineralogical and photometric analysis of v-type asteroids. In *European Planetary Science Congress* 12.
Medeiros, H., de León, J., Lazzaro, D., Popescu, M., Lorenzi, V., Pinilla-Alonso, N., Landsman, Z., Rizos, J., Morate, D., 2019. Compositional characterization of v-type candidate asteroids identified using the movis catalogue. Mon. Not. R. Astron. Soc. 488, 3866–3875.
Michtchenko, T., Lazzaro, D., Ferraz-Mello, S., Roig, F., 2002. Origin of the basaltic asteroid 1459 magnya: a dynamical and mineralogical study of the outer main belt. Icarus 158, 343–359.
Migliorini, A., De Sanctis, M., Lazzaro, D., Ammannito, E., 2017. Spectral characterization of v-type asteroids outside the vesta family. Mon. Not. R. Astron. Soc. 464, 1718–1726.
Migliorini, A., De Sanctis, M., Lazzaro, D., Ammannito, E., 2018. Spectroscopy of five v-type asteroids in the middle and outer main belt. Mon. Not. R. Astron. Soc. 475, 353–358.
Mommert, M., 2017. PHOTOMETRYPIPELINE: an automated pipeline for calibrated photometry. Astronomy and Computing 18, 47–53.
Moskovitz, N.A., Lawrence, S., Jedicke, R., Willman, M., Haghighipour, N., Bus, S.J., Gaidos, E., 2008. A spectroscopically unique main-belt asteroid: 10537 (1991 ry16). Astrophysical Journal, Letters 682, L57.
Moskovitz, N.A., Willman, M., Burbine, T.H., Binzel, R.P., Bus, S.J., 2010. A spectroscopic comparison of hed meteorites and v-type asteroids in the inner main belt, 208, pp. 773–788.
Muinonen, K., Shkuratov, Y., Ovcharenko, A., Piironen, J., Stankevich, D., Miloslavskaya, O., Kaasalainen, S., Josset, J.-L., 2002. The smart-1 amie experiment: implication to the lunar opposition effect. Planetary and Space Science 50, 1339–1344.
Muinonen, K., Belskaya, I.N., Cellino, A., Delbò, M., Levasseur-Regourd, A.-C., Penttilä, A., Tedesco, E.F., 2010a. A three-parameter magnitude phase function for asteroids. Icarus 209, 542–555.
Muinonen, K., Tyynelä, J., Zubko, E., Videen, G., 2010b. Coherent backscattering in planetary regoliths. In: Light Scattering Reviews, *5*. Springer, pp. 477–518.
Nesvorný, D., Roig, F., Gladman, B., Lazzaro, D., Carruba, V., Mothé-Diniz, T., 2008. Fugitives from the vesta family, *193*, pp. 85–95.
Oszkiewicz, D., Muinonen, K., Bowell, E., Trilling, D., Penttilä, A., Pieniluoma, T., Wasserman, L., Enga, M.-T., 2011. Online multi-parameter phase-curve fitting and application to a large corpus of asteroid photometric data. J. Quant. Spectrosc. Radiat. Transf. 112, 1919–1929.
Oszkiewicz, D.A., Bowell, E., Wasserman, L., Muinonen, K., Penttilä, A., Pieniluoma, T., Trilling, D.E., Thomas, C.A., 2012. Asteroid taxonomic signatures from photometric phase curves. Icarus 219, 283–296.
Oszkiewicz, D., Kankiewicz, P., Włodarczyk, I., Kryszczyńska, A., 2015. Differentiation signatures in the flora region. Astronomy & Astrophysics 584, A18.
Oszkiewicz, D.A., Skiff, B.A., Moskovitz, N., Kankiewicz, P., Marciniak, A., Licandro, J., Galiazzo, M.A., Zeilinger, W.W., 2017. Non-vestoid candidate asteroids in the inner main belt, 599, p. A107.
Oszkiewicz, D., Kryszczyńska, A., Kankiewicz, P., Moskovitz, N.A., Skiff, B.A., Leith, T.B., Ďurech, J., Włodarczyk, I., Marciniak, A., Geier, S., et al., 2019. Physical and dynamical properties of the unusual v-type asteroid (2579) spartacus. Astronomy & Astrophysics 623, A170.
Oszkiewicz, D., et al., 2020. Spin-rates of v-type asteroids. *submitted to Astronomy & Astrophysics*.
Penttilä, A., Shevchenko, V., Wilkman, O., Muinonen, K., 2016. H, g1, g2 photometric phase function extended to low-accuracy data. Planetary and Space Science 123, 117–125.
Pravec, P., Harris, A.W., Kušnirák, P., Galád, A., Hornoch, K., 2012. Absolute magnitudes of asteroids and a revision of asteroid albedo estimates from wise thermal observations. Icarus 221, 365–387.
Roig, F., Nesvorný, D., Gil-Hutton, R., Lazzaro, D., 2008. V-type asteroids in the middle main belt, *194*, pp. 125–136.
Sather, R., 1976. Minor planets and related objects. Xix. Shape and pole orientation of (39) laetitia. AJ 81, 67–73.
Scott, E.R., Greenwood, R.C., Franchi, I.A., Sanders, I.S., 2009. Oxygen isotopic constraints on the origin and parent bodies of eucrites, diogenites, and howardites. Geochim. Cosmochim. Acta 73, 5835–5853.
Shevchenko, V., 1997. Analysis of asteroid brightness-phase relations. SoSyR 31, 219.
Shevchenko, V.G., Belskaya, I.N., Muinonen, K., Penttilä, A., Krugly, Y.N., Velichko, F.P., Chiorny, V.G., Slyusarev, I.G., Gaftonyuk, N.M., Tereschenko, I.A., 2016. Asteroid observations at low phase angles. Iv. Average parameters for the new H, G1, G2 magnitude system. Planetary and Space Science 123, 101–116.
Shkuratov, Y.G., Starukhina, L., Kreslavsky, M., Opanasenko, N., Stankevich, D., Shevchenko, V., 1994. Principle of undulatory invariance in photometry of atmosphereless celestial bodies. Icarus 109, 168–190.
Shkuratov, Y., Korokhin, V., Shevchenko, V., Mikhalchenko, O., Belskaya, I., Kaydash, V., Videen, G., Zubko, E., Velikodsky, Y., 2018. A photometric function of planetary surfaces for gourmets. Icarus 302, 213–236.
Tonry, J.L., Stubbs, C.W., Lykke, K.R., Doherty, P., Shivvers, I.S., Burgett, W.S., Chambers, K.C., Hodapp, K.W., Kaiser, N., Kudritzki, R.P., Magnier, E.A., Morgan, J. S., Price, P.A., Wainscoat, R.J., 2012. The pan-STARRS1 photometric system, 750, p. 99.
Verbiscer, A.J., Veverka, J., 1995. Interpretation of the iau two-parameter magnitude system for asteroids in terms of hapke photometric theory. Icarus 115, 369–373.
Vereš, P., Jedicke, R., Fitzsimmons, A., Denneau, L., Granvik, M., Bolin, B., Chastel, S., Wainscoat, R.J., Burgett, W.S., Chambers, K.C., et al., 2015. Absolute magnitudes and slope parameters for 250,000 asteroids observed by pan-starrs ps1–preliminary results. Icarus 261, 34–47.
Wasson, J.T., 2013. Vesta and extensively melted asteroids: why hed meteorites are probably not from vesta. Earth Planet. Sci. Lett. 381, 138–146.
Waszczak, A., Chang, C.-K., Ofek, E.O., Laher, R., Masci, F., Levitan, D., Surace, J., Cheng, Y.-C., Ip, W.-H., Kinoshita, D., et al., 2015. Asteroid light curves from the palomar transient factory survey: rotation periods and phase functions from sparse photometry. Astron. J. 150, 75.

Appendix B

Publication II: Wilawer et al. (2022)

Monthly Notices of the ROYAL ASTRONOMICAL SOCIETY

MNRAS **513,** 3242–3251 (2022) https://doi.org/10.1093/mnras/stac1008

Asteroid phase curves using sparse *Gaia* DR2 data and differential dense light curves

E. Wilawer [1]★ D. Oszkiewicz,[1] A. Kryszczyńska,[1] A. Marciniak,[1] V. Shevchenko,[2] I. Belskaya,[2] T. Kwiatkowski,[1] P. Kankiewicz [3] J. Horbowicz,[1] V. Kudak,[4] P. Kulczak,[1] V. Perig[4] and K. Sobkowiak[1]

[1]*Astronomical Observatory Institute, Faculty of Physics, Adam Mickiewicz University, ul. Sloneczna 36, 60-286 Poznan, Poland*
[2]*Department of Astronomy and Space Informatics, V. N. Karazin Kharkiv National University, 4 Svobody Sq., Kharkiv 61022, Ukraine*
[3]*Institute of Physics, Jan Kochanowski University, ul. Uniwersytecka 7, 25-406 Kielce, Poland*
[4]*Laboratory of Space Researches, Uzhhorod National University, Daleka st. 2a, 88000, Uzhhorod, Ukraine*

Accepted 2022 April 4. Received 2022 April 4; in original form 2021 September 20

ABSTRACT

The amount of sparse asteroid photometry being gathered by both space- and ground-based surveys is growing exponentially. This large volume of data poses a computational challenge owing to both the large amount of information to be processed and the new methods needed to combine data from different sources (e.g. obtained by different techniques, in different bands, and having different random and systematic errors). The main goal of this work is to develop an algorithm capable of merging sparse and dense data sets, both relative and differential, in preparation for asteroid observations originating from, for example, *Gaia*, *TESS*, ATLAS, LSST, *K2*, VISTA, and many other sources. We present a novel method to obtain asteroid phase curves by combining sparse photometry and differential ground-based photometry. In the traditional approach, the latter cannot be used for phase curves. Merging those two data types allows for the extraction of phase-curve information for a growing number of objects. Our method is validated for 26 sample asteroids observed by the *Gaia* mission.

Key words: minor planets, asteroids: general – catalogues – techniques: photometric.

1 INTRODUCTION

Asteroid phase curves describe the dependence of asteroid brightness on the geometry of scattering determined by the phase angle, namely the angle between the directions to the observer and the Sun as seen from the asteroid. Phase curves are of general interest because they allow us (1) to probe the surface properties (such as regolith particle size, surface roughness, porosity) of asteroids; (2) compute the absolute magnitude, which is related to the asteroid size and albedo; and (3) determine various physical properties of asteroids, for example the taxonomic type (Shevchenko et al. 2016; Oszkiewicz et al. 2021).

Typical asteroid magnitude phase curves are linear in the phase angle range 8°–40° and become non-linear at larger angles, where they are influenced by surface roughness on the topographic scale. At small phase angles, the so-called opposition effect is observed, which appears as a non-linear increase of the asteroid brightness towards opposition. According to our current knowledge, the opposition effect is formed by coherent back-scattering and shadow-hiding effects, the linear part is determined by the shadow-hiding effect and the contribution of single-particle scattering, and at large phase angles a contribution of the shadow-hiding effect appears at all roughness scales (e.g. Muinonen et al. 2002). Shadow hiding is caused by single scattering, and the effect is more pronounced for dark surfaces and less evident for bright surfaces, where multiple scattering is more dominant. The coherent back-scattering mechanism dominates for high-albedo surfaces. This explains the strong dependence of phase-curve behaviour on the albedo of the asteroid (Belskaya & Shevchenko 2000). The linear phase slope can be used for a reliable estimation of the albedo of asteroids from phase-curve measurements (Belskaya & Shevchenko 2018; Belskaya & Shevchenko 2000; Oszkiewicz et al. 2021; Shevchenko et al. 2021). The phase-curve behaviour also depends on wavelength. For moderate- and high-albedo asteroids whose albedos increase with wavelength, so-called phase-reddening is observed (see Reddy et al. 2015).

Several advanced photometric models have been proposed to describe phase curves: Hapke's (Hapke 1963, 1966, 1981, 1984, 1986, 2002, 2008, 2012; Hapke & Wells 1981), Akimov's (Akimov 1975, 1979, 1988) and Shkuratov's (Shkuratov et al. 2011). However, owing to the limited accuracy of photometric observations, in most cases empirical phase functions with only two to three parameters are used to fit phase curves. The H, G phase function was developed by Bowell et al. (1989) and adopted by the International Astronomical Union (IAU) in 1985. However, with increasing numbers of observations it became clear that the H, G function overestimates the absolute magnitude of low-albedo objects and underestimates it for high-albedo objects. Therefore, two new H, G_1, G_2 and H, G_{12} functions were proposed by Muinonen et al. (2010). The system was later improved by Penttilä et al. (2016). A new H, G_{12}^* system was proposed to supersede the previous H, G_{12} function. In the new model, one linear function of first degree is used to describe the dependence of G_1 and G_2, in contrast to the two functions used before. Furthermore, the use of one-parameter phase functions was

★ E-mail: wilawerek@amu.edu.pl

proposed for objects with a small number of observations and/or low-quality photometry. In these functions, only the absolute magnitude H is fitted, and the G_1, G_2 parameters are assumed for each taxonomic type, for example as in Shevchenko et al. (2016). For observations obtained at phase angles greater than 8° (such as those obtained by for example the *Gaia* mission), only the linear part of the phase curve can be fitted. The directional coefficient β of the linear function is correlated with the geometric albedo (Belskaya & Shevchenko 2018).

Traditionally, phase curves are derived from relative photometry[1] dense light curves that are obtained from targeted ground-based observations. Currently, these high-quality phase curves are available for a few hundred asteroids, and the increase in the number of objects is small (Shevchenko et al. 2016). This is mostly due to the time-consuming nature of these observations and to the careful planning and calibration required to obtain them (Shevchenko 1997; Shevchenko et al. 2002, 2016; Pravec et al. 2012; Oszkiewicz et al. 2021). Those standard observations allow us to account for changes in brightness owing to aspect (if enough data are gathered and the shape can be determined), irregular shape, and rotation. The latter is often referred to as the light-curve amplitude correction (LC-AC hereafter). Owing to the fact that light-curve morphology changes with phase angle and the minima are usually more affected than the maxima, the maximum of light curves is typically used to construct phase curves (Shevchenko et al. 2002). On the other hand, phase curves derived from sparse photometry available from surveys are numerous but often burdened with large uncertainties. This is mostly caused by not accounting for the rotational brightness modulation (LC-AC) and manifests as a large spread of points around the fitted phase function.

The application of phase functions to large amounts of sparse photometry data was started a decade ago. By processing a large amount of photometric data from the Lowell Observatory photometric data base, Oszkiewicz et al. (2011) found a homogeneity of phase-curve parameters in asteroid families and studied the distribution of these parameters for various taxonomic classes (Oszkiewicz et al. 2012). Similar studies were performed by Vereš et al. (2015) using the Pan-STARRS data and by Waszczak et al. (2015) using the Palomar Transient Factory survey data. Recently, Mahlke, Carry & Denneau (2021) and Ďurech et al. (2020) confirmed the wavelength dependence of phase-curve coefficients using the sparse ATLAS dual-band photometry. That effect has been studied since the 1970s (Millis, Bowell & Thompson 1976; Miner & Young 1976; Gradie, Veverka & Buratti 1980; Gradie & Veverka 1986; Reddy et al. 2012; Sanchez et al. 2012). Alvarez-Candal et al. (2021a) derived phase curves in the Sloan Digital Sky Survey (SDSS) bands for about 12 000 asteroids, but did not study the wavelength dependence in detail.

Colazo & Duffard (2020) determined the H, G parameters for about 4000 asteroids observed by the *Gaia* mission and available in the DR2 catalogue. They noted that the standard mean G slope value ($G = 0.15$) currently used by the Minor Planet Center differs from the value observed for the *Gaia* data set. Yoshida et al. (2020) presented over 40 000 phase curves obtained from serendipitous observations of asteroids present in the data from the Tomo-e Gozen transient survey aimed at detecting young supernovae. Lin et al. (2020) fitted the H, G phase function to about 1000 near-Earth asteroids observed by the Zwicky Transient Facility and assigned them a taxonomic type based on the G slope value.

Currently, the accuracy of phase curves derived from sparse photometry is very limited, and we need new approaches to achieve better accuracy. Muinonen et al. (2020) presented a method for the simultaneous inversion of rotation periods, pole orientations, shapes, and phase-curve parameters using Bayesian statistics. The method was applied to three asteroids having numerous data in the *Gaia* DR2 catalogue. Other efforts are ongoing. Martikainen et al. (2021) combined the *Gaia* data with the sparse and dense-in-time photometry from the Database of Asteroid Models from Inversion Techniques (DAMIT) to perform convex inversion and ellipsoid inversion and derived the linear slopes for about 20 asteroids. Alvarez-Candal et al. (2021b) used Bayesian statistics to account for rotational modulation in the SDSS multi-filter photometry. Colazo, Duffard & Weidmann (2021) fitted the H, G phase function to the *Gaia* DR2 data combined with relative photometry from the Asteroid Photometric Catalogue (Lagerkvist et al. 1995).

With the increasing amount of sparse photometric data, there is clearly a need for computationally efficient methods that can process large data volumes and at the same time reduce the uncertainty of the determined phase-curve parameters. This can be achieved by merging multiple measurements that are diverse in nature, which gives auxiliary knowledge unobtainable from sparse data alone. In this work, we present a new approach for obtaining asteroid phase curves from various information sources: combining the absolute but sparse *Gaia* data and data from ground-based differential photometry. Although straightforward, this approach has not yet been fully explored in the literature. In comparison to other works, it allows rotational brightness changes and complicated light-curve morphologies to be accounted for. The method presented here can be extended to other sparse photometric surveys.

In Section 2 we describe the data sources used in this study, and in Section 3 we consider the phase-curve fitting algorithm. The results are presented in Section 4, the discussion in Section 5, and a summary and plan for future work in Section 6.

2 DATA SOURCES

We use traditional differential ground-based photometric observations gathered at the Astronomical Observatory Institute of Adam Mickiewicz University in Poznań and absolute *Gaia* measurements. Combining these different data types (differential, dense-in-time photometry, and sparse but absolute photometry) allows us to account for the rotational component in the sparse photometry (through the inclusion of well-determined periods and higher than second-order Fourier series determined from ground-based differential photometry) and to derive the phase slope (β) parameter.

Routine asteroid photometric observations have been performed at Poznań Observatory since the 1990s, and thus decades of asteroid photometric observations are available. However, for the purpose of this work, we select only observations obtained in the *Gaia* DR2 era to ensure similar aspect angles and viewing geometries; that is, we use observations obtained in the years 2014–2016. Furthermore, we use only observations of asteroids that have both differential ground-based photometry and *Gaia* measurements obtained for at least three different phase angles. The observing log for these objects is summarized in Table 1, in which we include rotational periods, aspect changes, time ranges of observations, the number of dense light curves, the number of Julian days of *Gaia* observations, and the number of transits registered by *Gaia* for each asteroid.

[1]By relative photometry we understand brightness measurements tied to a set of standard stars. Absolute photometry, as provided by *Gaia*, is tied to a laboratory source. Differential photometry results from the direct comparison of asteroid and stellar images present in the same field of view and is not tied to any particular magnitude scale.

Table 1. The columns present: the observed asteroid, the rotation period taken from Marciniak et al. (2015, 2018, 2019, 2021) and Shevchenko et al. (2021), the aspect change during the period of observation, the minimum phase angle observed by *Gaia*, the number of partial light curves obtained from ground-based telescopes, the number of Julian days of *Gaia* observations, and the number of transits registered by *Gaia*.

Asteroid	Rotation period (h)	Aspect change (°)	Period of observations	$\alpha_{\min}$ (°)	N_{ground}	N_{Gaia}	N_{transit}
(70) Panopaea	15.812	–	2014-08-14–2015-02-11	18.03	15	6	14
(108) Hecuba	14.255	7	2015-03-05–2015-12-20	12.58	10	9	15
(109) Felicitas	13.194	40	2015-05-01–2016-02-24	20.31	13	5	6
(159) Aemilia	24.493	9	2015-01-08–2015-10-23	12.51	11	9	27
(195) Eurykleia	16.527	6	2014-09-24–2015-05-30	15.1	8	6	9
(202) Chryseis	23.671	10	2014-08-30–2015-01-21	13.65	9	3	4
(202) Chryseis	23.666	9	2015-09-07–2016-04-04	18.75	10	5	8
(260) Huberta	8.2895	10	2014-09-12–2015-02-07	13.9	11	4	6
(301) Bavaria	12.240	17	2015-03-01–2015-12-24	16.8	9	10	14
(305) Gordonia	12.893	7	2014-08-08–2015-02-11	13.26	13	5	5
(329) Svea	22.777	15	2014-07-30–2015-02-06	16.82	11	3	4
(362) Havnia	16.923	10	2015-07-01–2016-02-28	21.2	6	6	8
(380) Fiducia	13.716	7	2015-07-02–2016-02-27	20.3	8	6	9
(439) Ohio	37.46	16	2014-08-21–2015-02-06	13.55	12	5	10
(483) Seppina	12.723	9	2014-09-17–2015-04-17	14.31	5	6	7
(483) Seppina	12.721	12	2015-11-09–2016-05-09	14.78	5	3	3
(501) Urhixidur	13.174	12	2014-09-11–2015-04-29	13.6	10	7	10
(537) Pauly	16.301	10	2015-11-15–2016-05-20	12.07	8	7	9
(552) Sigelinde	17.143	8	2015-05-04–2016-02-20	12.52	5	11	20
(611) Valeria	6.982	11	2014-08-29–2015-02-13	16.17	3	4	6
(618) Elfriede	14.799	12	2014-08-28–2015-01-21	14.09	12	3	6
(618) Elfriede	14.799	12	2015-09-06–2016-04-28	14.97	6	4	6
(653) Berenike	12.488	14	2015-02-23–2015-10-28	17.35	7	6	8
(666) Desdemona	14.617	7	2014-11-06–2015-08-19	13.34	18	9	14
(666) Desdemona	14.617	13	2016-01-14–2016-07-23	13.59	9	5	6
(667) Denise	12.683	15	2014-12-29–2015-10-25	11.14	6	9	18
(667) Denise	12.683	4	2016-03-08–2016-08-31	12.5	9	3	5
(723) Hammonia	5.4349	–	2014-08-08–2015-02-03	14.32	17	5	14
(727) Nipponia	5.0692	–	2014-10-25–2015-05-29	21.83	5	4	6
(780) Armenia	19.898	17	2015-02-20–2015-10-28	13.66	24	8	13
(834) Burnhamia	13.874	6	2014-09-20–2015-05-31	11.24	10	9	17
(834) Burnhamia	13.879	8	2015-11-15–2016-05-19	13.47	7	5	6

For all asteroids, we verified the aspect changes based on all available models (usually two) and reported the largest aspect change. The aspect changes calculated with ISAM (Interactive Service for Asteroid Models) (Marciniak et al. 2012) were less than 15° for most of the observed objects during the observation period. In many cases, the aspect change of the objects is smaller than the uncertainties in the spin-axis coordinates. Light curves and periods for all asteroids except for (611) Valeria and (727) Nipponia were taken from Marciniak et al. (2015, 2018, 2019, 2021) and Shevchenko et al. (2021). Observing circumstances for 611 and 727 are summarized in Table A1.

We also used sparse, but absolute *Gaia* photometry (Prusti et al. 2016). The *Gaia* mission provided photometric data of millimagnitude accuracy for about 14 000 asteroids (DR2) (Brown et al. 2018; Spoto et al. 2018). Most objects were observed at phase angles in the range $5° < \alpha < 30°$, and thus *Gaia* does not cover the opposition area. Typically, observations obtained during transits in two *Gaia* fields of view are separated by 106.5 min and thus can be reduced to two points on a light curve during a single rotation. Those two points are reduced to a single point on the phase curve, as the change of the phase angle between two *Gaia* transits is negligible (except for near-Earth objects). In the current catalogue (DR2), the total number of observations for a particular asteroid is very low. As a consequence, sparse data points alone are not enough to obtain reasonable-quality phase curves. Therefore, merging with other data sources and/or information is necessary. Here, we focus on merging diverse data sets, as indicated in Table 1.

From the *Gaia* catalogue, we extracted the following columns for our 26 objects: *number_mp*, indicating the asteroid number; *epoch_utc*, the observing time; and *g_mag*, the brightness in the G band and the corresponding flux *g_flux* with its uncertainty *g_flux_error*. A constant value of 2455197.5 d needs to be added to *epoch_utc*. The G magnitude error is estimated as:

$$g_{\text{magerr}} = -2.5 \log_{10}\left(\frac{g_{\text{flux}} + g_{\text{fluxerr}}}{g_{\text{flux}}}\right). \quad (1)$$

Each asteroid data are divided into oppositions based on solar elongation at the date of observation. One opposition comprises data from 0° to 360° solar elongation. Each asteroid opposition contains *Gaia* observations from at least three separate Julian days (typically there are two transits per Julian day) and at least one observing night from ground-based observatories covering all phases of the rotational period.

3 PHASE-CURVE FITTING ALGORITHM

The differential ground-based photometry is composed together with absolute *Gaia* measurements to determine the rotational phases at

which the *Gaia* points were obtained. The common fit allows for interpolation of the maximum brightness from the fitted Fourier series. The interpolated maximum brightnesses for the *Gaia* points taken at different phase angles are then used in the construction of phase curves.

Similarly, the synthetic light curves generated from asteroid shape models can be composed with the *Gaia* data. This approach is, however, burdened with (1) uncertainty arising from propagating the uncertainty of the rotation period, and thus an inability to properly determine the rotational phase, and (2) light-curve amplitude uncertainties arising from shape models accuracy. This problem is minimized in our approach by the requirement for the same epoch for the dense and sparse photometry.

Generally, differential photometry can be re-calibrated to the *Gaia G* band, using one of the all-sky photometric catalogues. This, however, could possibly introduce unwanted systematic effects owing to the difference between photometric bands of *Gaia* and ground-based observations. These systematic effects are not well established at the moment and thus are impossible to correct for.

In this work we focus on composing together the differential ground-based photometry with the *Gaia* absolute photometry. We outline our procedure below.

First, we use the PERFIT program (Kwiatkowski et al. 2021) to fit the standard Fourier series to the combined differential and absolute photometry. We determine the shape of the composite light curve and synodic period. We usually use 4–6 orders of the series; however, sometimes higher orders are required. The fitted function is

$$V(t) = \overline{V} + \sum_{k=1}^{n} \left(A_k \sin \frac{2\pi k(t - t_0)}{P} + B_k \cos \frac{2\pi k(t - t_0)}{P} \right), \quad (2)$$

where $\overline{V}$ is the average brightness for a single light curve, A_k and B_k are the Fourier series coefficients, P is the synodic period, t is the time of observation, and t_0 is the time of the first observation. For a fixed synodic period, that relationship is linear and can be fitted using a least-squares method. The fitted parameters become $\overline{V}$ (separate for each light curve), A_k and B_k. A range of synodic periods is scanned to produce a plot of the quality of the fit (measured by χ^2 per degree of freedom) versus the trial period and to find the best matching solution.

Provided that the data are relative or absolute in nature, the $\overline{V}$ plus half of the peak-to-peak amplitude (obtained from the Fourier fit) determines the maximum brightness ($V_{\max}$). We thus further select only the $V_{\max}$ originating from absolute *Gaia* data and use these to construct phase curves. Because *Gaia* observes asteroids mostly at phase angles away from opposition, only the linear part of the phase curve can be obtained. We thus use linear regression to fit the light-curve amplitude-corrected *Gaia* data. If relative photometry covering small phase angles is available (either dense or sparse from ground- or space-based observatories), full phase functions can be fitted. Therefore, this approach is capable of combining both dense and sparse data, relative, absolute and differential, providing a powerful tool for future-generation surveys.

In addition, because the largest uncertainties in correcting for light-curve amplitude arise from uncertainties in the synodic period, we perform an additional calibration step. That is, we sample the rotation period within the estimated uncertainty and select the period that leads to the smallest χ^2 of the linear phase-curve fit.

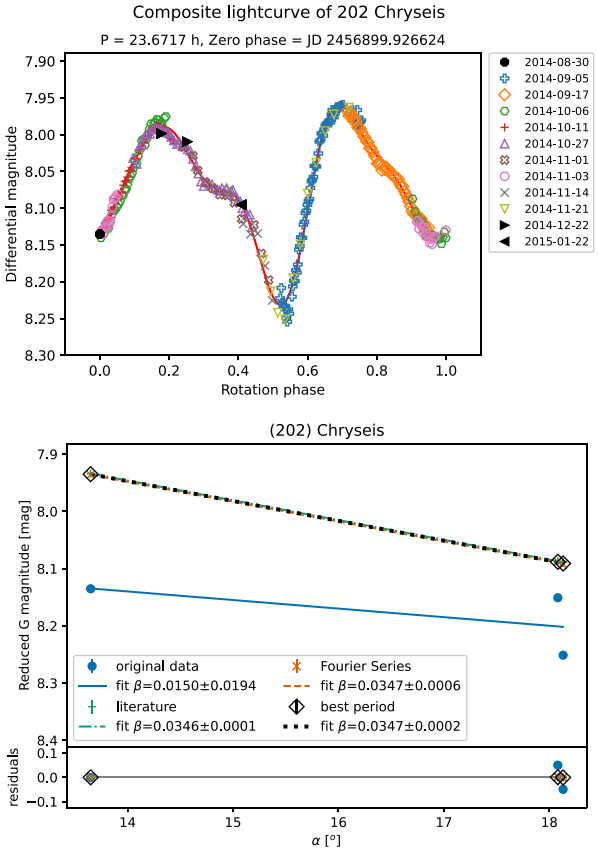

Figure 1. Upper panel: composite light curve for asteroid (202) Chryseis combining *Gaia* observations (black bold) and ground-based observations (coloured) with a derived light-curve shape (solid red line). Bottom panel: linear part of the phase curve for asteroid (202) Chryseis. The original *Gaia* data reduced to 1-au distance and a linear fit to these are shown in blue. Light-curve amplitude-corrected *Gaia* data based on the literature, the derived and adjusted periods and corresponding fits are shown in green, orange and black, respectively. Error bars show the uncertainty of the brightness in magnitude. Residuals are shown at the very bottom.

4 RESULTS

4.1 *Gaia* data and differential ground-based photometry

We fitted the linear part of the phase curves to 32 different oppositions of 26 asteroids that met the selection criteria described in Section 2.

In Figs 1 to 3, we present composite light curves and final linear functions fitted to the light-curve-corrected data for asteroids (202) Chryseis, (301) Bavaria and (305) Gordonia (plots for the other asteroids can be found in the Supporting Information available online). The *Gaia* data nicely complement the ground-based dense differential light curves. LC-AC depends on the rotation period. The three linear functions shown were fitted to the data with LC-AC derived based on periods from Marciniak et al. (2015, 2018, 2019, 2021) and Shevchenko et al. (2021) (green), a period found using Fourier series (orange), and a period that minimizes the linear phase function residuals (black). The fit to the raw DR2 data is shown in blue. Generally, the LC-AC linear functions are similar, as the periods are usually consistent within hundredths of an hour. A linear fit to the raw *Gaia* data (without the LC-AC) clearly can produce erroneous and sometimes even negative (physically incorrect) phase slopes (β). Furthermore, the scatter around the linear functions is

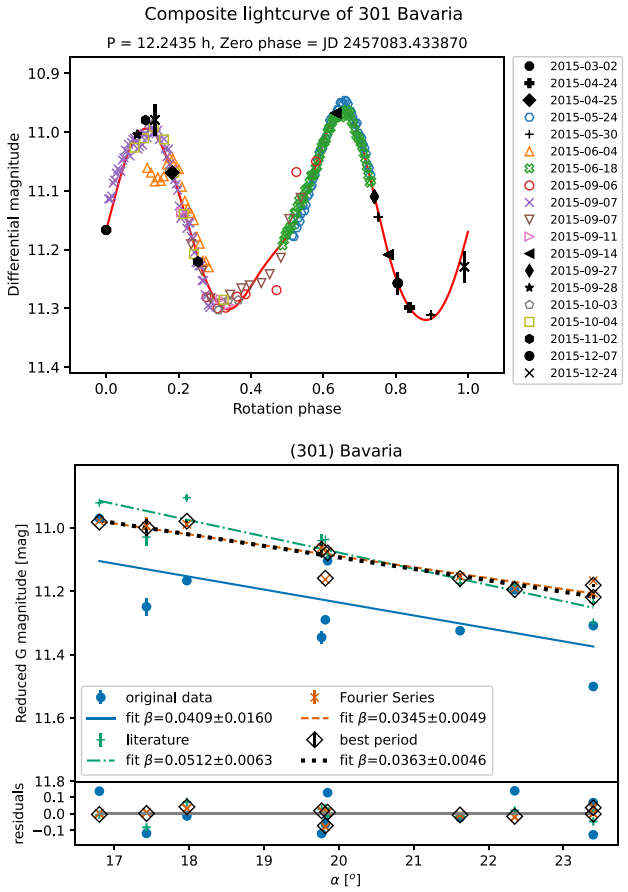

Figure 2. As Fig. 1, but for (301) Bavaria.

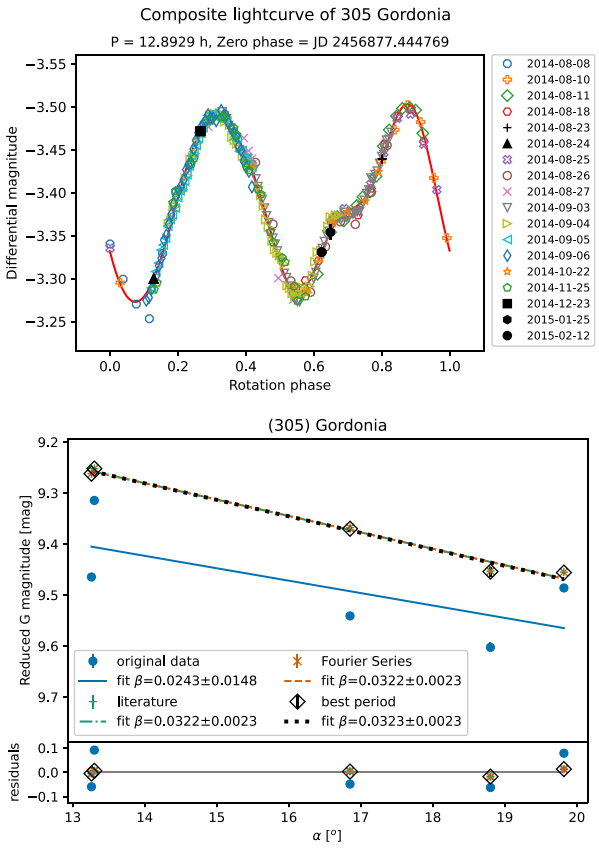

Figure 3. As Fig. 1, but for (305) Gordonia.

significantly reduced (e.g. from ∼0.15 to ∼0.02 mag in Fig. 3) compared with the linear function fitted to the unprocessed *Gaia* data. The reduction is larger for asteroids with high light-curve amplitude. This highlights the need for LC-AC when using sparse-in-time photometry. The reduction of the scatter is worse for asteroids with lower-quality light curves and for objects for which there is a gap in the coverage of the full rotational period. The linear LC-AC functions (Figs 1 to 3) correspond to light-curve maxima, and thus are usually shifted vertically compared with the raw *Gaia* data fit. The marked uncertainties in Figs 1 to 3 include only the single-point photometric uncertainty of the *Gaia* measurements and do not include the uncertainty arising from the propagation of synodic period uncertainty or synodic period changes.

The resulting β phase-slope values are listed in Table 2 along with the period that resulted in the best-fitting curve, Tholen taxonomic type (Neese 2010), and geometric albedos taken from the *AKARI* (Usui et al. 2011), *IRAS* (Tedesco et al. 2004), and *WISE* (Mainzer et al. 2019) catalogues. Data from different oppositions were fitted separately. The phase-slope values derived from different apparitions are typically within 1σ uncertainty of each other. The differences may arise from different aspect angles and irregularities of the shape. Further uncertainties may originate from errors in photometry, period estimation and LC-AC.

Fig. 4 shows the correlation between the linear slope β derived in this work and the geometric albedo. The solid black line represents the relationship $\beta = 0.016 - 0.022\log p_{\rm V}$ found by Belskaya & Shevchenko (2018) for the *V*-band slopes, and the shaded areas represent 1σ, 2σ and 3σ error envelopes. The solid red line represents the function we fitted to the *Gaia G* magnitudes, which is different for every albedo source:

$$\begin{aligned} \beta_{\rm AKARI} &= 0.025 - 0.013\log p_{\rm V}, \\ \beta_{\rm IRAS} &= 0.022 - 0.015\log p_{\rm V}, \\ \beta_{\rm WISE} &= 0.025 - 0.013\log p_{\rm V}. \end{aligned} \tag{3}$$

We plot only points for which the accuracy is better than 20 per cent. It can be seen that our results are in good agreement with Belskaya & Shevchenko (2018). The relationships derived in equation (3) are for the *Gaia G* band. Owing to the sparse nature of the data, we consider these relationships to be rough estimates. Obtaining better relationships is not possible because it will probably never be possible to use the the sparse data to improve the results based on accurate dense photometry.

4.2 Simulation of uncertainties

We checked how the time separation between dense and sparse observations (in assumption, differential and relative, respectively) and the noise of the dense observations affect the value and uncertainty of the derived slope parameter β. We selected the asteroid (159) Aemilia to perform our simulation, as it has the largest light-curve amplitude among our objects.

First, using observational data, we derived the mean JD time of ground-based data and set it to be the middle date of a week. Then we used ISAM to generate full synthetic light curves for three randomly chosen nights in a week and added 0.01-, 0.03- and 0.05-mag random Gaussian noise to them.

Table 2. Period used for composite light curves, geometric albedos from *AKARI* (Usui et al. 2011), *IRAS* (Tedesco et al. 2004), and *WISE* (Mainzer et al. 2019), linear slopes coefficients derived from the light-curve-corrected *Gaia* data, and Tholen taxonomic type from Neese (2010). In cases where there were a few entries for a given object in a given albedo catalogue, the entry with the lowest albedo uncertainty was taken.

Asteroid	Period (h)	p_v *AKARI*	p_v *IRAS*	p_v *WISE*	Phase slope $[\frac{\text{mag}}{\text{deg}}]$	Taxonomic type
(70) Panopaea	15.8078	0.05 ± 0.002	0.07 ± 0.004	0.038 ± 0.007	0.0283 ± 0.0070	C
(108) Hecuba	14.2587	0.213 ± 0.007	0.192 ± 0.035	0.148 ± 0.013	0.0325 ± 0.0082	S
(109) Felicitas	13.1915	0.086 ± 0.003	0.06 ± 0.003	0.036 ± 0.009	0.0252 ± 0.0079	GC
(159) Aemilia	24.4822	0.059 ± 0.003	0.061 ± 0.003	0.064 ± 0.014	0.0382 ± 0.0042	C
(195) Eurykleia	16.5269	0.055 ± 0.002	0.053 ± 0.002	0.051 ± 0.008	0.0388 ± 0.0052	C
(202) Chryseis	23.6645	0.245 ± 0.007	0.178 ± 0.023	0.232 ± 0.037	0.0399 ± 0.0101	S
(202) Chryseis	23.6717	0.245 ± 0.007	0.178 ± 0.023	0.232 ± 0.037	0.0347 ± 0.0002	S
(260) Huberta	8.2883	0.054 ± 0.002	0.034 ± 0.005	0.044 ± 0.01	0.0408 ± 0.0186	CX:
(301) Bavaria	12.2435	0.06 ± 0.002	0.056 ± 0.003	0.057 ± 0.007	0.0363 ± 0.0046	–
(305) Gordonia	12.8929	0.234 ± 0.008	0.169 ± 0.01	0.238 ± 0.036	0.0323 ± 0.0023	S
(329) Svea	22.7646	0.049 ± 0.001	0.037 ± 0.002	0.039 ± 0.007	0.0117 ± 0.0143	C
(362) Havnia	16.9327	0.062 ± 0.002	–	0.061 ± 0.008	0.0308 ± 0.0134	XC
(380) Fiducia	13.7205	0.053 ± 0.002	0.051 ± 0.002	0.066 ± 0.005	0.0150 ± 0.0081	C
(439) Ohio	37.4550	0.037 ± 0.001	0.036 ± 0.002	0.042 ± 0.004	0.0430 ± 0.0078	X:
(483) Seppina	12.7219	0.172 ± 0.004	0.136 ± 0.007	0.184 ± 0.066	0.0401 ± 0.0103	S
(483) Seppina	12.7207	0.172 ± 0.004	0.136 ± 0.007	0.184 ± 0.066	0.0604 ± 0.0148	S
(501) Urhixidur	13.1738	0.079 ± 0.002	0.068 ± 0.004	0.052 ± 0.009	0.0399 ± 0.0051	–
(537) Pauly	16.3019	0.283 ± 0.008	0.239 ± 0.05	0.322 ± 0.03	0.0127 ± 0.0129	DU:
(552) Sigelinde	17.1532	0.051 ± 0.002	0.034 ± 0.003	0.036 ± 0.005	0.0438 ± 0.0025	–
(611) Valeria	6.9788	0.115 ± 0.003	0.091 ± 0.005	0.124 ± 0.008	0.0362 ± 0.0050	S
(618) Elfriede	14.7980	0.06 ± 0.002	0.058 ± 0.007	0.05 ± 0.005	0.0583 ± 0.0174	C
(618) Elfriede	14.7974	0.06 ± 0.002	0.058 ± 0.007	0.05 ± 0.005	0.0463 ± 0.0039	C
(653) Berenike	12.4876	0.173 ± 0.006	0.177 ± 0.011	0.085 ± 0.017	0.0858 ± 0.0435	S
(666) Desdemona	14.7686	0.105 ± 0.006	0.095 ± 0.005	0.095 ± 0.015	0.0638 ± 0.0375	–
(666) Desdemona	14.6148	0.105 ± 0.006	0.095 ± 0.005	0.095 ± 0.015	0.0353 ± 0.0020	–
(667) Denise	12.6840	0.062 ± 0.003	0.057 ± 0.003	0.062 ± 0.01	0.0401 ± 0.0037	–
(667) Denise	12.6840	0.062 ± 0.003	0.057 ± 0.003	0.062 ± 0.01	0.0455 ± 0.0037	–
(723) Hammonia	5.4351	0.294 ± 0.031	0.121 ± 0.017	0.352 ± 0.048	0.0145 ± 0.0052	–
(727) Nipponia	5.0692	0.212 ± 0.01	0.141 ± 0.018	0.479 ± 0.053	0.0863 ± 0.0175	DT
(780) Armenia	19.8799	0.046 ± 0.002	0.047 ± 0.002	0.039 ± 0.003	0.0423 ± 0.0114	–
(834) Burnhamia	13.8753	0.082 ± 0.007	0.068 ± 0.004	0.071 ± 0.008	0.0403 ± 0.0035	GS:
(834) Burnhamia	13.8764	0.082 ± 0.007	0.068 ± 0.004	0.071 ± 0.008	0.0252 ± 0.0061	GS:

Next, to simulate *Gaia* observations, for three randomly selected days in each of the following 10 weeks, we generated a synthetic light curve, picked a single observing point, and assigned a sigma equal to 0.003 (the median of all *Gaia* points sigma). Finally, we created 30 different data sets containing all possible combinations of differently noised synthetic ground-based data mixed with simulated *Gaia* points from 1 to 10 weeks apart from dense ground-based ones. We performed the calibration and phase-curve fitting described in Section 3 on all data sets. The obtained light curves and phase curves can be found in the Supporting Information available online. Fig. 5 shows the dependence of the β parameter and its uncertainty on the time span between observations.

First, the dependence of the data-separation time-span on the slope uncertainty is non-linear and relies on the number of rotations in the separation time span, the period uncertainty, and the phase difference created by the difference in the synodic and sidereal periods and the rotational phase of the sparse data. In addition, based on this single simulation, we recommend that the dense observations should not have σ values larger than 0.03 mag.

5 DISCUSSION

The largest source of uncertainty in phase-curve studies based on sparse data arises from the lack of or an inaccurate LC-AC, as the sparse data randomly sample light curves of generally unknown shape, rotation period and amplitude. Therefore phase curves constructed from sparse photometry commonly have a large scatter around the fitted phase function. Naturally, the scatter is larger for objects with a large light-curve amplitude, which for some objects can reach even $>\sim$1 mag (Warner, Harris & Pravec 2009). Absolute magnitudes derived from the scattered phase curves typically correspond to light-curve-averaged brightnesses. Moreover, the average is taken from points that are not uniformly sampled over the rotation period but depend on survey cadence, and this may introduce biases into the derived phase-curve parameters.

For example, Oszkiewicz et al. (2011) and Mahlke et al. (2021) did not correct for light-curve amplitude for the majority of their data. The estimated absolute magnitudes from Oszkiewicz et al. (2011) thus correspond to brightness averages over randomly sampled light curves from multiple oppositions, and those by Mahlke et al. (2021) to randomly sampled light curves over a single opposition. Waszczak et al. (2015) simultaneously fitted phase curves together with the rotational component (using second-order Fourier series fits representing simple ellipsoidal shapes) using sparse photometry from the Palomar Transient Factory. Vereš et al. (2015) used sinusoidal fits to describe light curves composed of sparse data and to determine the maximum brightness. That approach does not take into account the changes in synodic period or complicated light-curve morphology.

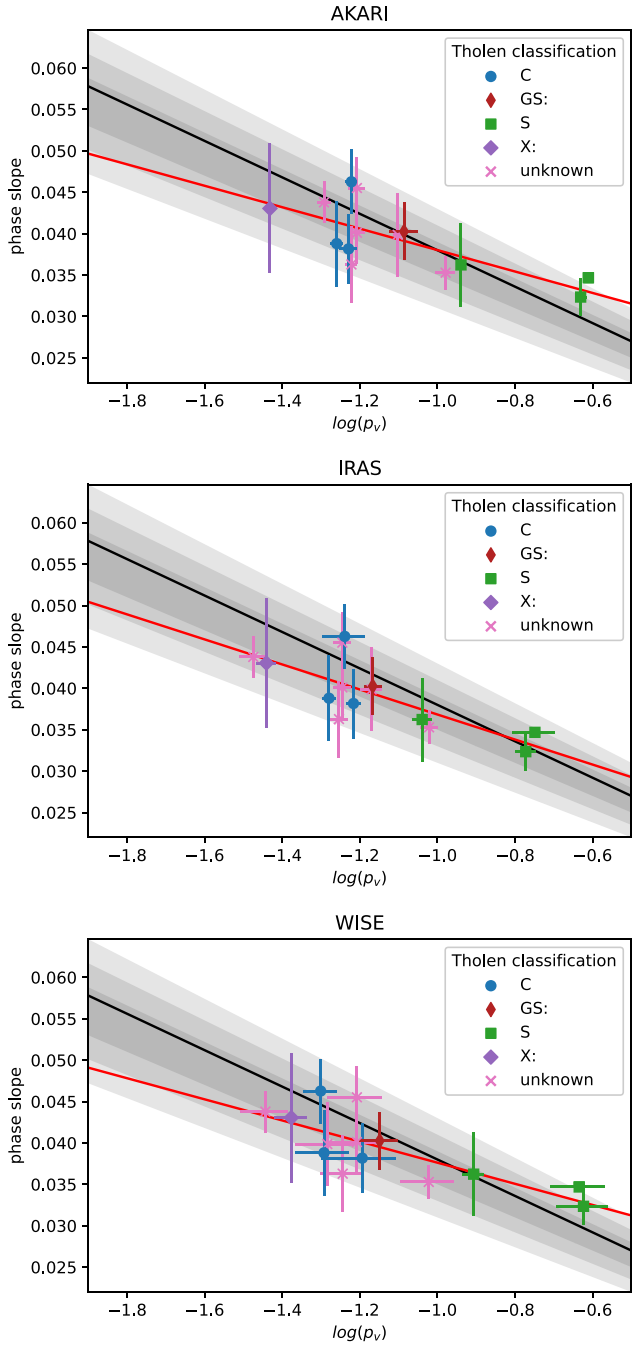

Figure 4. Correlation between the slope of asteroid phase curves and the albedo. The black line with the envelope depicts $\beta = 0.016 - 0.022 \log p_v$ with 1σ, 2σ and 3σ (Belskaya & Shevchenko 2018), the red line shows a function fitted to the data points, and the points are objects from this study.

Alvarez-Candal et al. (2021a) used Bayesian statistics to account for possible light-curve amplitudes and periods. Their study did not consider aspect changes in different oppositions and was based on a few data points per object, resulting in large uncertainties. Colazo et al. (2021) combined mean magnitudes (averaged over photometric measurements obtained by *Gaia*, given that there was more than one transit per Julian day) with ground-based relative *V*-band photometry from Lagerkvist et al. (1995). The ground-based data were obtained at different epochs and thus at different aspects compared with the *Gaia*

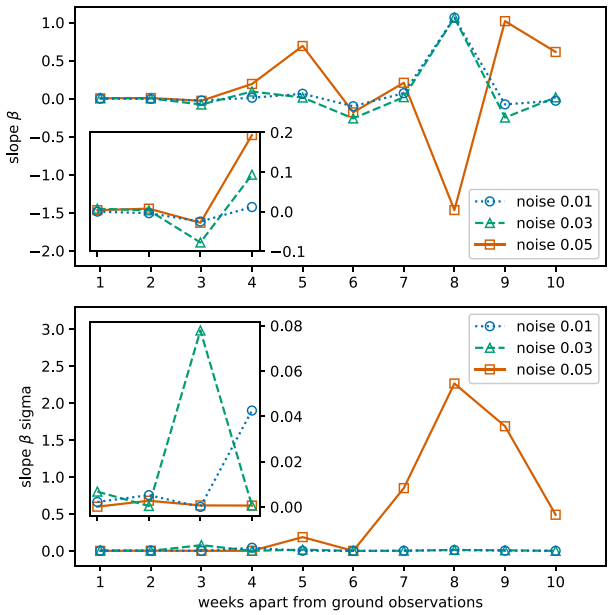

Figure 5. Data-separation time-span dependence for synthetic observations of asteroid (159) Aemilia. The plot shows changes of the slope value β (upper) and its uncertainty (bottom) depending on the time-distance of sparse observations. The inset graphs are close-up views of the range 1–4 weeks.

data. In the *Gaia* DR2 documentation, the brightest measurements among photometric points obtained on a single night are selected for phase-curve analysis. In general, approximate light-curve correction methods could lead to a larger spread in points around the phase function and thus to higher phase-curve parameter uncertainties.

Muinonen et al. (2020) and Martikainen et al. (2020) used a complex convex inversion method that allows for accurate LC-AC. However, if no dense light curves are available around the sparse data, the correction may similarly be inaccurate owing to model uncertainties. Moreover, if the shapes are derived based on sparse photometry they may not accurately reflect the light-curve morphology at *Gaia* epochs. Furthermore, because most asteroids have a poorly constrained shape and dimension along the *z*-axis, the transformation to the equatorial viewing geometry applied by the authors may introduce additional uncertainties (Bartczak & Dudzinski 2019).

In this work, we have presented an alternative to the methods mentioned above. The approach presented here is straightforward, computationally efficient, and has not yet been explored in the literature. Our approach allows for the incorporation of differential photometry, which traditionally is unusable for the construction of phase curves. The requirement of dense photometry close in time to the sparse measurements reduces the spread of data around the fitted phase function. In comparison to other works, this allows us to account for the complicated shape of the light-curve morphology beyond the second order of Fourier series, as often simplified in previous works. Because phase curves are derived from data from single oppositions, the resulting absolute magnitudes and phase-curve parameters correspond to that opposition.

This method should be used for asteroids for which the aspect changes are slow, which is generally the case for main-belt objects. As a precaution, we show a phase curve derived for asteroid (109) Felicitas in Fig. 6, which had a large aspect change of 40°.

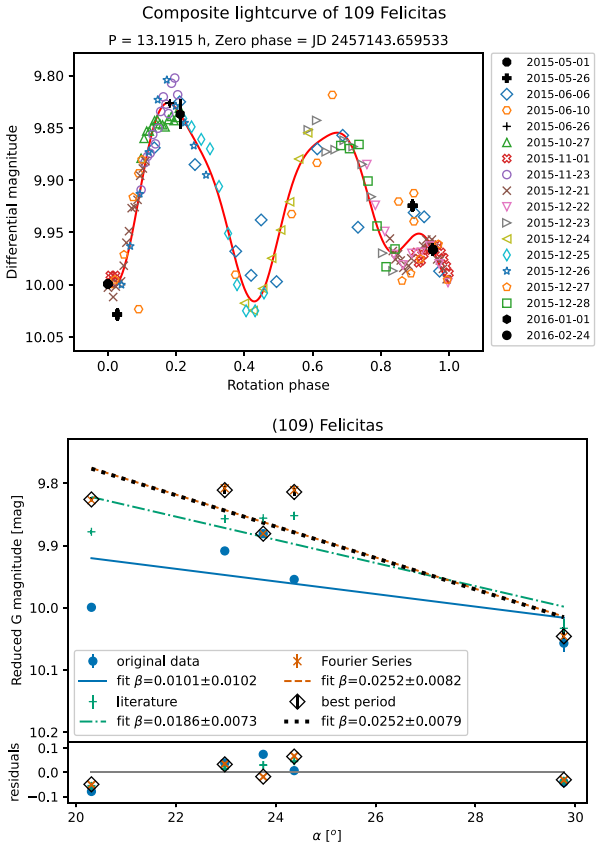

Figure 6. As Fig. 1, but for (109) Felicitas.

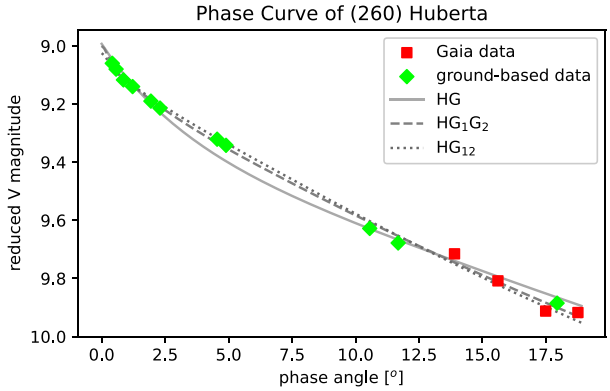

Figure 7. Full phase curve of (260) Huberta with fitted H, G, H, G_1, G_2 and H, G_{12} phase functions (solid, dashed and dotted lines, respectively).

There is almost no reduction of the original scatter around the linear phase curve.

In addition, we would like to point out that by combining calibrated ground-based observations with sparse data, a full phase curve can be obtained and phase-function parameters can be determined. As an example, we created a phase curve for the object (260) Hammonia combining ground-based V-filter data from Shevchenko et al. (2021) and data from *Gaia* DR2 (Fig. 7). *Gaia* magnitudes have been transformed to V Johnson–Cousins magnitudes using the transformation from Busso et al. (2018) and the colour index V-R taken from Shevchenko et al. (2021). The obtained phase function parameters are summarized in Table 3.

Table 3. Phase-function parameters for (260) Huberta.

H, G	$H = 8.99^{+0.02}_{-0.03}$
	$G = 0.20^{+0.02}_{-0.05}$
H, G_1, G_2	$H = 9.00^{+0.02}_{-0.03}$
	$G_1 = 0.69^{+0.08}_{-0.09}$
	$G_2 = 0.12^{+0.05}_{-0.04}$
H, G_{12}	$H = 9.01^{+0.01}_{-0.01}$
	$G_{12} = 0.66^{+0.13}_{-0.01}$

Generally, having accurate models and data close in time to the sparse data would be best for reducing the phase-curve uncertainties. Our method, by reproducing the complicated light-curve shape, reduces the uncertainty due to rotation and shape. However, it still cannot reproduce the changes in the synodic period, which can be obtained from models. Both spin/shape models and Fourier fits suffer from the propagation of synodic period uncertainty. The rotational phase uncertainty increases linearly with time (Bartczak & Dudzinski 2019). Thus, composing sparse data with dense light curves that have been obtained at a very different epoch may result in a large rotational phase discrepancy and thus induce additional errors in the interpolation of maximum brightness. Thus, having data very close in time to the sparse photometry will best reduce these sources of uncertainty.

Aspect changes also influence phase curves. Traditionally, phase curves are obtained for objects with small aspect changes (most main-belt objects) to avoid the uncertainties induced by aspect. The method of Martikainen et al. (2021) proposed computing so-called reference phase curves, namely phase curves in the equatorial geometry (often referred to as aspect-corrected). These, however, suffer from additional uncertainties arising from the shape models, which typically have large uncertainties in the z-axis. The use of dense absolute and relative photometry could help with this problem. These types of data can help us to constrain the axial ratio, and thus also improve the z-axis uncertainty.

6 SUMMARY AND FUTURE WORK

Because the number of photometric measurements for asteroids is growing exponentially in time, it is important to develop methods capable of combining these distributed data. In this work, we have presented an efficient method that is able to produce phase curves from combined dense and sparse photometry, and the rotational brightness modulation is accounted for. Moreover, we have shown that differential photometry (unusable for the construction of traditional phase curves) can be utilized with sparse data, aiding the light-curve correction. Furthermore, increasing the number of sparse data will allow for the combination of different data sets into 'denser' light curves, which in turn will provide a higher quality of phase curves.

In the future, we plan to develop a large photometric data base combining sparse and dense photometry from various publicly available data sources. This will include absolute, relative, and differential photometry.

Combining a larger amount of data will allow for a more accurate determination of phase function parameters for a large number of asteroids. This in turn will lead to a better determination of asteroid

sizes, albedos, and other surface properties that are correlated with phase-curve parameters. Furthermore, poorly understood problems such as phase-curve parameters relation to taxonomy, wavelength dependence, and aspect angle dependence can be studied given a large data base containing improved phase curves.

ACKNOWLEDGEMENTS

This work has been supported by grant no. 2017/25/B/ST9/00740 from the National Science Centre, Poland. VS and IB gratefully acknowledge support from the National Research Foundation of Ukraine (grant no. 2020.02/0371). DO was supported by the National Science Centre, Poland, grant no. 2017/26/D/ST9/00240. This work has made use of data from the European Space Agency (ESA) mission *Gaia* (https://www.cosmos.esa.int/gaia), processed by the *Gaia* Data Processing and Analysis Consortium (DPAC, https://www.cosmos.esa.int/web/gaia/dpac/consortium). Funding for the DPAC has been provided by national institutions, in particular the institutions participating in the *Gaia* Multilateral Agreement.

DATA AVAILABILITY

The majority of the photometric light curves are already available in the CDS (Centre de Données astronomiques de Strasbourg) archive. The remaining unpublished light curves will be submitted to CDS. Composite light curves and phase curves for the other objects in this work as well as for the simulated data are available in the online Supporting Information.

REFERENCES

Akimov L., 1988, Kinematika i Fizika Nebesnykh Tel, 4, 10
Akimov L. A., 1975, SvA, 19, 385
Akimov L. A., 1979, SvA, 23, 231
Alvarez-Candal A., Benavidez P., Bagatin A. C., Santana-Ros T., 2022, A&A, 657, A80
Alvarez-Candal A., Benavidez P., Bagatin A. C., Santana-Ros T., Corral S. J., 2021, The multi-wavelength phase curves of minor bodies from the SLOAN Moving Objects Catalog, Europlanet Science Congress 2021, online, 13-24 Sep 2021, EPSC2021-38
Bartczak P., Dudzinski G., 2019, MNRAS, 485, 2431
Belskaya I., Shevchenko V., 2000, Icarus, 147, 94
Belskaya I., Shevchenko V., 2018, Phase angle effects in brightness and polarization fordifferent classes of small Solar system bodies, Europlanet Science Congress 2018, 16–21 September 2018, Berlin, Germany, EPSC2018–730
Bowell E., Hapke B., Domingue D., Lumme K., Peltoniemi J., Harris A. W., 1989, Asteroids II. University of Arizona Press, United States, p. 524
Brown A. et al., 2018, A&A, 616, A1
Busso G. et al., 2018, Gaia DR2 Documentation, Chapter 5, Gaia DR2 documentation, European Space Agency; Gaia Data Processing and Analysis Consortium, online athttps://gea.esac.esa.int/archive/documentation/GDR2
Colazo M., Duffard R., 2020, H-G determination of 4000 asteroids from GAIA-DR2, Europlanet Science Congress 2020, online, 21 Sep – 9 Oct 2020, EPSC2020-406
Colazo M., Duffard R., Weidmann W., 2021, MNRAS, 504, 761
Ďurech J., Tonry J., Erasmus N., Denneau L., Heinze A., Flewelling H., Vančo R., 2020, A&A, 643, A59
Gradie J., Veverka J., 1986, Icarus, 66, 455
Gradie J., Veverka J., Buratti B., 1980, in Lunar and Planetary Science Conf. Proc., Pergamon Press, United States, p. 799
Hapke B., 1963, J. Geophys. Res. , 68, 4571
Hapke B., 1966, AJ, 71, 333
Hapke B., 1981, J. Geophys. Res.: Solid Earth, 86, 3039
Hapke B., 1984, Icarus, 59, 41
Hapke B., 1986, Icarus, 67, 264
Hapke B., 2002, Icarus, 157, 523
Hapke B., 2008, Icarus, 195, 918
Hapke B., 2012, Icarus, 221, 1079
Hapke B., Wells E., 1981, J. Geophys. Res.: Solid Earth, 86, 3055
Kwiatkowski T. et al., 2021, A&A, 656, A126
Lagerkvist C., Magnusson I., Belskaya A., Erikson M., Dohlgren M., Barucci M., 1995, NASA Planetary Data System, online, Asteroid Photometric Catalog V1.1. EAR-A-3-DDR-APC-LIGHTCURVE-V1.1
Lin Z.-Y., Cheng C.-C., Chang C.-K., Tseng W.-L., Ip W.-H., 2020, Statistical analysis of asteroid taxonomic signatures from magnitude phase function, Europlanet Science Congress 2020, online, 21 September - 9 October 2020, EPSC2020-994
Mahlke M., Carry B., Denneau L., 2021, Icarus, 354, 114094
Mainzer A. K., Bauer J. M., Cutri R. M., Grav T., Kramer E. A., Masiero J. R., Sonnett S., Wright E. L., 2019, NEOWISE Diameters and Albedos V2.0. Available at: https://sbn.psi.edu/pds/resource/neowisediam.html
Marciniak A. et al., 2012, A&A, 545, A131
Marciniak A. et al., 2015, Planet. Space Sci., 118, 256
Marciniak A. et al., 2018, A&A, 610, A7
Marciniak A. et al., 2019, A&A, 625, A139
Marciniak A. et al., 2021, A&A, 654, A87
Martikainen J., Fedorets G., Penttilä A., Muinonen K., 2020, Asteroid phase curve parameters from Gaia photometry, Europlanet Science Congress 2020, online, 21 Sep - 9 Oct 2020, EPSC2020-654
Martikainen J., Muinonen K., Penttilä A., Cellino A., Wang X. B., 2021, A&A, 649, A98
Millis R., Bowell E., Thompson D., 1976, Icarus, 28, 53
Miner E., Young J., 1976, Icarus, 28, 43
Muinonen K., Piironen J., Shkuratov Y. G., Ovcharenko A., Clark B. E., 2002, Asteroid Photometric and Polarimetric Phase Effects. University of Arizona Press, Tucson, AZ, p. 123
Muinonen K., Belskaya I. N., Cellino A., Delbò M., Levasseur-Regourd A.-C., Penttilä A., Tedesco E. F., 2010, Icarus, 209, 542
Muinonen K., Torppa J., Wang X.-B., Cellino A., Penttilä A., 2020, A&A, 642, A138
Neese C., 2010, NASA Planetary Data System, online, Asteroid Taxonomy V6.0. EAR-A-5-DDR-TAXONOMY-V6.0
Oszkiewicz D., Muinonen K., Bowell E., Trilling D., Penttilä A., Pieniluoma T., Wasserman L., Enga M.-T., 2011, J. Quant. Spectrosc. Radiative Transfer, 112, 1919
Oszkiewicz D. A., Bowell E., Wasserman L., Muinonen K., Penttilä A., Pieniluoma T., Trilling D. E., Thomas C. A., 2012, Icarus, 219, 283
Oszkiewicz D. et al., 2021, Icarus, 357, 114158
Penttilä A., Shevchenko V., Wilkman O., Muinonen K., 2016, Planet. Space Sci., 123, 117
Pravec P., Harris A. W., Kušnirák P., Galád A., Hornoch K., 2012, Icarus, 221, 365
Prusti T. et al., 2016, A&A, 595, A1
Reddy V. et al., 2012, Icarus, 217, 153
Reddy V., Dunn T. L., Thomas C. A., Moskovitz N. A., Burbine T. H., 2015, Asteroids IV. University of Arizona Press, United States, p. 43
Sanchez J. A., Reddy V., Nathues A., Cloutis E. A., Mann P., Hiesinger H., 2012, Icarus, 220, 36
Shevchenko V., 1997, Solar System Research, 31, 219
Shevchenko V., Belskaya I., Krugly Y. N., Chiomy V., Gaftonyuk N., 2002, Icarus, 155, 365
Shevchenko V. G. et al., 2016, Planet. Space Sci., 123, 101
Shevchenko V. G. et al., 2021, Planet. Space Sci., 202, 105248
Shkuratov Y., Kaydash V., Korokhin V., Velikodsky Y., Opanasenko N., Videen G., 2011, Planet. Space Sci., 59, 1326
Spoto F. et al., 2018, A&A, 616, A13
Tedesco E. F., Noah P. V., Noah M., Price S. D., 2004, NASA Planetary Data System, online, IRAS Minor Planet Survey. IRAS-A-FPA-3-RDR-IMPS-V6.0
Usui F. et al., 2011, PASJ, 63, 1117
Vereš P. et al., 2015, Icarus, 261, 34

Warner B. D., Harris A. W., Pravec P., 2009, Icarus, 202, 134
Waszczak A. et al., 2015, AJ, 150, 75
Yoshida F. et al., 2020, Phase curves of >40,000 small solar system bodies obtained bythe Tomo-e Gozen transient survey, Europlanet Science Congress 2020, online, 21 Sep - 9 Oct 2020, EPSC2020-330

SUPPORTING INFORMATION

Supplementary data are available at *MNRAS* online.

Figure S1. (70) Panopaea.
Figure S2. (108) Hecuba.
Figure S3. (159) Aemilia.
Figure S4. (195) Eurykleia.
Figure S5. (202) Chryseis.
Figure S6. (260) Huberta.
Figure S7. (329) Svea.
Figure S8. (362) Havnia.
Figure S9. (380) Fiducia.
Figure S10. (439) Ohio.
Figure S11. (483) Seppina.
Figure S12. (483) Seppina.
Figure S13. (501) Urhixidur.
Figure S14. (537) Pauly.
Figure S15. (552) Sigelinde.
Figure S16. (611) Valeria.
Figure S17. (618) Elfriede.
Figure S18. (618) Elfriede.
Figure S19. (653) Berenike.
Figure S20. (666) Desdemona.
Figure S21. (666) Desdemona.
Figure S22. (667) Denise.
Figure S23. (667) Denise.
Figure S24. (723) Hammonia.
Figure S25. (727) Nipponia.
Figure S26. (780) Armenia.
Figure S27. (834) Burnhamia.
Figure S28. (834) Burnhamia.
Table S1. Set of figures same as Fig. 1 showing how the time separation (rows) between dense and sparse observations (in assumption, differential and relative, respectively) and the noise (columns) of the dense observations affects light curves and phase curves for simulated data of (159) Aemilia.

Please note: Oxford University Press is not responsible for the content or functionality of any supporting materials supplied by the authors. Any queries (other than missing material) should be directed to the corresponding author for the article.

APPENDIX A: OBSERVATIONAL DETAILS

Table A1. Observing circumstances (date of observation, ecliptic longitude λ, ecliptic latitude β, phase angle α, observer and observing site) for the new ground-based light curves of (611) Valeria and (727) Nipponia used in this paper.

Date	λ (°)	β (°)	α (°)	Observer	Site
(611) Valeria					
2014-10-04	22.61	− 3.21	4.34	K. Sobkowiak	Borowiec, Poland
2014-10-24	18.07	− 4.78	4.99	A. Marciniak	Borowiec, Poland
(727) Nipponia					
2015-02-17	140.83	4.58	3.52	J. Horbowicz	Borowiec, Poland
2015-02-18	140.78	4.60	3.60	V. Kudak, V. Perig	Derenivka, Ukraine
2015-03-17	135.60	6.61	14.77	P. Kankiewicz	Kielce, Poland
2015-03-19	135.42	6.71	15.38	A. Marciniak	Borowiec, Poland
2015-04-15	135.68	7.63	21.02	P. Kulczak	Borowiec, Poland

This paper has been typeset from a TEX/LATEX file prepared by the author.

B.1 Supplementary material

SUPPLEMENTARY FIGURES

The graphs shown in Fig. 1 to 28 and in Table 1 consist of two parts: upper and bottom. Upper part is a composite lightcurve for a given asteroid combining Gaia observations (black bold) and ground-based observations (color) with a derived lightcurve shape (solid red line). Bottom part shows a linear part of the phase curve. Original Gaia data reduced to 1 au distance and a linear fit to those is shown in blue. Lightcurve amplitude corrected Gaia data based on literature, derived and adjusted period and corresponding fits are shown in green, orange and black respectively. Error bars show uncertainty of brightness in magnitude. Residuals are shown at the very bottom.

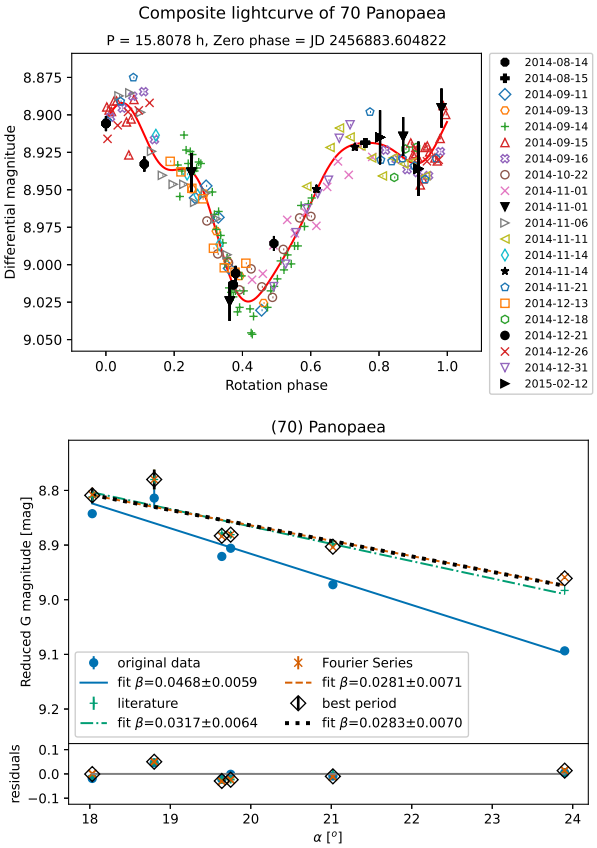

Figure 1. (70) Panopaea

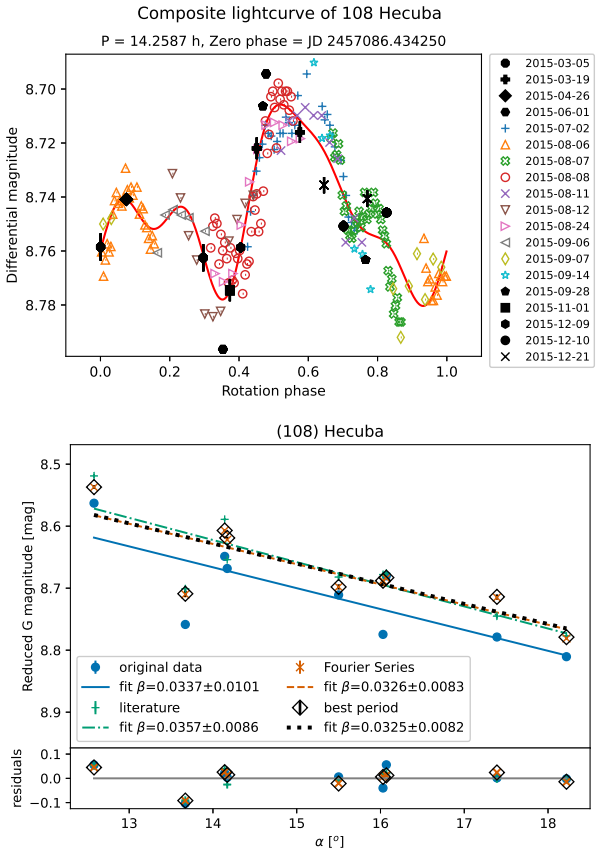

Figure 2. (108) Hecuba

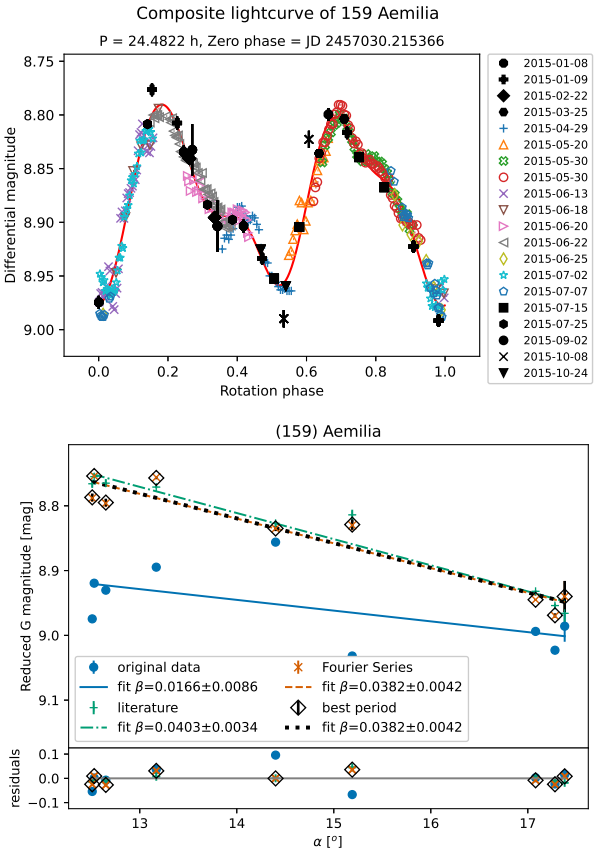

Figure 3. (159) Aemilia

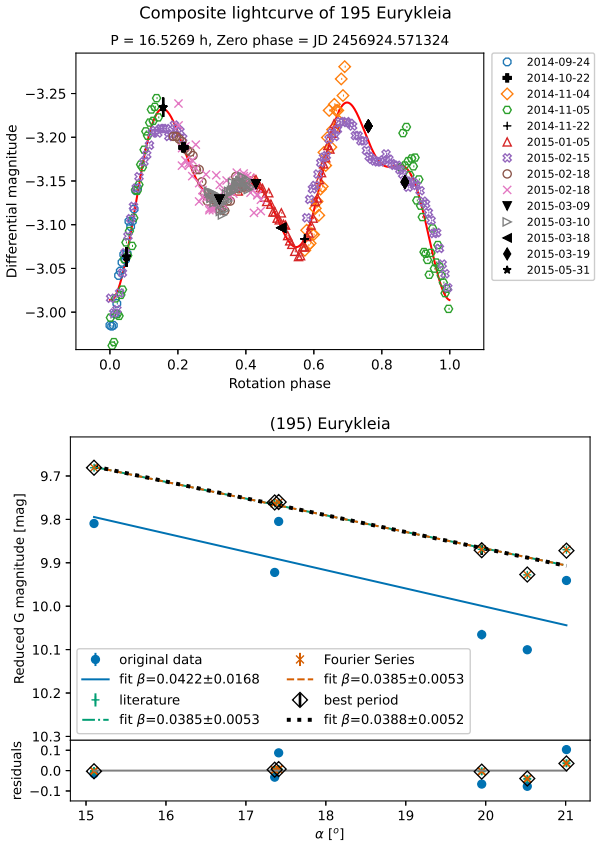

Figure 4. (195) Eurykleia

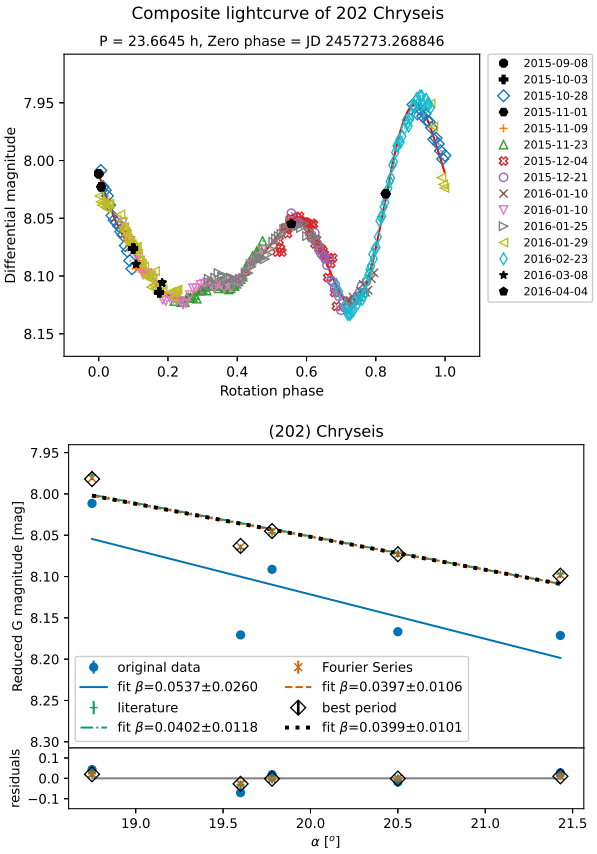

Figure 5. (202) Chryseis

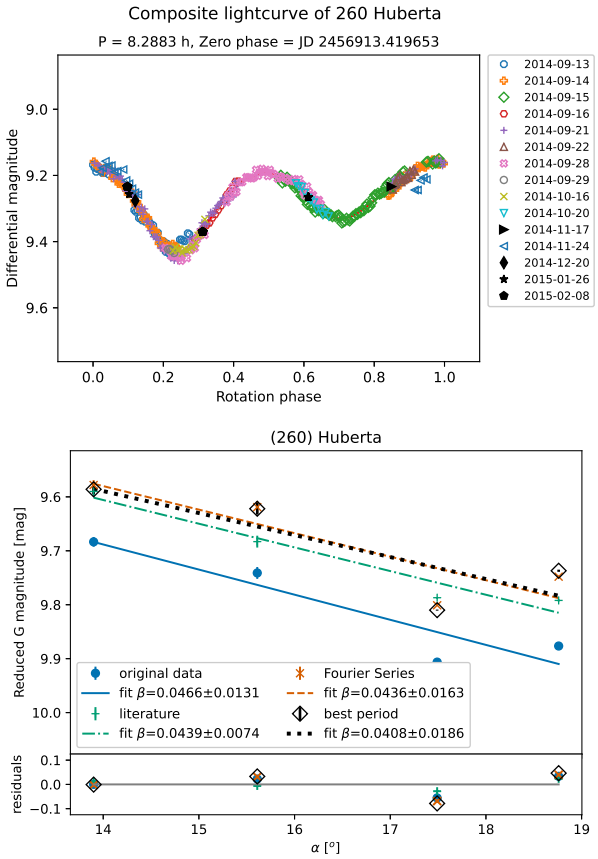

Figure 6. (260) Huberta

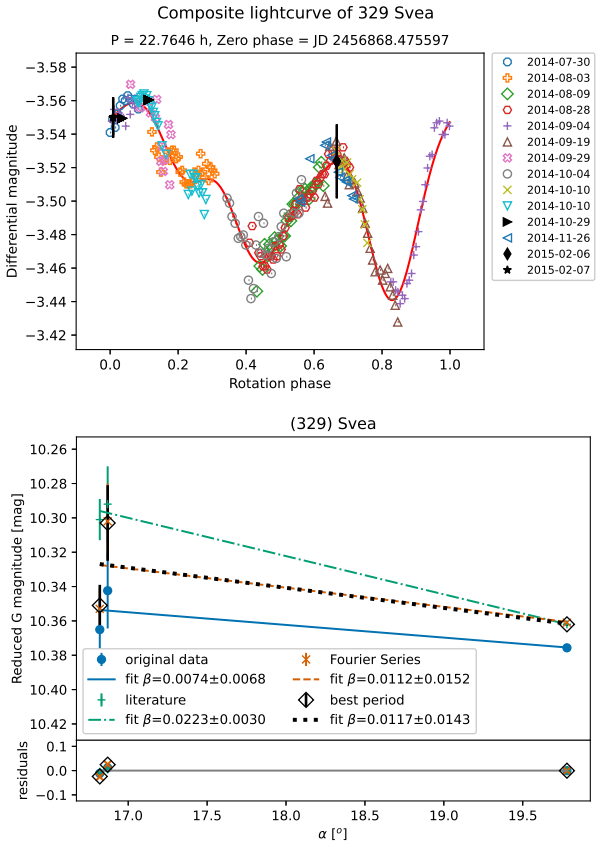

Figure 7. (329) Svea

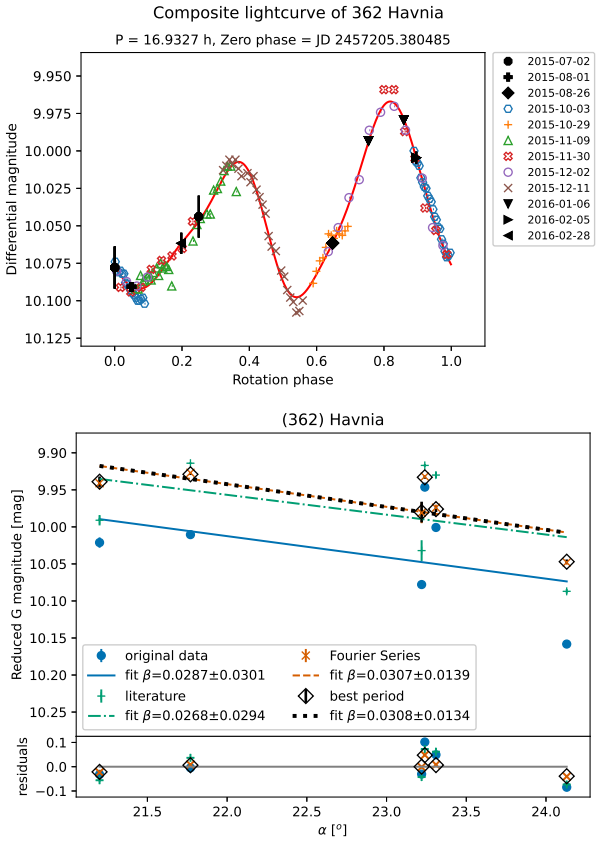

Figure 8. (362) Havnia

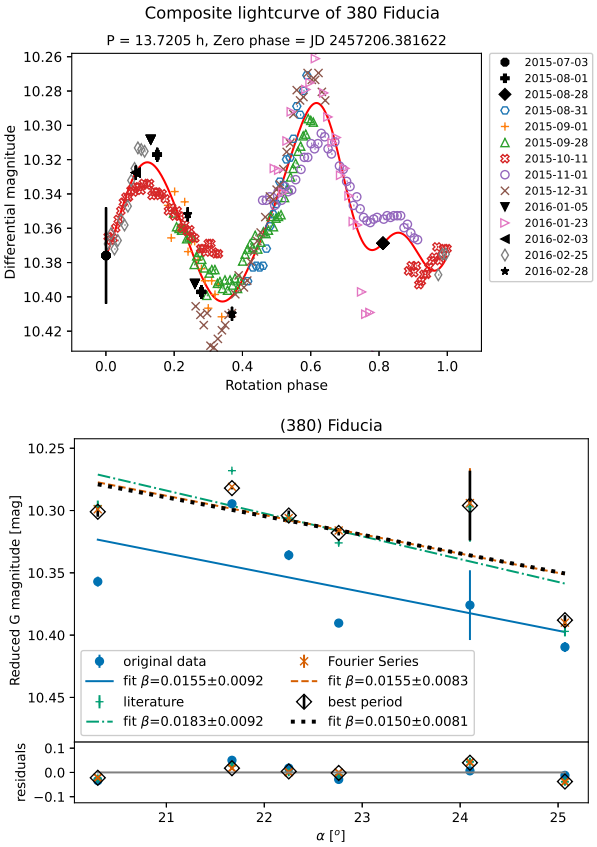

Figure 9. (380) Fiducia

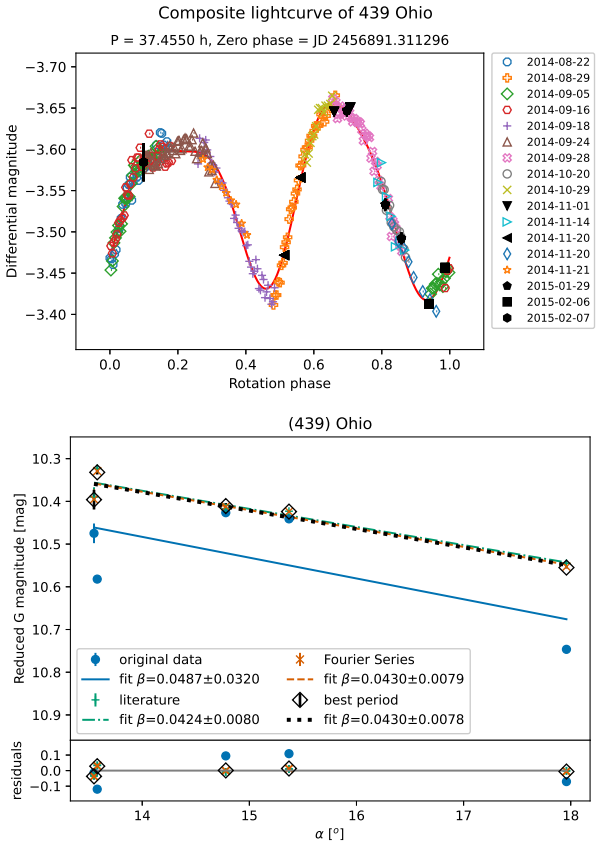

Figure 10. (439) Ohio

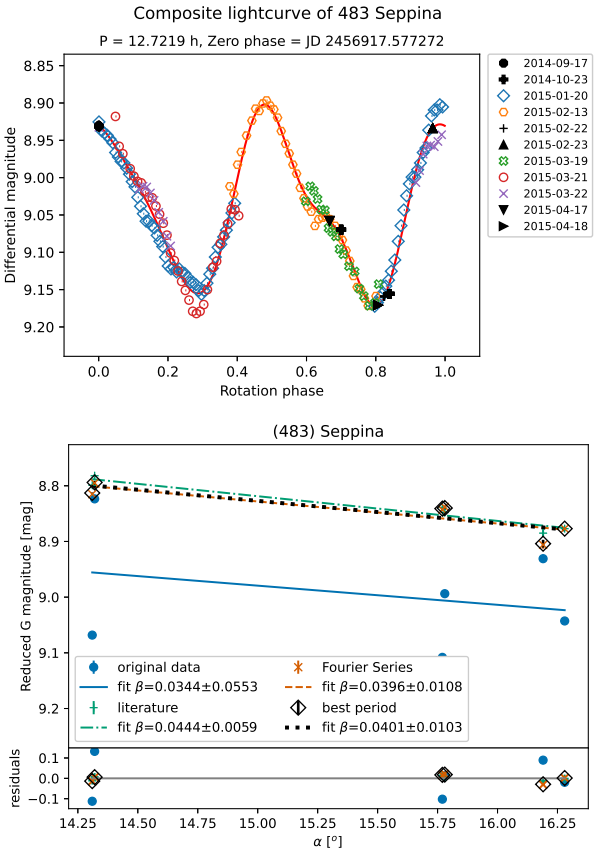

Figure 11. (483) Seppina

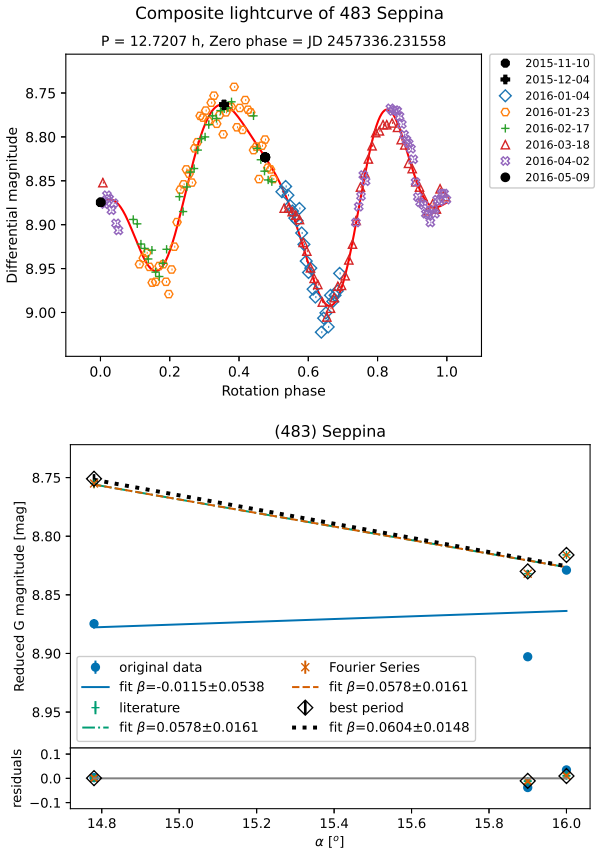

Figure 12. (483) Seppina

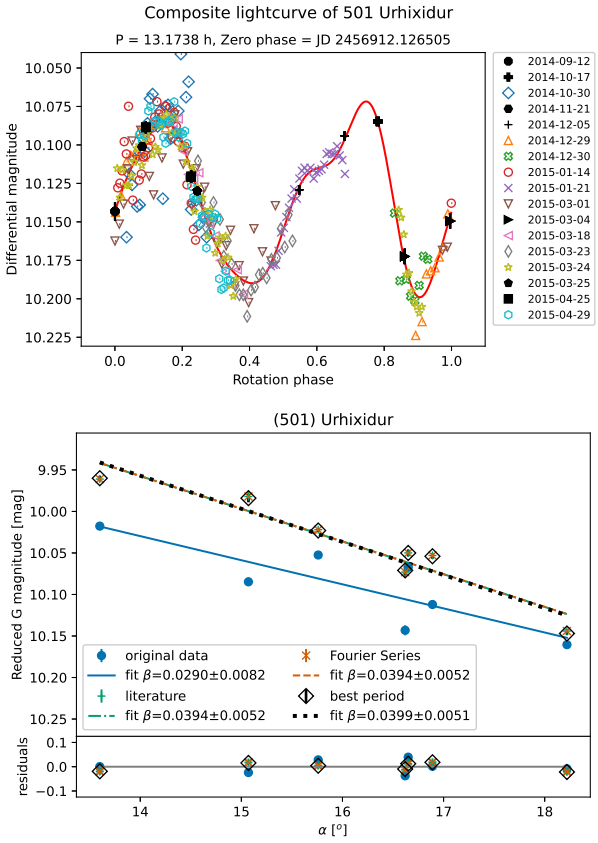

Figure 13. (501) Urhixidur

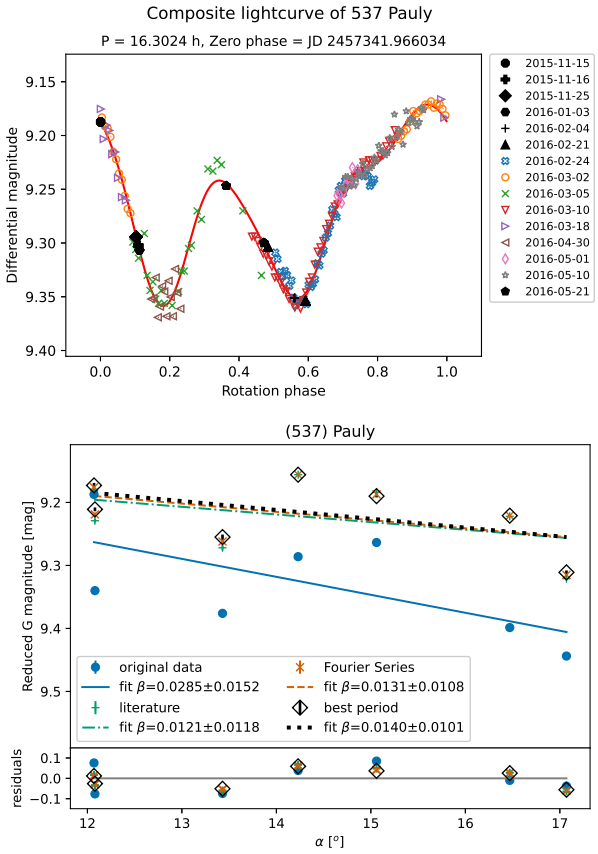

Figure 14. (537) Pauly

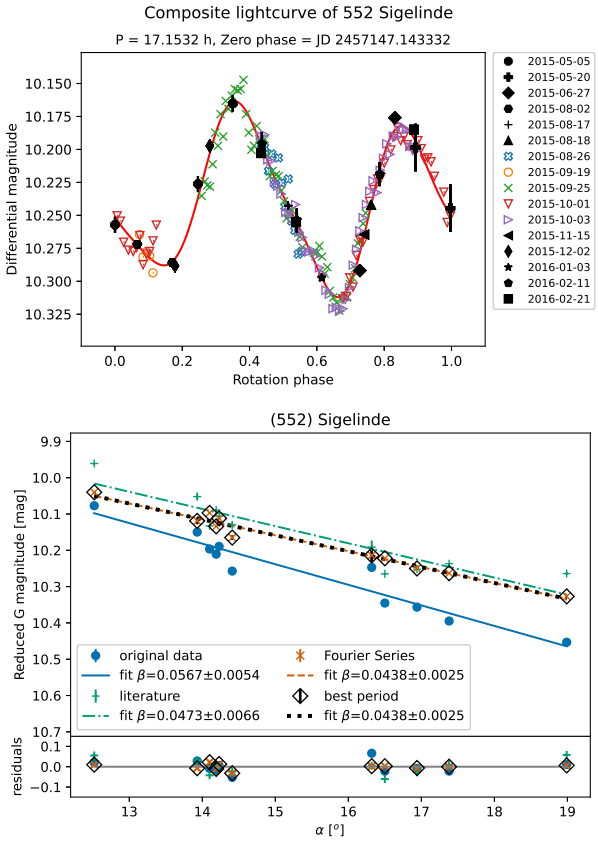

Figure 15. (552) Sigelinde

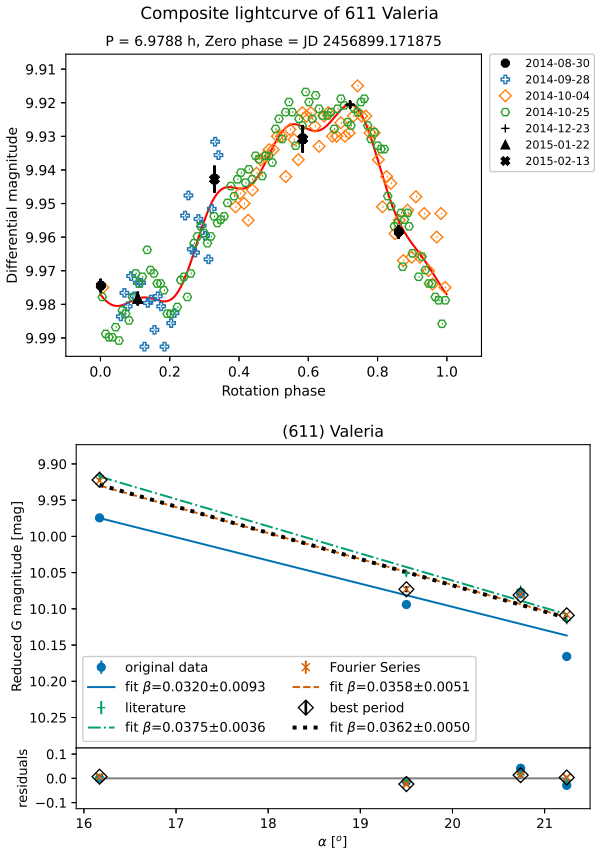

Figure 16. (611) Valeria

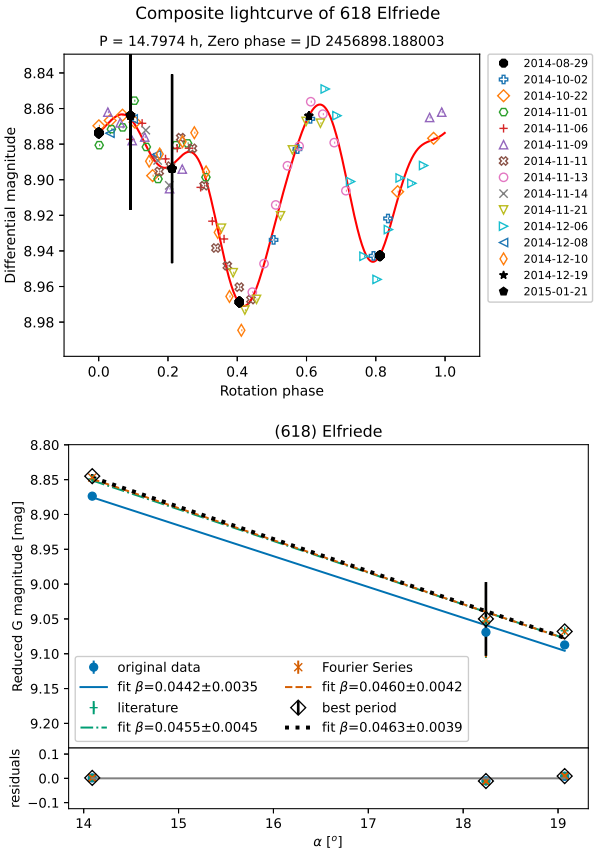

Figure 17. (618) Elfriede

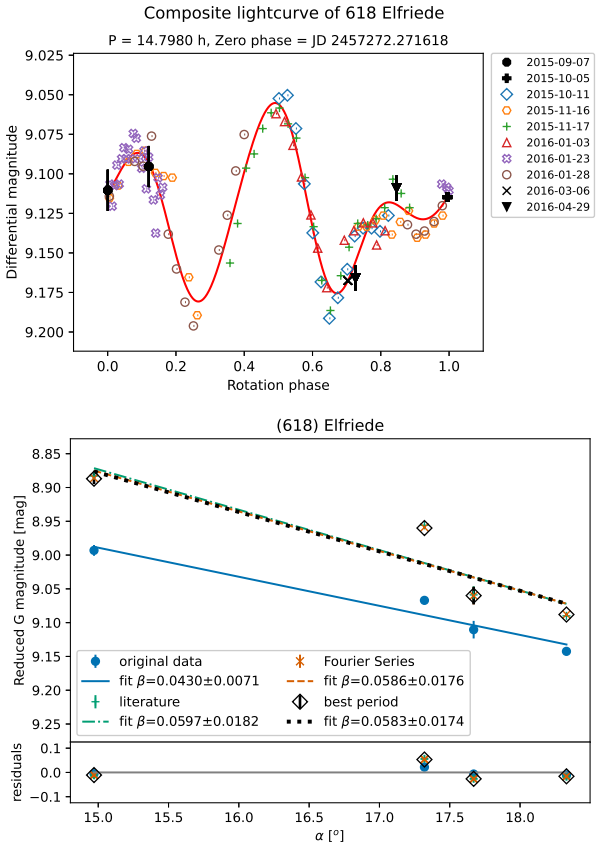

Figure 18. (618) Elfriede

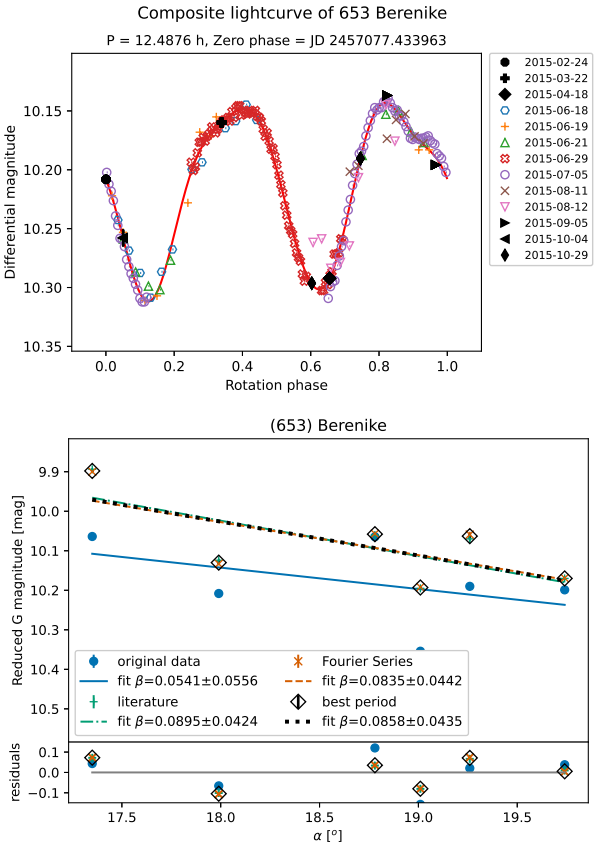

Figure 19. (653) Berenike

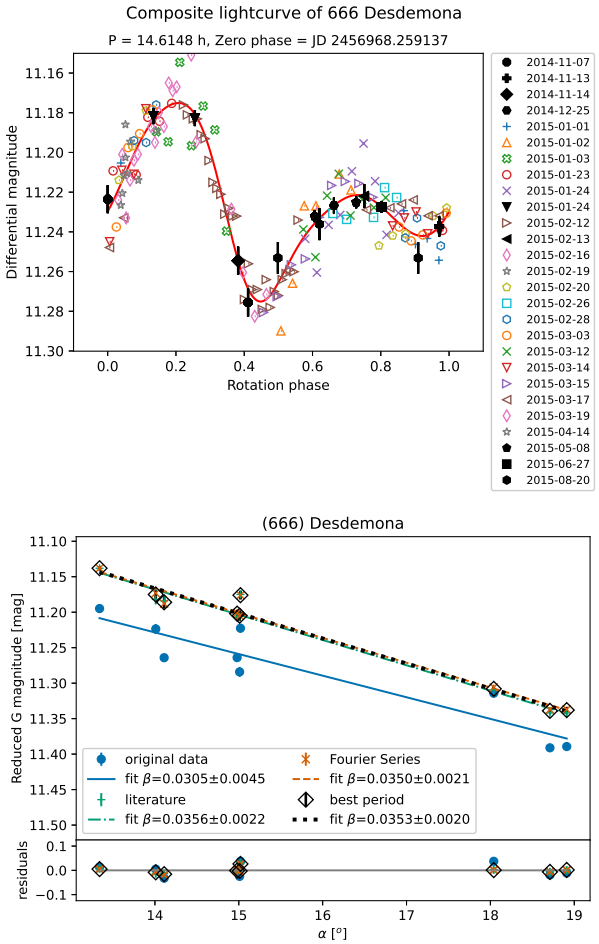

Figure 20. (666) Desdemona

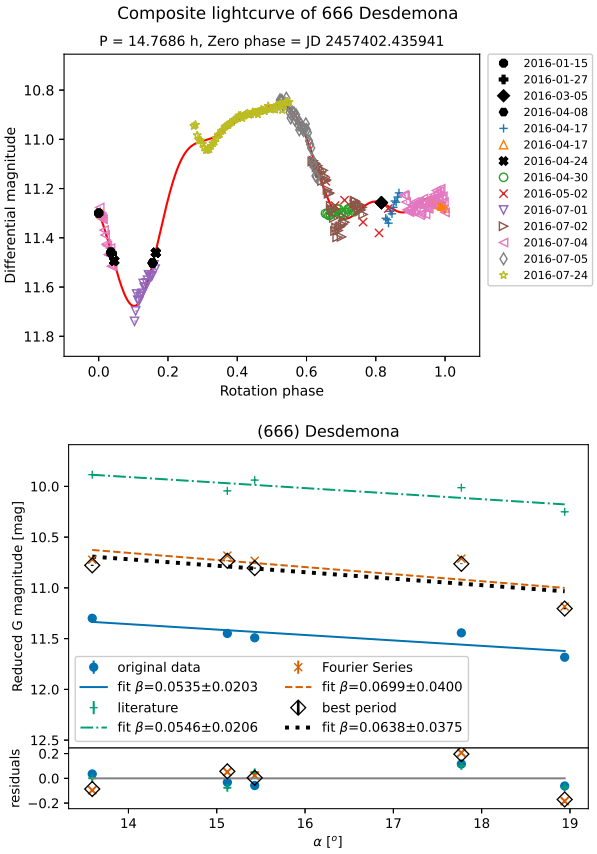

Figure 21. (666) Desdemona

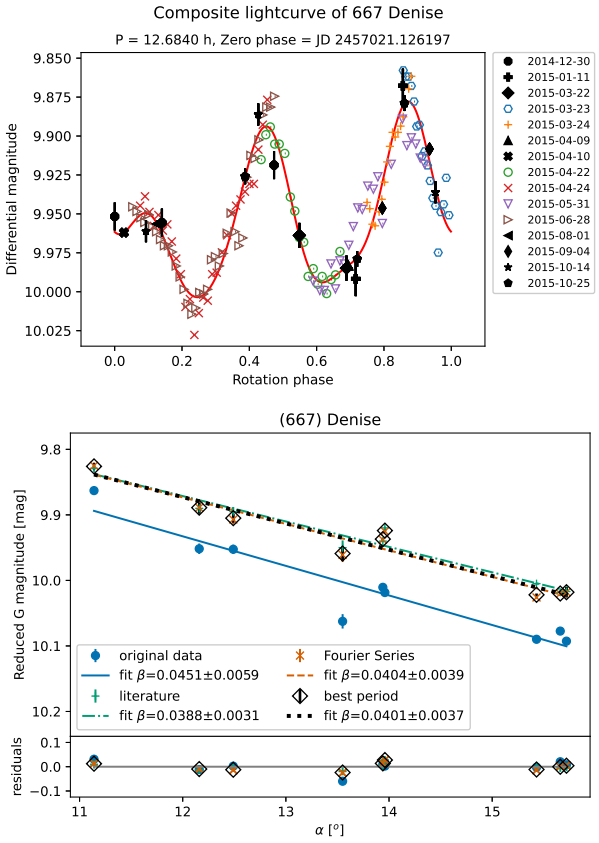

Figure 22. (667) Denise

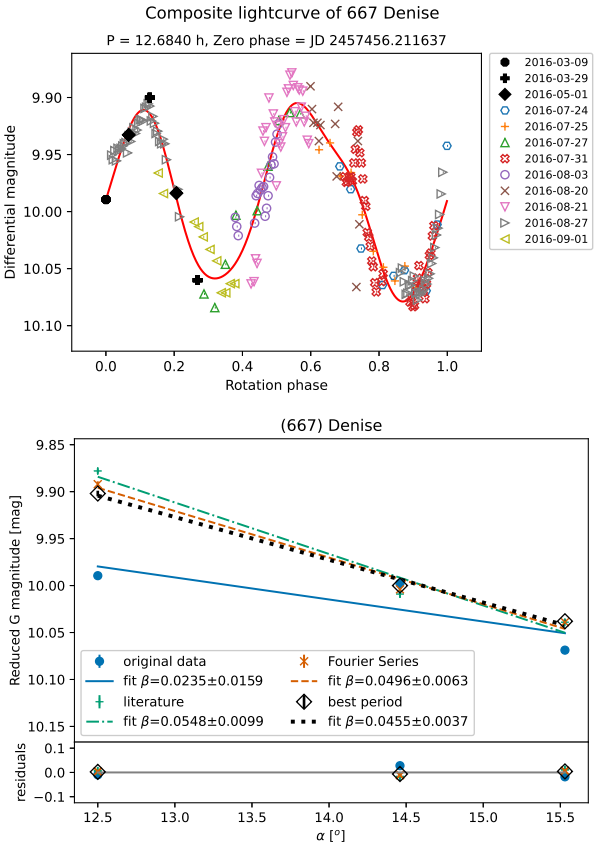

Figure 23. (667) Denise

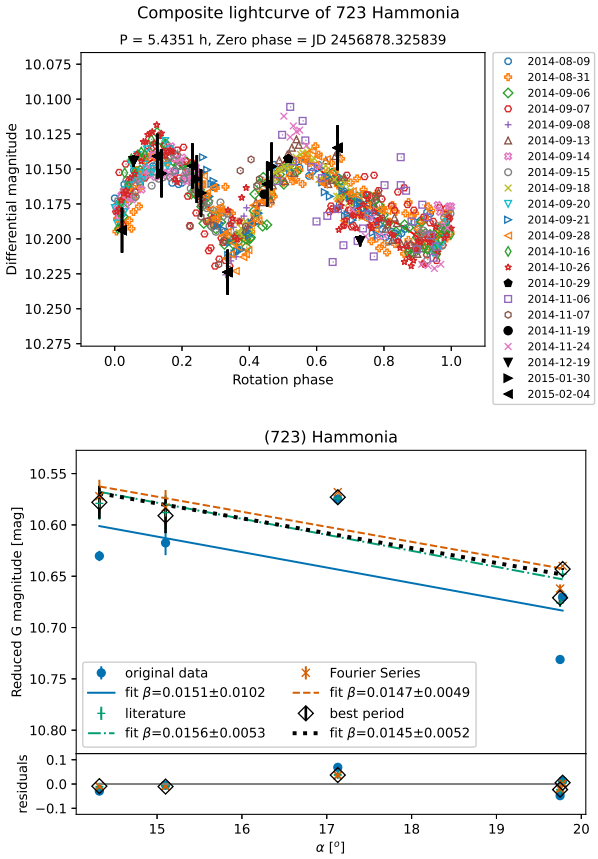

Figure 24. (723) Hammonia

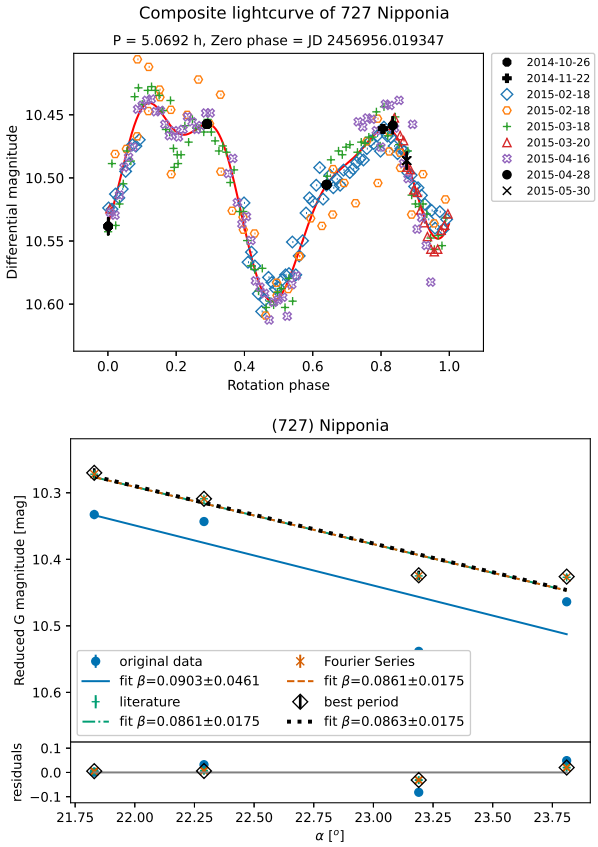

Figure 25. (727) Nipponia

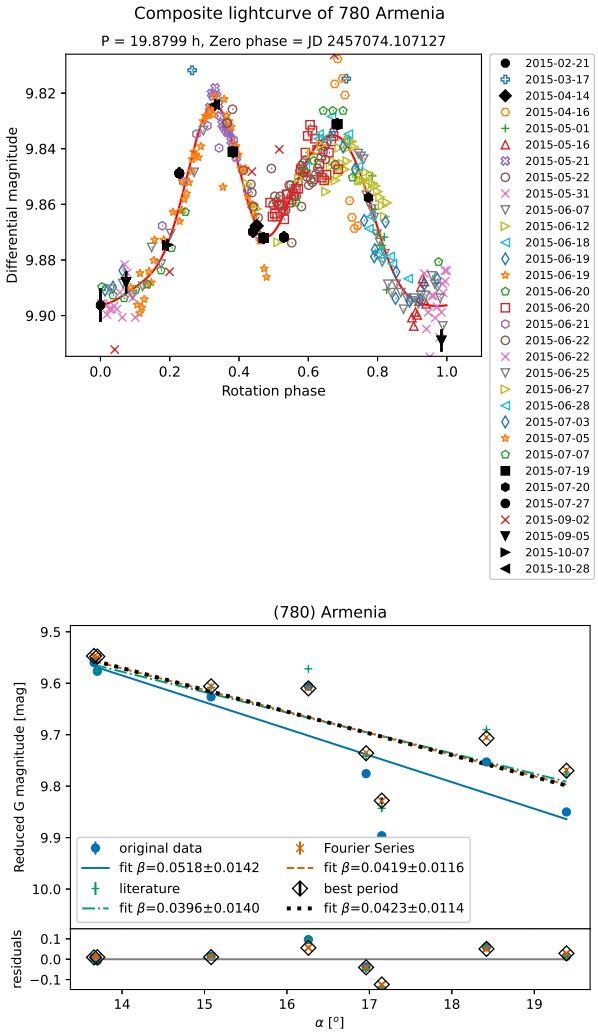

Figure 26. (780) Armenia

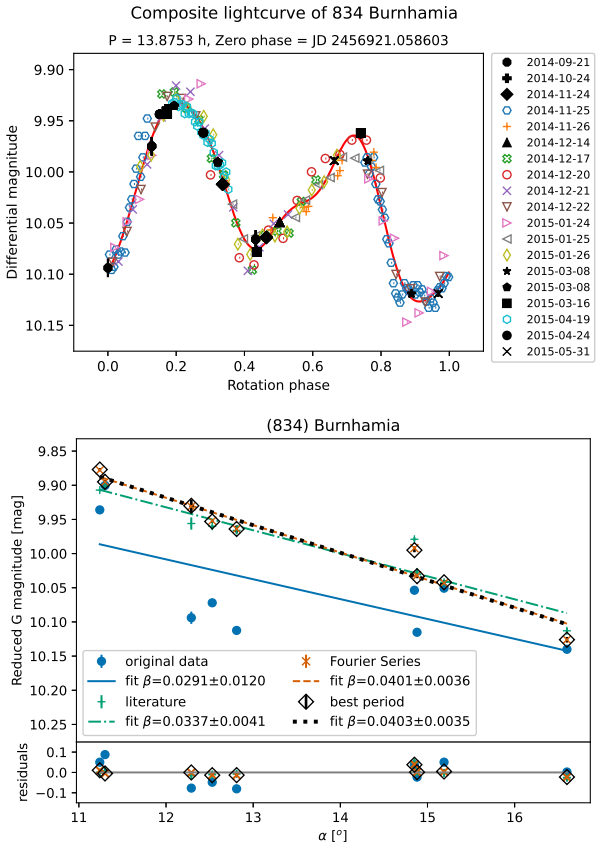

Figure 27. (834) Burnhamia

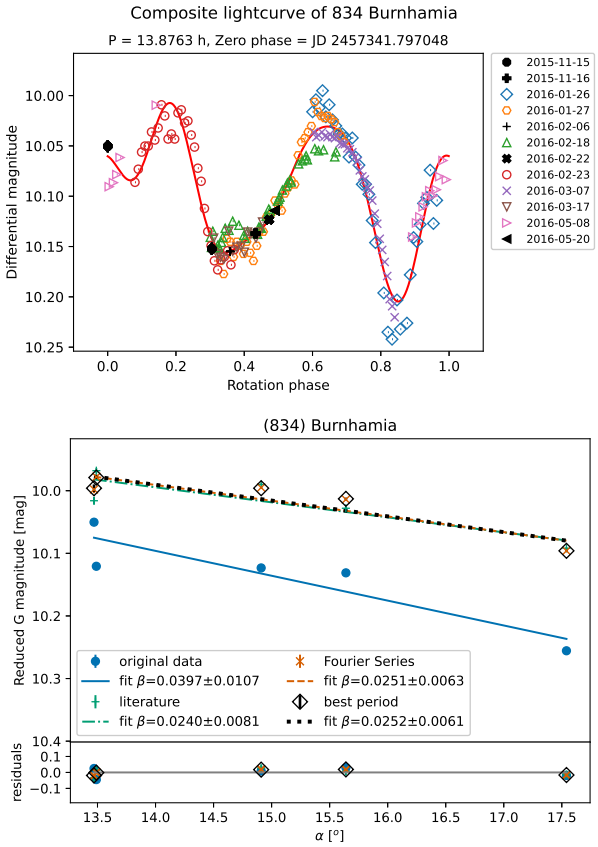

Figure 28. (834) Burnhamia

Table 1: Set of figures same as Fig. 1 showing how the time separation (rows) between dense and sparse observations (in assumption, differential and relative, respectively) and the noise (columns) of the dense observations affects lightcurves and phase curves for simulated data of (159) Aemilia.

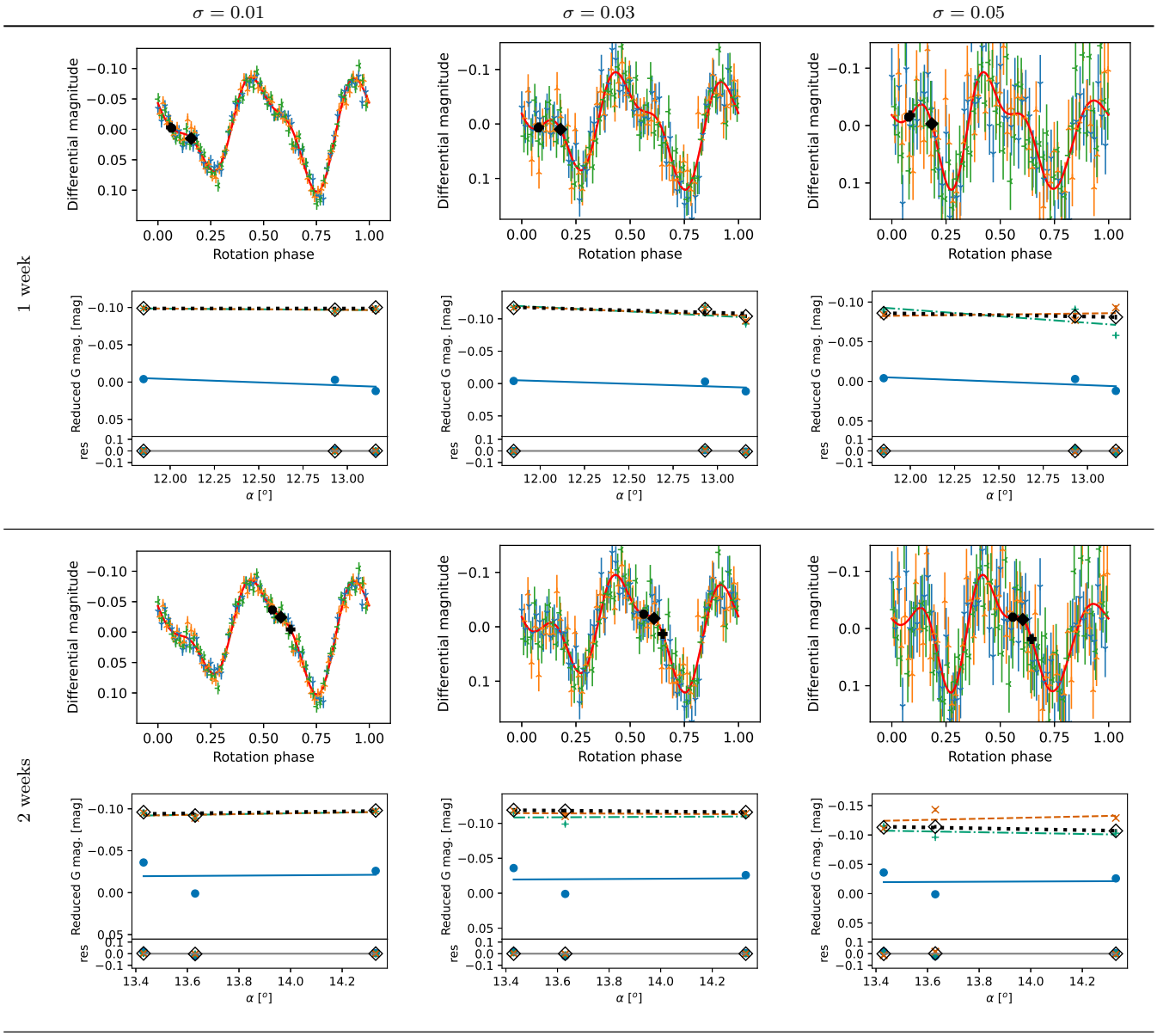

Table 1: Set of figures same as Fig. 1 showing how the time separation (rows) between dense and sparse observations (in assumption, differential and relative, respectively) and the noise (columns) of the dense observations affects lightcurves and phase curves for simulated data of (159) Aemilia.

	$\sigma = 0.01$	$\sigma = 0.03$	$\sigma = 0.05$
3 weeks	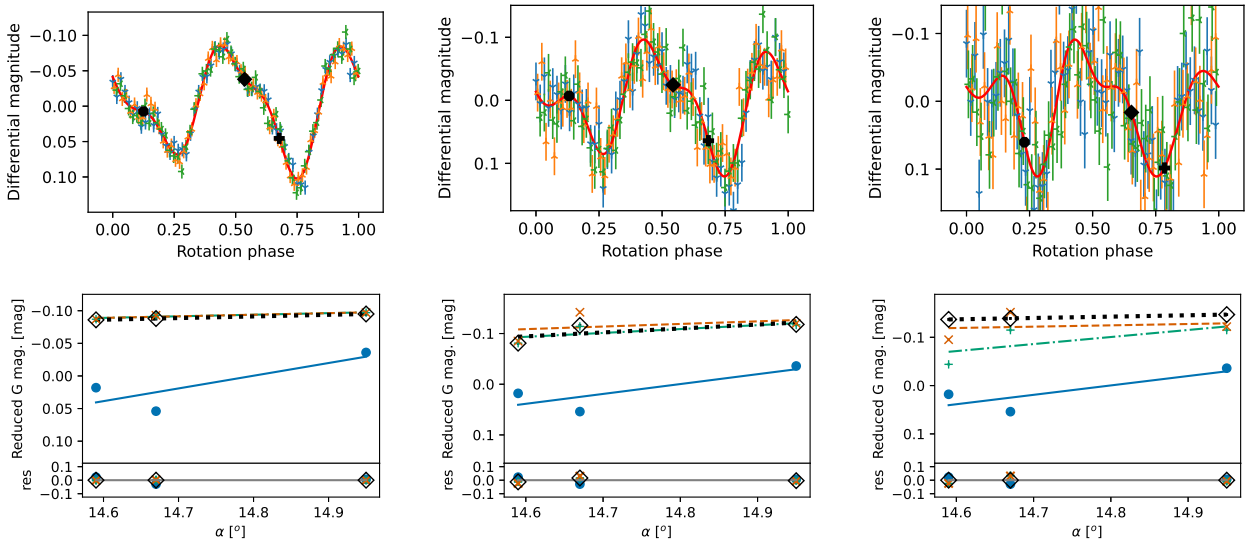		
4 weeks	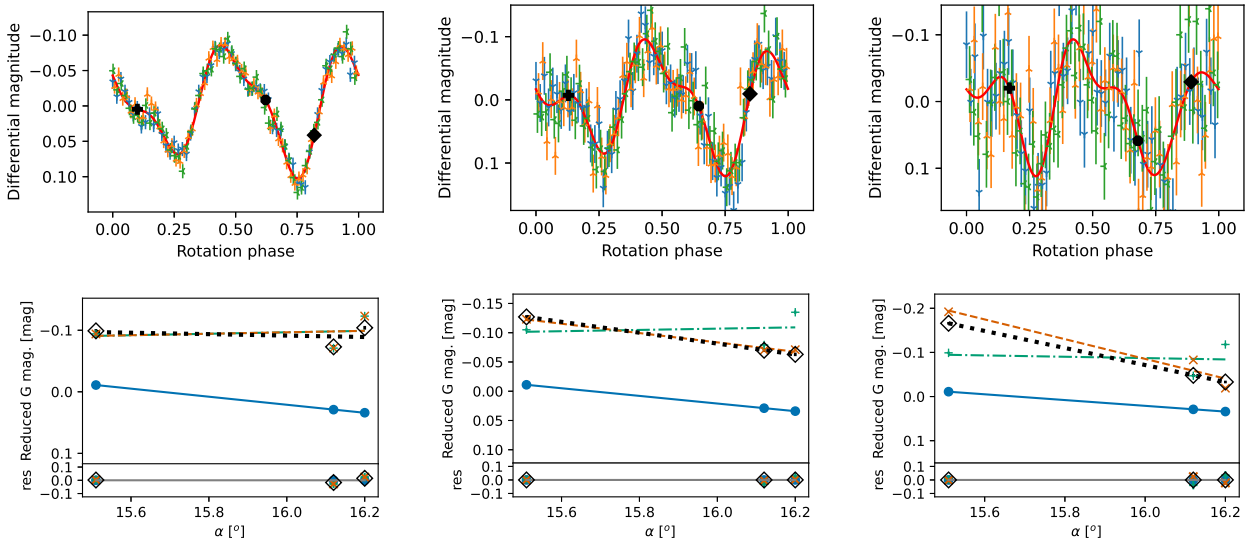		

Table 1: Set of figures same as Fig. 1 showing how the time separation (rows) between dense and sparse observations (in assumption, differential and relative, respectively) and the noise (columns) of the dense observations affects lightcurves and phase curves for simulated data of (159) Aemilia.

	$\sigma = 0.01$	$\sigma = 0.03$	$\sigma = 0.05$
5 weeks	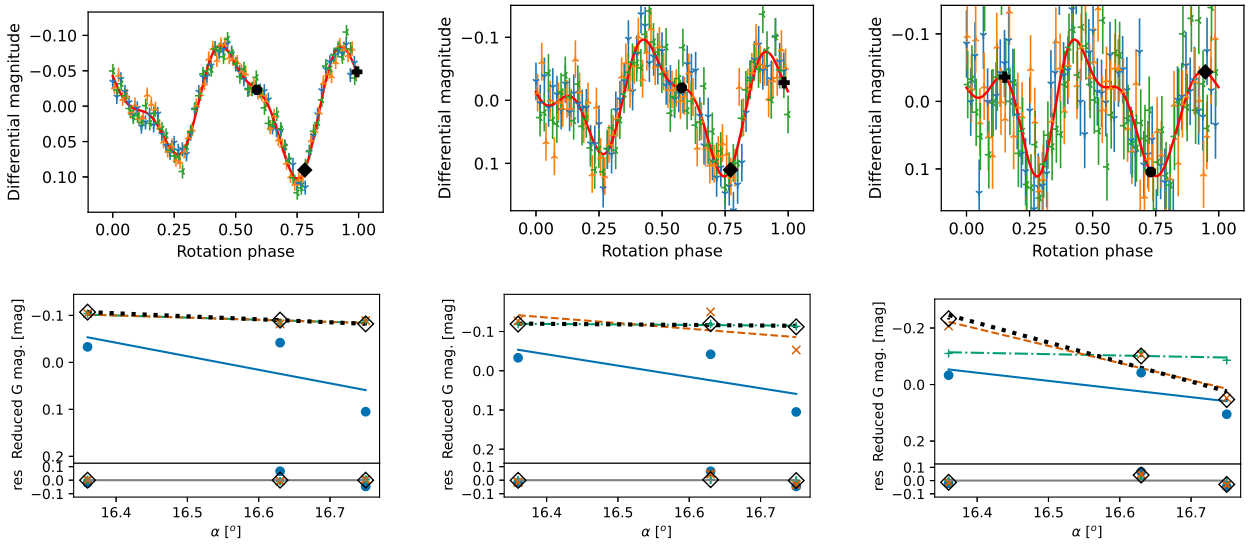		
6 weeks	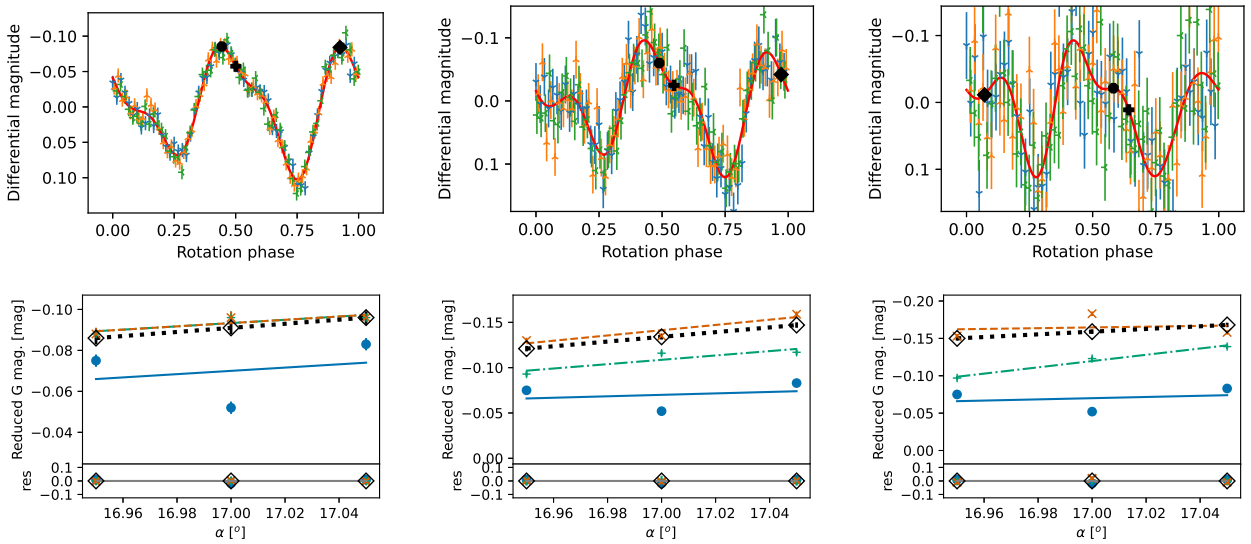		

Table 1: Set of figures same as Fig. 1 showing how the time separation (rows) between dense and sparse observations (in assumption, differential and relative, respectively) and the noise (columns) of the dense observations affects lightcurves and phase curves for simulated data of (159) Aemilia.

	$\sigma = 0.01$	$\sigma = 0.03$	$\sigma = 0.05$
7 weeks	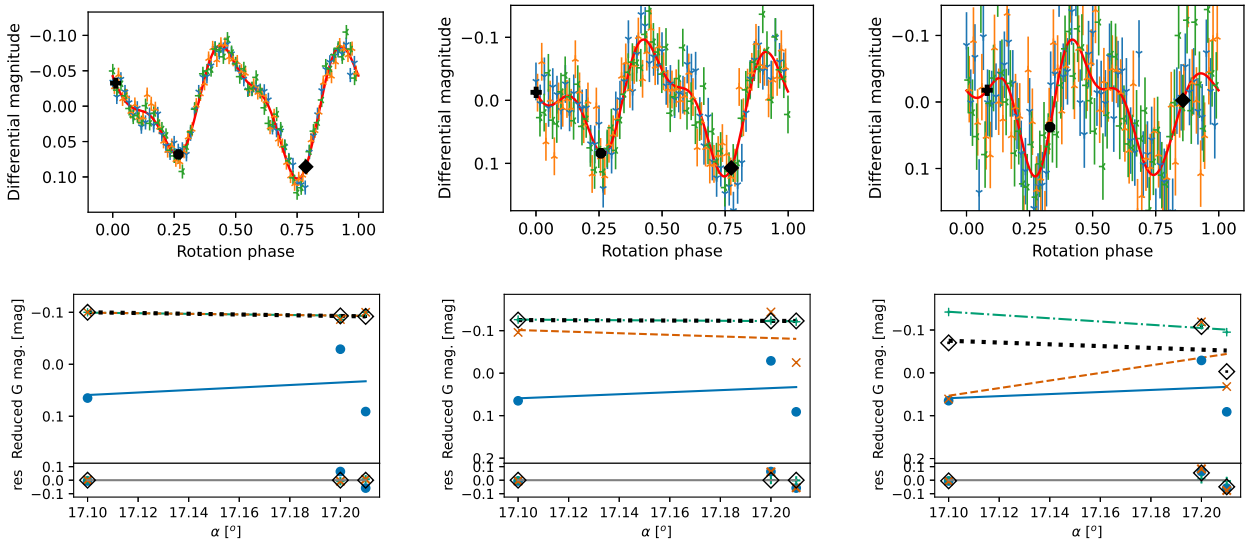		
8 weeks	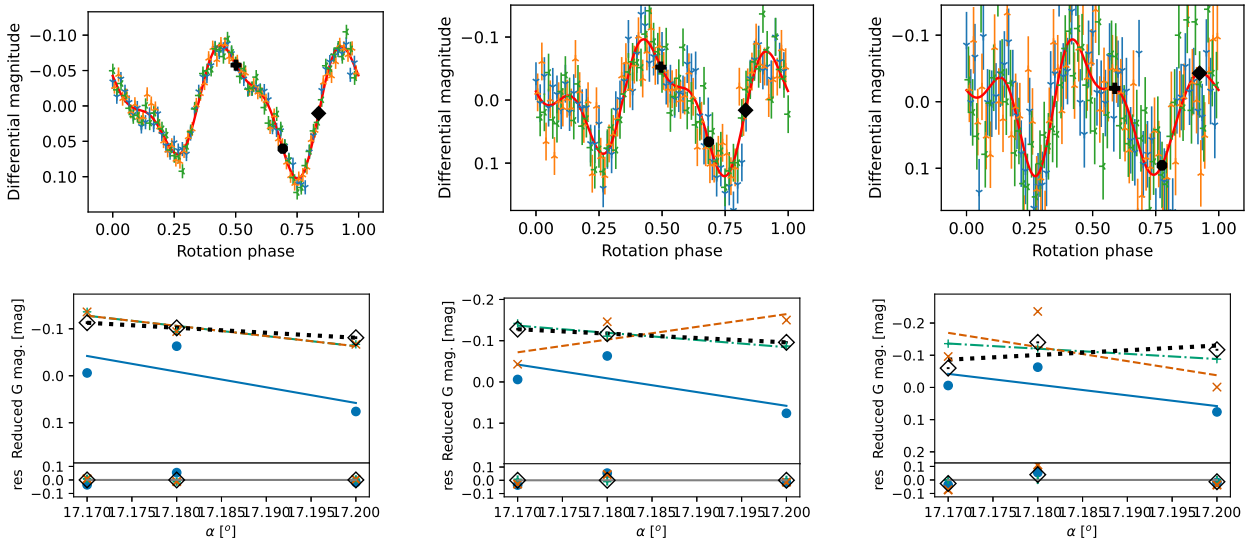		

Table 1: Set of figures same as Fig. 1 showing how the time separation (rows) between dense and sparse observations (in assumption, differential and relative, respectively) and the noise (columns) of the dense observations affects lightcurves and phase curves for simulated data of (159) Aemilia.

	$\sigma = 0.01$	$\sigma = 0.03$	$\sigma = 0.05$
9 weeks	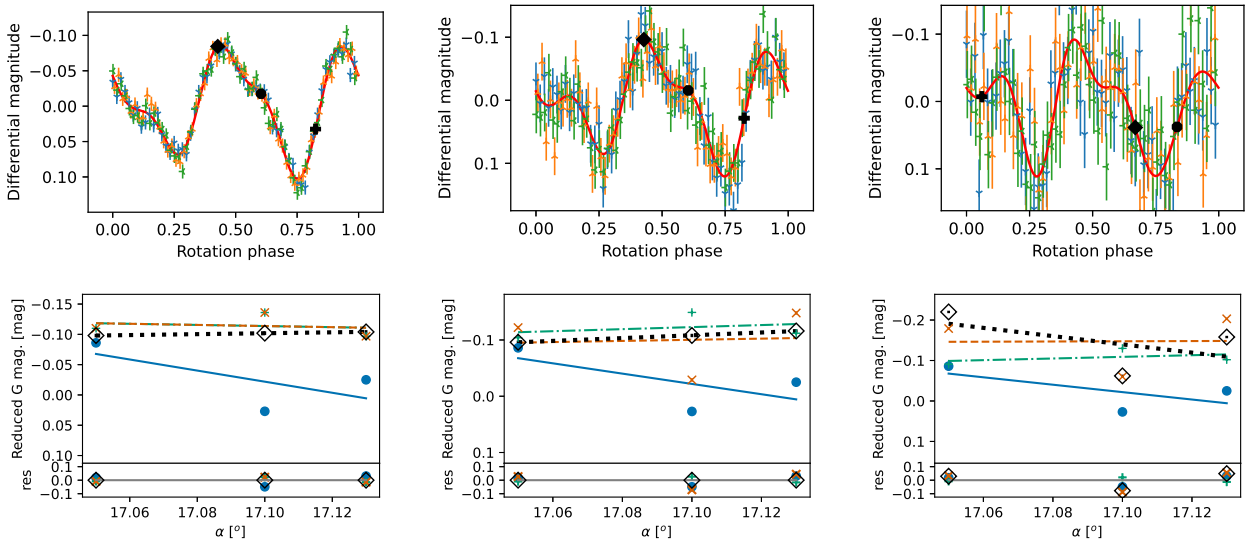		
10 weeks	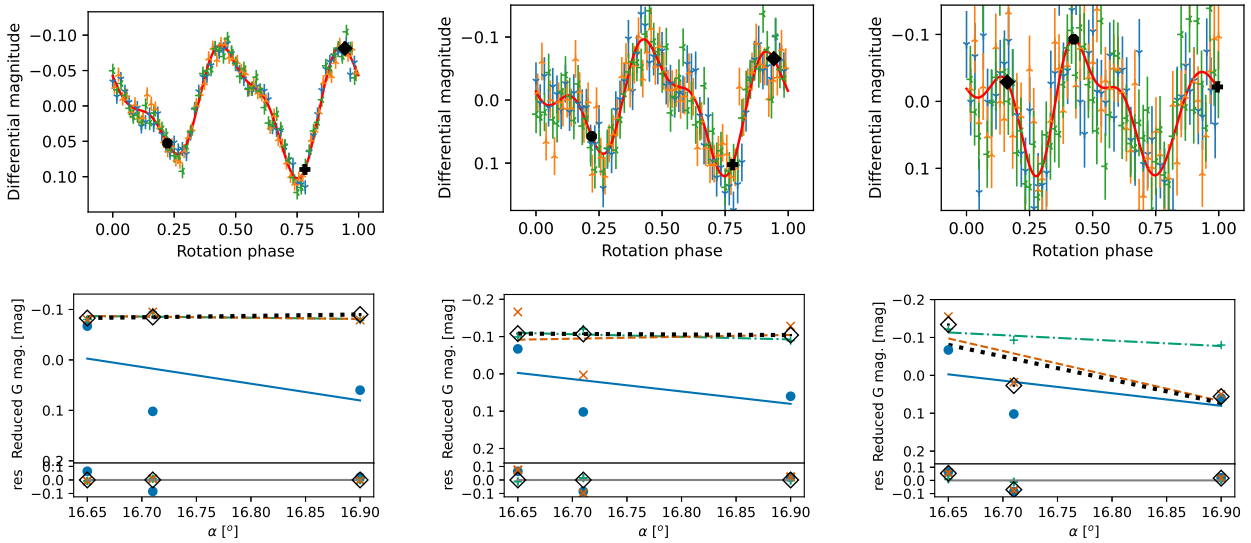		

Appendix C

Publication III: Wilawer et al. (2024)

Monthly Notices of the ROYAL ASTRONOMICAL SOCIETY

MNRAS **531,** 2802–2816 (2024) https://doi.org/10.1093/mnras/stae1282
Advance Access publication 2024 May 30

Phase curve wavelength dependency as revealed by shape- and geometry-corrected asteroid phase curves

E. Wilawer [1]★ K. Muinonen,[2] D. Oszkiewicz [1] A. Kryszczyńska[1] and M. Colazo [1]

[1]*Astronomical Observatory Institute, Faculty of Physics, Adam Mickiewicz University, ul. Słoneczna 36, 60-286 Poznań, Poland*
[2]*Department of Physics, University of Helsinki, PO Box 64, FI-00014 Helsinki, Finland*

Accepted 2024 May 10. Received 2024 April 15; in original form 2023 November 20

ABSTRACT

We investigate the photometric properties of 35 well-observed asteroids using dense ground-based and sparse ATLAS survey data. Focusing on two-colour photometric phase functions, derived using inverse methods, we explore the wavelength dependence. Our study reveals distinct (G_1, G_2) domains for cyan and orange filters, especially among some S-complex asteroids. For other asteroids, substantial uncertainties prevail, or their distributions of phase curve parameters overlap, precluding definitive conclusions on wavelength dependence. Notably, for S-complex objects, the effect appears systematic, characterized by lower G_2 values in the cyan filter. The effect can be explained by considering the known geometric albedo correlation: higher albedo corresponds to flatter, whereas lower albedo corresponds to steeper phase curves. In the case of equal albedo, asteroids with red spectral slopes have a more pronounced opposition effect in red and asteroids with blue spectral slopes in blue filters. We explore the variation of slope differences of orange and cyan phase curves with phase angle. For most asteroids, the largest nominal variation is observed at phase angles $< 10^\circ$. This suggests that the phase colouring for the orange–cyan colour slope is more pronounced at small phase angles. Through meticulous analysis of the opposition effect amplitudes, we also pinpoint preferred rotational pole solutions. We identify inconsistencies between phase curve parameters and spectral types in specific cases. The shape- and geometry-corrected phase curves signify an important advancement in studying asteroid photometric behaviour and may offer a deeper understanding of surface and regolith properties previously obscured by these effects, such as surface roughness.

Key words: techniques: photometric – minor planets, asteroids: general – catalogues.

1 INTRODUCTION

Asteroids are small rocky bodies in our Solar System. In general, they have an irregular shape, are covered by regolith, and typically rotate about their principal axis of inertia.

Over the years, asteroid photometry has been a successful technique for the study of these objects. On one hand, asteroid light curves allow us to calculate the rotation periods of asteroids and estimate their shapes and states of spin. On the other hand, by studying their phase curves, one can determine the variation of the disc-integrated brightness in time and phase angle (the Sun-asteroid-observer angle).

Various phase function models have been developed to describe this dependence. The H, G phase function (Bowell et al. 1989) was adopted by the International Astronomical Union in 1985. The H, G system works well for describing phase curves in wide phase angle ranges, but cannot accurately fit the opposition effect, especially for very dark or bright objects (Belskaya & Shevchenko 2000). The IAU decided to replace the old H, G system with the H, G_1, G_2 system (Muinonen et al. 2010b) as their recommended tool in 2012. Penttilä et al. (2016) introduced a two-parameter function known as H, G_{12}^*. This function was designed to address potential bias issues that could arise when utilizing the existing H, G_1, G_2 fitting procedure, especially when dealing with low-accuracy observations that exhibit significant variations in magnitude. None the less, there are situations in which the quantity of observations is limited, making it challenging to employ either the three-parameter or two-parameter model. In such instances, the authors suggest employing a one-parameter H-function. To execute this fitting, average values of the G_1 and G_2 or G_{12} parameters are employed based on the object's taxonomic class. Several photometric models have been introduced to provide a better representation of phase curves: Hapke's (Hapke 2002, 2008, 2012), Akimov's (Akimov 1975, 1979, 1988), and Shkuratov model (Shkuratov et al. 2011).

The photometric phase curve can provide valuable insight into the asteroid's surface properties, including geometric albedo, composition, porosity, roughness, and the distribution of grain sizes. For instance, when observing asteroids at phase angles greater than 10°, steep phase curves are indicative of objects with low albedo and exposed regolith. Conversely, flat phase curves may suggest high-albedo objects with a significant amount of light scattering within their regolith (Oszkiewicz et al. 2012).

At smaller phase angles, we observe the so-called opposition effect, characterized by a non-linear increase in asteroid brightness as it approaches phase angles close to zero. According to our current understanding, two primary mechanisms contribute to this phe-

★ E-mail: wilawerek@amu.edu.pl

nomenon: shadow-hiding and coherent backscattering (Muinonen et al. 2010a). Shadow-hiding occurs as an asteroid approaches solar opposition because shadows cast by surface irregularities become less visible from the observer's perspective. In contrast, coherent backscattering is a phenomenon where light beams taking different optical paths to reach the observer interfere constructively. This effect becomes particularly pronounced as the asteroid approaches solar opposition and dominates in the case of high-albedo surfaces (Belskaya & Shevchenko 2000; Muinonen et al. 2002; Dlugach & Mishchenko 2013).

By comparing the colour indices (or spectra) of an object taken at the different phase angles, one can observe a phase-colouring effect also called wavelength dependency. Specifically, for most objects, with increasing phase angle, the brightness observed at longer wavelengths decreases less significantly than at shorter wavelengths, thus a reddening effect is observed. This behaviour was observed in many Solar System objects such as Moon (Gehrels, Coffeen & Owings 1964), asteroids (Clark et al. 2002; Reddy et al. 2012; Schröder et al. 2012; Li et al. 2013; Le Corre et al. 2023), or comets (Fornasier et al. 2020). A similar effect was recently found by Ayala-Loera et al. (2018) and Alvarez-Candal et al. (2019) for transneptunian objects (TNOs). The authors found a strong anticorrelation between the absolute colour H_V–H_R and the corresponding photometric phase function slope differences. In particular, the redder objects were found to have steeper phase curves in the R filter, whereas the bluer objects had steeper phase curves in the V filter.

Additionally, the photometric phase curve can act as an indicator of an asteroid's taxonomic type, especially when spectral data are unavailable (Penttilä et al. 2016; Shevchenko et al. 2016, 2021). This connection between phase curve shape and taxonomy has been extensively investigated. Lagerkvist & Magnusson (1990) conducted a comprehensive analysis, determining absolute magnitudes and parameters for 69 asteroids using the H, G magnitude system. They calculated mean values of the G parameter for the S, M, and C taxonomic classes, highlighting the variability of the G parameter across these classes. Harris & Young (1989) examined mean slope parameter values for different taxonomic groups, contributing to the understanding of this relationship. Oszkiewicz et al. (2012) approximated the G_{12} distributions for taxonomic complexes using a Gaussian distribution and concluded that while G_{12} is related to surface characteristics, it is often insufficient to uniquely assign a taxonomic complex to individual asteroids. However, in some instances, G_{12} values can provide clues about asteroid taxonomic complexes, with the C complex being the most distinguishable. Shevchenko et al. (2016) determined the parameters of the H, G_1, G_2 magnitude systems for the main asteroid types. In more recent work, Mahlke, Carry & Denneau (2021) investigated the feasibility of conducting taxonomy based on photometric systems H, G_1, G_2, and H, G_{12}^*, using data from Asteroid Terrestrial-impact Last Alert System (ATLAS; Heinze et al. 2018). Their study concluded that the H, G_{12}^* model, when applied to serendipitous observations, does not effectively categorize target taxonomy. Conversely, the parameters characterizing H, G_1, G_2 phase curves contain substantial taxonomic information, even when observations are sparse. For example, asteroid classifications characterized by medium to high albedo, such as S-, M-, and E-types, tend to cluster in regions of small photometric slopes, while low-albedo B-, C-, D-, and P-types present much larger slopes.

Traditionally, asteroid photometry was performed with ground-based telescopes, organizing extensive observational campaigns to obtain densely sampled light curves. For example, Groeneveld & Kuiper (1954) initiated a thorough investigation of the brightness of asteroids at the McDonald Observatory, which led to the publication of a ten-part scientific series. In the fifth paper in this series, Gehrels (1956) sets out to find an accurate magnitude–phase relation, especially for small phase angles. The author decided to work with the asteroid (20) Massalia since during his observations, it reached phase angle values very close to zero. Years later, Gehrels & Tedesco (1979) published the absolute magnitudes and phase coefficients of 60 asteroids observed in surveys at McDonald and Palomar Observatories (van Houten et al. 1970). Harris & Young (1983, 1989), on the other hand, reported 85 phase curves obtained in an exhaustive observing campaign at the Table Mountain Observatory. Oszkiewicz et al. (2021) presented well-determined phase curves for 20 V-type asteroids for the first time. A limitation of this practice (construct phase curves from dense light curve data) is the fact that it is rather time-consuming to extend it to a sample of several thousand asteroids. Specifically, Pravec et al. (2012) and Shevchenko et al. (2022) obtained catalogues of phase curve parameters for 583 and 400 objects, respectively, over observing campaigns spanning approximately three decades each.

Nowadays, thanks to large photometric surveys, a vast amount of data on asteroid populations is available. For example, the catalogue of Solar System objects of *Gaia* DR2 (Spoto et al. 2018) and DR3 (Riello et al. 2021; Tanga et al. 2023) contains more than 160 000 objects, even though the mission was not designed to observe Solar System objects, but to observe stars in the Milky Way. *Gaia* DR2 contains observations of 14 000 asteroids, while *Gaia* DR3 has data on 156 801 asteroids. On the other hand, the Sloan Digital Sky Survey (York et al. 2000) was a photometric and spectroscopic survey designed to study extragalactic objects. The final version of the Moving Object Catalogue (MOC; Ivezić et al. 2001) includes 471 569 objects in our Solar System (out of which 104 449 were linked to known asteroids), obtained from December 2001 to March 2007. The *Transiting Exoplanet Survey Satellite* (*TESS*) mission (Woods et al. 2021), designed to find exoplanets around nearby stars, provided more than 10 million observations of some 42 000 Solar System objects. In addition, there are also surveys designed to study asteroids, such as Lincoln Near-Earth Asteroid Research (LINEAR; Stokes et al. 2000), Pan-STARRS (Chambers & Pan-STARRS Team 2018), and the aforementioned ATLAS.

Several authors conducted research on phase curves using sparse data gathered from surveys, including the ones mentioned above and others. Oszkiewicz et al. (2011) employed recalibrated data from the Minor Planet Center to fit phase curves for approximately 500 000 asteroids. Waszczak et al. (2015) applied a combined rotation and phase function model to fit 54 296 sparsely sampled asteroid light curves from the Palomar Transient Factory survey. Vereš et al. (2015) employed a Monte Carlo technique to calculate the absolute magnitudes and slope parameters of 240 000 asteroids observed by the Pan-STARRS1 telescope. Ďurech et al. (2020) studied the phase curves of 2750 asteroids by applying the light curve inversion to ATLAS data. Mahlke et al. (2021) retrieved the absolute magnitudes and slope parameters of 94 777 asteroids in two photometric bands using Bayesian parameter inference. Alvarez-Candal et al. (2022) processed the SDSS multifilter photometry to obtain ∼15 000 phase curves in various photometric bands.

However, these vast catalogues also have a disadvantage: the fact that they contain sparse data, results in poorly constrained viewing geometry of the object at the time of observation. The consequence of this lack of information is that the points of maximum brightness at each epoch will not necessarily correspond to the maximum of the light curve. Therefore, they would not constitute a consistent data set if one wants to compare phase curves of different asteroids

(Martikainen et al. 2021). Furthermore, Shevchenko et al. (2022) found systematic biases in absolute magnitudes derived based on sparse survey data as compared to precise ground-based photometry and Jackson et al. (2022) demonstrated the influence of the asteroid shape on the derived phase curves.

One solution to take advantage of the strengths (and overcome the disadvantages) of both types of data is to combine them. This type of analysis has already been carried out in the past. Colazo, Duffard & Weidmann (2021) combined *Gaia* sparse photometry with dense data from the Asteroid Photometric Catalogue (APC; Lagerkvist et al. 1995), using the mean of the *Gaia* magnitudes in the case of more than one transit per Julian day. One limitation of this approach is that the APC photometric data pertain to light curves published up to 1993, whereas the *Gaia* DR2 observations span from 2014 to 2016. Consequently, we are constructing phase curves using data obtained under different observing geometries. On the other hand, Wilawer et al. (2022) introduced a method for deriving asteroid phase curves by combining sparse photometric data with differential ground-based photometry. They utilized sparse photometry data from *Gaia* and differential photometry data from the Astronomical Observatory Institute of Adam Mickiewicz University in Poznań collected during the *Gaia* DR2 era, ensuring similar aspect angles and viewing geometries (observations conducted between 2014 and 2016). The differential ground-based photometry, along with absolute *Gaia* measurements, was integrated to determine the rotational phases corresponding to the *Gaia* data points. The interpolated maximum brightness values from *Gaia* data points taken at various phase angles were then employed in constructing the phase curves.

In this paper, we combine dense ground-based observations with sparse ATLAS photometry. It is worth noting that ATLAS magnitudes are absolute and ground-based photometry is differential. Moreover, they might cover different ranges of phase angles, requiring different phase function models (Muinonen et al. 2022). In order to merge both data sets and obtain phase curves suitable for direct comparisons between objects, we calculate the phase curve of a spherical object with surface properties equivalent to that of the asteroid thus removing the effects of shape and viewing geometry (Muinonen et al. 2020, 2022; Martikainen et al. 2021).

In this work, we determine phase curves of 35 asteroids based on a combined dense ground-based and sparse survey data using the method of Muinonen et al. (2020, 2022). In Section 2, we discuss the data utilized in this study. Section 3 summarizes the phase curve computation method and its adaptation to a supercomputer. The results are presented in Section 4 and the conclusions are presented in Section 5.

2 DATA

In this work, we use dense differential ground-based data for deriving asteroid models and to generate the proposal density for the sidereal rotational period and spin axes coordinates. Next, the sparse ATLAS data were used to calculate the phase function parameters assuming fixed shapes. Such set of data sources was chosen because ATLAS data alone are not sufficient to determine an accurate model with the precision required for this research.

We utilized differential ground-based photometric observations collected at the Astronomical Observatory Institute of Adam Mickiewicz University in Poznań. Our primary focus is on determining the parameters of the photometric phase functions H, G_1, G_2. Therefore, our criteria for selecting the asteroids we investigated in this work included having a well-defined object model, accurately determined periods and pole coordinates, as well as the availability of photometric data used to establish this model. These accurate parameters are required to remove the influence of the object shape and the observing geometry from the phase curves. After reviewing the literature, we selected 35 asteroids from 11 publications: Hanus et al. (2013), Kryszczyńska (2013), Marciniak et al. (2008, 2009a, b, 2011, 2012, 2018, 2019, 2021), and Oszkiewicz et al. (2019).

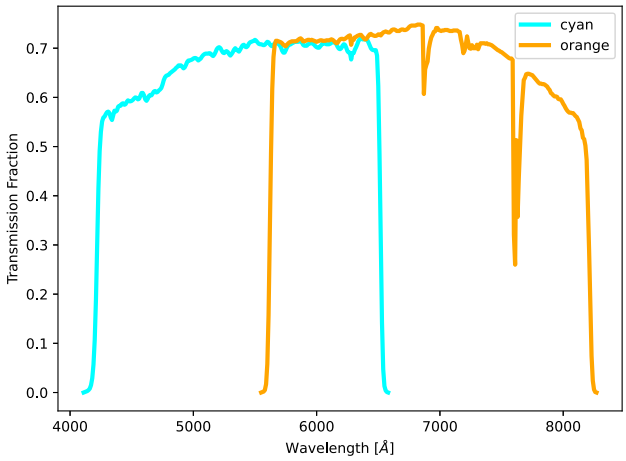

Figure 1. Transmission curves for cyan and orange ATLAS filters (Rodrigo & Solano 2020).

For deriving phase curve parameters, we made use of the ATLAS survey photometry. The ATLAS sky survey aims to detect near-Earth asteroids (NEAs) and consists of a total of four telescopes located at Haleakalā (operational since 2015) and Mauna Loa (operational since 2017) in Hawaii, El Sauce Observatory in Chile, and Sutherland Observing Station in South Africa (both operational since 2022) (Heinze et al. 2018). Observations are conducted using two distinct filters: cyan (420–650 nm) and orange (560–820 nm). The precise transmission characteristics of these filters are depicted in Fig. 1. Since its inception, the ATLAS survey has observed over 150 000 asteroids. We obtained dual-band photometric data from the ATLAS Solar System Catalogue (SSCAT) Version 1 (Denneau et al. 2022). After filtering the data for objects outside our area of interest, we were left with a total of 78 299 observation points. Typically, for a given object, the number of observations in the orange filter is three times greater than in the cyan filter.

The software we used for our calculations required us to format our observational data in the manner used by the DAMIT data base (Durech, Sidorin & Kaasalainen 2010). This necessitated adding the Sun's and Earth's ecliptic asteroid-centric Cartesian coordinates (x, y, z) in au to the original ATLAS photometric data for each observation point.

Table 1 contains a summary of the data used for the completed calculations, presenting the rotation period, pole solutions, data source, the number of dense ground-based observations, as well as the number of observations, and the minimum and maximum phase angle for each ATLAS filter.

3 METHODS

3.1 Asteroid forward model

The Lommel–Seeliger surface reflection coefficient is utilised for the modelling of light scattering in asteroid surfaces (Muinonen et al.

Table 1. Period, ecliptic longitude (λ), and latitude (β) for one or two pole solutions, data origin, number of ground-based dense light curves, number of observations, minimum and maximum phase angles in cyan and orange ATLAS filters.

Asteroid	Period [h]	λ_1 [°]	β_1 [°]	λ_2 [°]	β_2 [°]	Reference	dense n_{lc}	cyan n_{obs}	cyan α_{min} [°]	cyan α_{max} [°]	orange n_{obs}	orange α_{min} [°]	orange α_{max} [°]
(73) Klytia	8.283 070	44	83	266	68	1	21	214	1.56	23.18	995	1.05	23.24
(94) Aurora	7.226 191	58	16	242	4	2	21	241	2.71	20.33	650	3.15	20.22
(127) Johanna	12.799 530	98	−60	261	−70	3	33	285	4.65	22.75	806	1.05	22.85
(159) Aemilia	24.47 8690	139	68	348	59	4	45	298	1.22	20.74	1003	1.22	20.73
(174) Phaedra	5.750 249	266	5			2	36	297	1.08	23.76	655	0.89	24.06
(195) Eurykleia	16.521 780	101	71	352	83	5	51	272	2.18	21.35	768	2.34	21.35
(202) Chryseis	23.670 200	94	−49	261	−34	6	70	233	2.29	20.32	760	2.48	20.90
(219) Thusnelda	59.710 600	300	−66			6	116	226	1.47	32.79	790	1.25	32.82
(223) Rosa	20.277 200	22	18	203	26	6	58	231	1.25	19.56	896	0.32	20.17
(301) Bavaria	12.240 900	226	70	46	61	5	30	248	2.75	23.37	891	1.57	23.26
(335) Roberta	12.027 130	105	48	297	54	5	52	213	2.42	28.28	919	0.26	28.39
(350) Ornamenta	9.180 410	184	−29			7	37	272	8.12	21.64	777	4.76	21.62
(352) Gisela	7.480 082	16	−40	201	−43	8	26	218	2.91	30.73	894	1.59	30.72
(355) Gabriella	4.828 994	159	88	341	83	3	16	217	1.38	25.76	975	1.93	25.75
(377) Campania	11.664 400	47	67	196	66	1	34	185	3.23	23.50	917	0.77	23.51
(378) Holmia	4.440 425	130	60	286	76	1	13	284	1.75	21.86	906	1.04	23.68
(380) Fiducia	13.717 200	202	44	21	34	5	37	269	2.81	25.09	833	1.15	25.11
(435) Ella	4.622 802	59	64	247	58	3	18	232	2.06	28.90	919	1.24	28.91
(468) Lina	16.478 380	74	68	255	68	5	40	218	0.89	23.40	860	0.07	23.53
(483) Seppina	12.720 980	356	60	127	47	6	56	268	2.48	18.21	935	1.81	18.20
(487) Venetia	13.341 330	78	3	252	3	4	34	237	5.08	23.62	827	2.22	23.94
(501) Urhixidur	13.172 030	49	84	262	66	6	61	310	5.49	21.23	775	5.61	21.24
(538) Friederike	46.739 900	328	−59	168	−58	5	98	270	2.88	21.79	934	0.96	22.03
(747) Winchester	9.414 807	166	−44	296	−61	9	44	213	5.00	29.27	771	4.46	29.47
(770) Bali	5.818 942	68	50	262	45	8	21	275	0.56	31.42	644	0.13	31.47
(771) Libera	5.890 423	64	−78			7	20	196	4.28	28.95	952	2.69	29.16
(800) Kressmannia	4.460 971	156	56	328	59	8	28	220	0.94	32.24	724	0.53	32.23
(834) Burnhamia	13.875 940	77	60	256	69	5	32	303	0.96	22.85	865	1.14	23.23
(849) Ara	4.116 391	10	−25	223	−40	9	20	235	5.07	23.00	878	5.47	22.98
(923) Herluga	29.728 200	218	−68	334	−53	6	51	175	5.08	27.22	883	2.16	27.61
(995) Sternberga	11.195 110	27	−20	222	−26	6	75	249	1.99	27.74	976	1.61	27.76
(1088) Mitaka	3.035 300	125	−53	285	−66	8	20	254	3.30	31.70	664	2.34	31.68
(1130) Skuld	4.807 640	25	42	200	36	10	28	238	1.02	33.83	658	0.28	34.07
(1219) Britta	5.575 565	164	−79			8	25	231	3.44	28.88	737	0.44	29.09
(2579) Spartacus	3.636 028	312	−57	113	−60	11	37	204	2.74	29.47	727	2.86	29.67

Notes. List of references: 1. Marciniak et al. (2008); 2. Marciniak et al. (2011); 3. Marciniak et al. (2012); 4. Marciniak et al. (2018); 5. Marciniak et al. (2019); 6. Marciniak et al. (2021); 7. Marciniak et al. (2009b); 8. Kryszczyńska (2013); 9. Marciniak et al. (2009a); 10. Hanus et al. (2013); 11. Oszkiewicz et al. (2019).

2022):

$$R_{LS}(\mu, \mu_0, \phi) = 2p\Phi_{11}(\alpha)\frac{1}{\mu + \mu_0},$$
$$\mu_0 = \cos\iota,$$
$$\mu = \cos\epsilon, \quad (1)$$

where p is the geometric albedo, α is the phase angle, ι and ϵ are the angles of incidence and emergence, respectively, measured from the outward normal vector of a surface element, and ϕ denotes the azimuth angle, with the Sun at $\phi = 0°$. The phase function Φ_{11} is expressed as the ratio

$$\Phi_{11}(\alpha) = \frac{\Phi(\alpha)}{\Phi_{LS}(\alpha)},$$
$$\Phi_{LS}(\alpha) = 1 - \sin\tfrac{1}{2}\alpha \tan\tfrac{1}{2}\alpha \ln(\cot\tfrac{1}{4}\alpha),$$
$$\Phi_{11}(0) = \Phi(0) = \Phi_{LS}(0) = 1, \quad (2)$$

where Φ_{LS} is the phase function corresponding to a spherical asteroid with isotropic single scattering $\Phi_{11} = 1$. The definition of Φ by equation (2) implies that Φ can then be modelled using the H, G_1, G_2 photometric phase function (Muinonen et al. 2010b), optimized to describe the observed disc-integrated phase curves of asteroids.

Alternatively, we can make use of a three-parameter linear-exponential model for Φ on the magnitude scale, supported by the observational evidence that asteroid phase curves tend to be linear at moderately large phase angles outside the angular regime of the opposition effect, $10° \leq \alpha \leq 50°$:

$$-2.5 \lg \Phi(\alpha) = -m_0 \exp\left(-\frac{\alpha}{\alpha_0}\right) + m_0 + \beta_0\alpha,$$
$$0° \leq \alpha \leq 50°, \quad (3)$$

where m_0 and α_0 are the amplitude and angular width of the opposition effect, respectively, and β_0 is a slope parameter expressed in [mag/rad] (Muinonen et al. 2020). In the linear-exponential model of equation (3), the photometric slope at $\alpha = 20°$ equals

$$\beta_S(20°) = \beta_0 + \frac{m_0}{\alpha_0}\exp\left(-\frac{20°}{\alpha_0}\right). \quad (4)$$

A useful two-parameter model follows by fixing α_0 to a reasonable value (e.g. $\alpha_0 = 3°$), leaving m_0 and β_0 as free parameters.

In this work, we derive the H, G_1, G_2 phase function in two colours, cyan (subscript c) and orange (subscript o), and, typically, for each asteroid we have two symmetrical pole solutions (subscripts 1 and 2), giving us four pairs of parameters, (G_{1c_1}, G_{2c_1}), (G_{1o_1}, G_{2o_1}), (G_{1c_2}, G_{2c_2}), and (G_{1o_2}, G_{2o_2}). In deriving the spin and shape solutions using dense ground-based lightcurves, the results are independent of the phase function. For simplicity, there we use the two-parameter linear-exponential phase function.

In the case of the convex shape model, the parameters (unknowns) of the forward model are

$$\mathbf{P} = (P, \lambda, \beta, \varphi_0, s_{00}, \ldots, s_{l_{\max} l_{\max}}, G_1, G_2)^T, \tag{5}$$

where the parameters are, respectively, the rotation period, ecliptic pole longitude, ecliptic pole latitude, rotational phase at a given epoch t_0, the $(l_{\max}+1)^2 - l_{\min}^2$ spherical harmonics coefficients $s_{00}, \ldots, s_{l_{\max} l_{\max}}$ for the Gaussian surface density of the shape $l_{\max}$ and $l_{\min}$ denoting the maximum and minimum degrees), and the two H, G_1, G_2 phase function parameters. Here, the rotational phase φ_0 and the real-valued s_{00} are fixed as φ_0 is accounted for by the spherical harmonics coefficients, and the asteroid size information is omitted. Consequently, the total number of free parameters equals

$$N_{\mathrm{P}} = (l_{\max}+1)^2 - l_{\min}^2 + 4. \tag{6}$$

3.2 Inverse methods

The formulation of the inverse problem in terms of Bayesian inference in magnitude space, together with the observational error model, is described in detail by Muinonen et al. (2022). Likewise, a random walk Markov chain Monte Carlo method (MCMC) for characterizing the multidimensional probability density of the free parameters is thoroughly assessed by Muinonen et al. (2020). They give an MCMC proposal probability density based on the least squares solutions for virtual observations that they derive from the original observations by adding Gaussian random errors.

The present inverse problem includes a new MCMC processing method, due to the photometry in two colours requiring a separate treatment. Whereas the optimum solution would comprise sampling the spins, shapes, and photometric phase functions in several colours simultaneously using all existing observations, we have introduced a method that solves the inverse problems in two parts. First, we solve the inverse problem concerning the spin and shape parameters for the dense, differential ground-based photometry, without modelling the photometric phase function (using the linear-exponential model just to enable the computations). Secondly, we use the spin and shape solutions of the previous part in an additional MCMC treatment that samples both the photometric parameters (G_1, G_2) and the spin and shape parameters. For sampling (G_1, G_2), we make use of independent univariate Gaussian proposal densities for G_1 and G_2. At the same time, we sample the spin and shape parameters from the existing set of MCMC solutions. We carry out the processing separately for the cyan and orange photometry and obtain MCMC samples of (G_{1c}, G_{2c}) and (G_{1o}, G_{2o}). The present approach filters the spin and shape solutions for each colour. Compared to the optimum solution outlined above, the caveat is the fact that not all existing data points are utilized to obtain the best possible spins and shapes. However, we expect that (G_{1c}, G_{2c}) and (G_{1o}, G_{2o}) are treated in a satisfactory way with the present method.

The workflow of the inverse problem solution is described in Fig. 2. Initial spin parameters are taken from the literature (Table 1) and the initial shape parameters are entered as realistic ellipsoid axial ratios. The entire processing begins with an initial treatment of the photometric light curves (LCSPLI). The light curves are classified as differential or absolute, and as dense or sparse (based on the initial rotation period), resulting in four classes of data. Cubic spline fits with statistically determined numbers of nodes (based on the Bayesian information criterion) are provided for dense light curves. Initial error models are assigned for the different classes of light curves on the basis of the RMS values of the spline fits to the dense light curves and input values for the sparse light curves.

Thereafter, the initial spherical harmonics coefficients of the Gaussian surface density are computed from the Gaussian surface density of the ellipsoid described by the input axial ratios (CXI -1). The next steps are the computation of the least squares solution with a simplified and fixed observational error model (CXI 01) and the iterative simultaneous refinement of the least squares solution and the error model (CXI 02). The output of the latter step constitutes the key to the forthcoming processing.

The large numbers of least squares solutions are then computed for the virtual light curves produced by adding Gaussian errors to the original light curves, involving a modification of the error model to account for the increased errors (CXI 03). These virtual solutions are then utilized in the random walk MCMC computations (CXI 05). Additional randomization using the Gaussian probability density is introduced along a line in the parameter phase space connecting two virtual solutions.

As described above, the sparse light curves in two colours are finally treated with the help of MCMC spin and shape solutions from dense ground-based light curves (CXI 06). Finally, parameter statistics are computed in order to describe the MCMC solutions obtained (MCSTAT).

3.3 Adaptation to a supercomputer

The method described in Section 3 is highly demanding in terms of computational power. Consequently, all our calculations using LCI software were executed at the Poznań Supercomputing and Networking Center (PCSS). LCI comprises multiple modules, and output files from one module are often used as input files for the subsequent module. To streamline the computations, we created BASH wrapper scripts that invoke the respective LCI modules step by step and oversee file management.

The entire course of a single experiment (a set of computations for a given object, with the initial period and pole positions specified, for the cyan and orange ATLAS filters) is depicted in Fig. 2. The red rounded rectangles define the starting and ending points of a workflow diagram. The rectangular elements represent steps in the process or actions to be taken: the green elements correspond to LCI modules, while the grey ones signify operations on files. It should be noted that the CXI 05, which modifies the content of the *par.out* file, and the CXI 06 steps are executed in parallel $N = 5$ times, after which the output files (*mcmc1.out* and *mcmc2.out*) from all CXI 06 threads are consolidated into single files, subsequently serving as input files for MCSTAT. Trapezoids indicate inputs or outputs of data within a workflow process. Among them, the following are notable: purple represents dense observations (used in steps from LCSPLI through CXI 05), cyan represents sparse ATLAS data in the cyan filter, and orange represents sparse ATLAS data in the orange filter (both of the latter two are used in CXI 06). Furthermore, the CXI 06 step requires modification of the *par.out* file generated in the CXI 02 step. In the CXI 06 step, there is a change in the fitted photometric function from linear-exponential to H, G_1, G_2. As a result, the initial parameter values of the phase curve need to be altered in the *par.out* file.

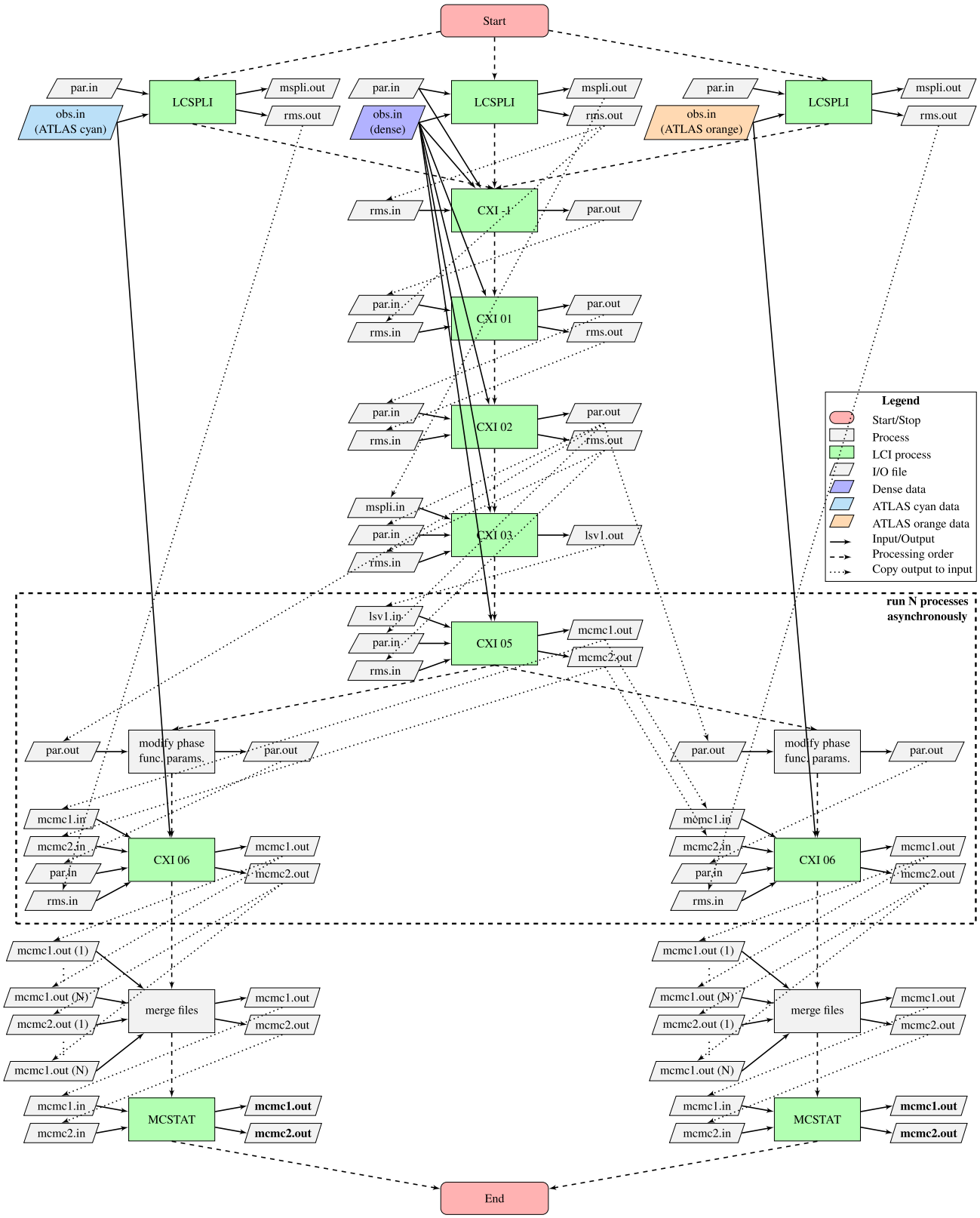

Figure 2. LCI computations flowchart. The red rounded rectangles define the starting and ending points of a workflow diagram. The rectangular elements represent steps in the process or actions to be taken: the green elements correspond to LCI modules, while the grey ones signify operations on files. Solid lines with arrows connect input and output files with their respective processes, while dashed lines indicate the step-by-step computational process, and dotted lines represent the copying of output files, serving as input files for the subsequent process.

Solid lines with arrows connect input and output files with their respective processes, while dashed lines indicate the step-by-step computational process, and dotted lines represent the copying of output files, serving as input files for the subsequent process.

For each asteroid, for both spin vectors (when applicable), we conducted an extensive analysis by generating 1000 virtual least squares solutions. Subsequently, 5000 MCMC samples were generated for each of the ATLAS filters based on these solutions. It is important to note that this study imposed significant computational demands, requiring more than 170 000 hours of computations. Due to time constraints on the cluster, a portion of the calculation remained unfinished, as the time required for completion exceeded the specified maximum time limit for a single job.

4 RESULTS

We obtained pairs of G_1 and G_2 photometric phase function parameters in both cyan and orange ATLAS filters, typically for two symmetric pole solutions. The results, along with the Tholen taxonomic class (supplemented by SMASSII when not available) from the Planetary Data System (Tholen 1989; Bus & Binzel 2002; Neese 2017) and the geometric albedos from the Asteroid Catalog using AKARI (Usui et al. 2013), are summarized in Table 2. Both supplementary catalogues were chosen because their data covered the largest portion of our asteroids set out of available catalogues. Furthermore, AKARI albedos have lower uncertainties for the objects studied compared to IRAS (Tedesco et al. 2004) and NEOWISE (Mainzer et al. 2019).

We illustrate the results for three different example asteroid cases (figures for the remaining objects are given in the supplementary material available online). Figs 3, 6, and 9 show the derived distributions of the parameters G_1 and G_2 in the cyan and orange filters for two symmetric sets of initial pole coordinates, together with the mean values and their standard deviations for each distribution (crosses). Figs 4, 7, and 10 show the phase curves for the mean values derived from the G_1 and G_2 distributions, while the absolute magnitude H is set to 0. The bottom row of these figures illustrates the colour slope. The colour slope was derived as the difference of the derivatives of the photometric phase function H, G_1, G_2 with respect to the phase angle in the orange and cyan filters. Shaded envelopes represent 1σ uncertainties. By comparison of slopes in both filters, one can observe a reddening or blueing effect at small phase angles (solid red and dashed blue lines on the plots, respectively). Note that, at phase angles larger than 10^o, the colour slope value is almost zero, so the effect is negligible. The effect may be more pronounced for phase curves in filters that are more separated in wavelengths.

Figs 5, 8, and 11 show $G_\perp = \frac{1}{2}(G_1 + G_2)$ and $G_\parallel = \frac{1}{2}(G_1 - G_2)$ parameters values computed from mean values of G_1 and G_2 parameters with uncertainties for two pole solutions in cyan and orange ATLAS filters. Dotted blue and dashed red diagonal lines indicate consecutive values of parameters G_1 and G_2, respectively, while the solid green line shows consecutive G_{12} values.

Asteroid (73) Klytia (Figs 3, 4, and 5) exhibits a Gaussian-like distribution of the parameters G_1 and G_2. The noticeable differences in accuracy and the size of the distributions are caused by a significant disparity in the number of observations in the cyan filter (214) and the orange filter (995). Both of the initial pole coordinates lead to similar and realistic phase function parameter values, well in agreement with the spectral S-type. A maximum absolute colour slope of about 0.06 $\frac{mag}{deg}$ is observed for a phase angle of 0.26°.

Asteroid (435) Ella (Figs 6, 7, and 8) shows less constrained distributions; however, the majority of the probability mass is concentrated within a well-defined Gaussian-like region. The distribution of the G_1 and G_2 parameters for the two different passbands are clearly separated from each other, highlighting the colour dependence of the phase curve. Both sets of initial pole coordinates produce identical and realistic values for G_1 and G_2 in the respective filters. Additionally, the maximum colour slope of approximately 0.18 $\frac{mag}{deg}$ occurs at a phase angle of 0.25°.

The asteroid (487) Venetia (Figs 9, 10, and 11) shows a strongly non-Gaussian distribution for the cyan filter and more constrained in orange. Additionally, the values of the G_1 and G_2 parameters obtained for the two initial pole coordinates differ significantly from each other, resulting in distinct phase curves and a colour slope of as high as 0.65 $\frac{mag}{deg}$. Marciniak et al. (2018) highlight that the pole solution with $\lambda = 252°$ and $\beta = 3°$ (right column in Fig. 9) is the preferred solution. Our results show an unrealistic opposition effect for the first solution and therefore are consistent with Marciniak et al. (2018) and complement the preferred solution. This is the only case in our current study where the obtained phase curves exhibit such significant differences between the pole coordinates.

Based on the combined results obtained for all asteroids, 3 conclusions can be drawn:

(i) Some of the MCMC results are particularly good in separating the different G_1, G_2 domains for different filters highlighting the phase curve wavelength dependence. Most of the asteroids fitting this category belong to the S-complex [e.g. (73) Klytia, (174) Phaedra, (352) Gisela, (355) Gabriella, (378) Holmia, (483) Seppina, (770) Bali, (771) Libera, (800) Kressmannia, (995) Sternberga]. For other asteroids, significant uncertainties persisted or their distributions of phase curve parameters overlapped, making it difficult to draw definitive conclusions regarding wavelength dependence. For the studied S-types, this effect appears to be systematic, with smaller G_2 values observed in the cyan filter. This phenomenon can be elucidated by taking into account the established albedo correlation: objects with higher albedos display flatter phase curves, whereas those with lower albedos demonstrate steeper phase curves. Specifically, S-complex asteroids have lower albedos in the cyan filter than in the orange filter, leading to steeper phase curves in the cyan filter. In contrast, for C-complex asteroids, the disparities in albedos between the two filters are less significant, posing a greater challenge in distinguishing the effect in the phase curve parameter space.

(ii) For double-pole cases, where the corresponding G_1, G_2 domains overlapped for the two poles, we only indicate that they were determined correctly, even if the poles remain uncertain.

(iii) In double-pole cases, if the corresponding domains of G_1, G_2 differ, the parameters align with the pole solution. This may suggest the possible existence of a preferred pole solution (as described in the case of (457) Venetia, more on this in further detail later).

We further explore the relationship between the parameters G_1 and G_2, in relation to the taxonomic classes of Tholen (Tholen 1989) as shown in Fig. 12. The black curve illustrates the theoretical relationship between the parameters G_1 and G_2 as presented in Muinonen et al. (2010b). The dashed lines represent the boundaries for realistic phase curve parameters. The upper boundary is derived from $G_1 + G_2 \leq 1$, the lower boundary assumes that the opposition effect is not greater than a factor of 2, thus $G_1 + G_2 \geq \frac{1}{3}$. Two solutions (for asteroids (487) Venetia and (849) Ara) lie outside those boundaries and thus correspond to the less preferred rotational pole. Furthermore, one can observe a division into two clusters corresponding to objects with steep and shallow photometric slopes (low- and high-albedo objects). These clusters correspond to two broad classes, namely the C-complex and the S-complex, encompassing asteroids

Table 2. Computed mean values G_1 and G_2 with associated uncertainties from both cyan and orange ATLAS filters, obtained using one or two pole solutions (described in Table 1). The Tholen taxonomic class, supplemented by SMASSII (indicated by an asterisk) when not applicable, is referenced from (Neese 2017), and albedo values are sourced from the AKARI mission catalogue (Usui et al. 2011).

				cyan		orange	
				G_1	G_2	G_1	G_2
Asteroid	Taxa	Albedo	Solution				
(73) Klytia	S	0.217 ± 0.006	1	0.321 ± 0.077	0.320 ± 0.024	0.349 ± 0.029	0.358 ± 0.009
			2	0.288 ± 0.058	0.349 ± 0.019	0.347 ± 0.028	0.368 ± 0.009
(94) Aurora	CP	0.053 ± 0.003	1	0.114 ± 0.091	0.376 ± 0.039	0.588 ± 0.141	0.282 ± 0.037
			2	0.590 ± 0.120	0.085 ± 0.040	0.813 ± 0.168	0.061 ± 0.043
(127) Johanna	CX	0.065 ± 0.002	1	0.453 ± 0.174	0.114 ± 0.040	0.528 ± 0.057	0.158 ± 0.017
			2	0.460 ± 0.185	0.120 ± 0.042	0.491 ± 0.071	0.150 ± 0.025
(159) Aemilia	C	0.059 ± 0.003	1	0.627 ± 0.076	0.091 ± 0.029	0.684 ± 0.047	0.081 ± 0.017
			2	0.620 ± 0.065	0.075 ± 0.026	0.561 ± 0.037	0.116 ± 0.013
(174) Phaedra	S	0.187 ± 0.005	1	0.359 ± 0.056	0.392 ± 0.016	0.125 ± 0.031	0.428 ± 0.010
(195) Eurykleia	C	0.055 ± 0.002	1	0.381 ± 0.048	0.182 ± 0.016	0.671 ± 0.073	0.105 ± 0.023
			2	0.543 ± 0.106	0.129 ± 0.033	0.746 ± 0.085	0.069 ± 0.026
(202) Chryseis	S	0.245 ± 0.007	1	–0.049 ± 0.076	0.435 ± 0.019	0.043 ± 0.039	0.443 ± 0.011
			2	0.169 ± 0.066	0.346 ± 0.017	0.133 ± 0.050	0.418 ± 0.013
(219) Thusnelda	S	0.184 ± 0.006	1	0.368 ± 0.049	0.301 ± 0.017	0.173 ± 0.030	0.396 ± 0.007
(223) Rosa	X	0.037 ± 0.002	1	0.798 ± 0.122	0.061 ± 0.046	0.967 ± 0.056	–0.002 ± 0.025
			2	0.807 ± 0.124	0.086 ± 0.045	1.023 ± 0.055	–0.034 ± 0.026
(301) Bavaria	C∗	0.060 ± 0.002	1	0.442 ± 0.091	0.147 ± 0.025	0.719 ± 0.067	0.085 ± 0.021
			2	0.387 ± 0.078	0.164 ± 0.022	0.709 ± 0.065	0.086 ± 0.020
(335) Roberta	FP	0.055 ± 0.002	1	0.878 ± 0.220	–0.003 ± 0.074	0.966 ± 0.091	0.001 ± 0.027
			2	0.725 ± 0.168	0.110 ± 0.051	0.775 ± 0.081	0.136 ± 0.023
(350) Ornamenta	C	0.058 ± 0.002	1	0.191 ± 0.143	0.190 ± 0.027	0.391 ± 0.189	0.175 ± 0.033
(352) Gisela	S	0.249 ± 0.008	1	0.144 ± 0.063	0.411 ± 0.014	0.194 ± 0.028	0.420 ± 0.007
			2	0.225 ± 0.057	0.397 ± 0.014	0.146 ± 0.028	0.432 ± 0.008
(355) Gabriella	S∗	0.207 ± 0.010	1	0.285 ± 0.048	0.339 ± 0.015	0.301 ± 0.032	0.352 ± 0.007
			2	0.313 ± 0.049	0.340 ± 0.016	0.300 ± 0.034	0.350 ± 0.008
(377) Campania	PD	0.057 ± 0.002	1	0.447 ± 0.097	0.139 ± 0.029	0.711 ± 0.053	0.084 ± 0.017
			2	0.403 ± 0.083	0.206 ± 0.022	0.553 ± 0.040	0.130 ± 0.014
(378) Holmia	S	0.261 ± 0.009	1	0.241 ± 0.039	0.325 ± 0.013	0.341 ± 0.027	0.288 ± 0.009
			2	0.239 ± 0.042	0.328 ± 0.015	0.295 ± 0.026	0.314 ± 0.008
(380) Fiducia	C	0.053 ± 0.002	1	0.478 ± 0.136	0.176 ± 0.032	0.662 ± 0.064	0.154 ± 0.016
			2	0.581 ± 0.103	0.152 ± 0.026	0.751 ± 0.094	0.123 ± 0.025
(435) Ella	DCX	0.106 ± 0.003	1	0.811 ± 0.074	0.169 ± 0.028	0.584 ± 0.042	0.165 ± 0.013
			2	0.814 ± 0.068	0.167 ± 0.027	0.626 ± 0.043	0.152 ± 0.013
(468) Lina	CPF	0.059 ± 0.002	1	0.800 ± 0.123	0.030 ± 0.048	0.638 ± 0.032	0.116 ± 0.014
			2	0.732 ± 0.100	0.057 ± 0.038	0.619 ± 0.031	0.121 ± 0.014
(483) Seppina	S	0.172 ± 0.004	1	0.159 ± 0.049	0.279 ± 0.016	0.235 ± 0.035	0.308 ± 0.009
			2	0.178 ± 0.056	0.268 ± 0.017	0.266 ± 0.038	0.291 ± 0.009
(487) Venetia	S	0.239 ± 0.008	1	–0.140 ± 0.208	0.372 ± 0.023	0.626 ± 0.069	0.337 ± 0.015
			2	0.382 ± 0.161	0.372 ± 0.024	0.210 ± 0.058	0.439 ± 0.012
(501) Urhixidur	unknown	0.079 ± 0.002	1	0.260 ± 0.083	0.149 ± 0.021	0.092 ± 0.139	0.192 ± 0.027
			2	0.255 ± 0.079	0.160 ± 0.026	0.475 ± 0.254	0.111 ± 0.053
(538) Friederike	unknown	0.064 ± 0.002	1	0.459 ± 0.091	0.157 ± 0.029	0.630 ± 0.051	0.129 ± 0.020
			2	0.442 ± 0.084	0.165 ± 0.026	0.709 ± 0.050	0.100 ± 0.019
(747) Winchester	PC	0.052 ± 0.002	1	0.519 ± 0.144	0.063 ± 0.046	0.571 ± 0.098	0.079 ± 0.028
			2	0.556 ± 0.217	0.063 ± 0.062	0.768 ± 0.163	0.039 ± 0.040
(770) Bali	S	0.304 ± 0.010	1	0.172 ± 0.041	0.467 ± 0.016	0.129 ± 0.023	0.461 ± 0.009
			2	0.167 ± 0.046	0.471 ± 0.017	0.139 ± 0.021	0.450 ± 0.008
(771) Libera	X	0.141 ± 0.008	1	0.223 ± 0.123	0.296 ± 0.018	0.408 ± 0.062	0.331 ± 0.009
(800) Kressmannia	S	0.202 ± 0.008	1	0.373 ± 0.043	0.274 ± 0.014	0.263 ± 0.029	0.370 ± 0.009
			2	0.363 ± 0.048	0.264 ± 0.016	0.259 ± 0.025	0.363 ± 0.008
(834) Burnhamia	GS:	0.082 ± 0.007	1	0.601 ± 0.064	0.150 ± 0.029	0.577 ± 0.035	0.173 ± 0.013
			2	0.584 ± 0.060	0.158 ± 0.027	0.550 ± 0.035	0.189 ± 0.013
(849) Ara	M	0.287 ± 0.013	1	–0.005 ± 0.176	0.336 ± 0.013	0.077 ± 0.102	0.429 ± 0.019
			2	0.366 ± 0.188	0.318 ± 0.023	0.119 ± 0.062	0.292 ± 0.007
(923) Herluga	unknown	0.037 ± 0.002	1	0.552 ± 0.234	0.036 ± 0.061	0.878 ± 0.108	0.020 ± 0.031
			2	0.567 ± 0.223	0.089 ± 0.051	0.883 ± 0.112	0.047 ± 0.031
(995) Sternberga	unknown	0.134 ± 0.006	1	0.575 ± 0.079	0.274 ± 0.019	0.159 ± 0.025	0.400 ± 0.006
			2	0.496 ± 0.074	0.259 ± 0.020	0.098 ± 0.023	0.395 ± 0.007
(1088) Mitaka	S	0.276 ± 0.034	1	0.642 ± 0.120	0.227 ± 0.020	0.632 ± 0.059	0.333 ± 0.013
			2	0.450 ± 0.122	0.300 ± 0.016	0.583 ± 0.037	0.395 ± 0.012

Table 2 – *continued*

Asteroid	Taxa	Albedo	Solution	cyan G_1	cyan G_2	orange G_1	orange G_2
(1130) Skuld	unknown	0.244 ± 0.033	1	0.269 ± 0.045	0.334 ± 0.015	0.242 ± 0.023	0.369 ± 0.009
			2	0.233 ± 0.037	0.340 ± 0.013	0.243 ± 0.023	0.367 ± 0.009
(1219) Britta	unknown	0.223 ± 0.013	1	0.367 ± 0.088	0.337 ± 0.018	0.143 ± 0.029	0.416 ± 0.008
(2579) Spartacus	V*		1	0.293 ± 0.091	0.451 ± 0.016	0.522 ± 0.042	0.446 ± 0.010
			2	0.271 ± 0.088	0.381 ± 0.016	0.398 ± 0.056	0.421 ± 0.009

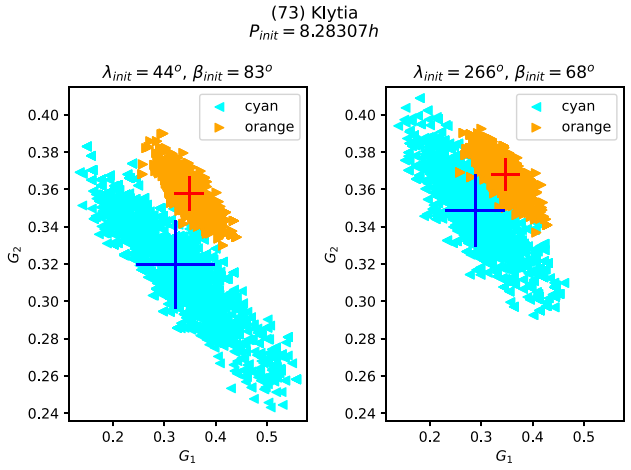

Figure 3. G_1 and G_2 parameter samples using MCMC with two different initial pole solutions for asteroid (73) Klytia in cyan and orange ATLAS data. Mean values with uncertainties are represented by blue and red crosses.

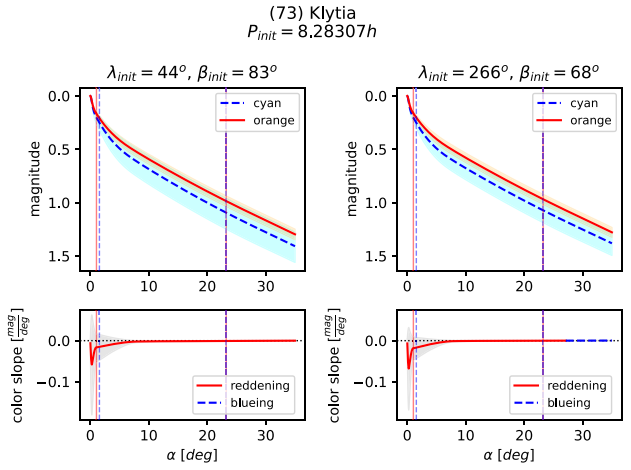

Figure 4. Top: phase curves obtained for asteroid (73) Klytia using the H, G_1, G_2 magnitude phase function, with mean values from MCMC sampling for G_1 and G_2 parameters, absolute magnitude H was assumed as 0. The shaded envelope represents the range that encompasses the minimum and maximum parameter values. Bottom: colour slope, representing the difference between the first derivatives of the phase function with respect to the phase angle in the two filters. Vertical lines encompass the range of observed phase angles separately in both filters mentioned in Table 1.

with varying taxonomic affiliations, including those with an unknown classification. This is further depicted in Fig. 13 comparing the phase curve parameter values obtained with the albedo obtained from the AKARI mission (Usui et al. 2011). The distribution of asteroids

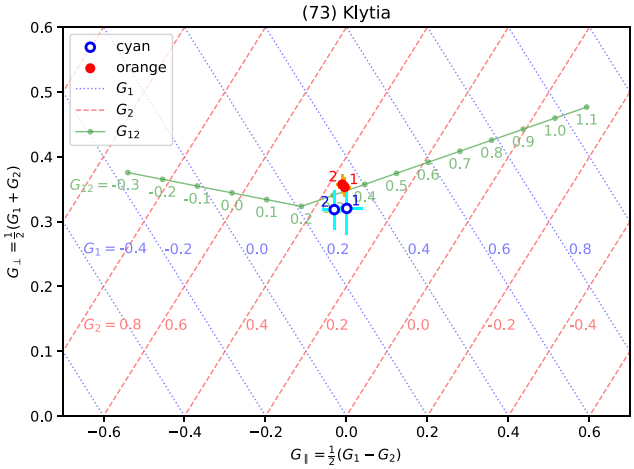

Figure 5. $G_\perp = \frac{1}{2}(G_1 + G_2)$ and $G_\parallel = \frac{1}{2}(G_1 - G_2)$ parameters values computed from mean values of G_1 and G_2 parameters with uncertainties for two pole solutions in cyan and orange ATLAS filters for asteroid (73) Klytia. Dotted blue and dashed red diagonal lines indicate consecutive values of parameters G_1 and G_2, respectively. The solid green line shows consecutive G_{12} values.

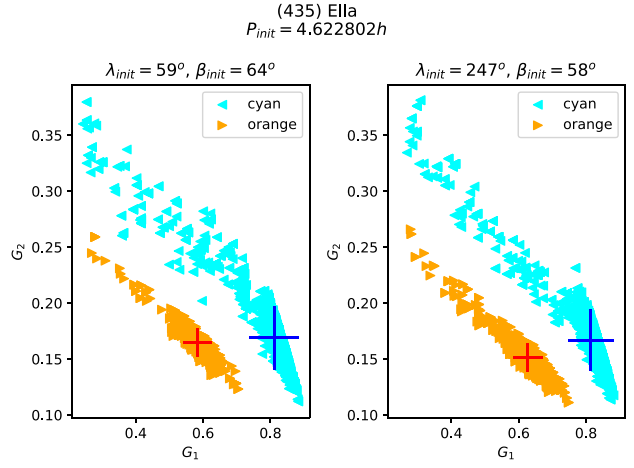

Figure 6. As in Fig. 3 for the asteroid (435) Ella.

follows the expected pattern: objects with low albedo have high G_1 values and low G_2 values, whereas objects with high albedo exhibit low-G_1 values and high-G_2 values. For objects with low albedo, the spread of the parameter values for G_1 is noticeably greater than that for G_2.

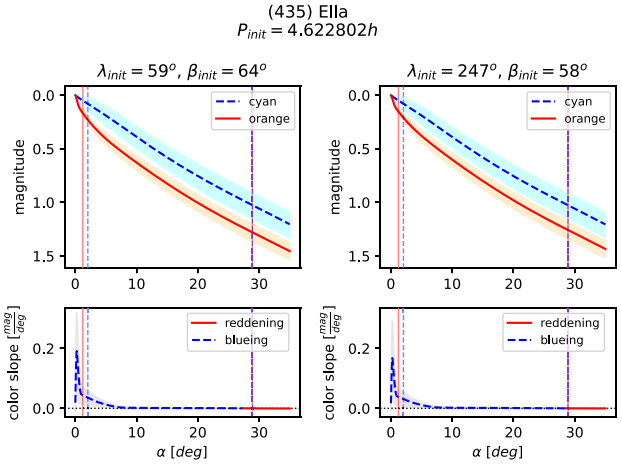

Figure 7. As in Fig. 4 for the asteroid (435) Ella.

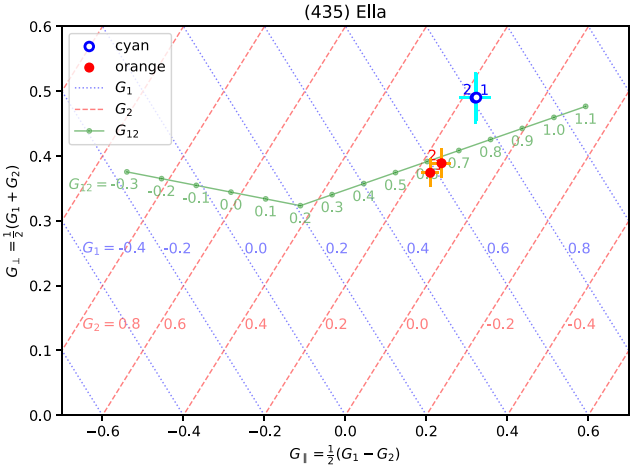

Figure 8. As in Fig. 5 for the asteroid (435) Ella.

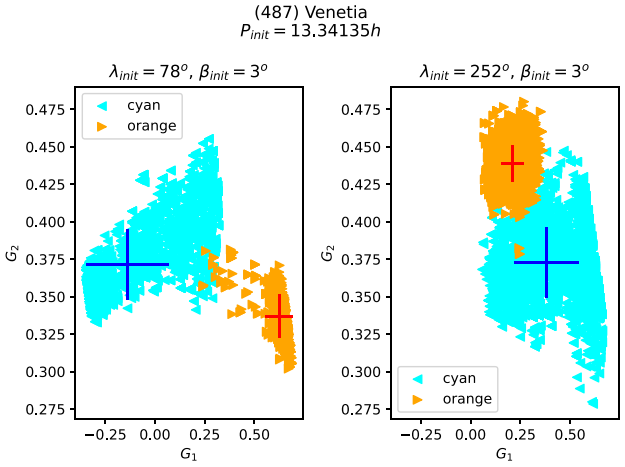

Figure 9. As in Fig. 3 for the asteroid (487) Venetia.

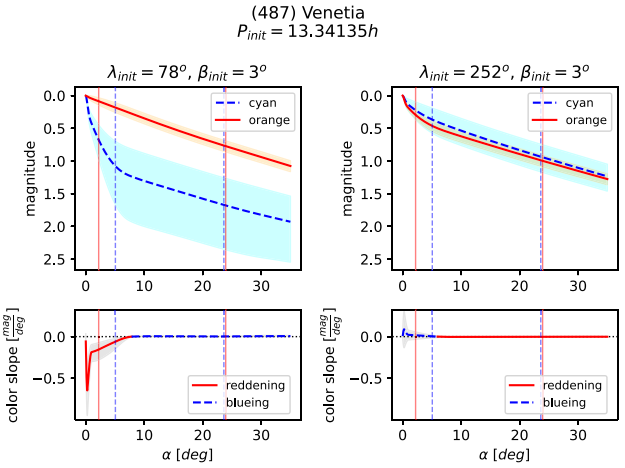

Figure 10. As in Fig. 4 for the asteroid (487) Venetia.

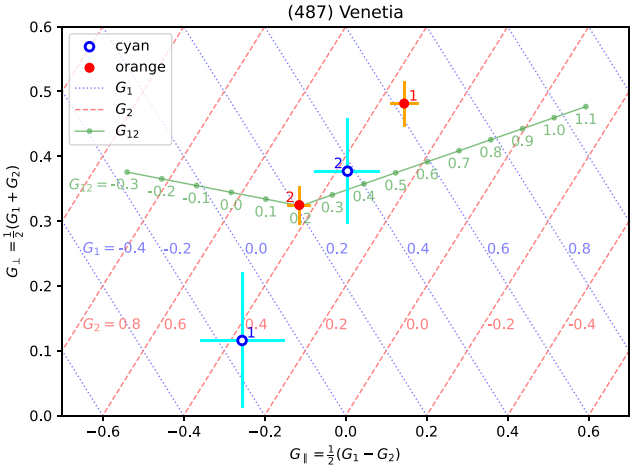

Figure 11. As in Fig. 5 for the asteroid (487) Venetia.

Next, we analyse changes in the colour slope. As shown in the colour slope versus phase angle figures in the supplementary material, the variation in the colour slope is conspicuous for most of our objects at phase angles between 0° and 10° and remains nearly zero beyond 10°. Notably, the *Gaia* DR3 observations, spanning over 10°–35° in phase angle, raised concerns about phase reddening affecting the obtained asteroid spectra (Cellino et al. 2020). This potential impact introduces complexity in the comparison of *Gaia* spectra with older taxonomic schemes and may introduce biases in the determination of mineralogy. Therefore, we highlight that any spectroscopic measurements should be internally consistent, as the colour slope appears constant over this range of phase angles for most objects.

We further analysed the parameters $G_\perp = \frac{1}{2}(G_1 + G_2)$ and $G_\parallel = \frac{1}{2}(G_1 - G_2)$ parameters for individual objects in the context of realistic values for the amplitude of the opposition effect and the linear slope at 20°, as well as the consistency with spectral type. Figs 14 and 15 show the distribution of the parameters $G_\perp$ and $G_\parallel$ for complex C- and S-complex asteroids. Generally, C-complex asteroids have higher values of $G_\parallel$ and the S-complex object lower. The S-complex objects are mostly located in the area of large opposition effect amplitude. Several outliers are observed among the C- and S-complex asteroids; these show unrealistic slopes or opposition effect

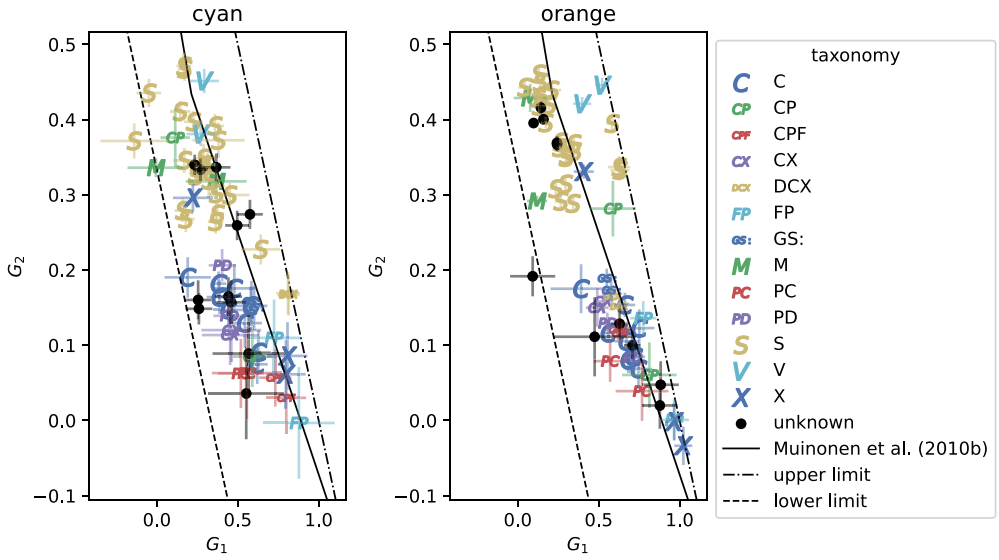

Figure 12. Mean G_1 and G_2 values with uncertainties obtained in this work, differentiated by taxonomic class according to Tholen classification, supplemented by the SMASSII when not available (Tholen 1989; Bus & Binzel 2002; Neese 2017) for both cyan and orange ATLAS filters. In cases, where both pole coordinates yielded results, they are represented as two separate points on the graph. The solid black line represents the relation between parameters as in Muinonen et al. (2010b). The dashed–dotted and dashed lines constrain the allowed values of G_1 and G_2 (Muinonen et al. 2010b).

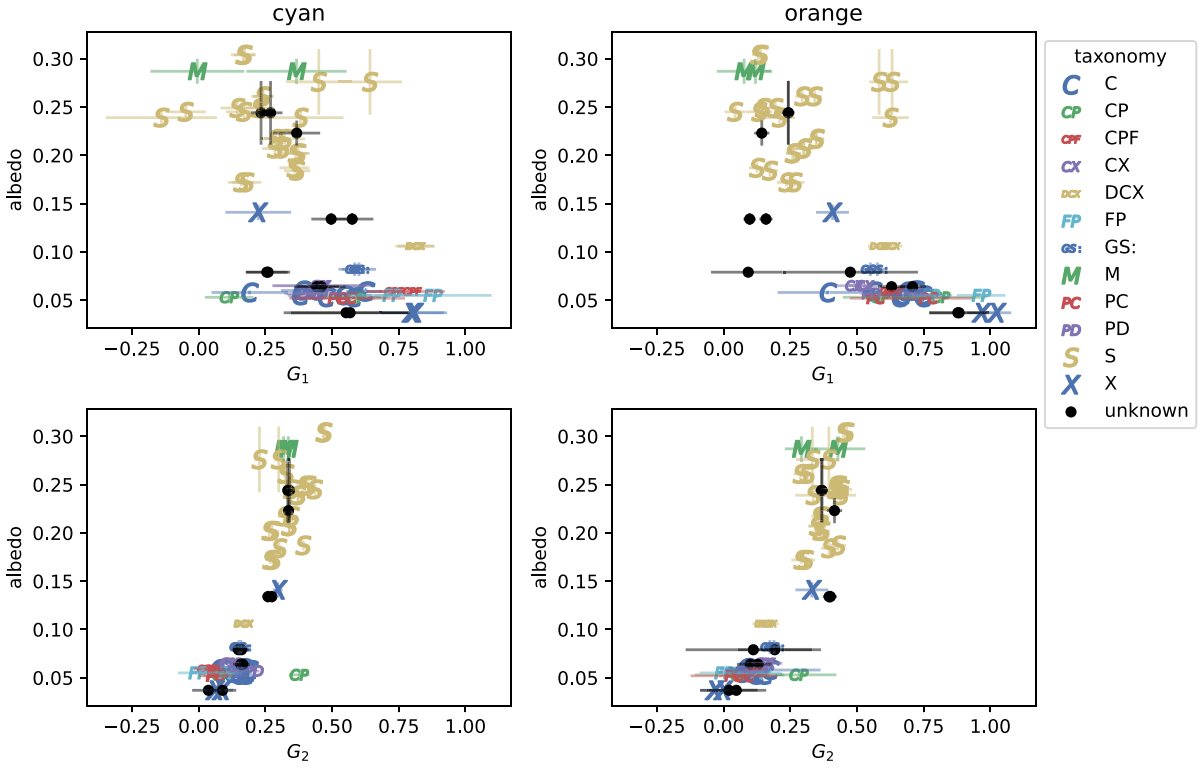

Figure 13. Relationship between G_1 (upper row) and G_2 (bottom row) with albedo, sourced from the AKARI mission (Usui et al. 2011), for both cyan and orange ATLAS filters. Points are differentiated by Tholen taxonomic class, supplemented by the SMASSII when not applicable (Tholen 1989; Bus & Binzel 2002; Neese 2017).

amplitudes. Furthermore, some solutions for S-complex asteroids have $G_\perp$ and $G_\parallel$ more consistent with C-complex objects. This can be explained by specific surface properties, erroneous taxonomic type classification, or one of two symmetric solutions may be preferred.

Collectively, we can divide the results into several groups:

(i) Objects with one realistic solution and one solution with unrealistically large opposition-effect amplitudes. These are typically objects for which the photometric data did not cover the opposition effect well – there were either no data at small phase angles ($<3^\circ$) or the data were sparse. In this case, one of the pairs $G_\perp$ and $G_\parallel$ should

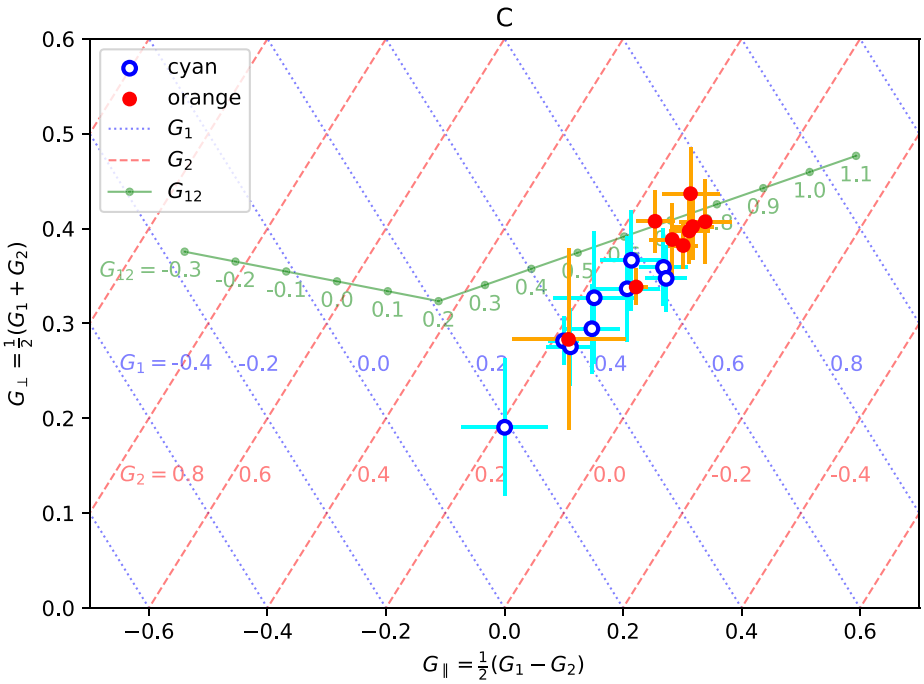

Figure 14. $G_\perp = \frac{1}{2}(G_1 + G_2)$ and $G_\parallel = \frac{1}{2}(G_1 - G_2)$ parameters values computed from mean values of G_1 and G_2 parameters with uncertainties for two pole solutions in cyan and orange ATLAS filters for C taxonomic class. Dotted blue and dashed red diagonal lines indicate consecutive values of parameters G_1 and G_2, respectively. The solid green line shows consecutive G_{12} values.

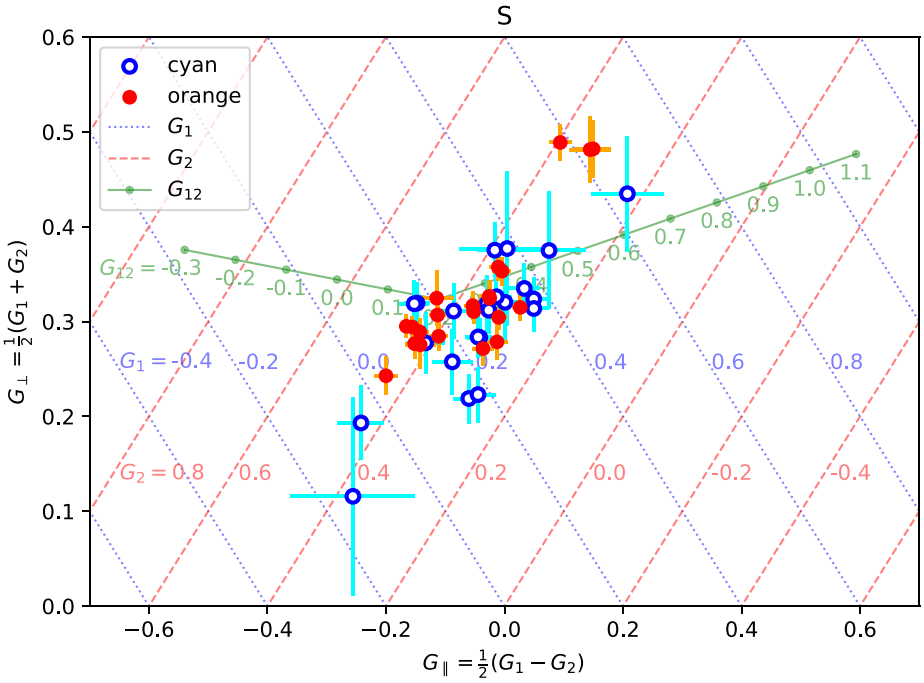

Figure 15. As in Fig. 14 for the S taxonomic class.

be rejected, and the other suggests the correct pole solution. This is, for example, the case for asteroid (487) Venetia, as discussed before. Other examples include asteroids (94) Aurora, (202) Chryseis, (849) Ara, and (2156) Spartacus. For these objects, we found too large amplitude of the opposition effect for the first pole solution; results for the second pole solution are more realistic. However, the $G_\perp$ and $G_\parallel$ uncertainties are large.

(ii) Objects with realistic opposition effect for which the taxonomic type agrees with the phase curve parameters. Both of the $G_\perp$ and $G_\parallel$ pairs have realistic values of phase curve parameters,

and at least one of the two pairs $G_\perp$ and $G_\parallel$ is compatible with taxonomic type. This is then the preferred pole solution. Generally, steep phase curves are expected for low-albedo objects, and flat phase curves are typical for high-albedo asteroids. As expected, most of the C-complex asteroids studied in this work have steeper phase-curve slopes compared to those of the studied S-complex objects. Belskaya & Shevchenko (2018) find that the linear slope β (expressed in [mag/deg]) is related to the albedo as $\beta = 0.016–0.022\log(p_v)$. This can also be interpreted in terms of taxonomic type, e.g. the S-type objects with lower albedo in the cyan filter as compared to the orange filter are expected to have steeper phase curves in the cyan filter than in the orange filter. The opposite relation (steeper phase curves in orange and flatter curves in cyan) would be expected for the B-type asteroids. In the orange and cyan filters, which overlap in wavelength, the wavelength-dependent effect might be small and challenging to detect, especially for taxonomic types with minor albedo differences between those filters (such as C-complex objects and low-albedo bodies of the X-complex). This effect could be more easily noticeable in phase curves obtained with filters that are further apart, such as those in the visible and near-infrared wavelengths, especially for types with significant albedo differences in those filters (e.g. D- or A-type asteroids). However, we found multiple asteroids for which the derived parameters agree with the taxonomic type. Several asteroids fall into this category. Asteroid (73) Klytia exhibits solutions with realistic slopes and amplitudes, in agreement with its taxonomic type. For asteroid (94) Aurora, the second-pole solution demonstrates a more realistic slope, and its parameters align with the taxonomic type. Both pole solutions for (127) Johanna yield similar and overlapping phase curve parameters, within the expectation for a C- or X-complex asteroid. Similarly, (159) Aemilia displays solutions with realistic values, consistent with its spectral type. The asteroid (174) Phaedra has only one initial pole solution, with shallow slopes that are realistic and consistent with its spectral type. Asteroid (219) Thunselda exhibits a shallow slope in the orange filter, and the solution is realistic. For four other objects – (301) Bavaria, (335) Roberta, (352) Gisela, and (355) Gabriella – the results are realistic as well. Asteroid (350) Ornamenta has a single solution that aligns with its spectral slope. Regarding (377) Campania, the orange results are more consistent with the P-type (rather than the D-type), and the first solution is slightly preferred. For (378) Holmia, both solutions are plausible, with the amplitude in the opposition effect being less pronounced in the orange filter.

(iii) Objects for which the taxonomic type is not in agreement with the phase-curve parameters. These are solutions with realistic opposition effect amplitude values and slope values that do not match their taxonomic type. This could be explained by an erroneous identification of taxonomic type or specific surface properties. For example, S-complex asteroids with high surface roughness could have phase curve parameters more compatible with C-complex objects. Similarly, C-complex asteroids with high-packing density and smooth surface could end up in the S-complex phase curve parameter space. We found a single case – an X-type asteroid (223) Rosa – has phase-curve slope values more compatible with low albedo C-complex objects. Its phase curve parameters can also be explained by its low albedo.

(iv) Objects of no known taxonomic type. For objects of unknown taxonomic type, we indicate the probable taxonomic complex, that is, the complex that best matches their phase curve parameters. Six asteroids in our study do not have their taxonomic type determined. Three of these have phase curve parameters more compatible with S-complex objects ((1130) Skuld, (1219) Britta) and two with C-complex objects ((538) Friederike, (923) Herluga). Additionally, when considering albedo, (995) Sternberga may be classified as an X-complex asteroid. The classification of (501) Urhixidur is inconclusive.

5 CONCLUSIONS

We have derived phase curve parameters corrected for shape and geometry for 35 well-observed asteroids. We found that an unrealistic amplitude of the opposition effect or slope of the phase function can help discriminate the less plausible rotational pole solution, e.g. only bodies with a negative spectral slope (B-type) can give a minimal blueing. So, if an S-type asteroid shows blueing at certain phase angles, it is likely indicative of an inaccurate pole solution. For a few asteroids, we found that the G_1, G_2 parameters are well separated for the orange and cyan filters, highlighting the phase curve wavelength dependence. Most of the objects with well-separated G_1, G_2 domains in the different filters belonged to the S-complex asteroids. This can be explained using the relation of phase-curve slopes with geometric albedos – the S-complex asteroids should show more steep phase curves in the cyan filter, due to lower albedo in that bandpass. Analogically, similar predictions can be made for other taxonomic types. This could be further investigated by obtaining phase curves for objects with large albedo differences in two or more filters. Investigation of colour slope with phase angle indicates that the largest differences in the slopes occur at small phase angles and are negligible beyond 10° of phase angle.

It is important to mention that our objects have a limited number of data points at very small phase angles, which may result in less well-constrained phase curves and colour slopes in this phase angle range. Consequently, extrapolating phase curves at small phase angles leads to higher uncertainties, which demands a cautious interpretation of the observed differences at small phase angles. Despite this, we point out that similar behaviour was observed for (433) Eros by Muinonen et al. (2002) in a wider range of phase angles 2–3°. However, Muinonen et al. (2002) show disc-integrated multiwavelength phase curves derived from disc-resolved observations from the NASA NEAR Shoemaker spacecraft. Furthermore, observations of (433) Eros were made in the IR range from 0.946 to 1.932 μm, which cannot be directly compared to the cyan and orange ATLAS filters. The colour slopes at small phase angles should be further investigated in detail.

Most of the phase curves derived in this work are in agreement with the indicated taxonomic type. In some cases, it was possible to indicate a more plausible solution based on the alignment with implications of the taxonomic type on the steepness of phase curves in orange and cyan filters. For a few objects with an unknown taxonomic type, it was possible to indicate a more probable taxonomic complex based on the phase curve parameters. It is important to highlight that our conclusions are derived using nominal phase curves in cyan and orange filters for the specified set of objects. The observed effect may vary among different asteroids when considering different filters.

ACKNOWLEDGEMENTS

EW and AK were supported by grant no. 2017/25/B/ST9/00740 from the National Science Centre, Poland.

DO and MC were supported by grant no. 2022/45/B/ST9/00267 from the National Science Centre, Poland.

Research by KM supported by Research Council of Finland grants nos. 336546 and 345115.

The calculations in this work are supported by grant no. 602 from Poznan Supercomputing and Networking Center, Poland.

This work uses data from the University of Hawaii's ATLAS project, funded through NASA grants NN12AR55G, 80NSSC18K0284, and 80NSSC18K1575, with contributions from the Queen's University Belfast, STScI, the South African Astronomical Observatory, and the Millennium Institute of Astrophysics, Chile.

KM acknowledges the discussions about the colour phase effects with Dr Alvaro Alvarez-Candal, Dr Rene Duffard, and Dr Olga Munoz at Instituto de Astrofisica de Andalucia, Granada, Spain.

For language editing and translation, we utilized Writefull for Overleaf, Google Translate, DeepL, and ChatGPT.

DATA AVAILABILITY

This research utilized published and publicly available photometric data. The majority of the literature's dense photometric lightcurves are already available in the CDS (Centre de Données astronomiques de Strasbourg) archive. The sparse ATLAS survey data are publicly available at https://atlas.fallingstar.com.

REFERENCES

Akimov L. A., 1975, Soviet Ast., 19, 385
Akimov L. A., 1979, Soviet Ast., 23, 231
Akimov L. A., 1988, Kinematika i Fizika Nebesnykh Tel, 4, 10
Alvarez-Candal A., Ayala-Loera C., Gil-Hutton R., Ortiz J. L., Santos-Sanz P., Duffard R., 2019, MNRAS, 488, 3035
Alvarez-Candal A., Benavidez P. G., Bagatin A. C., Santana-Ros T., 2022, A&A, 657, A80
Ayala-Loera C., Alvarez-Candal A., Ortiz J. L., Duffard R., Fernández-Valenzuela E., Santos-Sanz P., Morales N., 2018, MNRAS, 481, 1848
Belskaya I. N., Shevchenko V. G., 2000, Icarus, 147, 94
Belskaya I., Shevchenko V., 2018, EPSC, 12, EPSC2018–730
Bowell E., Hapke B., Domingue D., Lumme K., Peltoniemi J., Harris A. W., 1989, in Asteroids II. Univ.Arizona Press, Tucson, AZ, p. 524
Bus S. J., Binzel R. P., 2002, Icarus, 158, 146
Cellino A., Bendjoya P., Delbo' M., Galluccio L., Gayon-Markt J., Tanga P., Tedesco E. F., 2020, A&A, 642, A80
Chambers K., Pan-STARRS Team, 2018, in American Astronomical Society Meeting Abstracts #231, American Astronomical Society, Washington, DC, p. 102.01
Clark B. E. et al., 2002, Icarus, 155, 189
Colazo M., Duffard R., Weidmann W., 2021, MNRAS, 504, 761
Denneau L., Tonry J., Heinze A., Fitzsimmons A., Erasmus N., Smartt S., Smith K., 2022, BAAS, 54, 504.08
Dlugach Z. M., Mishchenko M. I., 2013, Solar Syst. Res., 47, 454
Durech J., Sidorin V., Kaasalainen M., 2010, A&A, 513, A46
Ďurech J., Tonry J., Erasmus N., Denneau L., Heinze A., Flewelling H., Vančo R., 2020, A&A, 643, A59
Fornasier S. et al., 2020, A&A, 644, A142
Gehrels T., 1956, ApJ, 123, 331
Gehrels T., Tedesco E. F., 1979, AJ, 84, 1079
Gehrels T., Coffeen T., Owings D., 1964, AJ, 69, 826
Groeneveld I., Kuiper G. P., 1954, ApJ, 120, 200
Hanus J. et al., 2013, A&A, 551, A67
Hapke B., 2002, Icarus, 157, 523
Hapke B., 2008, Icarus, 195, 918
Hapke B., 2012, Icarus, 221, 1079
Harris A. W., Young J. W., 1983, Icarus, 54, 59
Harris A., Young J., 1989, Icarus, 81, 314
Heinze A. N. et al., 2018, AJ, 156, 241
Ivezić Ž. et al., 2001, AJ, 122, 2749
Jackson S. L., Rozitis B., Dover L. R., Green S. F., Kolb U. C., Andrews A. E., Lowry S. C., 2022, MNRAS, 513, 3076
Kryszczyńska A., 2013, A&A, 551, A102
Lagerkvist C. I., Magnusson P., 1990, A&AS, 86, 119
Lagerkvist C., Magnusson I., Belskaya A., Erikson M., Dohlgren M., Barucci M., 1995, NASA Planetary Data System. NASA, Washington, DC, p. EAR–A-3-DDR-APC-LIGHTCURVE-V1.0
Le Corre L., Sanchez J. A., Reddy V., Battle A., Cantillo D. C., Sharkey B., Jedicke R., Scheeres D. J., 2023, Planet. Sci. J., 4, 91
Li J.-Y. et al., 2013, Icarus, 226, 1252
Mahlke M., Carry B., Denneau L., 2021, Icarus, 354, 114094
Mainzer A. K., Bauer J. M., Cutri R. M., Grav T., Kramer E. A., Masiero J. R., Sonnett S., Wright E. L., 2019, NEOWISE Diameters and Albedos V2.0, NASA Planetary Data System. NASA, Washington, DC
Marciniak A. et al., 2008, A&A, 478, 559
Marciniak A. et al., 2009a, A&A, 498, 313
Marciniak A. et al., 2009b, A&A, 508, 1503
Marciniak A. et al., 2011, A&A, 529, A107
Marciniak A. et al., 2012, A&A, 545, A131
Marciniak A. et al., 2018, A&A, 610, A7
Marciniak A. et al., 2019, A&A, 625, A139
Marciniak A. et al., 2021, A&A, 654, A87
Martikainen J., Muinonen K., Penttilä A., Cellino A., Wang X. B., 2021, A&A, 649, A98
Muinonen K., Piironen J., Shkuratov Y. G., Ovcharenko A., Clark B. E., 2002, in Asteroids III. Univ. Arizona Press, Tucson, AZ, p. 123
Muinonen K., Tyynelä J., Zubko E., Videen G., 2010a, Coherent Backscattering in Planetary Regoliths. Springer, Berlin, Heidelberg, p. 477
Muinonen K., Belskaya I. N., Cellino A., Delbò M., Levasseur-Regourd A.-C., Penttilä A., Tedesco E. F., 2010b, Icarus, 209, 542
Muinonen K., Torppa J., Wang X. B., Cellino A., Penttilä A., 2020, A&A, 642, A138
Muinonen K., Uvarova E., Martikainen J., Penttilä A., Cellino A., Wang X., 2022, Front. Astron. Space Sci., 9, 821125
Neese C., 2017, Asteroid Taxonomy V1.0, NASA Planetary Data System. NASA, Washington, DC
Oszkiewicz D. A., Muinonen K., Bowell E., Trilling D., Penttilä A., Pieniluoma T., Wasserman L. H., Enga M. T., 2011, J. Quant. Spec. Radiat. Transf., 112, 1919
Oszkiewicz D. A., Bowell E., Wasserman L., Muinonen K., Penttilä A., Pieniluoma T., Trilling D. E., Thomas C. A., 2012, Icarus, 219, 283
Oszkiewicz D. et al., 2019, A&A, 623, A170
Oszkiewicz D. et al., 2021, Icarus, 357, 114158
Penttilä A., Shevchenko V., Wilkman O., Muinonen K., 2016, Planet. Space Sci., 123, 117
Pravec P., Harris A. W., Kušnirák P., Galád A., Hornoch K., 2012, Icarus, 221, 365
Reddy V. et al., 2012, Icarus, 217, 153
Riello M. et al., 2021, A&A, 649, A3
Rodrigo C., Solano E., 2020, in XIV.0 Scientific Meeting (virtual) of the Spanish Astronomical Society. Spanish Astronomical Society, Madrid, Spain, p. 182
Schröder S. E. et al., 2012, in Editorial LPI, ed., LPI Contributions Vol. 1667, Asteroids, Comets, Meteors 2012. Lunar and Planetary Institute, Houston, TX, p. 6328
Shevchenko V. G. et al., 2016, Planet. Space Sci., 123, 101
Shevchenko V. G. et al., 2021, Planet. Space Sci., 202, 105248
Shevchenko V. G. et al., 2022, A&A, 666, A190
Shkuratov Y., Kaydash V., Korokhin V., Velikodsky Y., Opanasenko N., Videen G., 2011, Planet. Space Sci., 59, 1326
Spoto F. et al., 2018, A&A, 616, A13
Stokes G. H., Evans J. B., Viggh H. E. M., Shelly F. C., Pearce E. C., 2000, Icarus, 148, 21
Tanga P. et al., 2023, A&A, 674, A12

Tedesco E. F., Noah P. V., Noah M., Price S. D., 2004, NASA Planetary Data System. NASA, Washington, DC, p. IRAS–A-FPA-3-RDR-IMPS-V6.0
Tholen D. J., 1989, in Binzel R. P., Gehrels T., Matthews M. S., eds, Asteroids II. Univ. Arizona Press, Tucson, AZ, p. 1139
Usui F. et al., 2011, PASJ, 63, 1117
Usui F., Kasuga T., Hasegawa S., Ishiguro M., Kuroda D., Müller T. G., Ootsubo T., Matsuhara H., 2013, ApJ, 762, 56
van Houten C. J., van Houten-Groeneveld I., Herget P., Gehrels T., 1970, A&AS, 2, 339
Vereš P. et al., 2015, Icarus, 261, 34
Waszczak A. et al., 2015, AJ, 150, 75
Wilawer E. et al., 2022, MNRAS, 513, 3242
Woods D. F. et al., 2021, PASP, 133, 014503
York D. G. et al., 2000, AJ, 120, 1579

SUPPORTING INFORMATION

Supplementary data are available at *MNRAS* online.

supplementary_material_final.pdf

Please note: Oxford University Press is not responsible for the content or functionality of any supporting materials supplied by the authors. Any queries (other than missing material) should be directed to the corresponding author for the article.

This paper has been typeset from a TEX/LATEX file prepared by the author.

C.1 Supplementary material

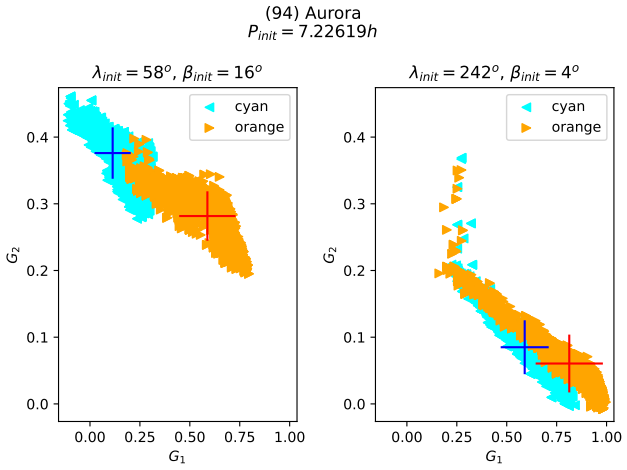

Figure 1. G_1 and G_2 parameter samples using MCMC with two different initial pole solutions for asteroid (94) Aurora in cyan and orange ATLAS data. Mean values with uncertainties are represented by blue and red crosses.

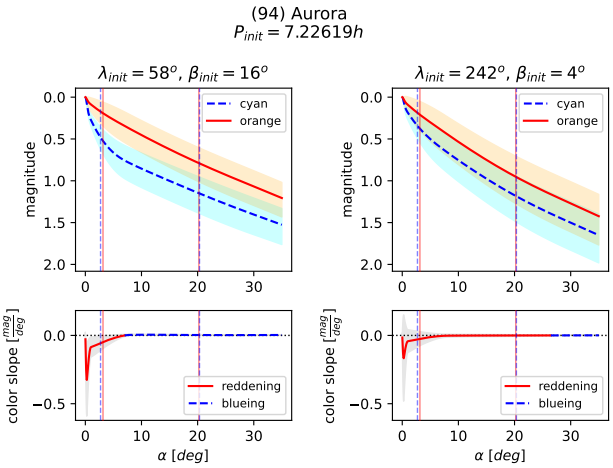

Figure 2. Top: phase curves obtained for asteroid (94) Aurora using the H, G_1, G_2 magnitude phase function, with mean values from MCMC sampling for G_1 and G_2 parameters, absolute magnitude H was assumed as 0. The shaded envelope represents the range that encompasses the minimum and maximum parameter values.
Bottom: color slope, representing the difference between the first derivatives of the phase function with respect to the phase angle in the two filters.
Vertical lines encompass the range of observed phase angles separately in both filters.

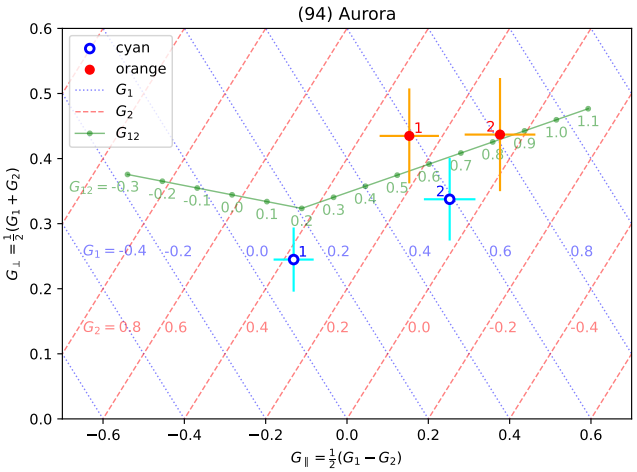

Figure 3. $G_\perp = \frac{1}{2}(G_1 + G_2)$ and $G_\parallel = \frac{1}{2}(G_1 - G_2)$ parameters values computed from mean values of G_1 and G_2 parameters with uncertainties for two pole solutions in cyan and orange ATLAS filters for asteroid (94) Aurora. Dotted blue and dashed red diagonal lines indicate consecutive values of parameters G_1 and G_2, respectively. The solid green line shows consecutive G_{12} values.

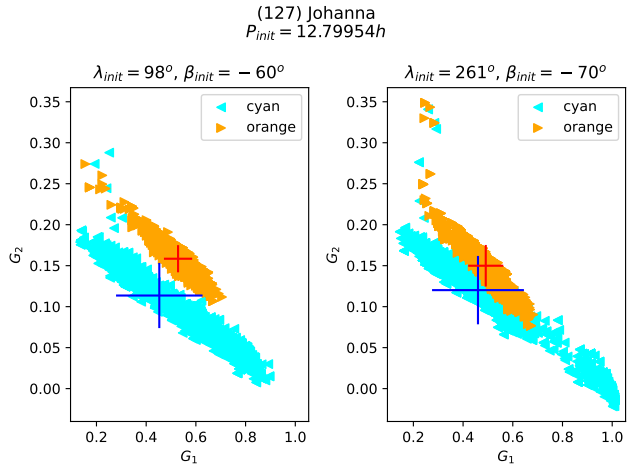

Figure 4. As in Fig. 1 for asteroid (127) Johanna.

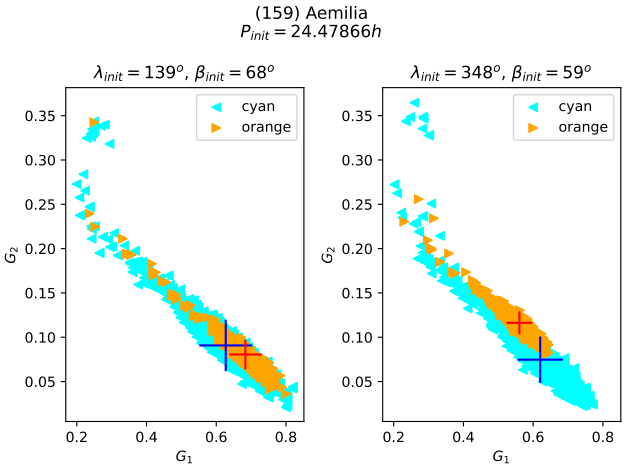

Figure 7. As in Fig. 1 for asteroid (159) Aemilia.

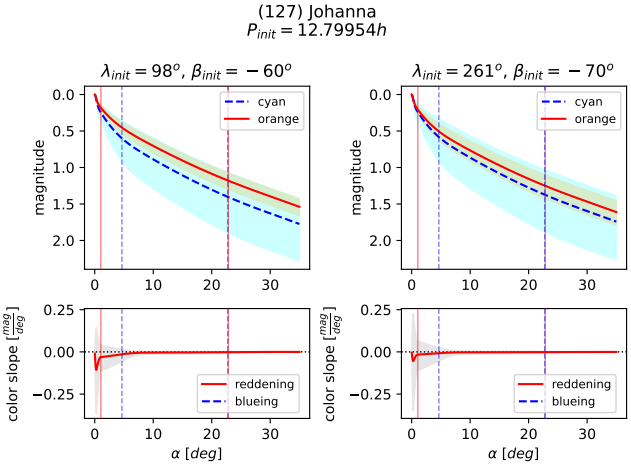

Figure 5. As in Fig. 2 for asteroid (127) Johanna.

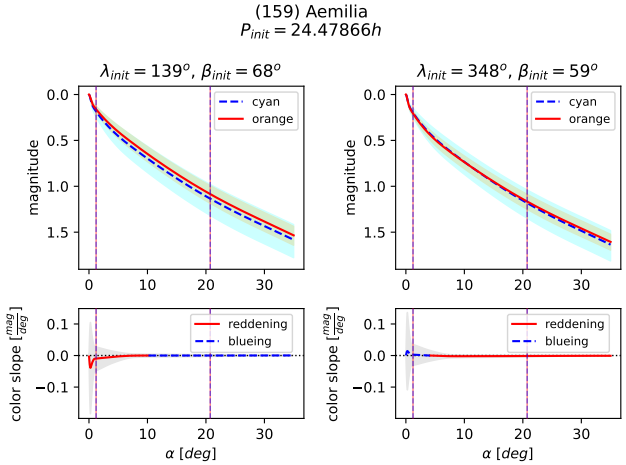

Figure 8. As in Fig. 2 for asteroid (159) Aemilia.

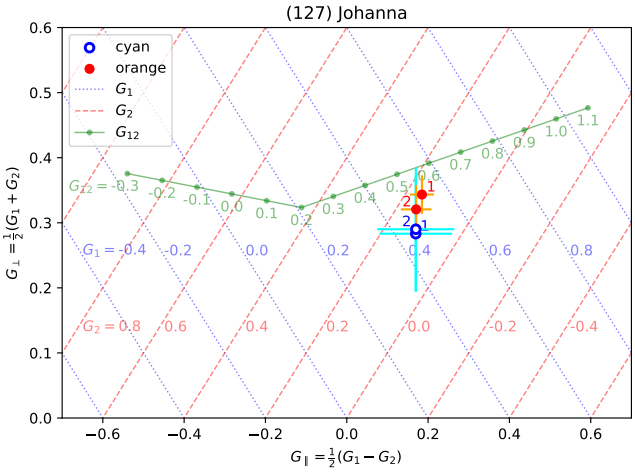

Figure 6. As in Fig. 3 for asteroid (127) Johanna.

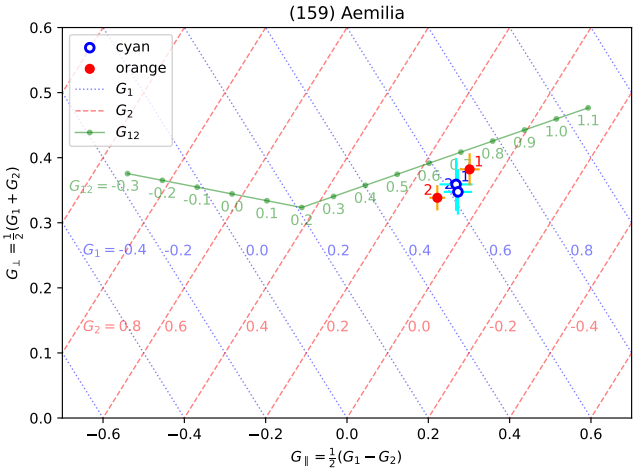

Figure 9. As in Fig. 3 for asteroid (159) Aemilia.

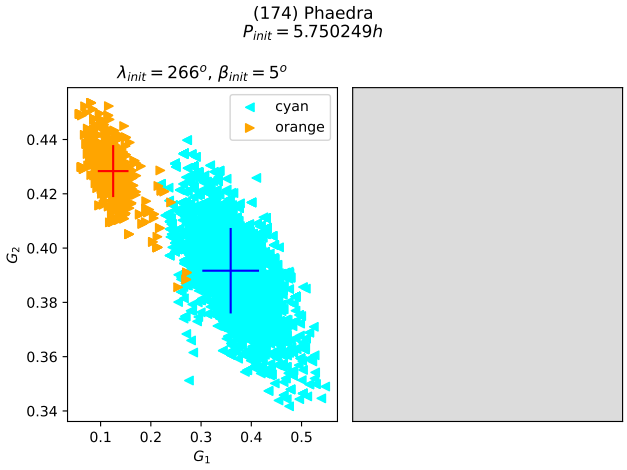

Figure 10. As in Fig. 1 for asteroid (174) Phaedra.

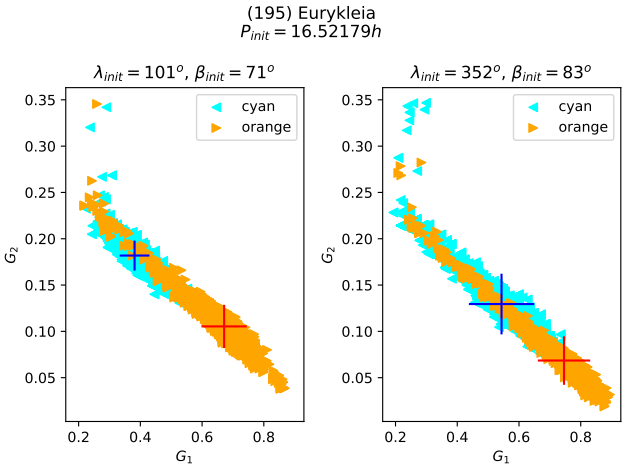

Figure 13. As in Fig. 1 for asteroid (195) Eurykleia.

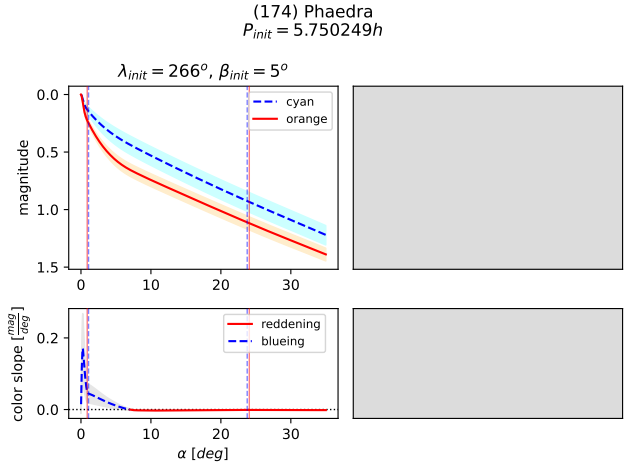

Figure 11. As in Fig. 2 for asteroid (174) Phaedra.

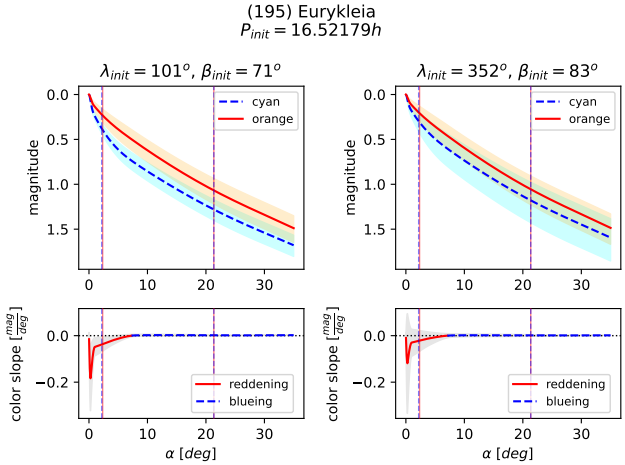

Figure 14. As in Fig. 2 for asteroid (195) Eurykleia.

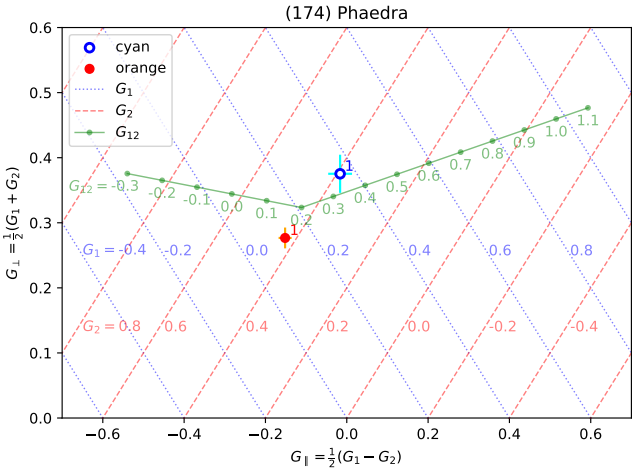

Figure 12. As in Fig. 3 for asteroid (174) Phaedra.

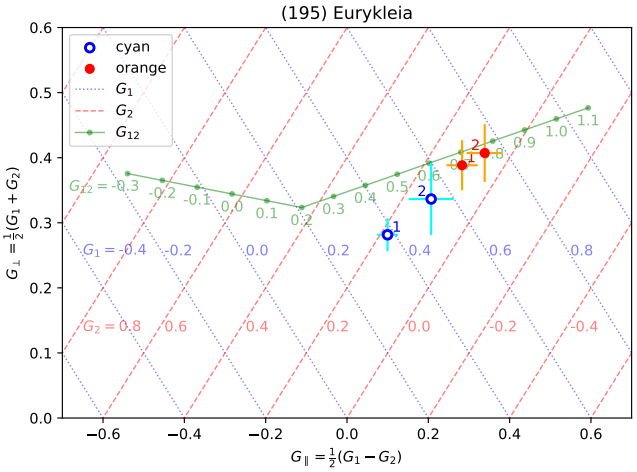

Figure 15. As in Fig. 3 for asteroid (195) Eurykleia.

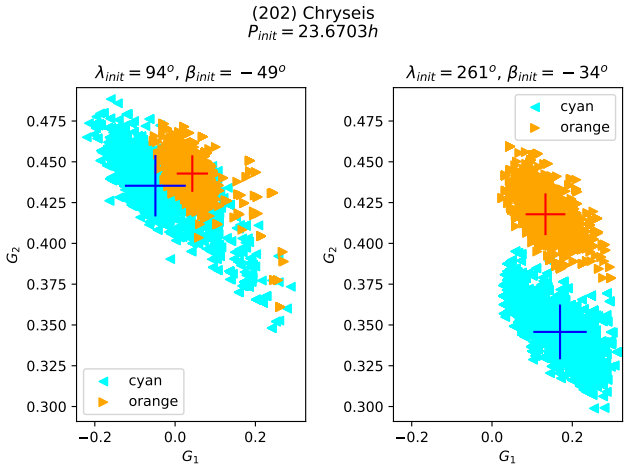

Figure 16. As in Fig. 1 for asteroid (202) Chryseis.

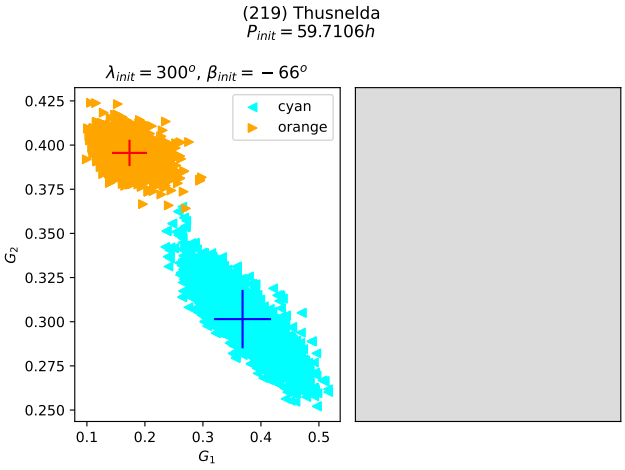

Figure 19. As in Fig. 1 for asteroid (219) Thusnelda.

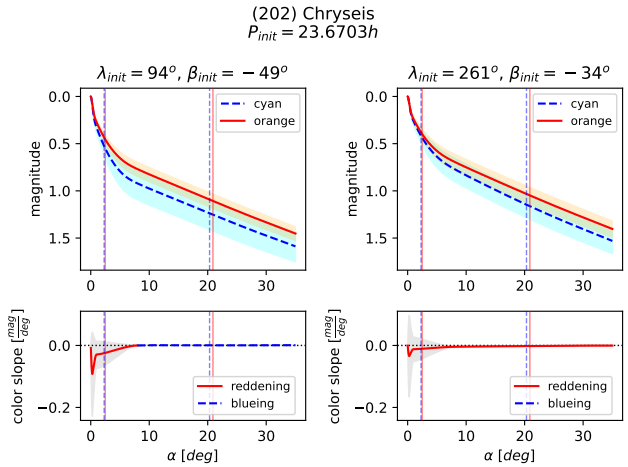

Figure 17. As in Fig. 2 for asteroid (202) Chryseis.

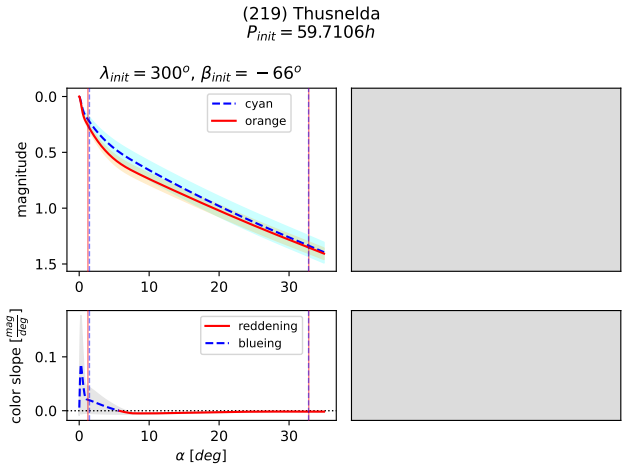

Figure 20. As in Fig. 2 for asteroid (219) Thusnelda.

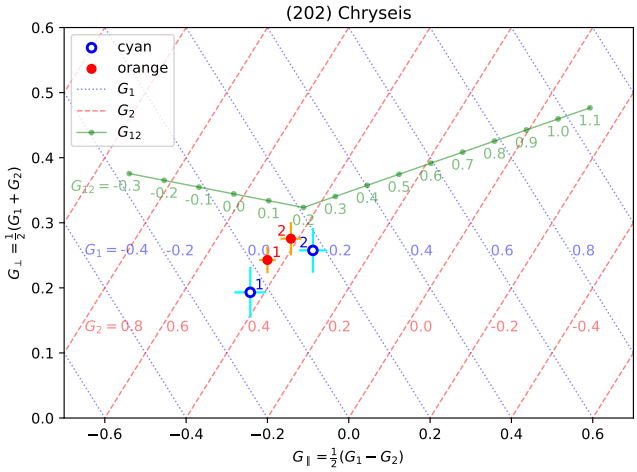

Figure 18. As in Fig. 3 for asteroid (202) Chryseis.

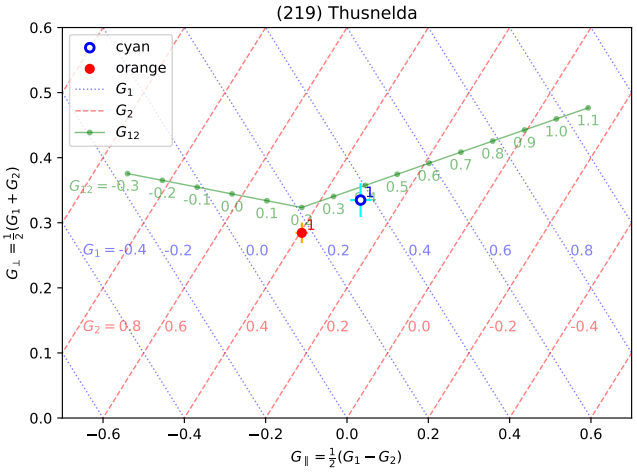

Figure 21. As in Fig. 3 for asteroid (219) Thusnelda.

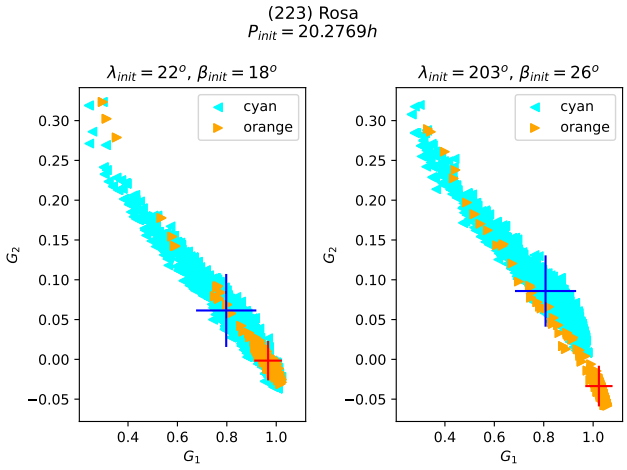

Figure 22. As in Fig. 1 for asteroid (223) Rosa.

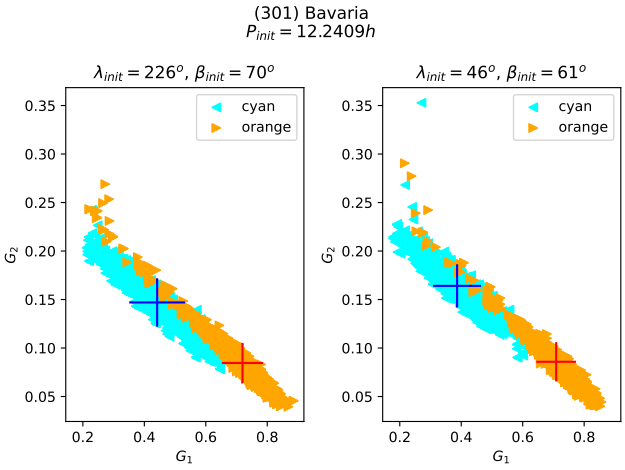

Figure 25. As in Fig. 1 for asteroid (301) Bavaria.

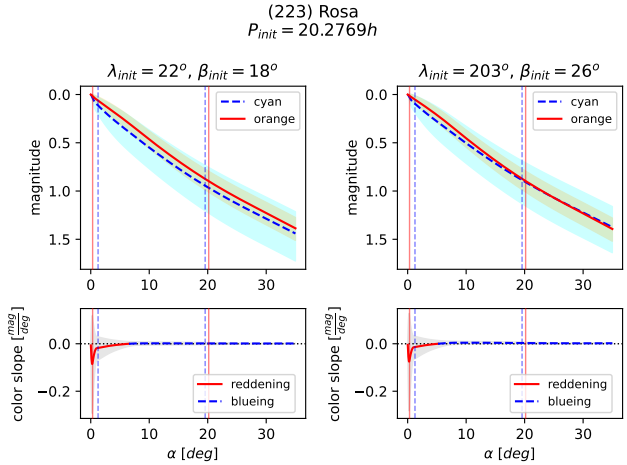

Figure 23. As in Fig. 2 for asteroid (223) Rosa.

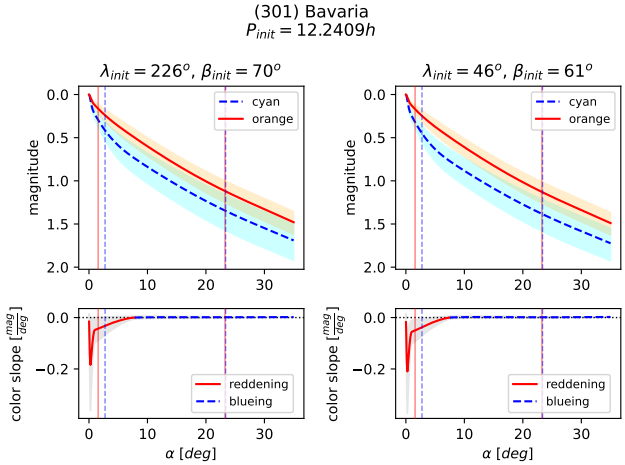

Figure 26. As in Fig. 2 for asteroid (301) Bavaria.

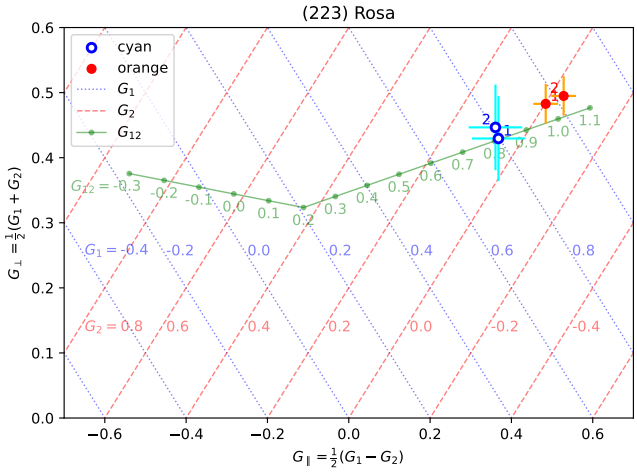

Figure 24. As in Fig. 3 for asteroid (223) Rosa.

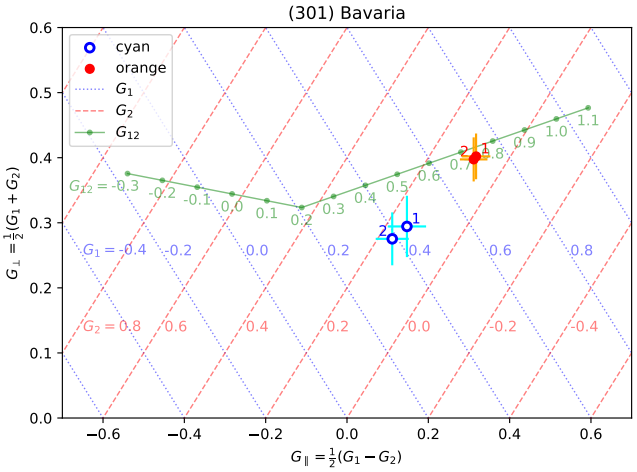

Figure 27. As in Fig. 3 for asteroid (301) Bavaria.

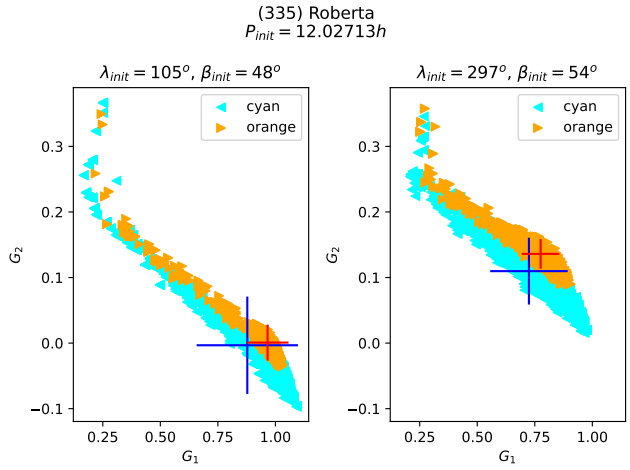

Figure 28. As in Fig. 1 for asteroid (335) Roberta.

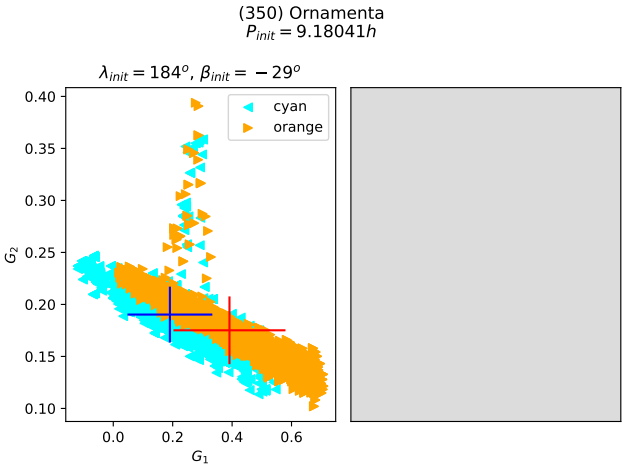

Figure 31. As in Fig. 1 for asteroid (350) Ornamenta.

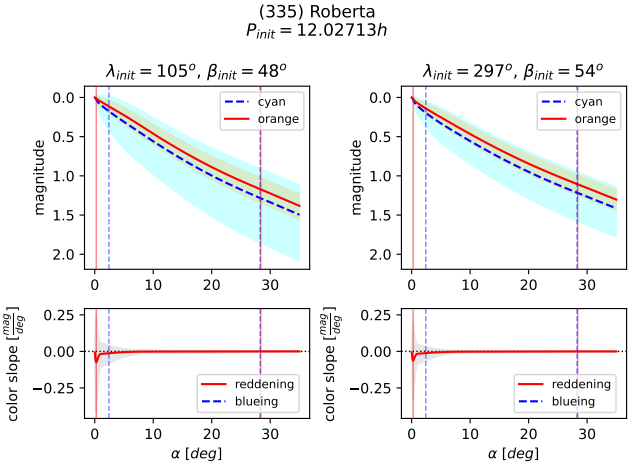

Figure 29. As in Fig. 2 for asteroid (335) Roberta.

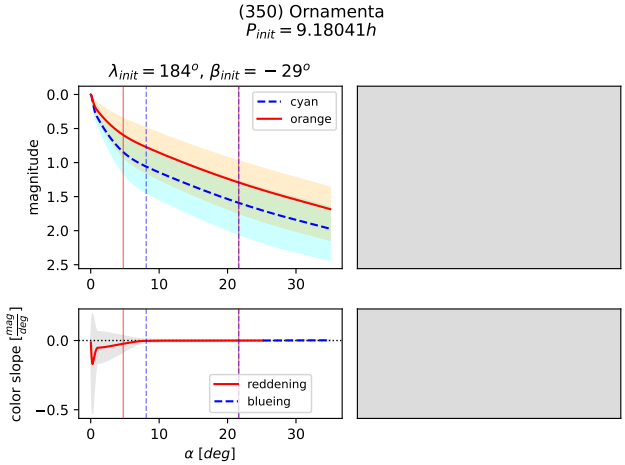

Figure 32. As in Fig. 2 for asteroid (350) Ornamenta.

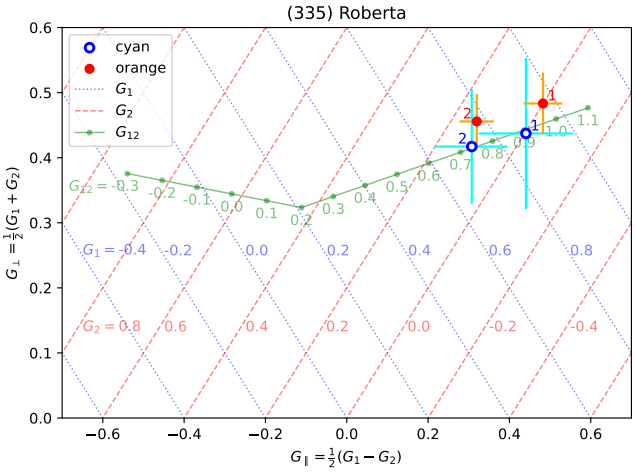

Figure 30. As in Fig. 3 for asteroid (335) Roberta.

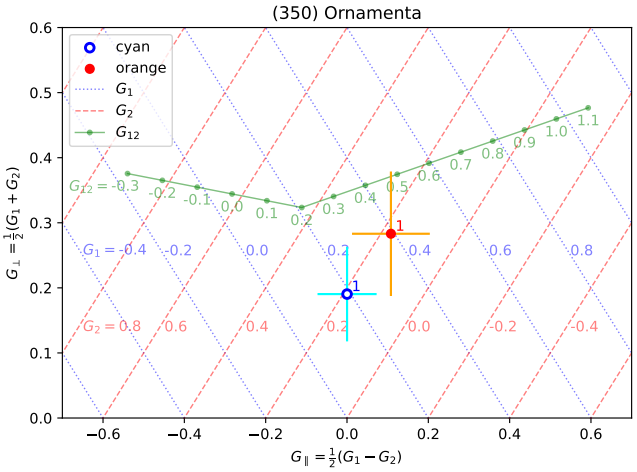

Figure 33. As in Fig. 3 for asteroid (350) Ornamenta.

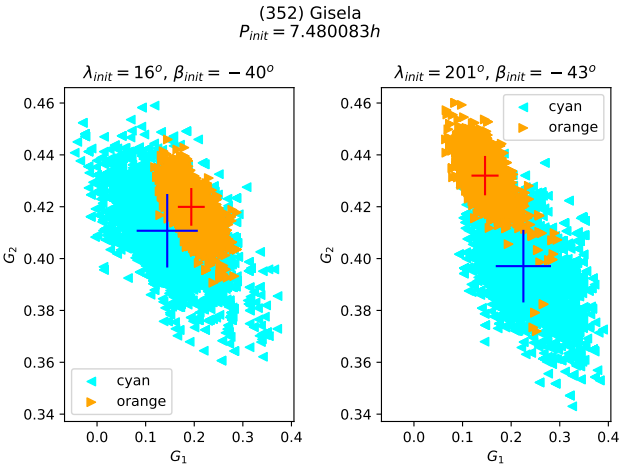

Figure 34. As in Fig. 1 for asteroid (352) Gisela.

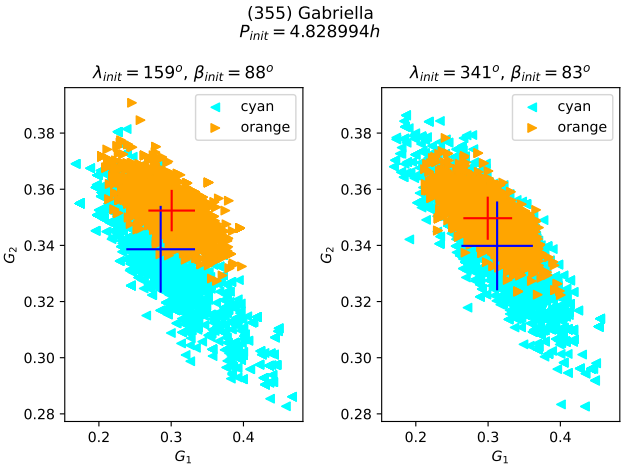

Figure 37. As in Fig. 1 for asteroid (355) Gabriella.

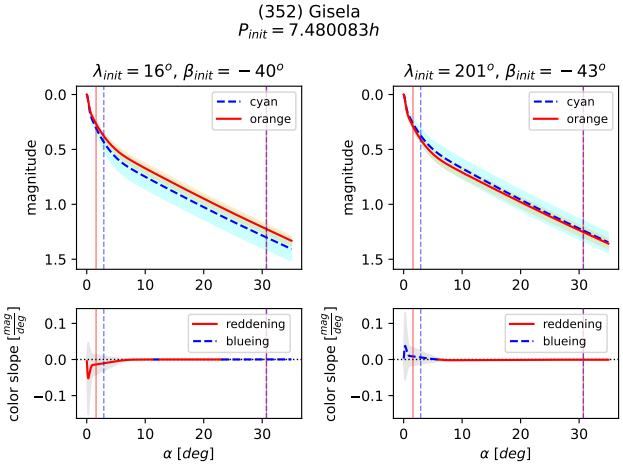

Figure 35. As in Fig. 2 for asteroid (352) Gisela.

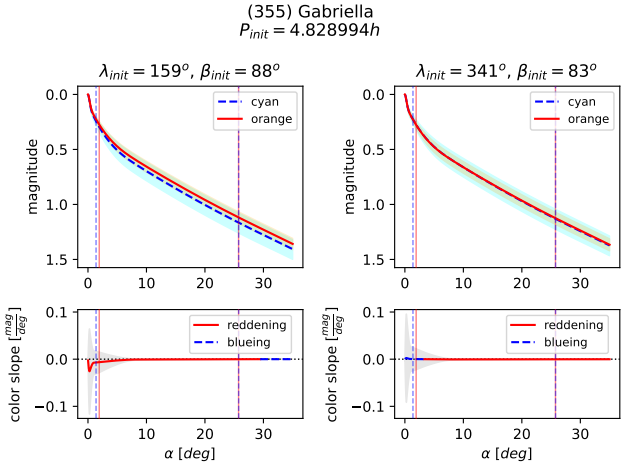

Figure 38. As in Fig. 2 for asteroid (355) Gabriella.

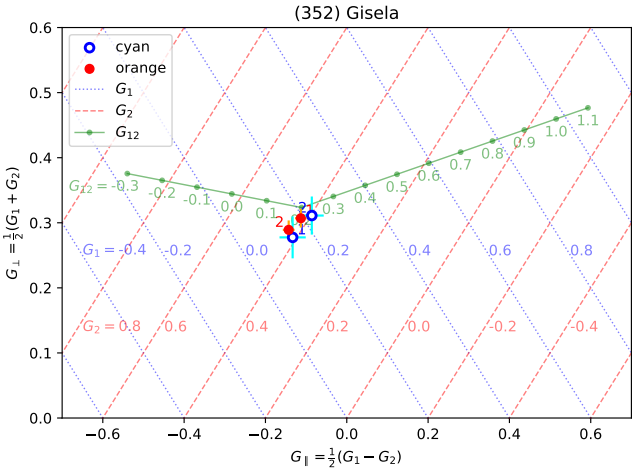

Figure 36. As in Fig. 3 for asteroid (352) Gisela.

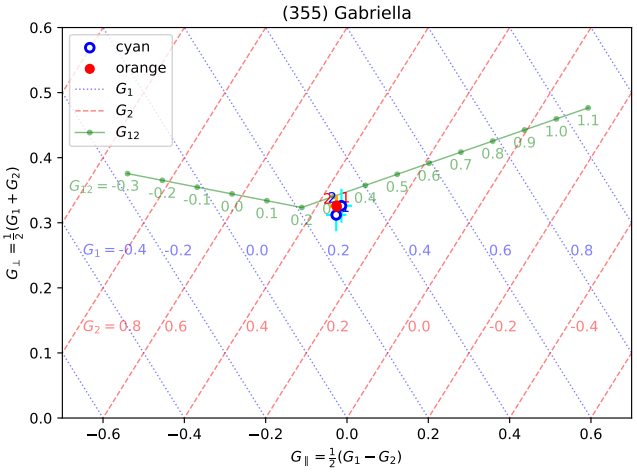

Figure 39. As in Fig. 3 for asteroid (355) Gabriella.

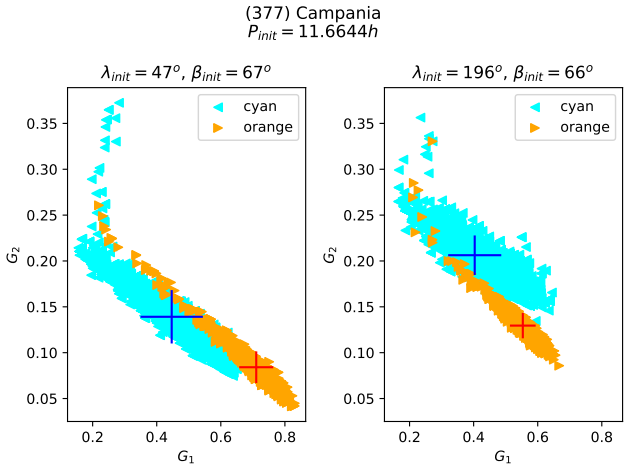

Figure 40. As in Fig. 1 for asteroid (377) Campania.

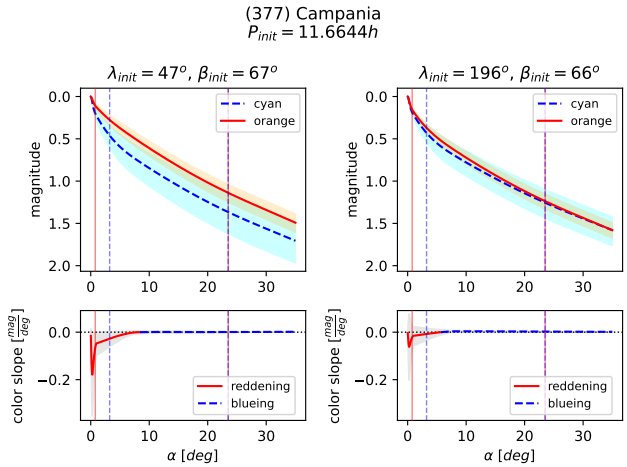

Figure 41. As in Fig. 2 for asteroid (377) Campania.

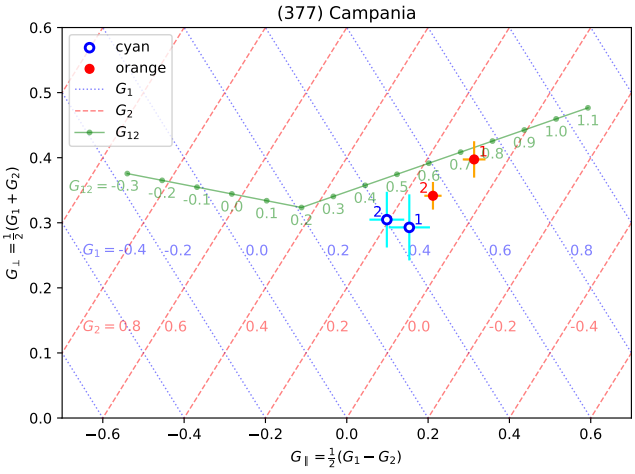

Figure 42. As in Fig. 3 for asteroid (377) Campania.

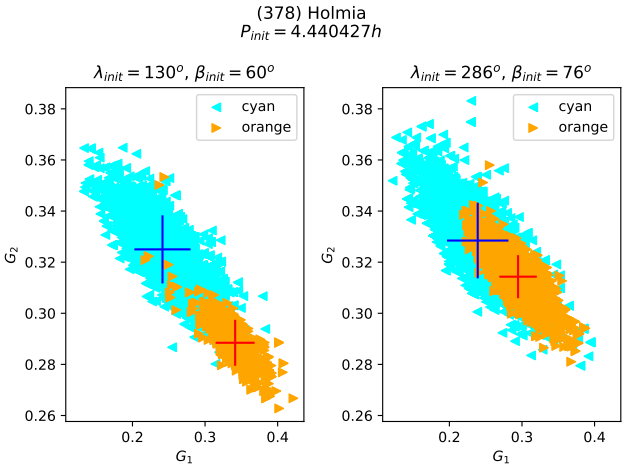

Figure 43. As in Fig. 1 for asteroid (378) Holmia.

Figure 44. As in Fig. 2 for asteroid (378) Holmia.

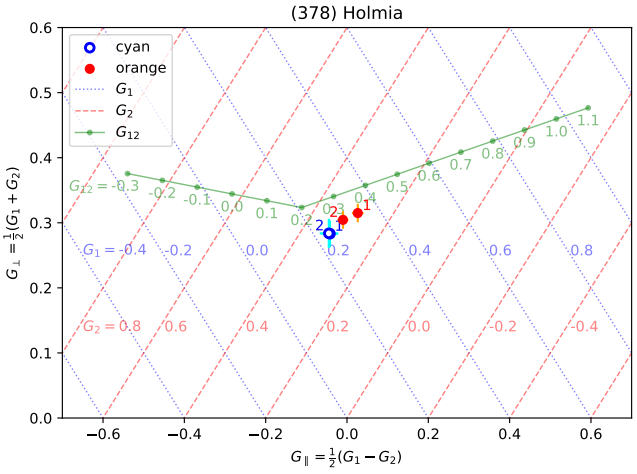

Figure 45. As in Fig. 3 for asteroid (378) Holmia.

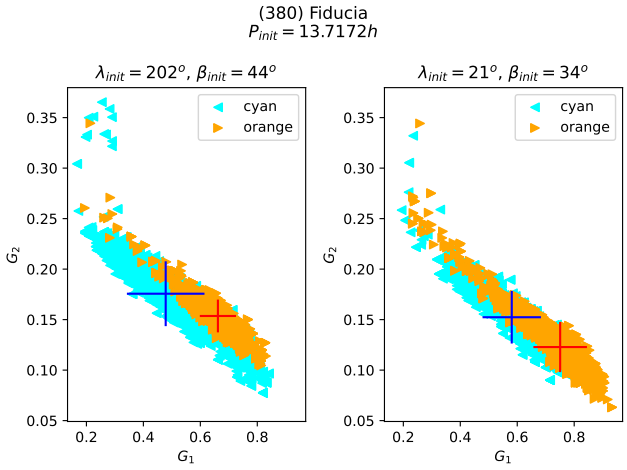

Figure 46. As in Fig. 1 for asteroid (380) Fiducia.

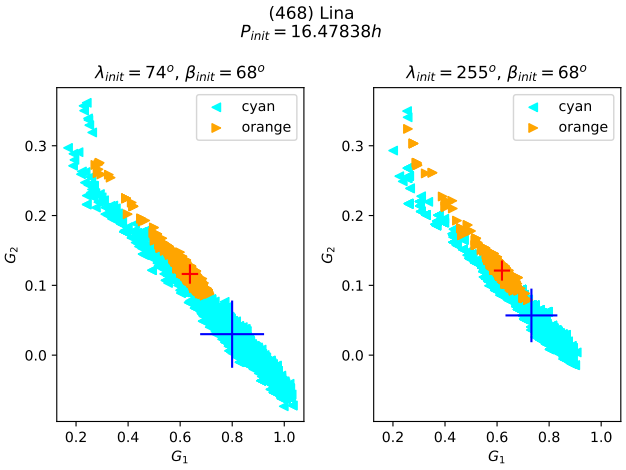

Figure 49. As in Fig. 1 for asteroid (468) Lina.

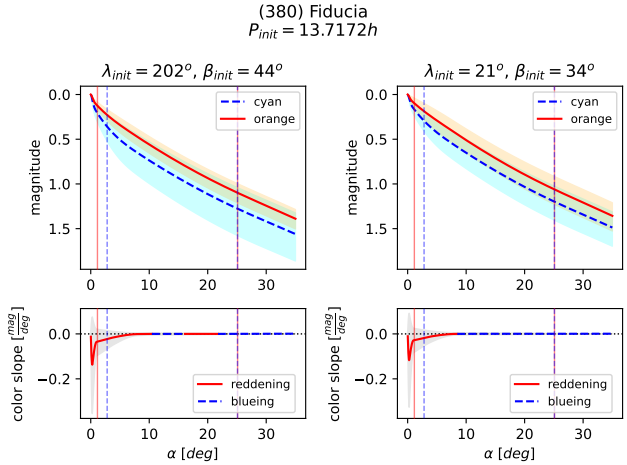

Figure 47. As in Fig. 2 for asteroid (380) Fiducia.

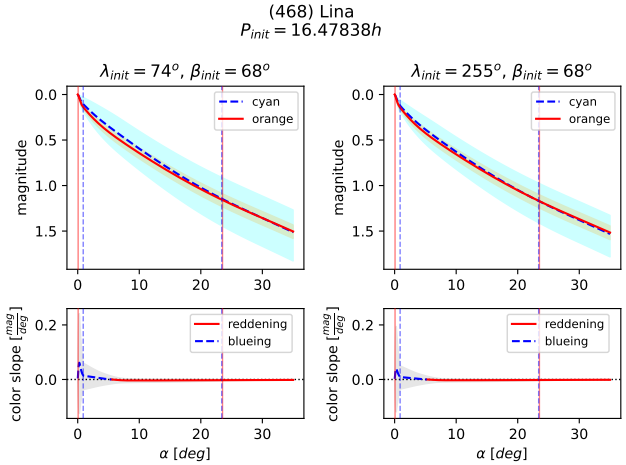

Figure 50. As in Fig. 2 for asteroid (468) Lina.

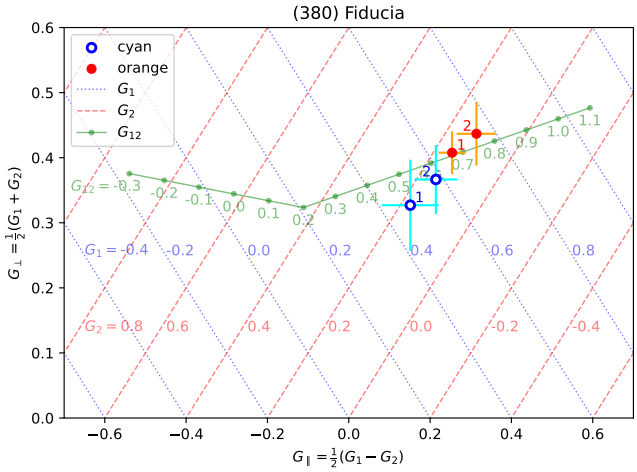

Figure 48. As in Fig. 3 for asteroid (380) Fiducia.

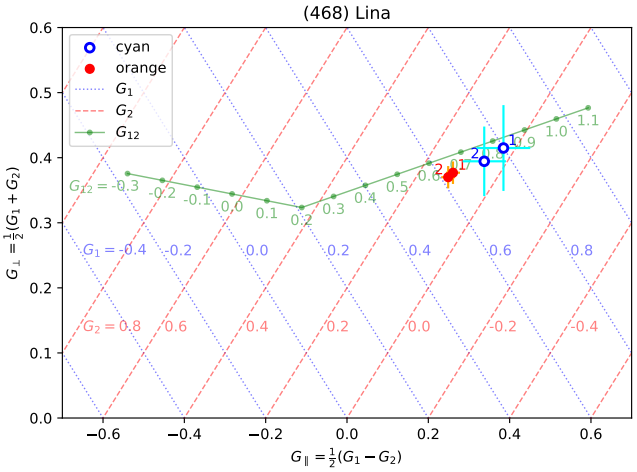

Figure 51. As in Fig. 3 for asteroid (468) Lina.

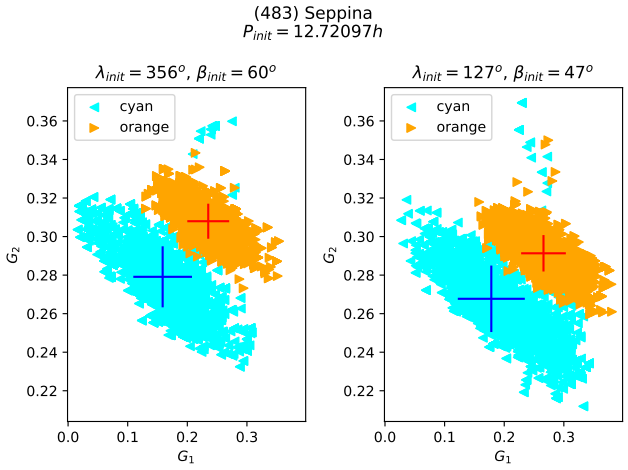

Figure 52. As in Fig. 1 for asteroid (483) Seppina.

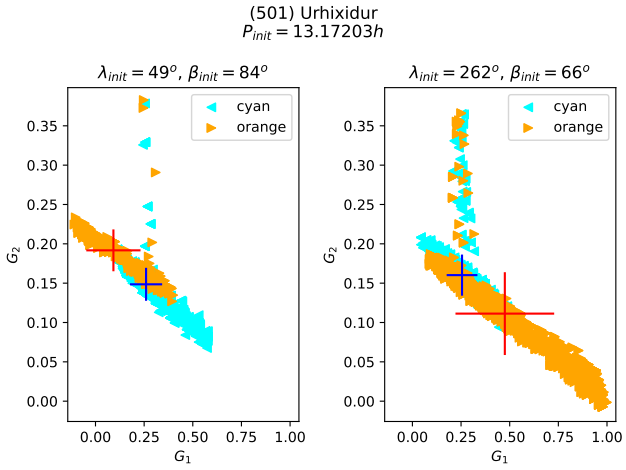

Figure 55. As in Fig. 1 for asteroid (501) Urhixidur.

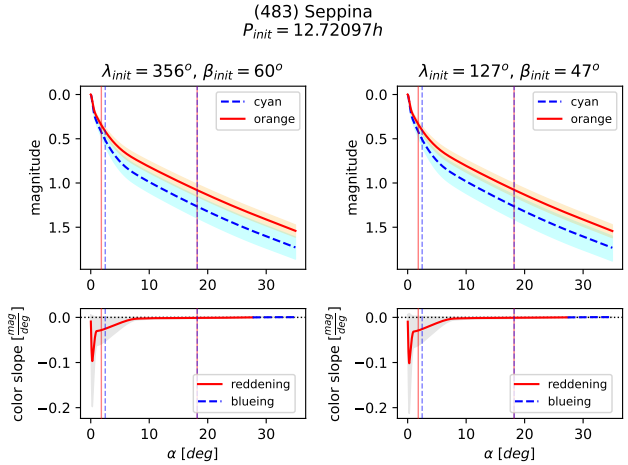

Figure 53. As in Fig. 2 for asteroid (483) Seppina.

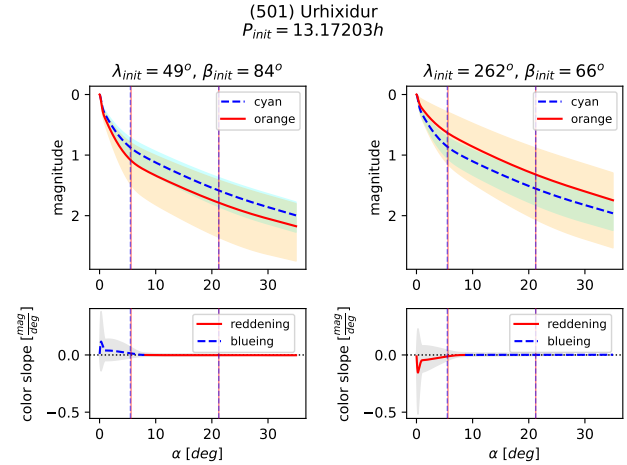

Figure 56. As in Fig. 2 for asteroid (501) Urhixidur.

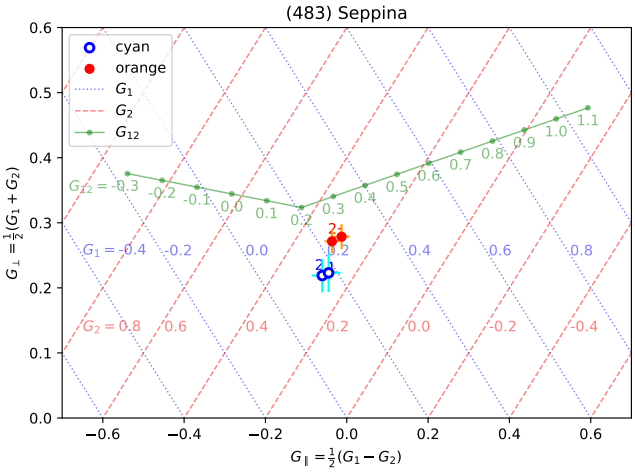

Figure 54. As in Fig. 3 for asteroid (483) Seppina.

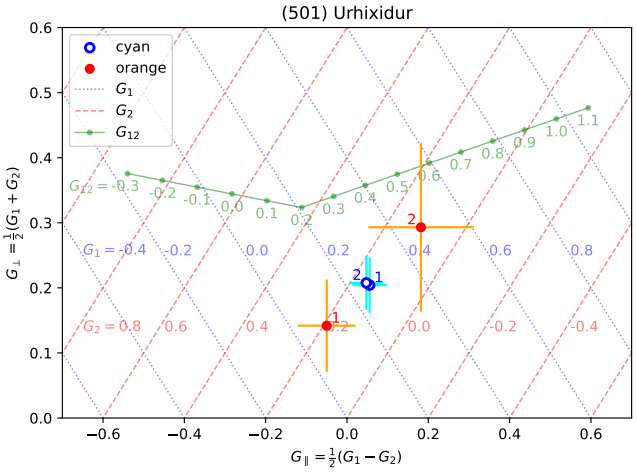

Figure 57. As in Fig. 3 for asteroid (501) Urhixidur.

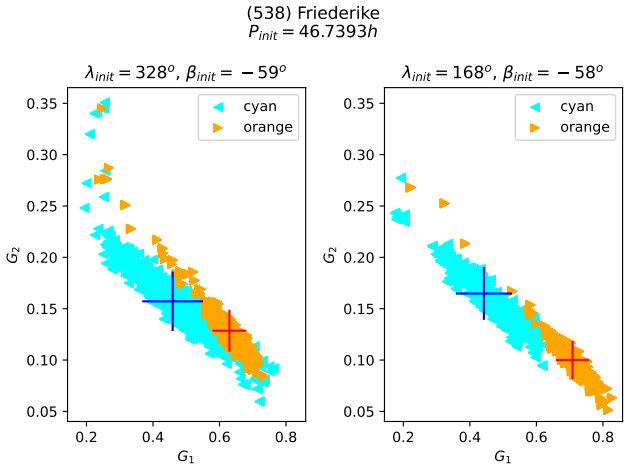

Figure 58. As in Fig. 1 for asteroid (538) Friederike.

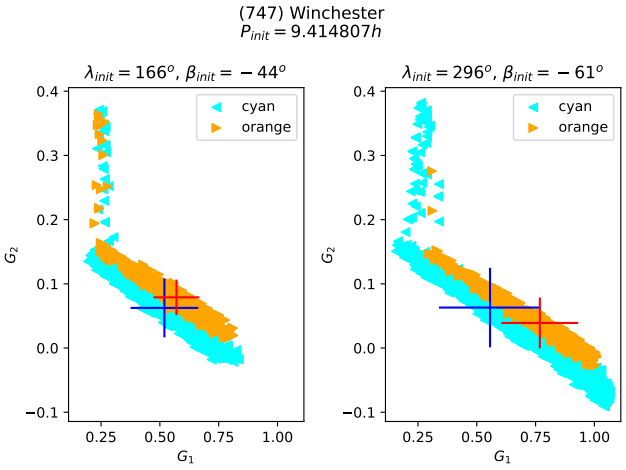

Figure 61. As in Fig. 1 for asteroid (747) Winchester.

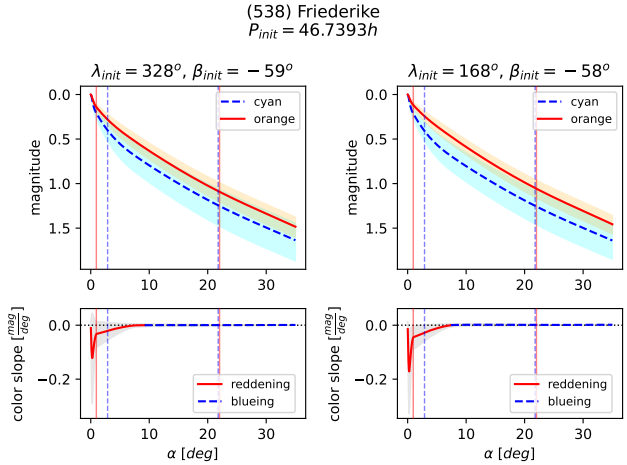

Figure 59. As in Fig. 2 for asteroid (538) Friederike.

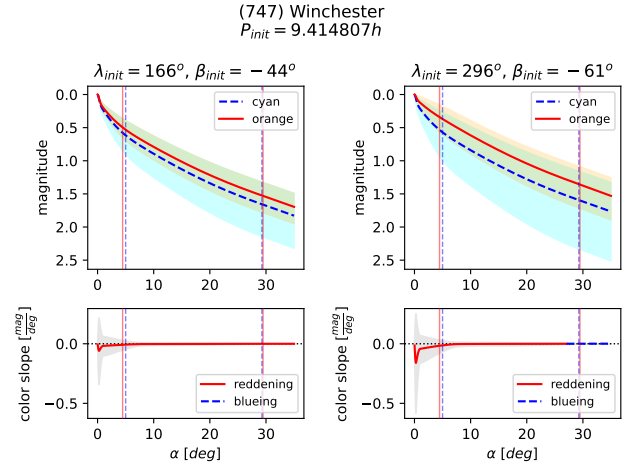

Figure 62. As in Fig. 2 for asteroid (747) Winchester.

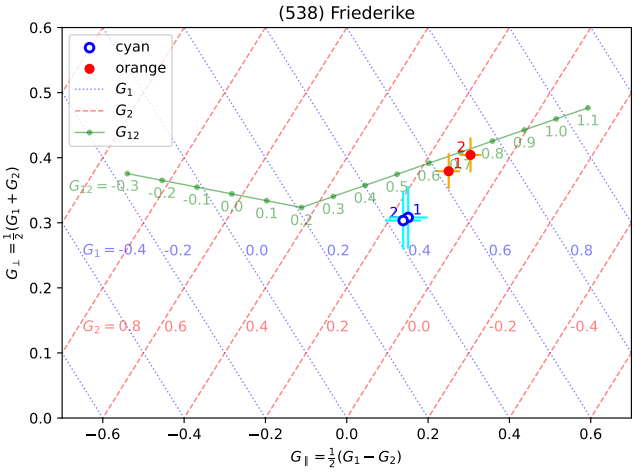

Figure 60. As in Fig. 3 for asteroid (538) Friederike.

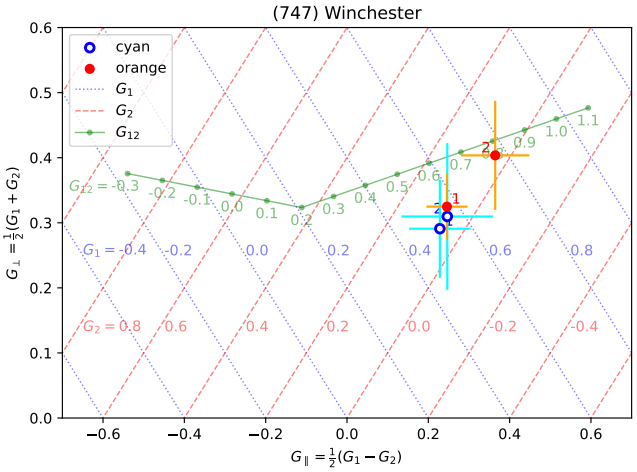

Figure 63. As in Fig. 3 for asteroid (747) Winchester.

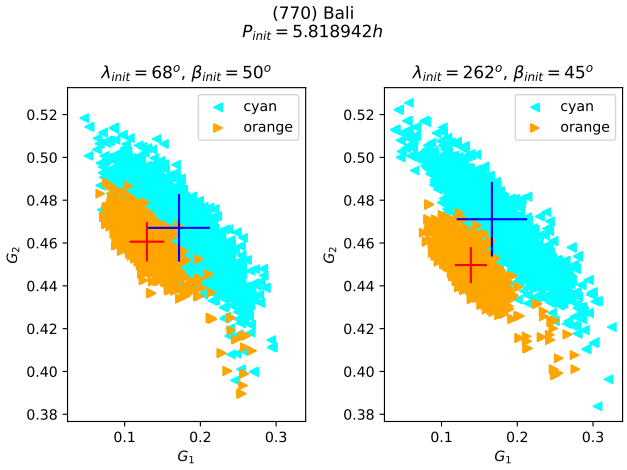

Figure 64. As in Fig. 1 for asteroid (770) Bali.

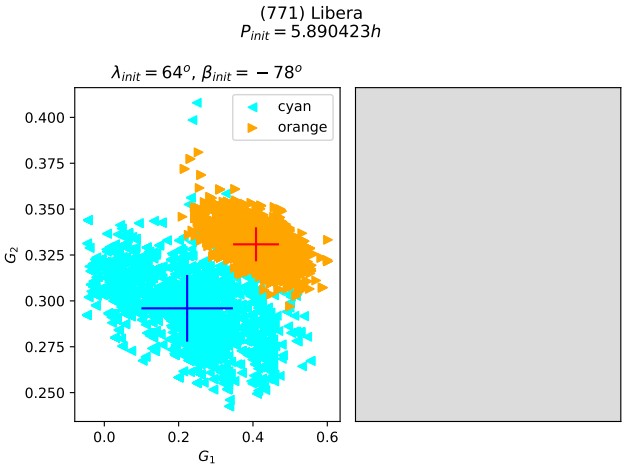

Figure 67. As in Fig. 1 for asteroid (771) Libera.

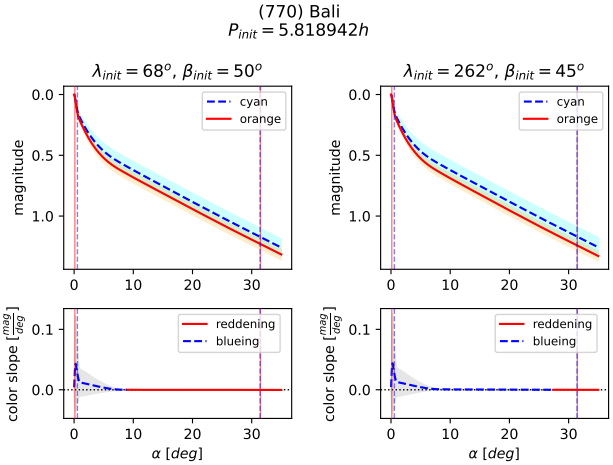

Figure 65. As in Fig. 2 for asteroid (770) Bali.

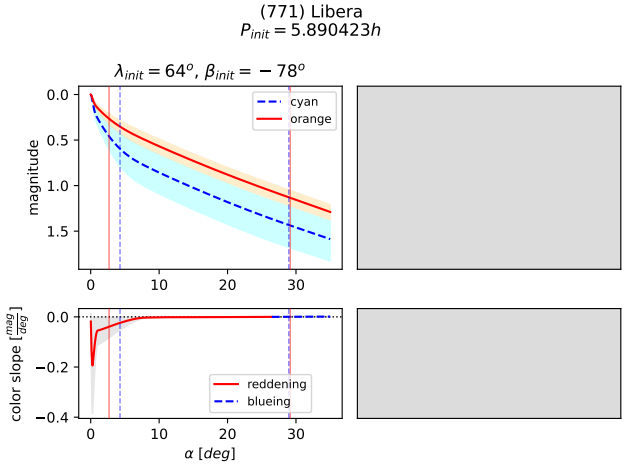

Figure 68. As in Fig. 2 for asteroid (771) Libera.

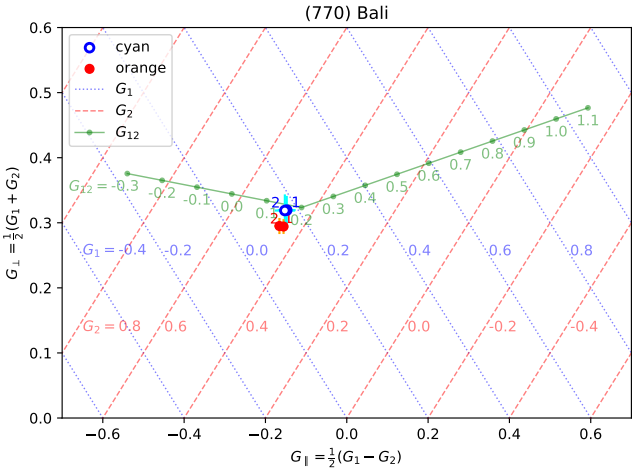

Figure 66. As in Fig. 3 for asteroid (770) Bali.

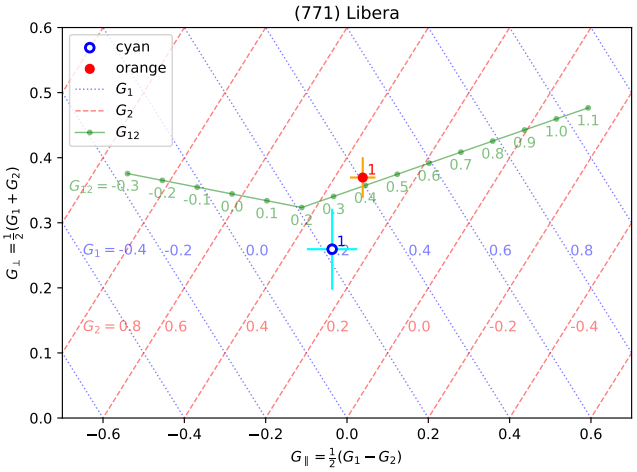

Figure 69. As in Fig. 3 for asteroid (771) Libera.

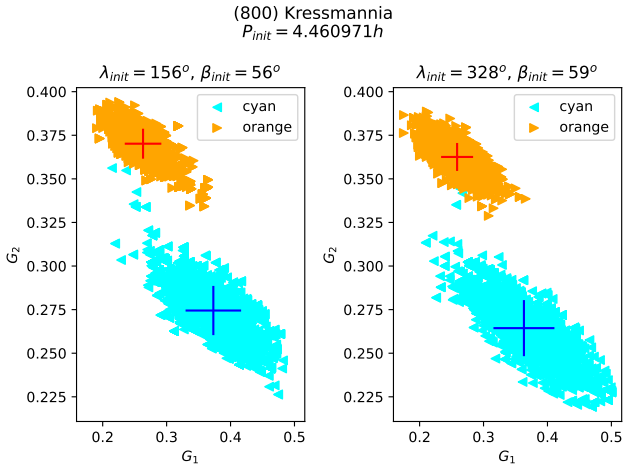

Figure 70. As in Fig. 1 for asteroid (800) Kressmannia.

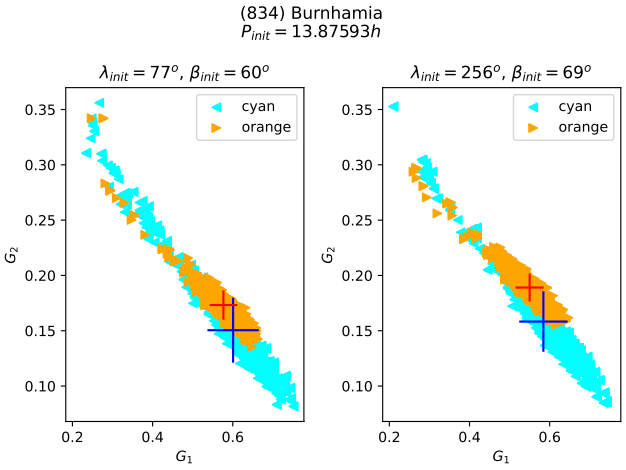

Figure 73. As in Fig. 1 for asteroid (834) Burnhamia.

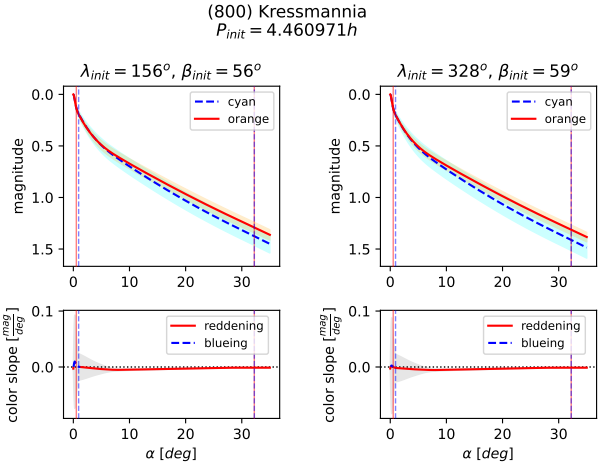

Figure 71. As in Fig. 2 for asteroid (800) Kressmannia.

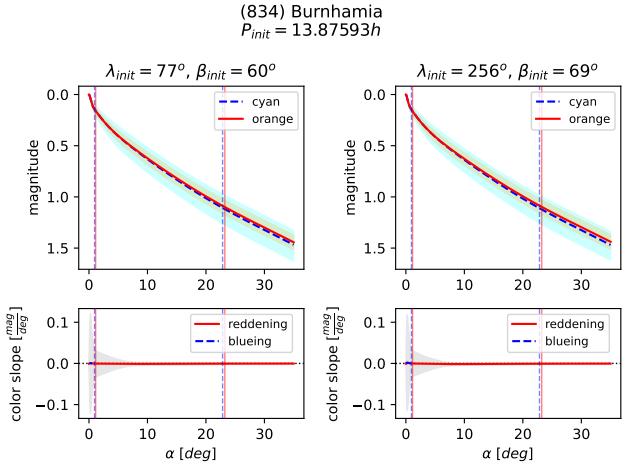

Figure 74. As in Fig. 2 for asteroid (834) Burnhamia.

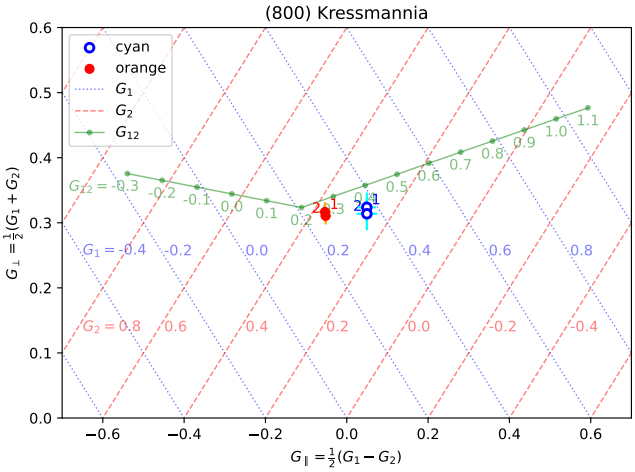

Figure 72. As in Fig. 3 for asteroid (800) Kressmannia.

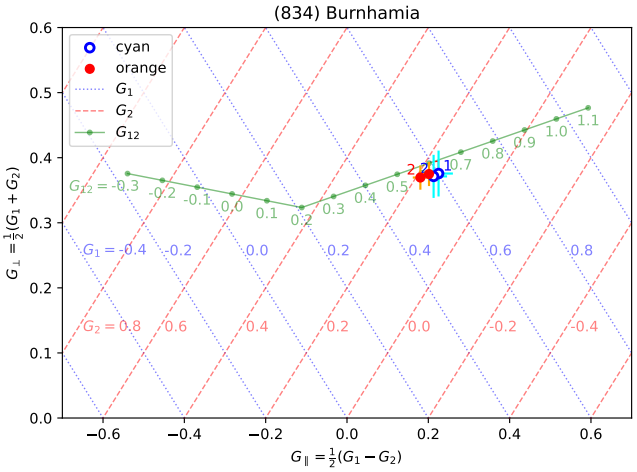

Figure 75. As in Fig. 3 for asteroid (834) Burnhamia.

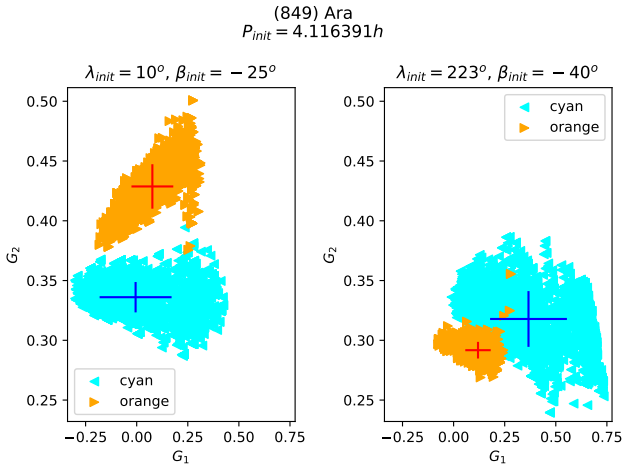

Figure 76. As in Fig. 1 for asteroid (849) Ara.

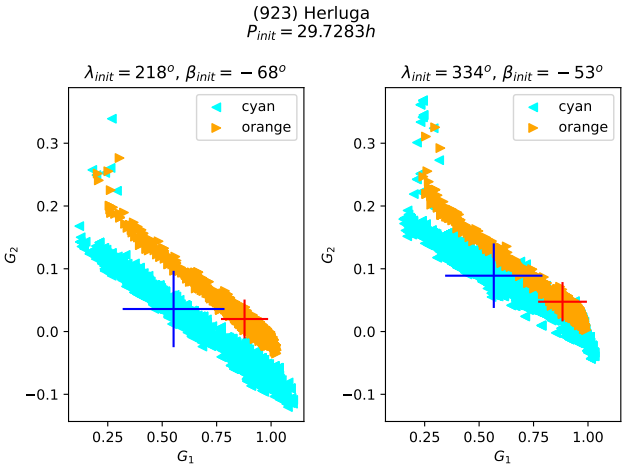

Figure 79. As in Fig. 1 for asteroid (923) Herluga.

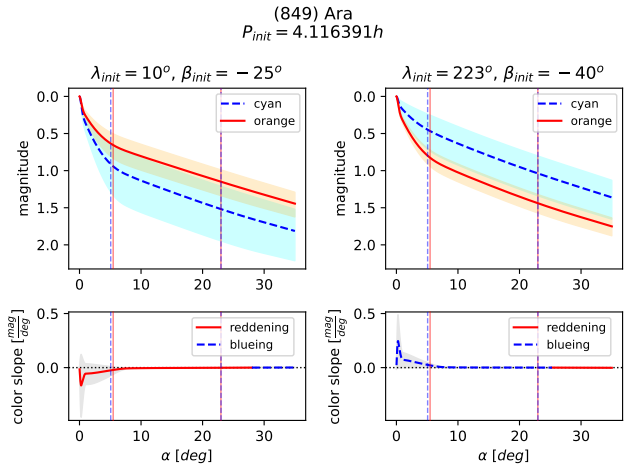

Figure 77. As in Fig. 2 for asteroid (849) Ara.

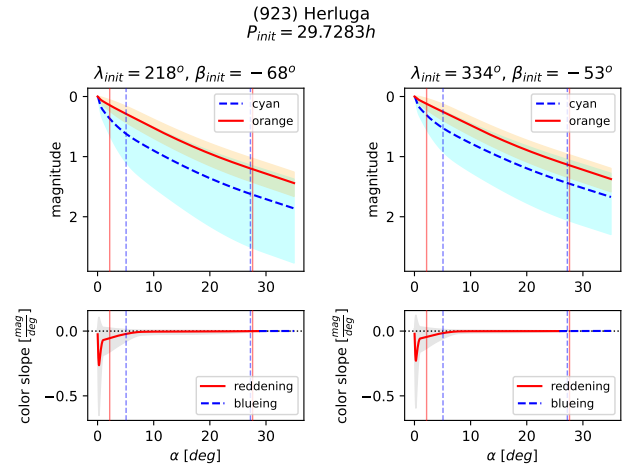

Figure 80. As in Fig. 2 for asteroid (923) Herluga.

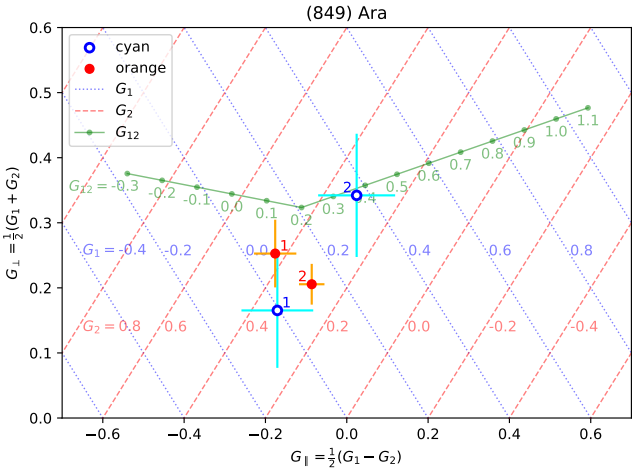

Figure 78. As in Fig. 3 for asteroid (849) Ara.

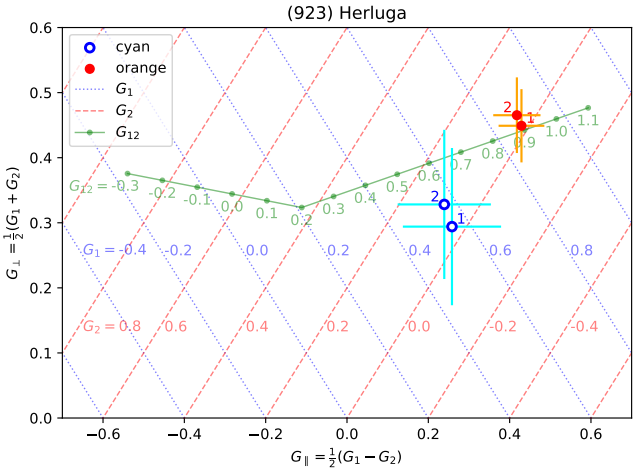

Figure 81. As in Fig. 3 for asteroid (923) Herluga.

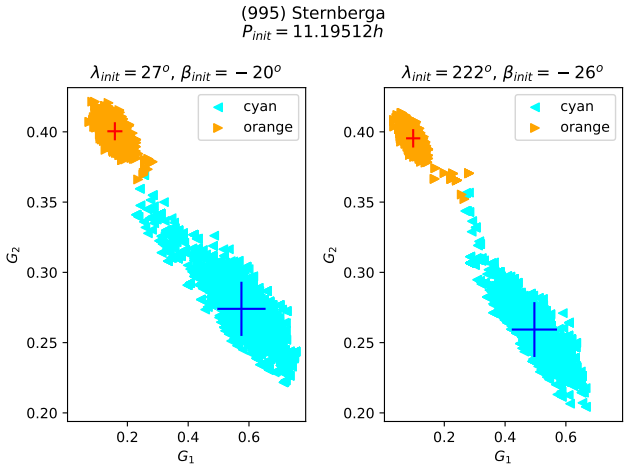

Figure 82. As in Fig. 1 for asteroid (995) Sternberga.

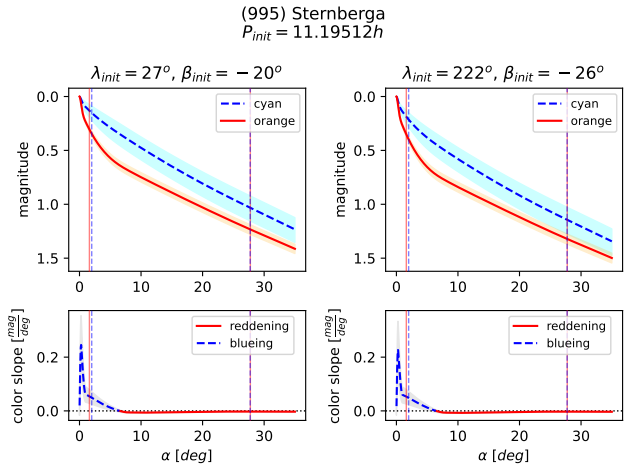

Figure 83. As in Fig. 2 for asteroid (995) Sternberga.

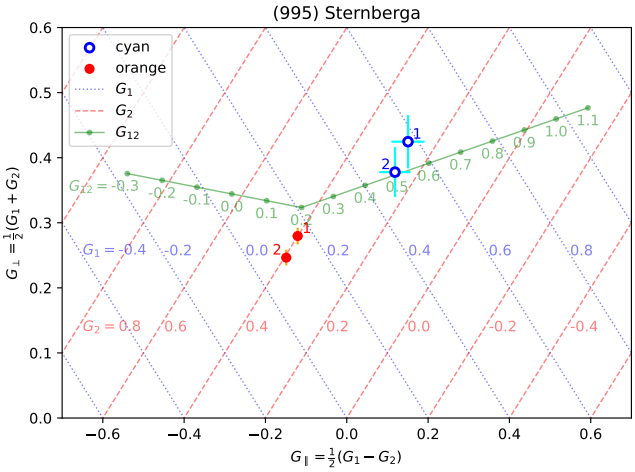

Figure 84. As in Fig. 3 for asteroid (995) Sternberga.

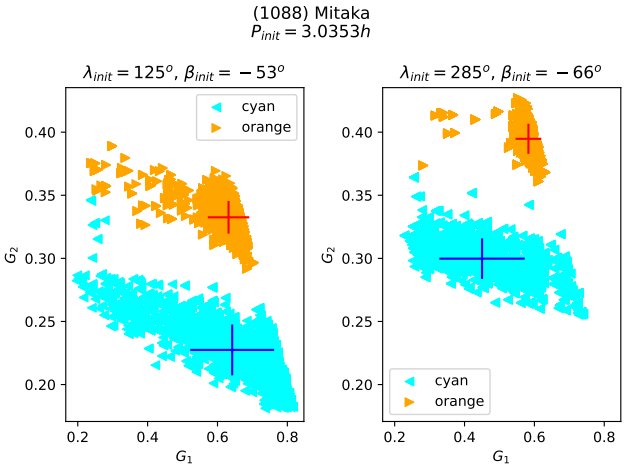

Figure 85. As in Fig. 1 for asteroid (1088) Mitaka.

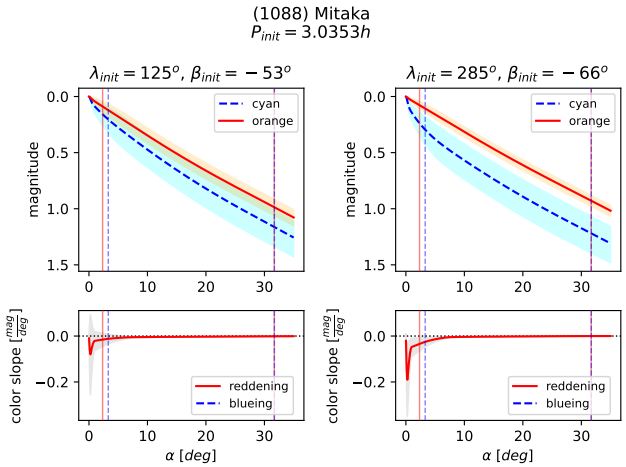

Figure 86. As in Fig. 2 for asteroid (1088) Mitaka.

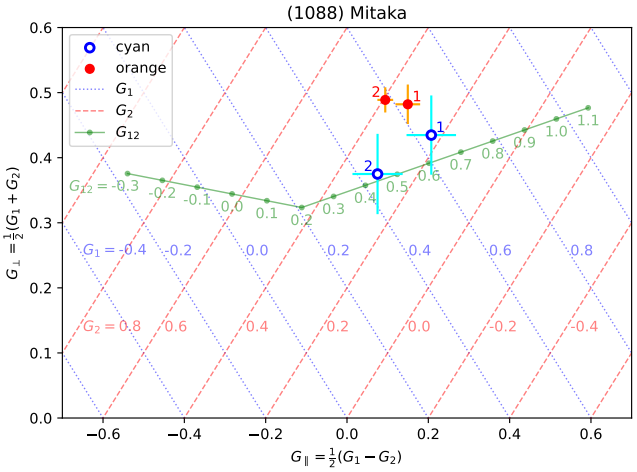

Figure 87. As in Fig. 3 for asteroid (1088) Mitaka.

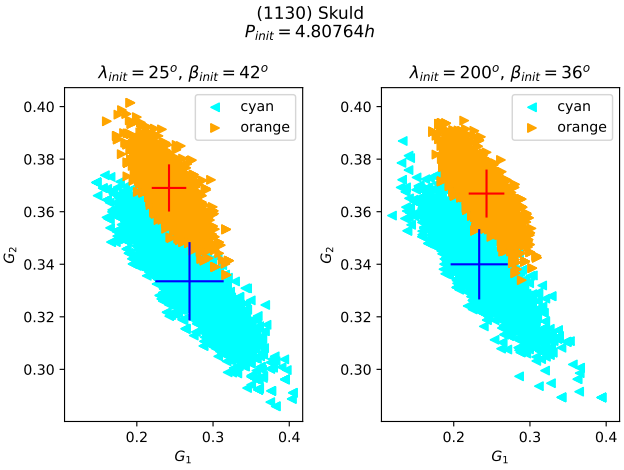

Figure 88. As in Fig. 1 for asteroid (1130) Skuld.

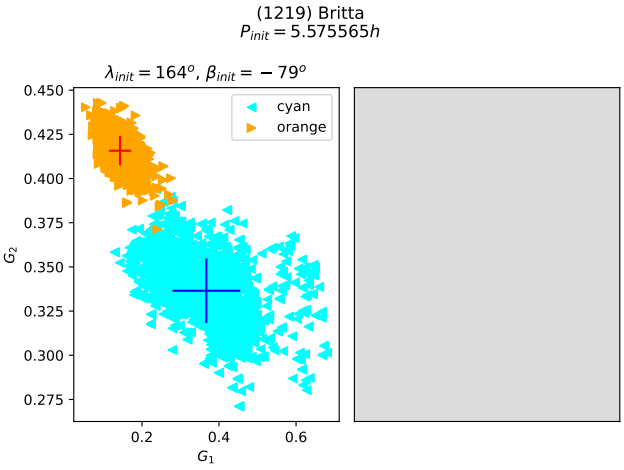

Figure 91. As in Fig. 1 for asteroid (1219) Britta.

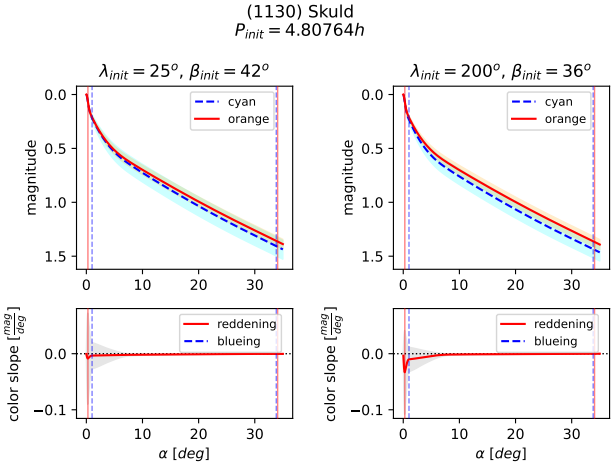

Figure 89. As in Fig. 2 for asteroid (1130) Skuld.

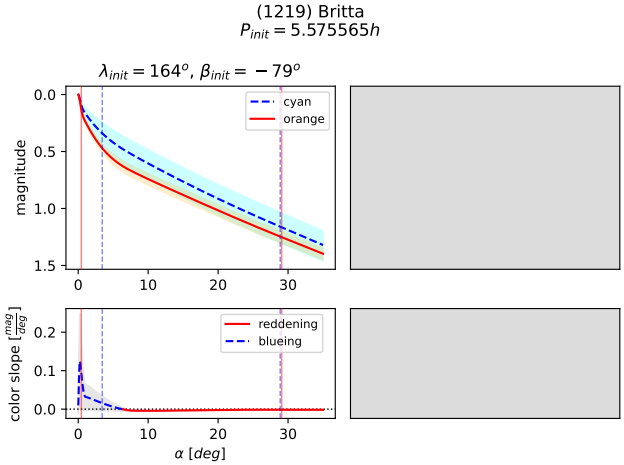

Figure 92. As in Fig. 2 for asteroid (1219) Britta.

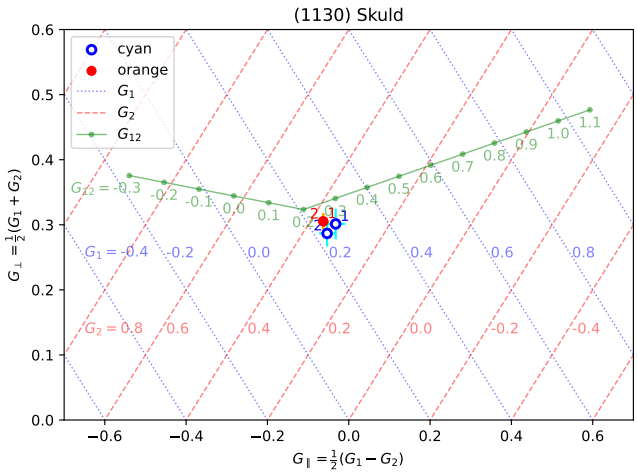

Figure 90. As in Fig. 3 for asteroid (1130) Skuld.

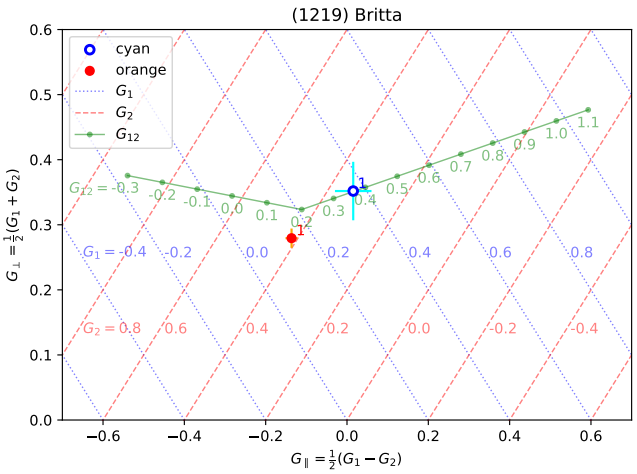

Figure 93. As in Fig. 3 for asteroid (1219) Britta.

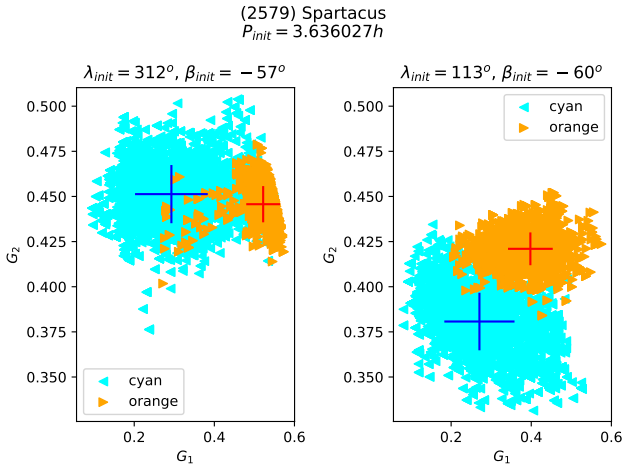

Figure 94. As in Fig. 1 for asteroid (2579) Spartacus.

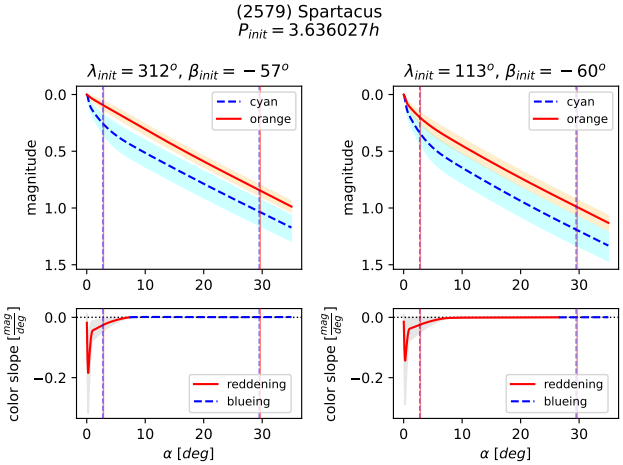

Figure 95. As in Fig. 2 for asteroid (2579) Spartacus.

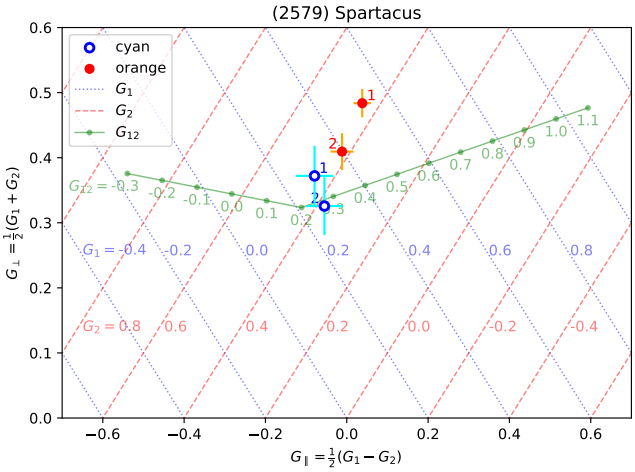

Figure 96. As in Fig. 3 for asteroid (2579) Spartacus.